

UNIVERSITÉ DU QUÉBEC

THÈSE PRÉSENTÉE À
L'UNIVERSITÉ DU QUÉBEC À TROIS-RIVIÈRES

COMME EXIGENCE PARTIELLE
DU DOCTORAT EN GÉNIE ÉLECTRIQUE

PAR
FARIS HAMOUD

CONTRIBUTION À L'AMÉLIORATION DES PERFORMANCES D'UNE ÉOLIENNE
À BASE DE GÉNÉRATRICE ASYNCHRONE À DOUBLE STATOR

SEPTEMBRE 2018

Université du Québec à Trois-Rivières

Service de la bibliothèque

Avertissement

L'auteur de ce mémoire ou de cette thèse a autorisé l'Université du Québec à Trois-Rivières à diffuser, à des fins non lucratives, une copie de son mémoire ou de sa thèse.

Cette diffusion n'entraîne pas une renonciation de la part de l'auteur à ses droits de propriété intellectuelle, incluant le droit d'auteur, sur ce mémoire ou cette thèse. Notamment, la reproduction ou la publication de la totalité ou d'une partie importante de ce mémoire ou de cette thèse requiert son autorisation.

UNIVERSITÉ DU QUÉBEC

THESIS PRESENTED TO
UNIVERSITÉ DU QUÉBEC À TROIS-RIVIÈRES

IN PARTIAL FULFILMENT OF THE REQUIREMENTS
OF THE DEGREE OF DOCTOR OF PHILOSOPHY
IN ELECTRICAL ENGINEERING

BY
FARIS HAMOUD

CONTRIBUTION IN PERFORMANCE IMPROVMENT OF WIND TURBINE BASED
DUAL STATOR WINDING INDUCTION GENERATOR

SEPTEMBER 2018

UNIVERSITÉ DU QUÉBEC À TROIS-RIVIÈRES

DOCTORAT EN GÉNIE ÉLECTRIQUE (PH.D.)

Programme offert par l'Université du Québec à Trois-Rivières

CONTRIBUTION À L'AMÉLIORATION DES PERFORMANCES D'UNE
ÉOLIENNE À BASE DE GÉNÉRATRICE ASYNCHRONE À DOUBLE STATOR

PAR

FARIS HAMOUD

Mamadou Lamine Doumbia, directeur de recherche Université du Québec à Trois-Rivières

Adel Omar Dahmane, président du jury Université du Québec à Trois-Rivières

Ahmed Chériti, codirecteur de recherche Université du Québec à Trois-Rivières

Mohamed Benhaddadi, évaluateur CEGEP du Vieux Montréal, évaluateur

Ambrish Chandra, évaluateur externe École de Technologie Supérieure

Abstract

This thesis is devoted to a new topology of wind energy conversion system based on self-excitation dual stator winding induction generator (SE-DSWIG), driven in variable speed for simultaneous grid-tied and stand-alone applications. SE-DSWIG is a promising technology that shows high efficiency for variable frequency applications in aerospace, maritime, vehicles and for extraction of hydro and wind power. In the literature, the proposed topologies, especially in variable speed operation, had a weak ability to deal with sudden and large speed variations, which induce voltage collapse and disturb the frequency. Hence, it's imperative to improve the low voltage ride through (LVRT) capability of SE-DSWIG and maintain the power flow at an adequate level even during wind speed variation or grid disturbance.

The contribution of this dissertation is built on the enhancement of power quality and the improvement of low-voltage ride-through capability of SE-DSWIG. Hence, a multi-converter based unified power quality conditioner (MC-UPQC) is used to sustain the power flow and to mitigate faults. MC-UPQC involves three converters connected back-to-back through an energy storage system. Two of them are connected in series to the SE-DSWIG terminals, while the other converter acts as a D-STATCOM and connected in shunt to the stator terminal which is linked with the grid. MC-UPQC proved its ability to compensate the supply voltage imperfection, enhance voltage and current at the point of common coupling (PCC) even in the presence of sudden faults, ameliorate the low voltage ride through (LVRT) capability, and synchronize the generator on the same frequency of the grid.

D-STATCOM, DVR and UPQC have been evaluated against voltage sag, swell, poor power factor, distorted voltage, unbalanced current and harmonics neutral current. A control strategy based sliding mode has been applied on D-STATCOM and a simple hysteresis technique was used to control the DVR, while the UPQC was supervised using an adaptive fuzzy logic control technique. The obtained results show high performance of these active compensators against the critical situations.

The SE-DSWIG was investigated in stand-alone and grid-connected operating modes. A multi-converter based unified power quality conditioner (MC-UPQC) has been used to improve the low voltage ride through (LVRT) capability of the generator.

A synchronous reference frame theory is used to supervise the series part of MC-UPQC, while an advanced cascade sliding mode control technique is applied to the shunt part. The analysis of the obtained results leads to conclude that the MC-UPQC ameliorates the performance of the SE-DSWIG in both grid-tied and stand-alone applications. MC-UPQC could compensate the supplied voltage disturbance, enhance voltage quality and current at the PCC even in the presence of sudden faults, ameliorate the LVRT capability, and synchronize the generator on the same frequency of the grid.

Acknowledgements

Praise is to Allah by Whose grace good deeds are completed. Praise is to Allah, Lord of the Worlds for his guidance, compassion in difficult moments, and help to finish this work.

Then, I would like to express my sincere gratitude to Professor Mamadou Lamine Doumbia, my thesis advisor, for his confidence, advice, availability, support, and contribution to the success of this work. Many thanks for his manner to deal with students, the way he encourages and respects them. Special thanks are expressed to Professor Ahmed Cheriti, thesis co-supervisor, for his availability, constructive criticisms, his encouragement. I want to express my grateful also to Nasserline Boudjerda, Professor at the University of Jijel, Algeria, for his help, moral support, he has always believed in me.

I would like to express my affectionate appreciation to parents for their prayers, unwavering faith, sacrifices and continuous encouragement to work hard during my academic education. May Allah prolong their lives. I want to thank my brothers, my sisters and my family for their unwavering support. This work is especially dedicated to my wife and my daughter Nada, who's with patience and continued support have helped me to carry out this work.

Finally, I want to thank all professors and staff of the electrical and computer engineering department, my colleagues Mohammed, Paul, Bekhada, Allal, Alain Innocent in the laboratory of power quality and energy conversion.

Table des matières

Abstract	iii
Acknowledgements	v
Table des matières.....	vi
Liste des tableaux.....	xv
Liste des figures	xvi
List of acronyms	xxiii
Chapitre 1 - Introduction.....	1
1.1 A brief history on the energy.....	1
1.2 Renewable resources: Status and Trends	3
1.2.1 Biomass energy.....	3
1.2.2 Geothermal energy.....	4
1.2.3 Ocean energy	5
1.2.4 Hydropower energy	6
1.2.5 Solar energy	6
1.2.6 Wind energy.....	6
1.3 Main parts of wind turbine	7

1.3.1	Power electronic devices in wind turbine	8
1.3.2	Generator in wind turbine	9
1.3.2.1	<i>Wound-rotor synchronous generator</i>	9
1.3.2.2	<i>Permanent synchronous generator</i>	10
1.3.2.3	<i>Double fed induction generator</i>	10
1.3.2.4	<i>Self-excitation induction generator</i>	11
1.3.3	Goals and challenges of Wind turbine industry	12
1.3.4	Self-excitation dual stator winding induction generator: State-of-the-art on multiphase generator.....	12
1.4	Research Goals	22
1.4.1	Main objective	22
1.4.2	Contribution of this thesis.....	23
1.4.3	Publications.....	24
1.4.4	Outline of thesis	24
Chapre 2 - Field oriented control of a dual stator winding induction motor with indirect speed regulation method.....		
2.1	Introduction	26
2.2	Description of the dual stator winding induction motor.....	27
2.3	Mathematical modeling of DSWIM in biphas system	27
2.3.1	Electric equations.....	28

2.3.2	Magnetic equations	28
2.3.3	Power consumption and electromagnetic torque of DSWIM ..	29
2.4	Dual stator winding induction motor for variable speed application ..	30
2.4.1	DSWIM fed directly from the grid	31
2.4.2	DSWIM fed by a voltage source inverter with PWM control ..	31
2.4.2.1	<i>Modelling of voltage source inverter</i>	31
2.4.2.2	<i>Open loop control of inverters using PWM</i>	33
2.4.3	Vector control of dual stator winding induction motor	34
2.4.3.1	<i>Principle of field-oriented vector control technique</i>	35
2.4.3.2	<i>Indirect vector control with speed regulation</i>	35
2.5	Numerical simulation and results discussion	42
2.5.1	Case study #1	42
2.5.2	Case study# 2	44
2.5.3	Case study# 3	45
2.6	Conclusion.....	49
Chapre 3 - Self-Excited-DSWIG for stand-alone application with passive		
compensator		50
3.1	Introduction	50
3.2	Description of SE-DSWIG	50
3.3	Mathematical modeling of SE-DSWIG	51

3.3.1	Electric equations.....	51
3.3.2	Magnetic equations	52
3.3.3	Excitation capacity bank model	53
3.4	Passive compensator.....	53
3.4.1	Passive compensator design for voltage sag.....	54
3.4.1.1	<i>Shunt compensator design</i>	55
3.4.1.2	<i>Series compensator design</i>	57
3.5	Modeling of the end-user	58
3.5.1	End-user with no-passive compensator	58
3.5.2	End-user with shunt passive compensator	59
3.5.3	End-user with series passive compensator.....	59
3.6	Numerical results and discussion	60
3.6.1	SE-DSWIG performance at no-load condition	61
3.6.2	SE-DSWIG performance feeding the end-user in the presence of shunt PC	65
3.6.3	SE-DSWIG performance feeding the end-user in the presence of series PC	66
3.6.4	SE-DSWIG performance with a step change in load impedance	68

3.6.5 SE-DSWIG performance with a step change in prime mover speed	72
3.7 Conclusion.....	74
Chapre 4 - Study of D-STATCOM and DVR for poor power correction, voltage sag and swell mitigation.....	76
4.1 Introduction	76
4.2 Distributed Static Synchronous Compensator (D-STATCOM).....	77
4.2.1 D-STATCOM configuration.....	78
4.2.1.1 <i>Mathematical modeling of the power system with D-STATCOM</i> 79	
4.2.1.2 <i>Phase-Locked-Loop</i>	81
4.2.2 Design of D-STATCOM components	82
4.2.2.1 <i>Estimation of DC-side voltage and capacitor</i>	82
4.2.2.2 <i>Estimation of the interfacing filter</i>	83
4.2.2.3 <i>Frequency response of the power system</i>	84
4.2.3 D-STATCOM operation and control design	87
4.2.3.1 <i>SMC application in the inner loop</i>	90
4.2.3.2 <i>SMC application in the outer loop</i>	93
4.3 Dynamic Voltage Restorer (DVR)	94
4.3.1 DVR configuration	94

4.3.2	Mathematical modeling of the power system with DVR	95
4.3.3	Design of DVR components	96
4.3.3.1	<i>Injected voltage rating</i>	96
4.3.3.2	<i>Apparent power of DVR</i>	97
4.3.3.3	<i>Current rating of DVR</i>	97
4.3.3.4	<i>DC-side voltage</i>	97
4.3.3.5	<i>DVR interfacing filter</i>	98
4.3.4	DVR operation and control	98
4.4	D-STATCOM and DVR performance analysis	99
4.4.1	Simulation results with D-STATCOM	100
4.4.2	Simulation results with DVR	104
4.5	Conclusion	108
Chapre 5 - A Study on the UPQC for power quality improvement		109
5.1	Introduction	109
5.2	Topology of the system under study with UPQC	112
5.2.1	Description of the system under study	112
5.2.2	Mathematical modeling of the system under study	113
5.2.3	Phasor diagram of UPQC	114
5.3	Control system design	115

5.3.1	Control strategy applied on DVR	116
5.3.2	Control strategy applied on D-STATCOM	117
5.3.3	Adaptive fuzzy logic controller design	121
5.4	UPQC performance analysis	126
5.4.1	Performance analysis of DVR against voltage sag and swell	127
5.4.2	Performance of DVR against distorted voltage	129
5.4.3	Performance analysis of D-STATCOM against harmonic current	132
5.4.4	Performance analysis of D-STATCOM against unbalanced and neutral currents	133
5.5	Conclusion.....	137
Chapre 6 - Performance improvement of SE-DSWIG using a MC-UPQC....		139
6.1	Introduction	139
6.2	Compact representation of SE-DSWIG mathematical equations.....	140
6.3	System under study with MC-UPQC	141
6.3.1	Mathematical modeling of the proposed power system	143
6.3.2	Passive damping LCL filter design.....	143
6.4	Control system design	147
6.4.1	D-STATCOM control.....	148
6.4.1.1	<i>Challenges of D-STATCOM</i>	148

6.4.1.2	<i>Cascade sliding mode controller design</i>	148
6.4.2	Control of Dynamic Voltage Restorer (DVR-I, DVR-II).....	155
6.4.2.1	<i>Estimation of the synchronizing unit vector</i>	155
6.4.2.2	<i>Description of the SRF Control Theory applied to DVR</i>	156
6.5	Numeric results and analysis.....	158
6.5.1	Characteristics of SE-DSWIG in off-grid and at no-load conditions.....	158
6.5.2	SE-DSWIG performance in variable speed with non- compensator	159
6.5.3	SE-DSWIG performance in variable speed with MC-UPQC	160
6.5.4	SE-DSWIG performance in standalone application with variable load.....	161
6.5.5	SE-DSWIG performance in grid connected conditions.....	163
6.5.6	Grid active and reactive power control.....	166
6.6	Conclusion.....	169
Chapitre 7 - Conclusion		171
Bibliography		174
Appendix A – Parameters of dual stator winding induction motor		187
Appendix B – Parameters of dual stator winding induction generator, passive compensator and the load impedance		188

Appendix C – Parameters of the system under study with D-STATCOM and DVR.....	189
Appendix D – Parameters of the system under study with UPQC	190
Appendix E – Parameters of the system under study with MC-UPQC	191
Appendix F – Résumé étendu	192

Liste des tableaux

Table 5-1	Fuzzy rules [148, 149].....	124
-----------	-----------------------------	-----

Liste des figures

Figure 1-1	Biomass path [13].....	4
Figure 1-2	Countries membership in ocean energy [15].....	5
Figure 1-3	Expansion of wind energy [11]	7
Figure 1-4	Fixed speed based wind turbine [21].....	8
Figure 1-5	Partial variable speed based wind turbine [21]	9
Figure 1-6	First topology based SE-DSWIG	14
Figure 1-7	wide-speed range operation of SE-DSWIG for DC power generation [43]	16
Figure 1-8	Topology proposed for microgrid operation [45].....	17
Figure 1-9	Topology proposed to improve the reactive power controllability [34]	18
Figure 1-10	SE-DSWING connected to the grid via back-to-back converter [48]	19
Figure 1-11	Topology proposed in [51].....	20
Figure 1-12	SE-DSWIG for hybrid AC & DC power generation topology [52]	21
Figure 2-1	Scheme of DSWIM	28
Figure 2-2	Controlled three-phase inverter	32
Figure 2-3	DSWIM with PWM based inverters	34
Figure 2-4	Rotor flux orientation in DQ frame	35
Figure 2-5	Indirect vector control technique.....	39
Figure 2-6	Block diagram of PI-current control	40
Figure 2-7	Block diagram of PI-speed control.....	40

Figure 2-8	Voltage decoupling block diagram.....	41
Figure 2-9	Electromagnetic torque at no-load	42
Figure 2-10	Rotor speed at no-load.....	43
Figure 2-11	Rotor flux at no-load	43
Figure 2-12	Three-phase currents of stator I at no-load.....	44
Figure 2-13	Electromagnetic torque at full-load.....	44
Figure 2-14	Rotor speed at full-load	45
Figure 2-15	Three-phase currents of stator I at full-load	45
Figure 2-16	Electromagnetic torque in open loop control	46
Figure 2-17	Rotor speed evolution in open loop control	46
Figure 2-18	Three-phase currents of stator I.....	47
Figure 2-19	Electromagnetic torque.....	47
Figure 2-20	Rotor speed evolution.....	47
Figure 2-21	Rotor flux	48
Figure 2-22	Direct and quadrature rotor flux components.....	48
Figure 2-23	Three-phase currents of stator I.....	48
Figure 3-1	SE-DSWIG scheme.....	51
Figure 3-2	Equivalent circuit of SE-DSWIG in DQ - frame.....	52
Figure 3-3	SE-DSWIG in stand-alone application.....	55
Figure 3-4	shunt and series passive compensator topologies.....	55
Figure 3-5	Phasor diagram of shunt passive compensator.....	57
Figure 3-6	Phasor diagram of series passive compensator	58
Figure 3-7	Magnetizing current	61
Figure 3-8	Magnetizing inductance versus magnetizing current	62
Figure 3-9	Stator I voltage evolution at no-load	62

Figure 3-10	Stator II voltage evolution at no-load.....	63
Figure 3-11	Stator I current evolution at no-load.....	63
Figure 3-12	Stator II current evolution at no-load	64
Figure 3-13	Phase shift between stator current and voltage	64
Figure 3-14	Rotor current evolution	64
Figure 3-15	Stator I voltage evolution in the presence of shunt PC	65
Figure 3-16	Stator II voltage evolution in the presence of shunt PC	65
Figure 3-17	Stator I current evolution in the presence of shunt PC.....	66
Figure 3-18	Stator II current evolution in the presence of shunt PC	66
Figure 3-19	Stator I voltage evolution in the presence of series PC	67
Figure 3-20	Stator II voltage evolution in the presence of series PC.....	67
Figure 3-21	Stator I current evolution in the presence of series PC	68
Figure 3-22	Stator II current evolution in the presence of series PC	68
Figure 3-23	Stator I voltage evolution with step change in load without SSPC.....	69
Figure 3-24	Stator II voltage evolution with step change in load without SSPC.....	69
Figure 3-25	Stator I current evolution with step change in load without SSPC.....	70
Figure 3-26	Stator II current evolution with step change in load without SSPC.....	70
Figure 3-27	Stator I voltage evolution with step change in load with SSPC.	70
Figure 3-28	Stator II voltage evolution with step change in load with SSPC	71
Figure 3-29	Stator I current evolution with step change in load with SSPC	71
Figure 3-30	Stator II current evolution with step change in load with SSPC	71
Figure 3-31	Rotor speed variation.....	72
Figure 3-32	Stator I voltage evolution with step change in speed with SSPC.....	72

Figure 3-33	Stator II voltage evolution with step change in speed with SSPC.....	73
Figure 3-34	Stator I current evolution with step change in speed with SSPC.....	73
Figure 3-35	Stator II current evolution with step change in speed with SSPC.....	73
Figure 4-1	D-STATCOM connected to the grid	77
Figure 4-2	Three legs voltage /current source converter	78
Figure 4-3	Configuration of D-STATCOM.....	79
Figure 4-4	Phase Locked Loop	82
Figure 4-5	Bode diagram of the transfer function.....	84
Figure 4-6	Bode diagram of power system transfer function with variation of L_f	85
Figure 4-7	Bode diagram of power system transfer function with variation of R_f	86
Figure 4-8	Phase margin variation with L_f	86
Figure 4-9	Phase margin variation with R_f	87
Figure 4-10	Sliding mode control process	88
Figure 4-11	Cascade SMC of D-STATCOM for power factor correction	90
Figure 4-12	Saturation function	93
Figure 4-13	DVR configuration	95
Figure 4-14	Phasor diagram of DVR intervention.....	96
Figure 4-15	Hysteresis control of DVR	99
Figure 4-16	Grid voltage and current in the case of inductive load.....	100
Figure 4-17	Grid voltage and current in the case of capacitive load	101
Figure 4-18	Active and reactive power transfer between the grid and D-STATCOM.....	101
Figure 4-19	D-STATCOM output current in DQ frame	102

Figure 4-20	D-STATCOM output current in ABC frame	103
Figure 4-21	D-STATCOM output voltage evolution.....	103
Figure 4-22	Grid voltage.....	103
Figure 4-23	DC-side voltage of D-STATCOM	104
Figure 4-24	Voltage swell occurs in the grid.....	105
Figure 4-25	DVR intervention against voltage swell.....	106
Figure 4-26	Load voltage after intervention against swells.....	106
Figure 4-27	Voltage sag occurs in the grid	106
Figure 4-28	DVR intervention against sag.....	107
Figure 4-29	Load voltage after intervention against sag.....	107
Figure 5-1	Topology of the UPQC in the proposed power system.....	112
Figure 5-2	Phasor diagram of the UPQC intervention (A): against voltage sag, (B): against voltage swell, (C): against current issues.[71].....	114
Figure 5-3	Control algorithm applied on the series part of the UPQC	117
Figure 5-4	Positive sequence detector [141].....	119
Figure 5-5	Block diagram of PLL circuit [141].....	120
Figure 5-6	Control algorithm applied on the shunt part of the UPQC.....	122
Figure 5-7	Membership function [147].....	123
Figure 5-8	Structure of the adaptive logic control[148].....	125
Figure 5-9	Disturbed voltage source generator.....	126
Figure 5-10	(A): Grid Voltage, (B): Compensating voltage, (C): Load terminals voltage (PCC)	127
Figure 5-11	Zoom of Figure 5-10	128
Figure 5-12	Active and reactive power at load terminals	129
Figure 5-13	(A): Grid voltage (with harmonic generator), (B): Compensating voltage, (C): Load terminals voltage	130

Figure 5-14	(A, B): Grid voltage and its harmonic spectrum (7 th harmonic generator) (C, D): Load terminals voltage and its harmonic spectrum	131
Figure 5-15	(A, B): Grid voltage and its harmonic spectrum (7 th , 11 th harmonic generator) (C, D): Load terminals voltage and its harmonic spectrum	131
Figure 5-16	(A): Load current, (B): Compensating current (C): Grid current.....	132
Figure 5-17	(A, B): Load current and its harmonic spectrum (C, D): Grid current, and its harmonic spectrum	132
Figure 5-18	Grid current evolution with unbalanced load	133
Figure 5-19	D-STATCOM output current	134
Figure 5-20	Load and grid neutral current evolution with D-STATCOM DC-side current	134
Figure 5-21	Grid active and reactive power.....	135
Figure 5-22	Grid current of phase A with and without D-STATCOM.....	136
Figure 5-23	Grid current of phase B with and without D-STATCOM.....	136
Figure 5-24	Grid current of phase C with and without D-STATCOM.....	137
Figure 6-1	System under study with MC-UPQC	142
Figure 6-2	<i>LCL</i> -filter bloc diagram	146
Figure 6-3	Frequency response of <i>LCL</i> -filter with and without damping resistor	147
Figure 6-4	Sliding mode control process	149
Figure 6-5	Saturation function	153
Figure 6-6	Control scheme applied on D-STATCOM.....	154
Figure 6-7	Sine and cosine estimating block diagram	156
Figure 6-8	Control scheme applied DVR-I and DVR-II.....	157
Figure 6-9	SE-DSWIG output voltage.....	158
Figure 6-10	Voltage magnitude evolution	159

Figure 6-11	SE-DSWIG output current	159
Figure 6-12	SE-DSWIG output voltage in speed variation	160
Figure 6-13	Frequency profile in variable speed	160
Figure 6-14	Output voltage in variable speed	161
Figure 6-15	Compensating voltage generated by DVR-I and DVR-II	161
Figure 6-16	Stator II output voltage	162
Figure 6-17	Compensating voltage	162
Figure 6-18	Load terminal voltage	163
Figure 6-19	Grid voltage sag and swell	163
Figure 6-20	Grid frequency evolution following the voltage sag and swell	164
Figure 6-21	Compensating voltage generated by MC-UPQC	164
Figure 6-22	Grid voltage magnitude	165
Figure 6-23	D-STATCOM active and reactive power transferred with the grid	165
Figure 6-24	Grid frequency at the presence of MC-UPQC	166
Figure 6-25	Grid current at the presence of MC-UPQC	166
Figure 6-26	Active and reactive power evolution during reactive power injection	167
Figure 6-27	Active and reactive power evolution during reactive power injection	168
Figure 6-28	Active and reactive power evolution during reactive power absorption	168
Figure 6-29	Active and reactive power in reference tracking test	169

List of acronyms

AFLC	Adaptive Fuzzy Logic Controller
CSP	Concentrating Solar Power
CPD	Customer Power Devices
CSC	Current Source Converter
DFIG	Double-Fed Induction Generator
DSWIM	Dual Stator Winding Induction Motor
D-SATCOM	Distributed Static Synchronous Compensator
DVR	Dynamic Voltage Restorer
EPRI	Electrical Power Research Institute
FACTS	Flexible AC Transmission System
GTO	Gate Turn-Off
IG	Induction Generator
IGBT	Insulated Gate Bipolar Transistors

IRENA	International Renewable Energy Agency
LVRT	Low Voltage Ride Through Capability
MC-UPQC	Multi-Converter Based Unified Power Quality Conditioner
NPCs	Neutral Point Clamped Converters
PAC	Parallel Active Compensator
PC	Passive Compensator
PCC	Point Common Coupling
PLL	Phase Locked Loop
PMSG	Permanent Magnet Synchronous Generator
PQ	Power Quality
PV	Photovoltaic
PWM	Pulse-Width Modulation Technique
RE	Renewable Energy
SAC	Series Active Compensator
SEC	Static Excitation Controller
SE-DSWIG	Self-Excited Dual Stator Winding Induction Generator

SE-IG	Self-Excitation Induction Generator
SMC	Sliding Mode Control
SPAC	Series-Parallel Active Compensator
SSPC	Series-Shunt Passive Compensator
SE4ALL	Sustainable Energy for All
UPQC	Unified Power Quality Conditioner
VSC	Voltage Source Converter
WR-SG	Wound-Rotor Synchronous Generator

Chaptre 1 - Introduction

1. Motivation

1.1 A brief history on the energy

Since ancient times, the human being has been striving for the domination of natural resources to compensate his weakness in face of the daily challenges and to facilitate life. He had exploited the wind power to push ships in maritime transportation around the then known world [1]. As well, thousands of years ago, people of China and Greek also discovered the benefit of solar energy. They built their houses and neighborhoods in a specific position to absorb the sunlight during the day and reject the heat into homes especially during the winter nights. More than that, historians have reported that the Greek people with the help of Archimedes had used sunlight as mass destruction weapon against roman navy forces, in which they concentrated the sunlight on their ships to burn them using a polished metal as a mirror [2]. In the fourth century, the people in the Far-East explored the coal and extract power from it for heating, melting metals and foundry. In the eighteenth century, the coal has been used on a large scale particularly with the emergence of the industrial revolution in Europe. In the end of 1800s, the first coal-fired steam based DC-current dynamo for power generation was proposed by Siemens [3]. A few years later, Thomas Edison established the first power station where the generator was driven using coal-fired. All power stations implemented at that time characterized by a DC-current and low voltage generation, for that, the end user was installed near the source to reduce losses [4]. At the beginning of the 1900s,

scientists have designed new AC-current alternators, transformers, and with the exploration of new natural resources such as oil, gas and, nuclear, it became possible to transport power over long distance and interconnects power stations between them, which increases the installed capacity [4]. Meantime, the electric power generation area attracts attention when it proved its great impact on the economic development. Thus, huge sums have been invested to enlarge the transmission and distribution grids which help to raise the access to electricity. Furthermore, authorities have encouraged and supported research and development in this field with the introduction of new technologies enabling to build huge thermal and nuclear stations which attain 1000 MW by the end of the 1980s [5].

Despite that, 1.2 billion of the worldwide people do not access to electricity and 85% of them live in the countryside according to the World Bank's sustainable energy for all (SE4ALL) database [6]. Moreover, according to the Electrical Power Research Institute (EPRI), losses due to outage and power quality issues, only in the USA, cost between 119 \$ and 188 \$ billions a year [7]. Besides, environmental organizations around the world called the attention about the rapid depletion of fossil fuels and the attendant global warming issue related to the high exploitation of these conventional resources such as oil, gas, and coal. Accordingly, we draw that the conventional methods of the power supply based on the installed of huge power stations and the extension of the power transmission grid are not economically feasible and technically so difficult. For example, in Canada, there are 200 000 people located in 280 rural areas which are not connected to the utility grid and use high cost and fossil fuels for power supply [8]. Thus, it is necessary to proceed to explore other potentials for promoting the electricity access, especially in the remote region, with less capital investment and with considering the reduction of greenhouse emissions.

1.2 Renewable resources: Status and Trends

Renewable energy (RE) knows a fast expansion since the first United Nations framework convention on climate change in Rio de Janeiro [9]. As well, in 1997, the Kyoto protocol has encouraged the worldwide nations to establish an energy policy by the exploitation of renewable resources [10]. More than this, the crisis of oil prices at the beginning of the new millennium, has boosted with a strong impulse researches towards safe and domestic alternative solutions. The renewable energy market provided more than 20% of the worldwide final energy consumption and has employed 9.8 million by the end of 2016 [11]. Renewable energies come from the displacement of natural elements from a position to another one, such as photons from the sun, movement of wind, water in rivers. It also is delivered through the transfer of natural resources from a state to another, like the fungal fermentation of animal wastes to get a biogas. Consequently, RE depends mainly on the exploration of constantly replenished natural resources to get power, which makes it eligible to supply people in rural areas with low cost and even in off-grid operating mode. This thesis is dedicated only to wind power generation, but we presented a short description of the most popular sources for supplying clean and renewable energies.

1.2.1 Biomass energy

The term of *biomass* summarises mechanisms of transforming residuals, wood wastes, municipal wastewater and solid wastes, livestock, etc, into other forms, which will be used as energy, through several processes such as thermal, and biological. The biomass industry has sharply increased and extended in new areas of the world, especially for heating and cooling, where it hosts 9% of the total renewable energy used in this field [11]. Biomass is also used to generate electricity by producing steam to drive turbines through a direct

combustion of feedstocks or bio-fuel. As well, the biomass gasification technique is used also to get hydrogen, methane and other gases used in several sectors[12]. Figure 1-1 recapitulates all the biomass path [13].

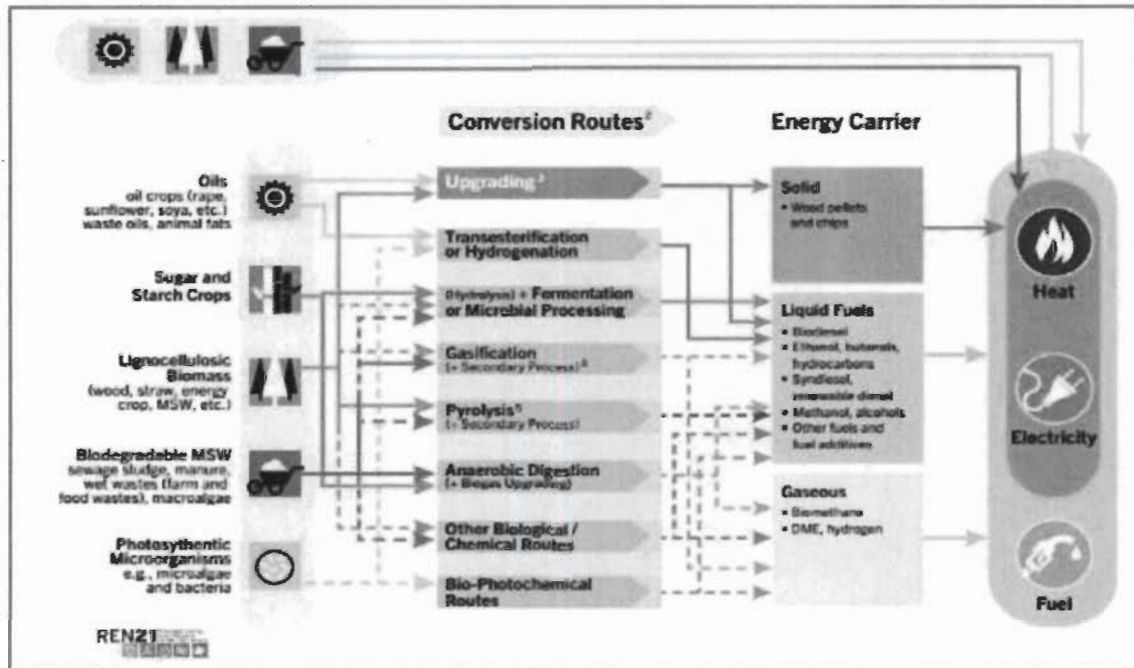


Figure 1-1 Biomass path [13]

1.2.2 Geothermal energy

Mainly, the geothermal energy based on the extraction of heat stored in the depths of the earth via various techniques such as dry steam power plants, flash power plant, binary cycle power plants, etc. [14]. To collect this energy, a fluid is injected into the interior of the earth where it collides with hot volcanic rocks, then returns to the surface carrying heat which will be used directly or exploited to generate electricity. In 2016, the global power generated using geothermal touched the edge of 12.7 GW, following the International Renewable Energy Agency (IRENA) affirmation [11].

1.2.3 Ocean energy

Ocean (marine) energy has a significant potential to share the burden of producing a clean and sustainable energy for the coastal communities. It contributes to the total energy production by 536 MW by the end of 2016, while ocean energy stakeholders have pledged to raise the proportion to 300 GW by 2050 [15]. However, it is still less-attractive compared to other renewable energies. In commercial-like approach, it requires the investment of high upfront. In 2001, the ocean energy has been installed in three countries, and then the number is increased to 25 countries in 2016, as shown in Figure 1-2. The extraction of power from ocean passes through numerous techniques, such as wave energy, tidal range, tidal currents and so on [16].

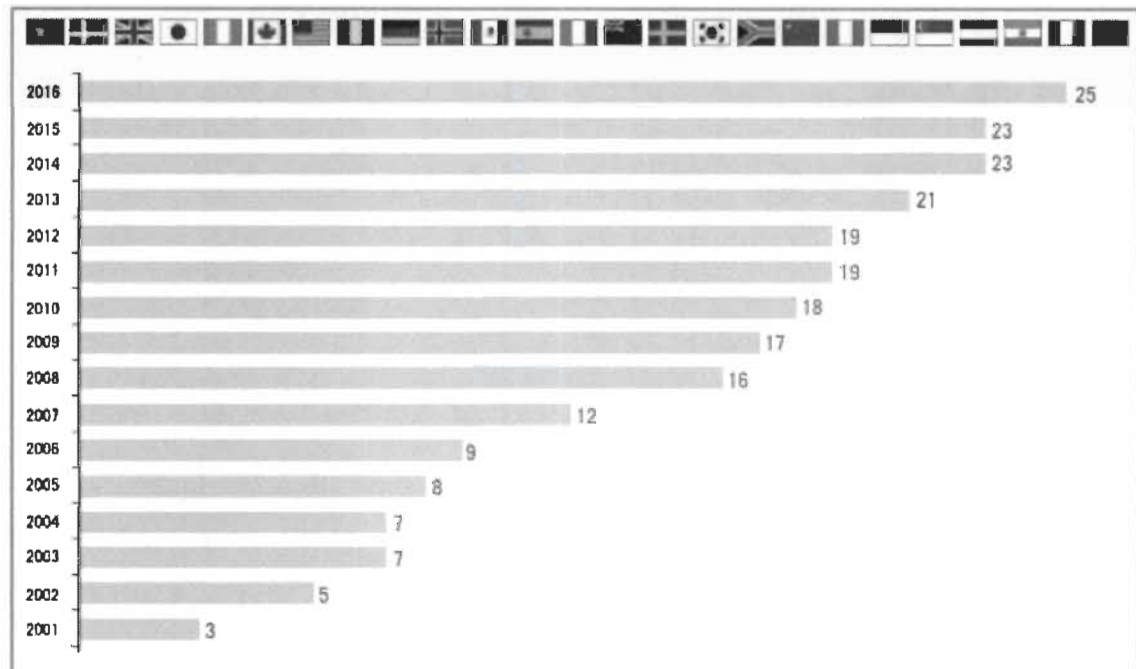


Figure 1-2 Countries membership in ocean energy [15]

1.2.4 Hydropower energy

Hydropower is the electromagnetic conversion of kinetic energy, captured from the water flow in rivers and dams, into an electric energy by using turbines. The hydropower stations vary from few kilowatts to hundreds of megawatts such as the biggest station in China by 22.44 GW [17]. In 2016, the global world hydropower installed capacity was increased by 25 GW arriving to 1.096GW [11]. The world-wide hydropower capacity and generation state vary from a country to another. In 2016, Canada has ranked the second in hydropower installed capacity after the China by 79 323 MW where it covers more than 97% of the Quebec total electricity needs [18].

1.2.5 Solar energy

The solar energy is the use of sunlight to produce electricity via photovoltaic (PV) system and concentrating solar power (CSP), or heating and cooling through thermal stations. PV-based energy depends on the conversion of sunlight into a direct current using PV- modules, while CSP-based energy produces electricity by the same procedure of PV, which will be used for heating water or any liquid or gas to get steam to drive turbines. The solar thermal technique is deduced for heating or cooling industrial and domestic spaces. The solar energy market knows a fast growth in 2016, practically with the historic drooping in PV modules prices by a rate of 29% to 0.41\$ per Watt [11].

1.2.6 Wind energy

Wind power bases on the conversion of wind energy into another sort of energy such as electricity. Nowadays, it becomes the most popular among renewable energies and a big contributor in the worldwide final power consumption by 487GW installed capacity in 2016

as illustrated in Figure 1-3. However, the penetration of wind energy in the total power consumption is relative from a country to another, for example, 45% in Denmark, without forgetting its historic date where the wind power production exceeds the country power consumption on November 3rd 2013 [19].

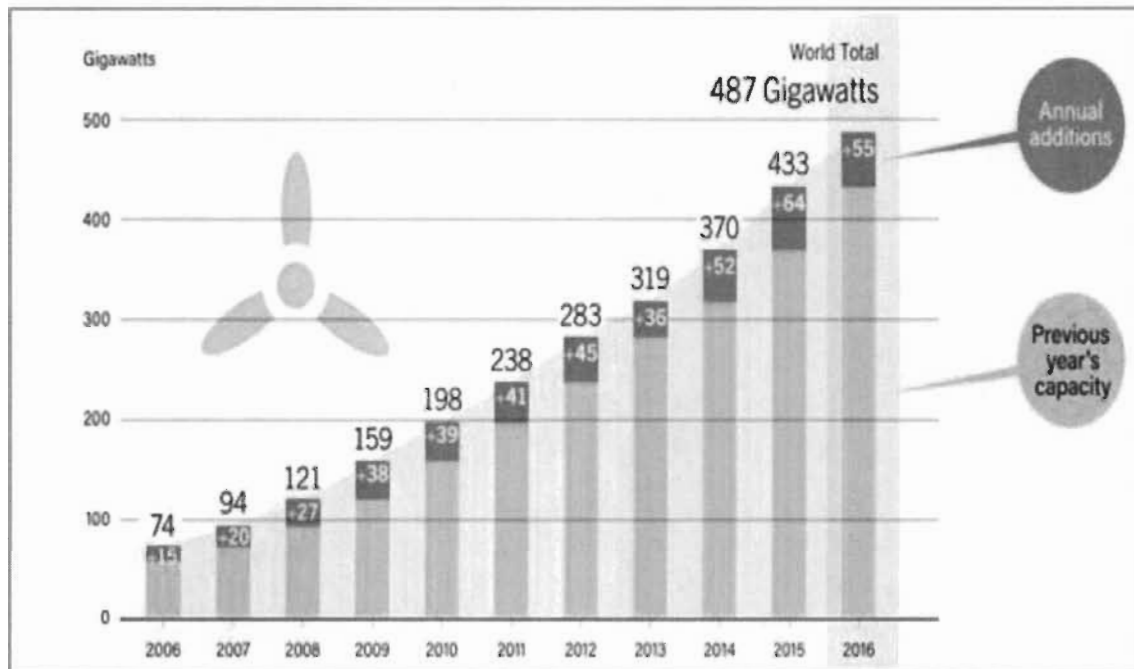


Figure 1-3 Expansion of wind energy [11]

1.3 Main parts of wind turbine

The classification of wind turbines depends on the area where they are implemented (offshore, onshore), type of generator, power electronic devices used for the power conversion. From a mechanical point of view, a wind turbine could be in a vertical or horizontal position, depending on the state of axis carrying blades. The mechanical part contains a rotor which is represented by the axis and blades, a gearbox, a tower and a supporting basis. The electrical part comprises a generator, power electronic devices, and a control system. The last one includes sensors, actuators, controllers, etc. [20].

1.3.1 Power electronic devices in wind turbine

The first generation of wind turbines operates at fixed speed where the generator is connected directly to the grid through a simple starter controlled by a thyristor as shown in Figure 1-4 [21].

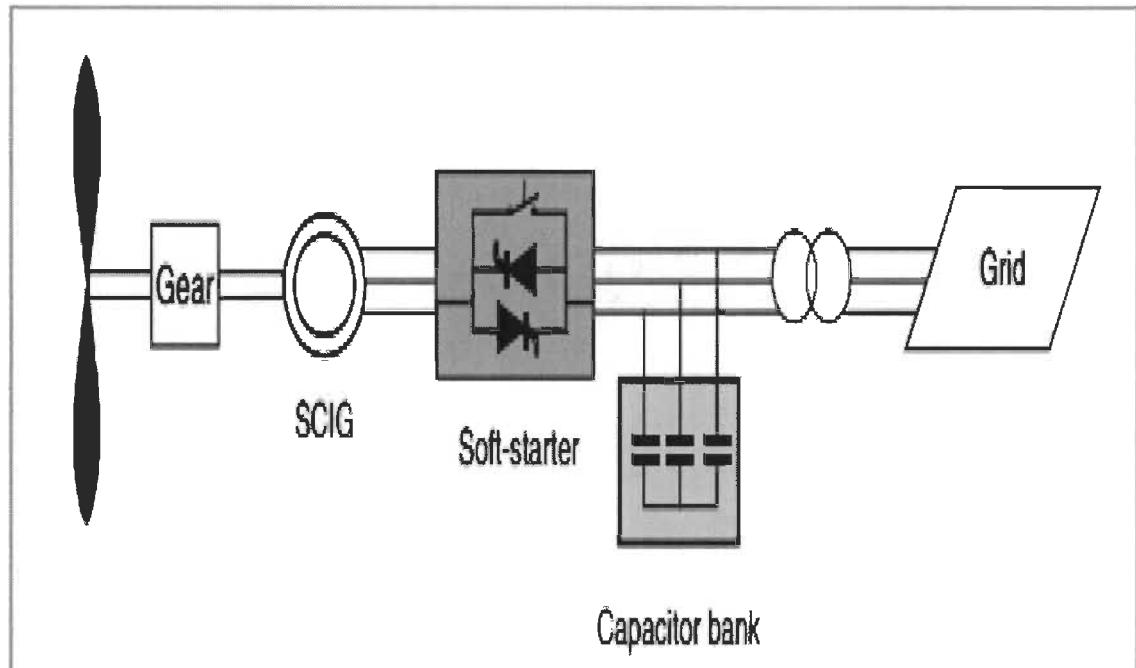


Figure 1-4 Fixed speed based wind turbine [21]

However, this topology (Figure 1-4) is sensitive to the speed variation resulting in an injection of harmonic into the grid [22]. By the emergence of semiconductors field, another generation of power electronic devices has been revealed by the end of the 1980s. It is represented by one stage converters based rectifier or a chopper, used to control the rotor resistance of a double-fed induction generator (Figure 1-5) that helps in damping the influence of wind speed fluctuations on the power quality [19]. With the beginning of the new century, an advanced category of multi-stage, bidirectional converters have appeared. It brings more flexibility and fast response for the control of active and reactive power and

enables the wind turbine to operate in full-scale variable speed, which improves its efficiency and increases the capture of power [23].

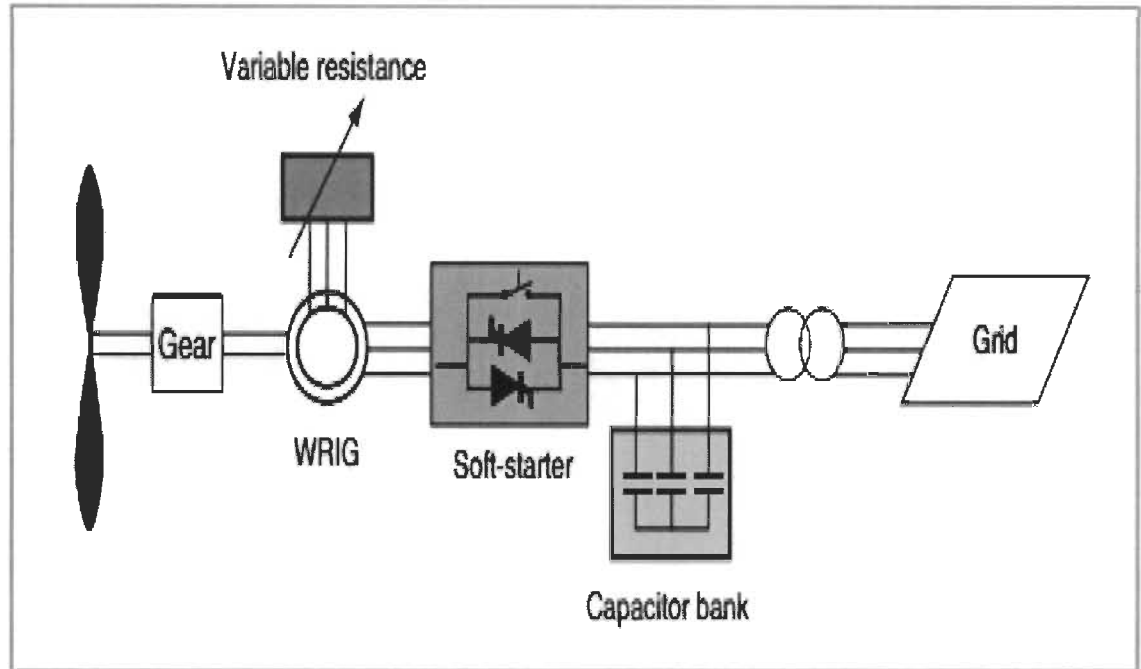


Figure 1-5 Partial variable speed based wind turbine [21]

1.3.2 Generator in wind turbine

Several topologies have been proposed in fixed speed, partial-variable speed and variable speed conditions, basing on: wound-rotor synchronous generator (WR-SG), permanent magnet synchronous generator (PMSG), double-fed induction generator (DFIG) and self-excitation induction generator (SE-IG) [19].

1.3.2.1 Wound-rotor synchronous generator

Basically, wound-rotor synchronous generator (WR-SG) has been widely used in a conventional steam-based power plant where it operates at high and constant speed. In the

start-up, the rotor of WR-SG should be connected to a DC current source to get the necessary excitation [24]. Occasionally, WR-SG is also used as a dynamic voltage and reactive power compensator especially in the off-grid operation. In wind power generation, WR-SG is connected through a full-scale back-to-back converter. The main drawback of WR-SG is the bulky volume and high cost i.e.; regular maintenance of collector rings and brushes is necessary since it needs an external source of excitation through the rotor [25].

1.3.2.2 Permanent synchronous generator

PMSG is more popular in wind energy application compared to WR-SG where it doesn't require an external excitation nor rings for the collection of reactive power. It also induces less-noise since the absence of a gearbox. It has been used in several applications such as HVDC, HVAC, low and medium voltage, using double stage back to back converters or three stages (AC-DC) -(DC-DC) -(DC-AC) based topologies [23]. The main disadvantage of PMSG is the risk of the demagnetization due to a peak in current or augmentation in temperature, and decrease in magnet effect over time [26].

1.3.2.3 Double fed induction generator

In the last few years, the DFIG dominates the industry of wind power. The first wind turbine based DFIG was operating in partial variable speed, in which the stator is directly linked to the grid and the rotor is connected to an adjustable resistance [22]. This topology has improved the wind turbine efficiency and increased the captured power with the enhancement of its quality. The value of the resistance varies with the variation of wind speed. Thus, the higher the speed is the more the resistance is bulky the higher the power loss is. For that, the speed variation tolerance is limited in order to decrease the power extracted

by the rotor. Since the 2000s, a new topology based DFIG has been proposed, where the rotor is also connected to the grid through a low size and cost back to back (BTB) converter. This solution permits controlling both the frequency and the rotor characteristics, which enhances the performance of the wind turbine in a wide interval of speed variation. Recently, researchers have explored a new topology using an AC-AC matrix converter instead of the BTB converter. This technique reduced the cost furthermore, where no dc side capacity or a battery is required, and also it simplifies the control strategy in which it is applied only to one converter. However, DFIG based topologies suffer from some disadvantage such partial scale power capacity, need of a periodic maintenance of slip rings and gearbox, high cost, high number of switches (18 switches in the matrix converter) which increases power loss, sensibility against the grid faults and poor ride-through capability [27].

1.3.2.4 Self-excitation induction generator

The use of Induction generators (IG) on large-scale returns to 1980s, where it has been used to build the Danish concept wind turbines. In this topology, the IG operates at fixed speed and is connected directly to the grid. While a fix-ratio gearbox is used to couple the IG with the rotor of the turbine[22]. By the advance of power electronic, another topology was proposed with the introduction of a full-scale BTB converter between the IG and grid. Such feature offers the possibility to control the generated power and enlarges the controllability of speed with a reduction in cost (no need of gearbox nor slip rings). Comparing to author generators, absolutely IG is more advantageous for several reasons. It is characterized by a small size machine, low-cost of operation and maintenance, brushless, high performance in variable speed condition and self-protection against short circuit and grid faults [28].

Nevertheless, this doesn't prevent the existence of some disadvantages, such as the weak control of voltage and frequency and needs of reactive power [25].

1.3.3 Goals and challenges of Wind turbine industry

Nowadays, the industry of wind turbines knows a fast progress, with a size turns around 7-8MW. The initiative targeted is to build 10-20 MW wind turbine and to reach an installed capacity cutting the edge of 800 GW by 2020 [19]. Several grid codes have been issued to manage the behavior of wind turbine. In which, even with the unpredictability of climate conditions and the fluctuation of wind speed, wind turbines should behave as a traditional power station in terms of power quality [29]. The wind turbine has to be also featured by the possibility to control the delivered active, reactive power and to offer support services for the utility grid characteristic, such as adjusting the frequency and enhancing the voltage profile, etc. [26]. In addition to that, wind turbine manufacturers are invited to promote new techniques to increase the generated power capacity, reduce the cost of maintenance, improve low voltage ride through capability (LVRT). In this sense, one of the most promising solutions in this area is the use of multiphase generators where the number of phases is more or equal to six. In the following, we present a survey on the multiphase generator, exactly a dual stator (six phases) induction generator.

1.3.4 Self-excitation dual stator winding induction generator: State-of-the-art on multiphase generator

Due to the high economic yield and with the same reason for preferring multiphase instead of single phase systems for the transportation of power, a new generation of multiphase generators (phases number is more or equal to six) has been strongly emerging

especially with the expansion of power electronics field [30]. This category brings a many advantages compared to the traditional three-phase generator. For example, since the number of phases is increased by two-time, also the generated power will be doubled without increasing the current per phase [31]. On the other hand, it also reduces harmonics, rotor losses, and torque ripples [23]. Multiphase generator penetrates the wind power generation field in grid-tied and stand-alone topologies. The additional degrees of freedom in multiphase generator allows it to inherit the conventional three-phase generator (such as DFIG) in the medium voltage operation (up to 8 MW), with more flexibility and high fault tolerance [32].

Among multiphase machines, self-excited dual stator winding induction generator (SE-DSWIG) have been proposed in many applications [33]. It consists of two identical three-phase winding sets which permit building several topologies [30]. Each three-phase winding set forms a stator, where the first one is called in such papers control winding and the second one is called power winding [34]. There is no physical contact between stators, that reduces the propagation of harmonics between them and enhance the electromagnetic compatibility in the power system [30].

In previous works, researchers proposed topologies in which the control winding (stator I) is connected to what they called, a static excitation controller (SEC), while the power winding (stator II) used to feed the end user as shown in Figure 1-6. The control winding with the SEC is used to compensate reactive power, to regulate voltage, enhance the frequency and to maintain the excitation of the generator [35]. This topology was proposed in standalone applications to meet the growing power request for the recent trend in wind power, aircraft, ships, automobiles, etc. [36].

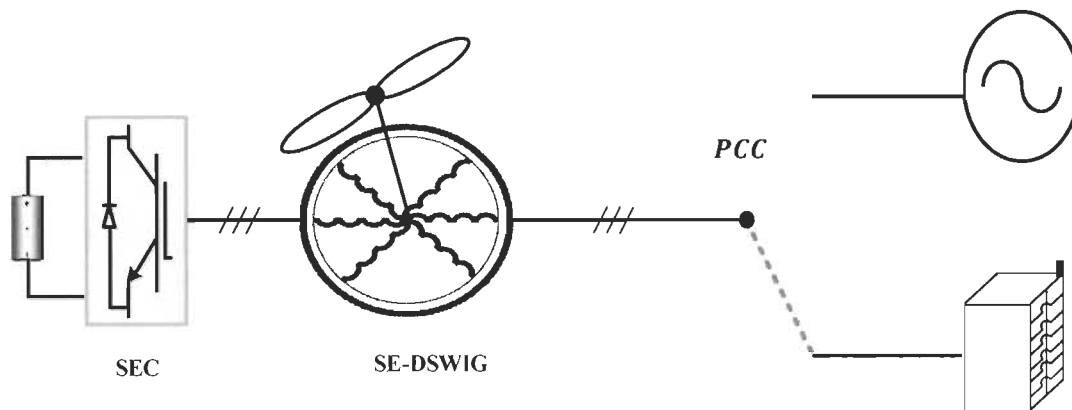


Figure 1-6 First topology based SE-DSWIG

In stand-alone applications, SE-DSWIG has been perfectly used in fixed and variable frequency ac systems, hydro and wind power extraction, as well as for simultaneous hybrid DC/AC output voltage supply. For instance, in [36], authors used SE-DSWIG in variable frequency AC application. The power winding set generates an AC power and the control winding set connected to the SEC. This later injects a variable reactive power into the machine to compensate the voltage dips and to stabilize frequency. At the same time, the SEC provides a DC voltage through its DC-bus supply. A control strategy based on the instantaneous slip frequency is applied to the SEC. Experimental results show good stability of voltage and frequency even with variation in load impedance. In [37], the power winding set feeds an unbalance load while the control winding through the SEC is used to regulate the positive sequence of the power winding set output voltage and current and to eliminate the negative sequences of the unbalanced load. In [35], authors used the same topology presented in Figure 1-7, where they tried to optimize the excitation capacitor with taking into account the generator parameters, prime mover speed, load variation, and the evolution of the wind turbine power curve. In this case, the SE-DSWIG has been used also for dc voltage application where the SEC acts as a rectifier for charging batteries and feeding dc current

load. In [38], Haijun Xue et al. made a comparison between four control strategies applied on SE-DSWIG for DC power generation. These control strategies are control-winding flux orientation control, control-winding voltage orientation control, control-winding direct power control, and instantaneous slip frequency control. All the proposed control strategies proved their capability in dc voltage generation with more superiority for the instantaneous slip frequency control in terms of DC voltage stability. In [39], Feifei Bu et al. proposed an asymmetrical analysis of the SE-DSWIG operating in variable frequency and feeding an unbalanced load. Results show that the SE-DSWIG has a good behavior even in unbalanced load scenario. The negative sequence and harmonic current generated by this fault don't propagate between stators. In [40], Kamal Nounou et al. evaluate the performance of the SE-DSWIG under variable speed and at different loads. A vector control strategy is built up and applied to the system basing on the method of indirect rotor flux orientation control which brought a good performance for the system. This work [41], presents a study on SE-DSWIG performance for variable frequency AC generation, feeding a variable capacitive-inductive load. The contribution of this work is established on the proposition of an improved instantaneous slip frequency control strategy applied on the SEC with considering the active and the reactive power consumed by loads. In [42], authors investigate the use of SE-DSWIG to generate DC voltage with both of stators through two rectifiers, using a control technique based on nonlinear input-output linearization. While in [43], Feifei Bu et al. proposed a 9-phase induction generator operates in very high-speed range. The power winding consists of six phases forming a dual stator, used for the DC voltage generation through two rectifiers. The DC-buses of both rectifiers are connected in shunt to maintain the DC voltage at an adequate level. The control winding is connected to a SEC which is used to enhance the SE-

DSWIG performance and to charge the battery as depicted in Figure 1-7. The SEC is controlled using the control-winding-flux orientation control strategy.

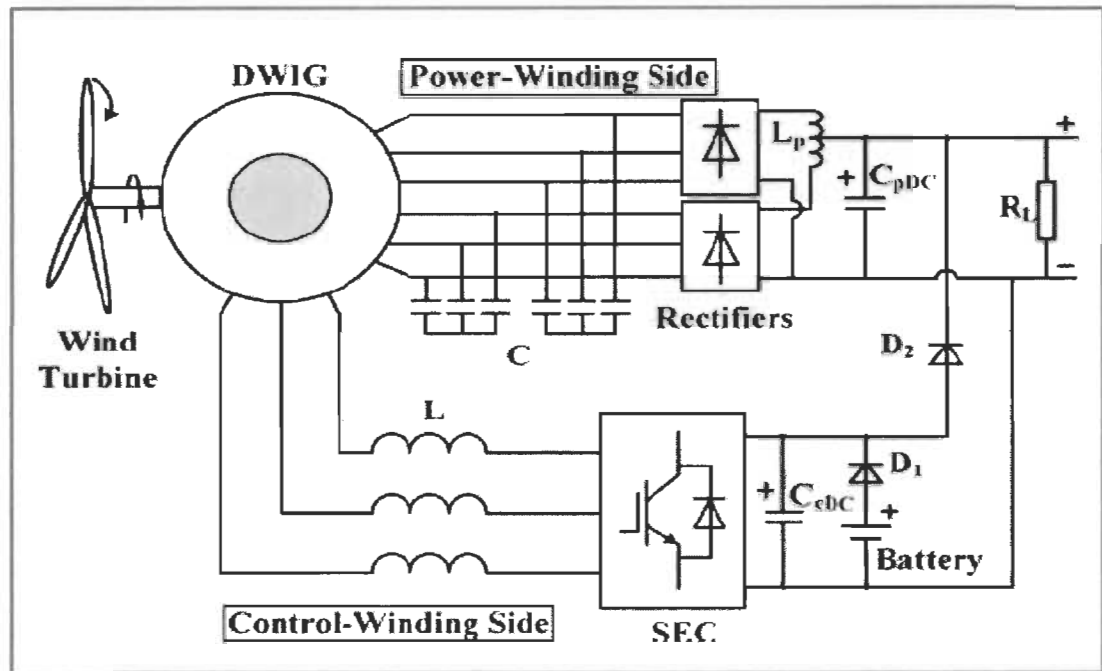


Figure 1-7 wide-speed range operation of SE-DSWIG for DC power generation [43]

To meet the growing electrical power demand for automobiles in term of electric power steering, heated seats, electronic ignition, etc., which is consistent with the evolution of electric vehicles, Malakondaiah Naidu et al. in [44] suggested the adoption of a new 42V-4kw power system based SE-DSWIG, instead of the Lundell alternator. In this topology, the power winding feeds loads through voltage source inverter and the control winding charged the battery through a diode bridge rectifier. In [45], SE-DSWIG has been used also in AC and DC-microgrid applications. The control winding is connected to a voltage source converter, forming DC-microgrid, while the power winding supplies load through AC-DC-AC converter forming an AC-microgrid (Figure 1-8). The proposed topology shows a good

performance in term of power quality in both AC and DC-microgrid. In [46], Saptarshi Basak et al. dealt with the improvement of power quality and mitigation of voltage disturbance. For that, they used passive compensators based on inductance and capacitance, inserted in series and shunt between the dual stators and inverters. However, details regarding the design of the passive compensators are missing.

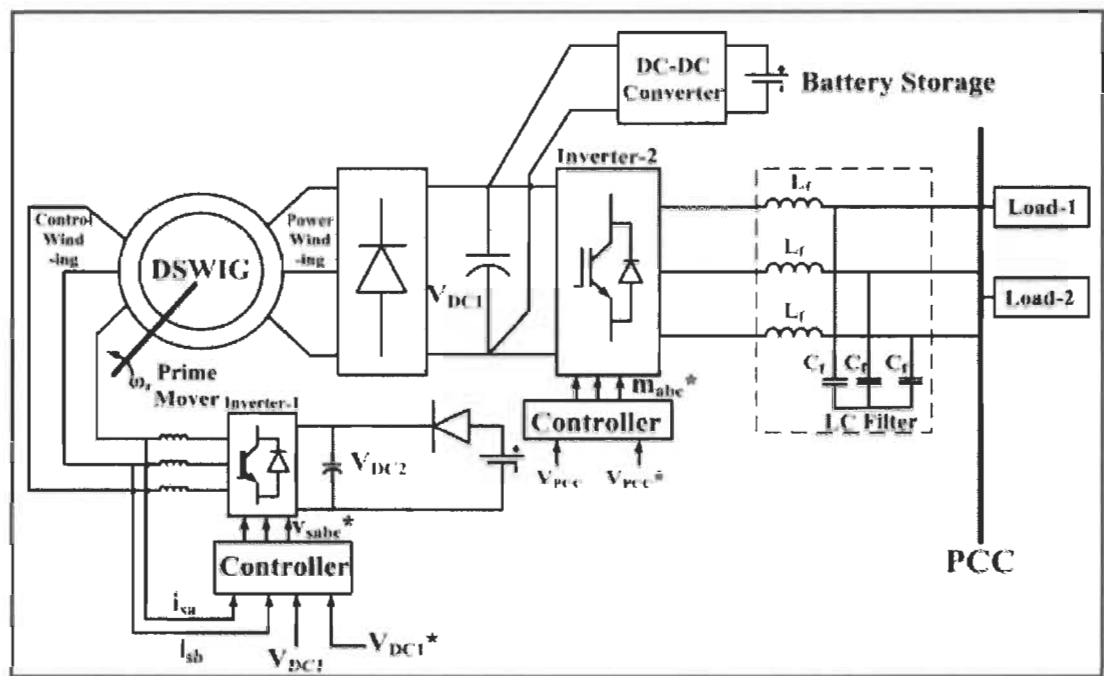


Figure 1-8 Topology proposed for microgrid operation [45]

In [47], G.K. Singh et al. made an in-depth study on the steady-state performance of SE-DSWIG in a standalone application. The SE-DSWIG is presented in simple shunt, short shunt, and long shunt configurations. The models are developed using the nodal admittance based graph theory, while the obtained matrix equations are solved using a genetic algorithm. Authors identified the parameters of the generator under study, as well as the values of the excitation capacitance in different configurations and under load and no-load conditions. In [30], a passive compensator based capacitance has been employed to improve the power

quality of a SE-DSWIG in standalone application. The proposed passive compensator shows a high efficiency against voltage sag and swell. In [34], the performance of SE-DSWIG in grid-tied function was investigated (Figure 1-9). Authors attempted to control the evolution of reactive power between the power winding and the grid in several fault scenarios emulated by a step variation. The SEC is connected to the control winding and supervised by the model reference adaptive control strategy. The proposed topology with the control technique enhanced the dynamic performance and the stability of the power system.

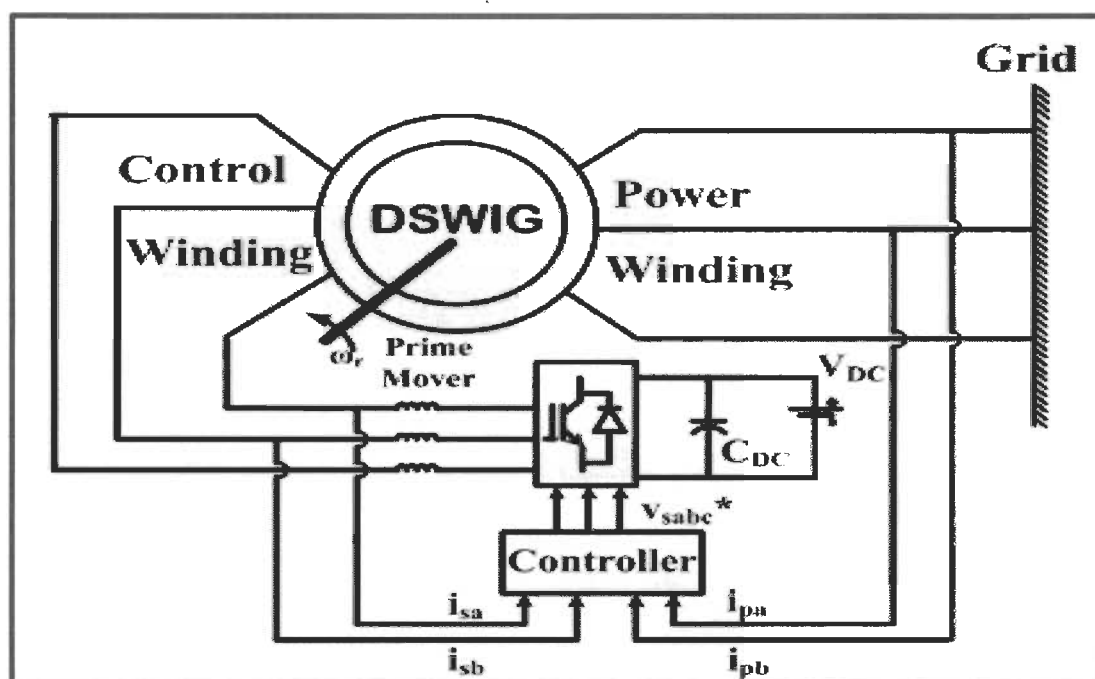


Figure 1-9 Topology proposed to improve the reactive power controllability [34]

It's remarkable that only a few attempts have been dealt with SE-DSWIG performance in variable speed applications such as in wind power generation. In [48], H. Amimeur et al. proposed a system of wind energy conversion based on SE-DSWIG. They used the MPPT technique to optimize the power for speed range under the nominal and to limit the power for wider speed ranges. The proposed topology based on the connection of SE-DSWIG into

the grid through an AC-DC-AC converter. The dual stators are used as a power winding (supplying power) and both are connected to a controlled rectifier. Both rectifiers are attached between them in DC-sides to maximise the power supplied, then connected to the grid through a single controlled inverter as shown in Figure 1-10. The SE-DSWIG is controlled using field oriented control strategy associated with sliding mode technique. The grid side converter is piloted using a classical feedback based PI controller. In [49], Samira Chekkal et al. proposed the same topology used in [48], however, a fuzzy logic control technique is used to control the torque instead of the MPPT technique to optimise the power of the conversion chain. This technique doesn't require any characteristics of the turbine or any exact mathematical model of the system.

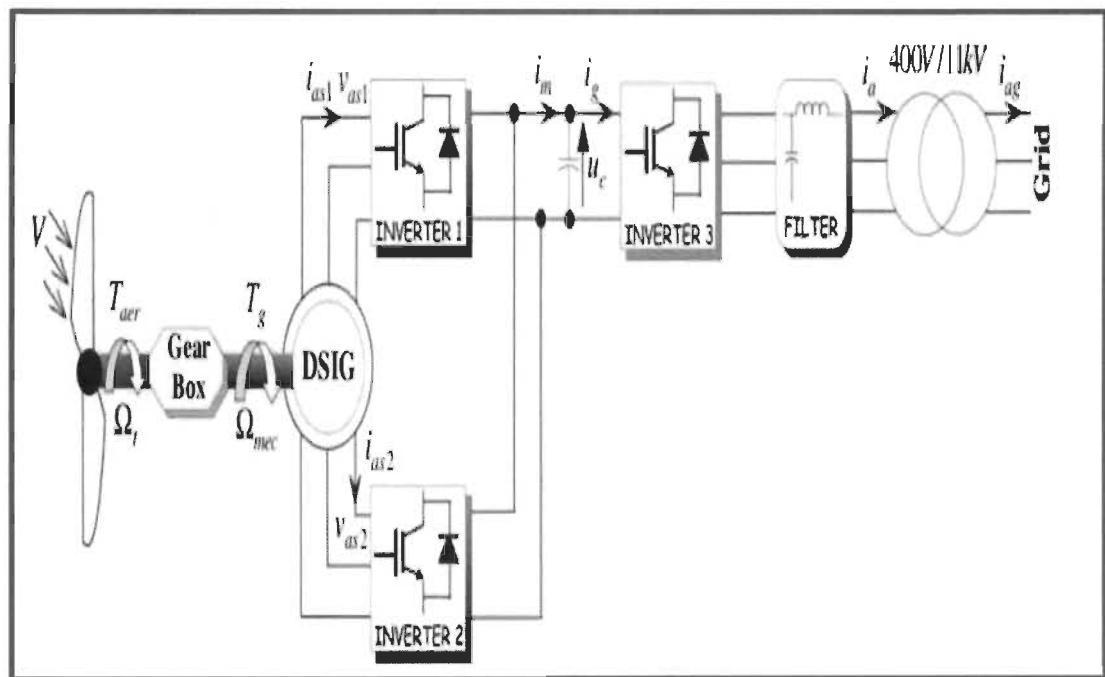


Figure 1-10 SE-DSWING connected to the grid via back-to-back converter [48]

In [50], Fatima AMEUR et al. also used the same topology explored in [48], but they applied direct power and flux control on the SE-DSWIG to improve the response of the power system.

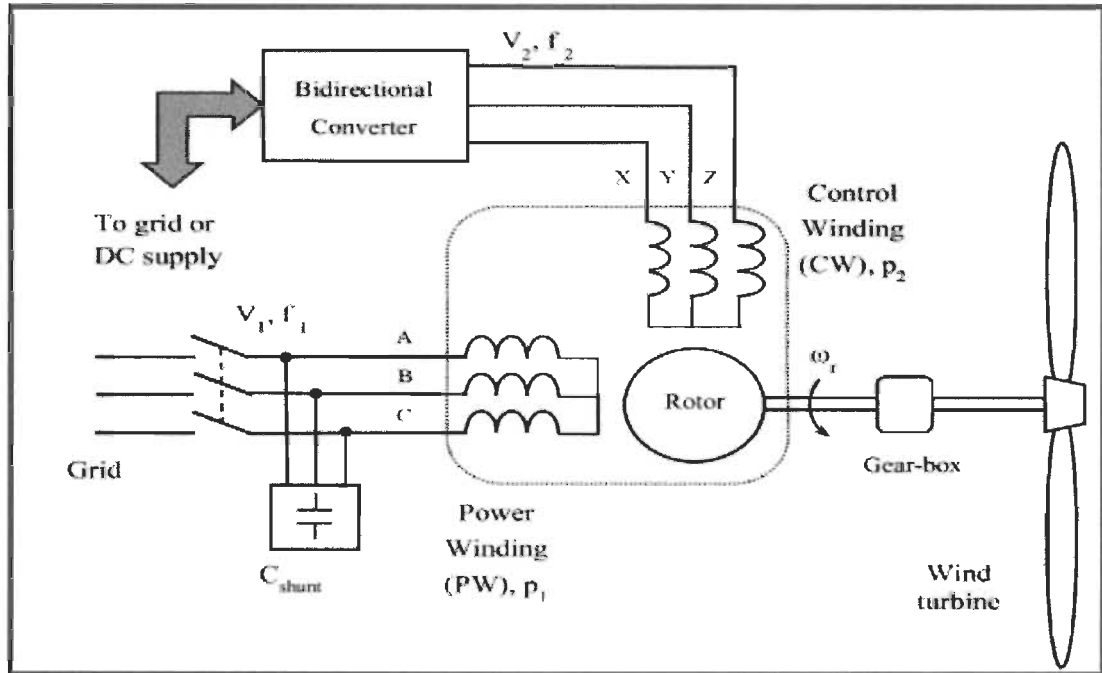


Figure 1-11 Topology proposed in [51]

In [51], authors investigated the act of SE-DSWIG in variable speed applications (Figure 1-11). The generator is connected directly to the grid through the power winding (PW), and a SEC is attached with the control winding (CW) side. The control winding pole number is three times the power winding pole number. This feature eliminates the electromagnetic interaction between stators and minimises furthermore the torque ripples in transient response. In [52], Feifei Bu et al. discussed the possibility to use SE-DSWIG for hybrid AC and DC microgrid application. The proposed topology consists of a power winding connected directly to the grid (Figure 1-12). The power winding improves the voltage and the frequency

of the AC grid, while the control winding is connected to a SEC and used to maintain the generator excitation and feeds DC loads.

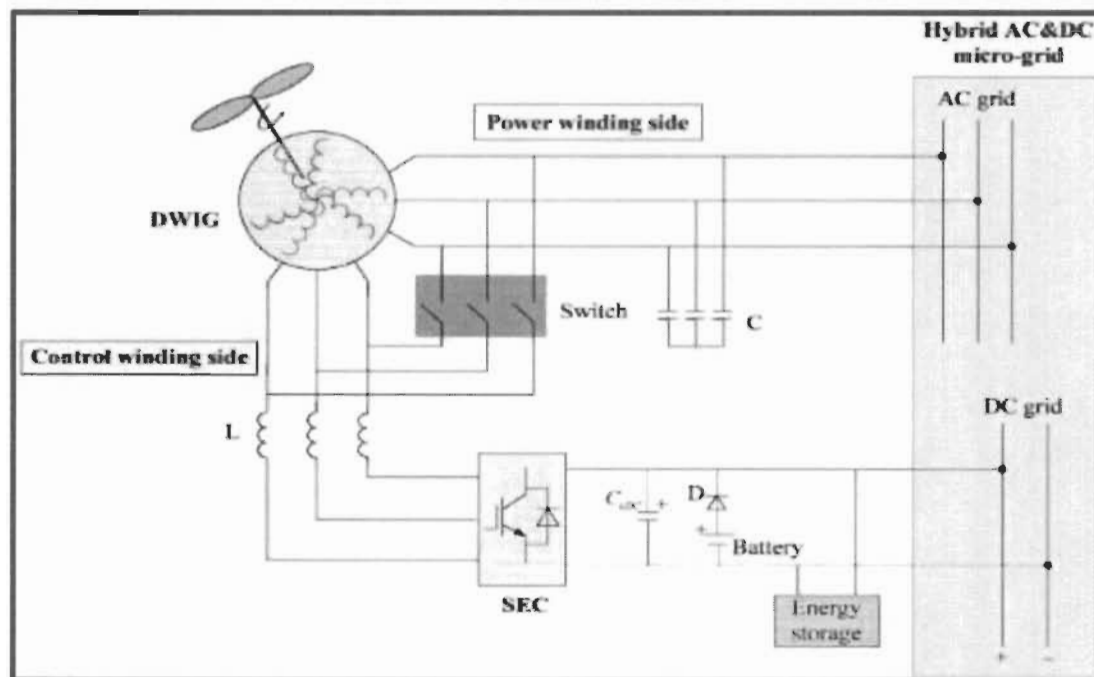


Figure 1-12 SE-DSWIG for hybrid AC & DC power generation topology [52]

In view of all papers that have been cited above, we conclude that the SE-DSWIG is a promising technology for standalone and grid-connected applications. It shows a high efficiency for variable frequency applications in aerospace, maritime, vehicles and for extraction of hydropower. In variable speed application, SE-DSWIG was driven with a sufficient speed in which it varies around the nominal speed. The MPPT technique is used to optimize the power at low speed and to limit it at high speed, that means remains power within acceptable nominal limits. While AC-DC-AC converter is used to synchronize the generator on the same frequency of the grid. Nevertheless, the proposed topologies, especially in variable speed operation, had a weak ability to deal with sudden and large speed variations, which induce voltage collapse and disturb the frequency. Hence, it's imperative

to improve the low voltage ride through capability of SE-DSWIG and maintaining the power flow at an adequate level even during wind speed variation or mains voltage sags.

1.4 Research Goals

In the literature, the power conversion systems based on SE-DSWIG are used in traditional topologies where the generator is connected to the grid through back-to-back converters. In addition to that, we did not find a strong study about the ability of maintaining the proposed topologies connected to the grid even at the presence of issues in terms of voltage sag and swell. Hence, the target of this thesis is to propose a new concept of power improvement in wind turbine based SE-DSWIG. The orientation of this thesis is twofold: the first one is the use of a dual stator induction generator to increase the generated power by two-time compared to a convention three-phase induction generator, and the second is to propose a new technique for the power quality improvement of a wind turbine in any scenario.

1.4.1 Main objective

The main objective of this thesis is highlighted as follows:

- Based on the literature, a depth investigation on SE-DSWIG and its advantages compared to the conventional three-phase induction machine was proposed.
- Exploration of a six-phase induction motor for a drive application.
- Design of a passive compensator based inductance and capacitance to ameliorate the performance of SE-DSWIG in a standalone application.

- Investigation on customer power devices (D-STATCOM, DVR, UPQC) and their capability to improve the power quality in a wind turbine based SE-DSWIG.
- Design and insertion of passive damping LCL filter between customer power devices and the grid, to elimination the penetration of harmonic.
- Low voltage ride through enhancement for the proposed wind turbine based SE-DSWIG
- Development of nonlinear and adaptive based sliding mode and fuzzy logic control strategies respectively, to ensure a smooth functioning of the multi-variable system (SE-DSWIG, UPQC).

1.4.2 Contribution of this thesis

- This work proposes a new topology of wind energy conversion systems based SE-DSWIG for grid-connected and standalone applications in the same time. SE-DSWIG is connected to the grid through the first stator and supplying an islanded microgrid through the second stator winding.
- Multi-converter based unified power quality conditioner (MC-UPQC) is connected between the grid/load and the generator to compensate the supply voltage imperfection, enhance voltage and current at the PCC even in the presence of sudden faults, ameliorate the LVRT capability, and synchronize the generator on the same frequency of the grid.
- The proposed MC-UPQC involves three converters connected back to back through an energy storage system, which permits exchanging active power between them.
- Two converters of MC-UPQC are acting as DVR where each one of them is connected through a series injection transformer at the dual stators terminals, while the third

converter behaves as a D-STATCOM and connected in shunt between the grid and the first stator through a passive damping LCL filter.

- Following the challenges entrusted by the MC-UPQC, a cascade sliding mode control technique is applied on D-STATCOM whereas a synchronous reference frame control theory is used to supervise both DVRs.

1.4.3 Publications

- F. Hamoud, M. L. Doumbia, and A. Cheriti, "Performance Study of a Self-Excitation Dual Stator Winding Induction Generator for Renewable Distributed Generation Systems," *Smart Grid and Renewable Energy*, vol. 7, p. 197, 2016.
- F. Hamoud, M. L. Doumbia, and A. Cheriti, "Hybrid PI-Sliding Mode Control of a voltage source converter based STATCOM," in *2014 16th International Power Electronics and Motion Control Conference and Exposition*, 2014, pp. 661-666.
- F. Hamoud, M. L. Doumbia, and A. Ch, "Power factor improvement in WECS using cascade PI control of passive damping LCL-filter," in *2015 International Conference on Sustainable Mobility Applications, Renewables and Technology (SMART)*, 2015, pp. 1-7.
- F. Hamoud, M. L. Doumbia, A. Chériti, and H. Teiar, "Power factor improvement using adaptive fuzzy logic control based D-STATCOM," in *Ecological Vehicles and Renewable Energies (EVER), 2017 Twelfth International Conference on*, 2017, pp. 1-6.
- F. Hamoud, M. L. Doumbia, and A. Chériti, "Voltage sag and swell mitigation using D-STATCOM in renewable energy based distributed generation systems," in *Ecological Vehicles and Renewable Energies (EVER), 2017 Twelfth International Conference on*, 2017, pp. 1-6.
- F. Hamoud, M. L. Doumbia, and A. Chériti, " Adaptive Fuzzy Logic Control Strategy to Improve the Power Quality Using UPQC-S," in *Energies, 2018 (submitted)*

1.4.4 Outline of thesis

The structure of this work is organized into seven chapters. The first one is devoted to an introduction, contains a survey on renewable energies, different topologies of wind energy-based generators and a state of the art of self-excitation dual stator induction generator. Chapter two evaluates the performance of a six-phase induction motor in drive applications.

The six-phase induction motor is fed with two inverters and is controlled using field oriented control with the indirect speed regulation method. The third chapter examines the behavior of SE-DSWIG that operates in a standalone application, with variable load and speed. A passive compensator is designed and used to mitigate issues in terms of voltage sag and swell. Chapter four presents a study on customer power devices (active compensator) based series and shunt compensators. Furthermore, it contains the step-by-step design method of passive damping LCL which will be used to eliminate switching ripples. Chapter five inspects another category more advanced of active compensator called unified power quality conditioner (UPQC). Chapter six is assessed the performance of the entire system proposed in this thesis. Finally, the general conclusion and the perspectives of this dissertation will be in the seventh chapter.

Chapitre 2 - Field oriented control of a dual stator winding induction motor with indirect speed regulation method

2.1 Introduction

Primarily, the idea of a multiphase machine was supported by the revolution of variable speed drive in high power application [53]. This attempt was boosted by several advantages coming from the augmentation of phase number (more than three). The multiphase feature of the machine gives high torque density with low pulsation and minimum harmonics [33]. Moreover, the power supply in drive application is segmented between two inverters that mean more degrees of freedom which implies high fault tolerance and more reliability [54-56]. The most important property of multiphase induction machine is the elimination of the space harmonics [57, 58]. These types of harmonics are the most dangerous issues that could bring malfunctioning to the counterpart three-phase induction machine. Space harmonics come from the disproportionate distribution of the magnetomotive force (FMM) in the air gap between the rotor and the stator [59, 60]. However, for a six-phase induction motor, the space harmonics are eliminated which brings more stability and reduces vibration [32, 54, 59]. Such advantages encourage industrial companies to use this technology in several motoring applications, e.g. the new generation of aircraft, propulsion, electric vehicles, locomotive traction [32]. In this sense, we can cite the Hyundai ultra high-speed elevator with nine phases, 1.1 MW motor [60], six-phase permanent machine for pumping oil [61], as well a fifteen phase, 15 MW induction machine for electric ship propulsion [31, 62, 63].

The aim of this chapter is to apply a vector control based field orientation technique on a dual stator winding induction motor (DSWIM). A description and mathematical modeling of DSWIM are presented. After that, we evaluate the performance of DSWIM in direct-fed from the grid, then we use two inverters controlled in open loop using the pulse-width modulation technique (PWM). Finally, the vector control technique is applied.

2.2 Description of the dual stator winding induction motor

Figure 2-1 illustrates the DSWIM scheme. It contains a dual three- winding sets. The first three winding set is referred $(\alpha_1, \alpha_2, \alpha_3)$ and noted as stator I, while the second three-winding set is denoted $(\beta_1, \beta_2, \beta_3)$ and called stator II. Every three-winding set of the stator is spatially shifted against the other by $\theta = 30^\circ$. Three phase-winding set called (r_1, r_2, r_3) forms a squirrel cage rotor and displaced compared to the first and second stator winding sets by angle θ_1 and θ_2 respectively. The topology of the six-phase induction machine prevents the propagation of any perturbation between the dual three windings, since the separation of the neutral point of both sets.

2.3 Mathematical modeling of DSWIM in biphas system

The modeling of DSWIM in biphas system involves the transformation of its equations from ABC frame to a DQ frame through Park crossing matrices given by [64]:

$$[P(\theta)] = \sqrt{\frac{2}{3}} \begin{bmatrix} \cos(\theta) & \cos(\theta - \frac{2\pi}{3}) & \cos(\theta + \frac{2\pi}{3}) \\ -\sin(\theta) & -\sin(\theta - \frac{2\pi}{3}) & -\sin(\theta + \frac{2\pi}{3}) \\ \frac{1}{\sqrt{2}} & \frac{1}{\sqrt{2}} & \frac{1}{\sqrt{2}} \end{bmatrix} \quad (2-1)$$

The mathematical modeling of the DSWIM in ABC frame is given in the electric and magnetic equations in DQ frame linked to a rotating field are the following [65]

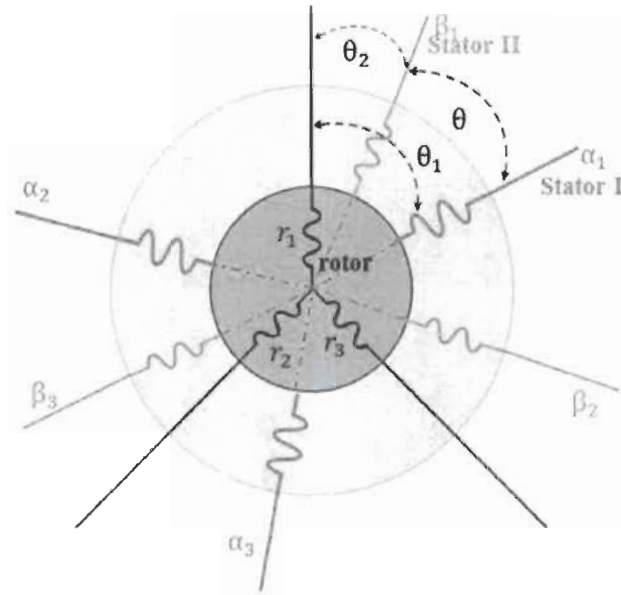


Figure 2-1 Scheme of DSWIM

2.3.1 Electric equations

$$V_{1d} = R_1 I_{1d} + \frac{d}{dt} \varphi_{1d} - \omega_s \varphi_{1q} \quad (2-2)$$

$$V_{1q} = R_1 I_{1q} + \frac{d}{dt} \varphi_{1q} + \omega_s \varphi_{1d} \quad (2-3)$$

$$V_{2d} = R_2 I_{2d} + \frac{d}{dt} \varphi_{2d} - \omega_s \varphi_{2q} \quad (2-4)$$

$$V_{2q} = R_2 I_{2q} + \frac{d}{dt} \varphi_{2q} + \omega_s \varphi_{2d} \quad (2-5)$$

$$V_{rd} = R_r I_{rd} + \frac{d}{dt} \varphi_{rd} - (\omega_s - \omega_r) \varphi_{rq} = 0 \quad (2-6)$$

$$V_{rq} = R_r I_{rq} + \frac{d}{dt} \varphi_{rq} + (\omega_s - \omega_r) \varphi_{rd} = 0 \quad (2-7)$$

2.3.2 Magnetic equations

The flux linkage equations of both stators and rotor in DQ frame are given by

$$\varphi_{1d} = L_1 I_{1d} + L_m (I_{1d} + I_{2d} + I_{rd}) \quad (2-8)$$

$$\varphi_{1q} = L_1 I_{1q} + L_m (I_{1q} + I_{2q} + I_{rq}) \quad (2-9)$$

$$\varphi_{2d} = L_2 I_{2d} + L_m (I_{1d} + I_{2d} + I_{rd}) \quad (2-10)$$

$$\varphi_{2q} = L_2 I_{2q} + L_m (I_{1q} + I_{2q} + I_{rq}) \quad (2-11)$$

$$\varphi_{rd} = L_r I_{rd} + L_m (I_{1d} + I_{2d} + I_{rd}) \quad (2-12)$$

$$\varphi_{rq} = L_r I_{rq} + L_m (I_{1q} + I_{2q} + I_{rq}) \quad (2-13)$$

2.3.3 Power consumption and electromagnetic torque of DSWIM

The absorbed power by the DSWIM is given by the expression (2-14).

$$P_A = V_{1d} * I_{1d} + V_{1q} * I_{1q} + V_{2d} * I_{2d} + V_{2q} * I_{2q} \quad (2-14)$$

Substituting voltages in (2-14) by their equivalents (2-2) -(2-7) it gives

$$P_A = A + B + C \quad (2-15)$$

With:

$$A = R_1 * I_{1d}^2 + R_1 * I_{1q}^2 + R_2 * I_{2d}^2 + R_2 * I_{2q}^2 \quad (2-16)$$

$$B = \frac{d\varphi_{1d}}{dt} I_{1d} + \frac{d\varphi_{1q}}{dt} I_{1q} + \frac{d\varphi_{2d}}{dt} I_{2d} + \frac{d\varphi_{2q}}{dt} I_{2q} \quad (2-17)$$

$$C = \omega_s [(\varphi_{1d} * I_{1d} + \varphi_{1d} * I_{1d}) - (\varphi_{1q} * I_{1q} + \varphi_{2q} * I_{2q})] \quad (2-18)$$

The absorbed power involves the power losses (2-16), following the Joule's heating phenomenon, the variation of electromagnetic energy (reserve energy) (2-17) and electromagnetic power (2-18) [64].

The electromagnetic torque is the multiplication of the electromagnetic power (2-18) and number of pole pair on the electric pulsation as follows

$$T_{em} = \frac{p \cdot C}{\omega_s} \quad (2-19)$$

Replacing C in (2-19) by its equivalent we get

$$T_{em} = p * [(\varphi_{1d} * I_{1d} + \varphi_{1d} * I_{1d}) - (\varphi_{1q} * I_{1q} + \varphi_{2q} * I_{2q})] \quad (2-20)$$

From (2-12) and (2-13), we extract the rotor current in DQ frame:

$$I_{rd} = \frac{1}{L_m + L_r} \{\varphi_{rd} - L_m(I_{1d} + I_{2d})\} \quad (2-21)$$

$$I_{rq} = \frac{1}{L_m + L_r} \{\varphi_{rq} - L_m(I_{1q} + I_{2q})\} \quad (2-22)$$

The electromagnetic torque equation becomes [65]

$$T_{em} = p \frac{L_m}{L_m + L_r} \{(I_{1q} + I_{2q})\varphi_{rd} - (I_{1d} + I_{2d})\varphi_{rq}\} \quad (2-23)$$

The mechanical equation of the DSWIM is given by [66, 67]

$$j \frac{d\Omega}{dt} + f\Omega = T_{em} - T_L \quad (2-24)$$

2.4 Dual stator winding induction motor for variable speed application

Three scenarios have been proposed to explore the behavior of the DSWIM. In the first one, the DSWIM is supplied directly from the grid without power electronic inverters. In the second scenario, we used two voltage inverters controlled in open loop with pulse width modulation technique. In the third scenario, the DSWIM is supervised by a vector control technique.

2.4.1 DSWIM fed directly from the grid

In this scenario, the first-three winding set (stator I) is supplied by a balanced three-phase power source modeled as follows:

$$\begin{cases} V_{sar1} = \sqrt{2}V_{rms} * \sin(\omega_s t) \\ V_{sbr1} = \sqrt{2}V_{rms} \sin(\omega_s t + \frac{2\pi}{3}) \\ V_{scr1} = \sqrt{2}V_{rms} \sin(\omega_s t - \frac{2\pi}{3}) \end{cases} \quad (2-25)$$

While the second three-phase winding (stator II) set is fed through a power source shift by $\theta = 30^\circ$ compared to the power source supplies stator I.

$$\begin{cases} V_{sar2} = \sqrt{2}V_{rms} * \sin(\omega_s t - \theta) \\ V_{sbr2} = \sqrt{2}V_{rms} \sin(\omega_s t - \theta + \frac{2\pi}{3}) \\ V_{scr2} = \sqrt{2}V_{rms} \sin(\omega_s t - \theta - \frac{2\pi}{3}) \end{cases} \quad (2-26)$$

2.4.2 DSWIM fed by a voltage source inverter with PWM control

2.4.2.1 Modelling of voltage source inverter

In this scenario, the DSWIM is supplied by two voltage source inverters control in open loop through a PWM technique. The speed and the torque are controlled by adjusting the frequency and the stator voltage magnitude, using inverters[64]. The inverter consists of three legs, every one contains two disjointed and complementary power switch (Figure 2-2).

The power switch (T) is composed of a transistor (T)-diode (D) combination where its action is translated by logic function given as follows

$$y_n = \begin{cases} 1 & T \text{ is closed and } K \text{ conducts} \\ 0 & T \text{ is open and } K \text{ is blocked} \end{cases} \quad (2-27)$$

With y_n is the commutation that could be zero or one. T is a thyristor. K is the combination between a diode and a thyristor as shown in Figure 2-2

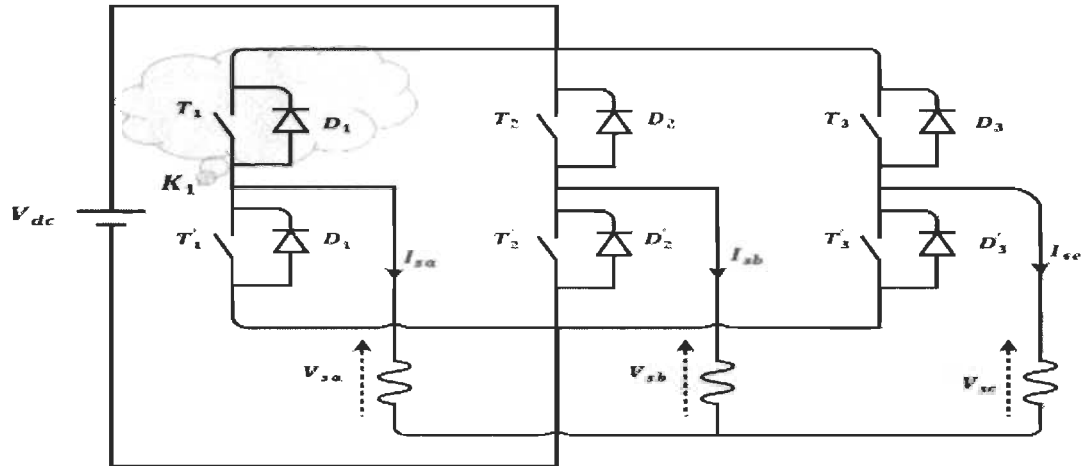


Figure 2-2 Controlled three-phase inverter

The phase to phase voltages are given in the following equations

$$V_{AB} = V_{sa} - V_{sb} = V_{dc}(y_1 - y_2) \quad (2-28)$$

$$V_{BC} = V_{sb} - V_{sc} = V_{dc}(y_2 - y_3) \quad (2-29)$$

$$V_{CA} = V_{sc} - V_{sa} = V_{dc}(y_3 - y_1) \quad (2-30)$$

In the equilibrium, the summation of three-phase voltage vectors is

$$V_{sa} + V_{sb} + V_{sc} = 0 \quad (2-31)$$

Resolving (2-27), (2-28) and (2-29) using (2-30) we get

$$\begin{cases} V_{sa} = \frac{V_{dc}}{3} (2y_1 - y_2 - y_3) \\ V_{sb} = \frac{V_{dc}}{3} (2y_2 - y_1 - y_3) \\ V_{sc} = \frac{V_{dc}}{3} (2y_3 - y_1 - y_2) \end{cases} \quad (2-32)$$

2.4.2.2 Open loop control of inverters using PWM

PWM technique is the comparison between a low-frequency modulating wave such as voltage, and a high-frequency triangular carrier wave to generate the control signal [64]. The PWM is characterized by two concepts; the first one is the modulation index, which is the ratio between the switching and fundamental frequencies. The second concept is the adjusting coefficient which is calculated through the ratio between the magnitude of the reference wave (voltage) and the peak value of the carrier wave. The switching frequency is determined by the triangular carrier wave.

In this case, the voltage references (reference wave) of the first inverter (feeds stator I) are given by

$$\begin{cases} V_{sar1} = V_{max} * \sin(\omega_s t) \\ V_{sbr1} = V_{max} \sin(\omega_s t - \frac{2\pi}{3}) \\ V_{scr1} = V_{max} \sin(\omega_s t + \frac{2\pi}{3}) \end{cases} \quad (2-33)$$

While the voltage references of the second inverter (feeds stator II) are

$$\begin{cases} V_{sar2} = V_{max} \sin(\omega_s t - \theta) \\ V_{sbr2} = V_{max} \sin(\omega_s t - \theta - \frac{2\pi}{3}) \\ V_{scr2} = V_{max} \sin(\omega_s t - \theta + \frac{2\pi}{3}) \end{cases} \quad (2-34)$$

The triangular carrier wave function is

$$V_{sm} = \begin{cases} V_m \left(4 \frac{t}{T_s} - 1 \right) & \text{if } 0 \leq t \leq \frac{T_s}{2} \\ V_m \left(-4 \frac{t}{T_s} + 3 \right) & \text{if } \frac{T_s}{2} \leq t \leq T_s \end{cases} \quad (2-35)$$

The full system contains DSWIM supplied with two PWM based voltage inverters is presented in Figure 2-3.

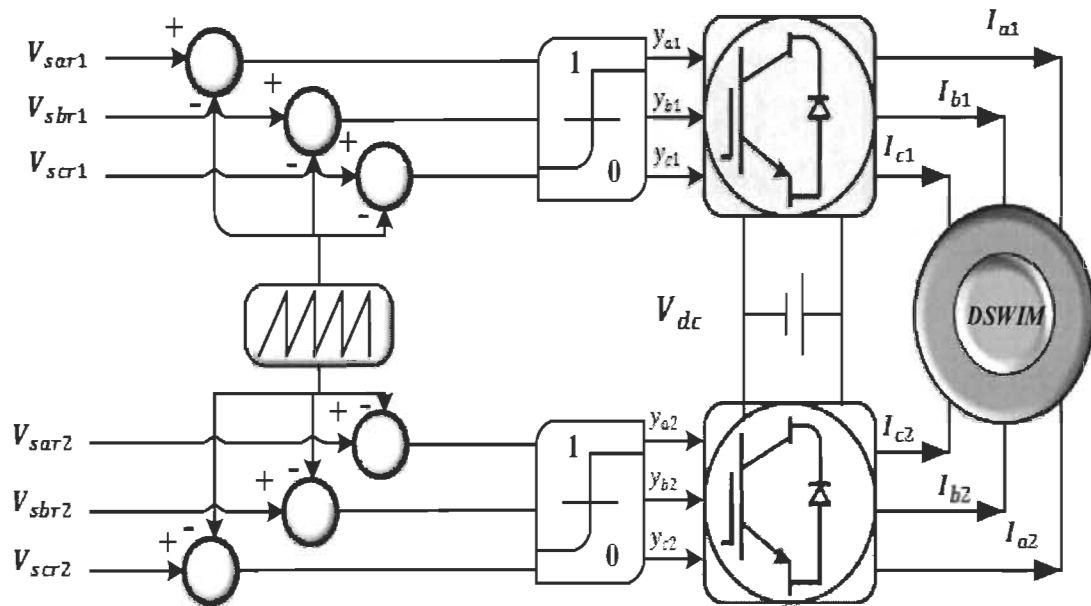


Figure 2-3 DSWIM with PWM based inverters

2.4.3 Vector control of dual stator winding induction motor

Initially, the vector control technique was explored by Blascke in 1972. However, it has been implemented only after the evolution of power electronic devices and microprocessors, since it requires complex arithmetic operations. In fact, it was proposed to overcome the difficulty of controlling induction motor due to its nonlinear feature. It gives the possibility to control the flux independently of torque which enables the induction motor to behave as separately excited DC motor [68].

2.4.3.1 Principle of field-oriented vector control technique

The vector control is the module and phase control of a flux vector, which could be oriented independently to the stator flux vector, airgap flux vector or rotor flux vector [66]. Due to its simplicity, the last one is selected in this work where the rotor flux vector is oriented to a reference frame axis rotating with the synchronous speed ω_s as depicted in Figure 2-4.

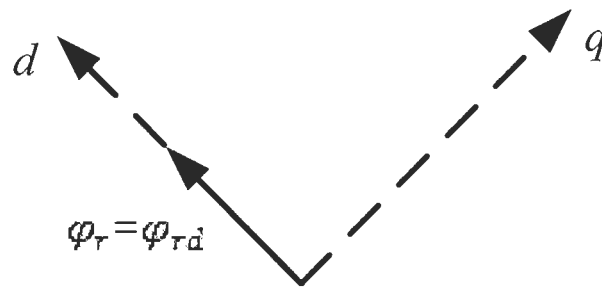


Figure 2-4 Rotor flux orientation in DQ frame

The quadratic component of the rotor flux is equal to zero that implies

$$\begin{cases} \varphi_r = \varphi_{rd} = \varphi_r^* \\ \varphi_{rq} = 0 \end{cases} \quad (2-36)$$

Hence, the electromagnetic torque equation (2-23)

$$T_{em} = p \frac{L_m}{L_m + L_r} (I_{1q} + I_{2q}) \varphi_r \quad (2-37)$$

2.4.3.2 Indirect vector control with speed regulation

The indirect vector control technique requires only the position of the rotor flux without its magnitude, for that, a speed sensor is needed. The rotor flux is oriented by adjusting the

stator voltage and current in transient response. This method is sensitive to parameters uncertainty.

The application of indirect vector control start by substituting (2-36) in the rotor current equations (2-21) and (2-22) we obtain:

$$I_{rd} = \frac{1}{L_m + L_r} \{ \varphi_r - L_m(I_{1d} + I_{2d}) \} \quad (2-38)$$

$$I_{rq} = \frac{-L_m}{L_m + L_r} (I_{1q} + I_{2q}) \quad (2-39)$$

Equation (2-39) can be written as:

$$I_{rq}(L_m + L_r) = -L_m(I_{1q} + I_{2q}) \quad (2-40)$$

Replacing (2-38) and (2-39) in (2-8),

$$\varphi_{1d} = \chi_1 I_{1d} + L_r \chi_1 I_{2d} + \chi_1 \varphi_r^* \quad (2-41)$$

$$\varphi_{1q} = \chi_1 I_{1q} + L_r \delta I_{2q} \quad (2-42)$$

$$\varphi_{2d} = \chi_2 I_{2d} + L_r \chi_2 I_{1d} + \delta \varphi_r^* \quad (2-43)$$

$$\varphi_{2q} = \chi_2 I_{2q} + L_r \delta I_{1q} \quad (2-44)$$

With

$$\chi_1 = L_1 + \delta L_r \quad (2-45)$$

$$\chi_2 = L_2 + \delta L_r \quad (2-46)$$

$$\delta = \frac{L_m}{L_m + L_r} \quad (2-47)$$

Substituting (2-36) in (2-6) and (2-7), we get:

$$\begin{cases} I_{rd} = 0 \\ I_{rq} = -\frac{\varphi_r^*}{R_r}(\omega_s - \omega_r) \end{cases} \quad (2-48)$$

Basing on (2-46), equation (2-38) becomes:

$$\varphi_r^* = L_m(I_{1d} + I_{2d}) \quad (2-49)$$

Basing on equation (2-1), (2-49) is given by:

$$\varphi_r^* = -I_{rq}(L_m + L_r) = L_m(I_{1q} + I_{2q}) \quad (2-50)$$

Substituting (2-41) to (2-44) and (2-50) in the stator voltage equations (2-2) to (2-5), we obtain:

$$V_{1d}^* = R_1 I_{1d} + L_1 \frac{d}{dt} I_{1d} - \omega_s^*(L_1 I_{1q} + \tau_s \varphi_r^* \omega_{gl}^*) \quad (2-51)$$

$$V_{1q}^* = R_1 I_{1q} + L_1 \frac{d}{dt} I_{1q} + \omega_s^*(L_1 I_{1d} + \varphi_r^*) \quad (2-52)$$

$$V_{2d}^* = R_2 I_{2d} + L_2 \frac{d}{dt} I_{2d} - \omega_s^*(L_2 I_{2q} + \tau_s \varphi_r^* \omega_{gl}^*) \quad (2-53)$$

$$V_{2q}^* = R_2 I_{2q} + L_2 \frac{d}{dt} I_{2q} + \omega_s^*(L_2 I_{2d} + \varphi_r^*) \quad (2-54)$$

With:

$$\begin{cases} \omega_{gl}^* = \omega_s^* - \omega_r \\ \tau_r = \frac{L_r}{R_r} \end{cases} \quad (2-55)$$

Introducing (2-39) in (2-48), we get the following:

$$\omega_{gl}^* = \omega_s^* - \omega_r = \frac{R_r L_m}{L_m + L_r} \frac{(I_{1q} + I_{2q})}{\varphi_r^*} \quad (2-56)$$

From (2-37), we obtain:

$$(I_{1q} + I_{2q}) = \frac{L_m + L_r}{pL_m} \frac{C_{em}^*}{\phi_r^*} \quad (2-57)$$

Based on (2-51) to (2-54), we deduce that the evolution of stator voltage affects the stator current, torque, and flux at the same time. For that, we introduce a control loop on the nonlinear part of (2-51) to (2-54), to supervise the stator current. The nonlinear part is defined as follows:

$$V_{1nd}^* = R_1 I_{1d} + L_1 \frac{d}{dt} I_{1d} \quad (2-58)$$

$$V_{1nq}^* = R_1 I_{1q} + L_1 \frac{d}{dt} I_{1q} \quad (2-59)$$

$$V_{2nd}^* = R_2 I_{2d} + L_2 \frac{d}{dt} I_{2d} \quad (2-60)$$

$$V_{2nq}^* = R_2 I_{2q} + L_2 \frac{d}{dt} I_{2q} \quad (2-61)$$

While the other part is named as:

$$V_{1ld}^* = \omega_s^* (L_1 I_{1q} + \tau_s \phi_r^* \omega_{gl}^*) \quad (2-62)$$

$$V_{1lq}^* = +\omega_s^* (L_1 I_{1d} + \phi_r^*) \quad (2-63)$$

$$V_{2ld}^* = \omega_s^* (L_2 I_{2q} + \tau_s \phi_r^* \omega_{gl}^*) \quad (2-64)$$

$$V_{2lq}^* = \omega_s^* (L_2 I_{2d} + \phi_r^*) \quad (2-65)$$

To achieve a totally decoupling, the stator voltages are defined as:

$$V_{1d}^* = V_{1nd}^* - V_{1ld}^* \quad (2-66)$$

$$V_{1q}^* = V_{1nq}^* + V_{1lq}^* \quad (2-67)$$

$$V_{2d}^* = V_{2nd}^* - V_{2ld}^* \quad (2-68)$$

$$V_{2q}^* = V_{2nq}^* + V_{2lq}^* \quad (2-69)$$

The representative scheme of indirect vector control technique is shown in Figure 2-5.

- *Defluxing block*

Generally, the rotor flux remains constant at its nominal value for speed less or equal the nominal of the motor, however for wide speed, the flux decrease to maintain the stator voltage. For that, we define the reference flux by the next equation [66].

$$\varphi_r^* = \begin{cases} \varphi_r^n & \text{if } \Omega \leq \Omega_n \\ \frac{\Omega_n}{\Omega} \varphi_r^n & \text{if } \Omega > \Omega_n \end{cases} \quad (2-70)$$

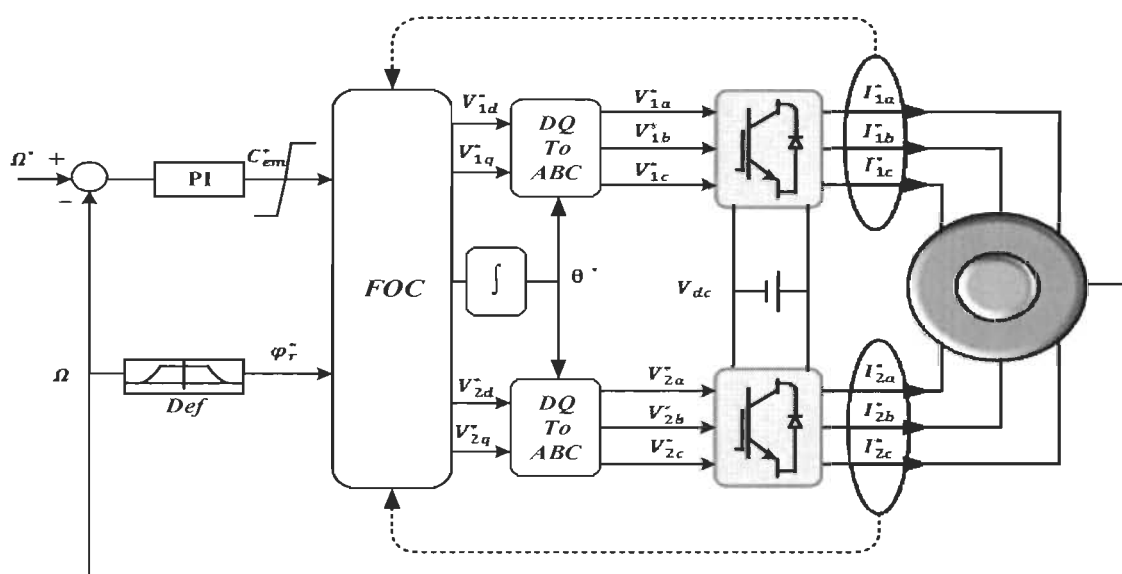


Figure 2-5 Indirect vector control technique

- *PI controller design*

The PI controller is used to regulate the speed and the stator currents. Figure 2-6 and Figure 2-7 show respectively the functional block diagram of the current and speed control.

The transfer function in close-loop of the stator current control can be written as following:

$$\frac{I_{1,2,d,q}}{I_{1,2,d,q}^*} = \frac{\frac{K_{il}}{L_{1,2}(s + \frac{K_{il}}{K_{pl}})}}{s^2 + \frac{R_{1,2} + K_{pl}}{L_{1,2}}s + \frac{K_{il}}{L_{1,2}}} \quad (2-71)$$

The identification of (2-71) with the second order polynomial equation implies the following:

$$\begin{cases} \omega_n^2 = \frac{K_{il}}{L_{1,2}} \\ \xi = \frac{(R_{1,2} + K_{pl})}{2\omega_n L_{1,2}} \end{cases} \quad (2-72)$$

The expression of K_{pl} and K_{il} is

$$\begin{cases} K_{pl} = 2\omega_n * L_{1,2} - R_{1,2} \\ K_{il} = L_{1,2} * \omega_n^2 \end{cases} \quad (2-73)$$

With the same procedure, we identify the $K_{p\Omega}$ and $K_{i\Omega}$

$$\begin{cases} K_{p\Omega} = 2\omega_n * K_f - j \\ K_{i\Omega} = K_f * \omega_n^2 \end{cases} \quad (2-74)$$

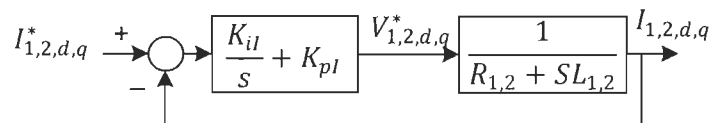


Figure 2-6 Block diagram of PI-current control

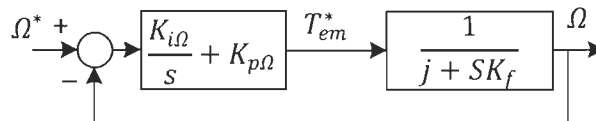


Figure 2-7 Block diagram of PI-speed control

From the previous equations, the voltage-decoupling block is depicted in Figure 2-8

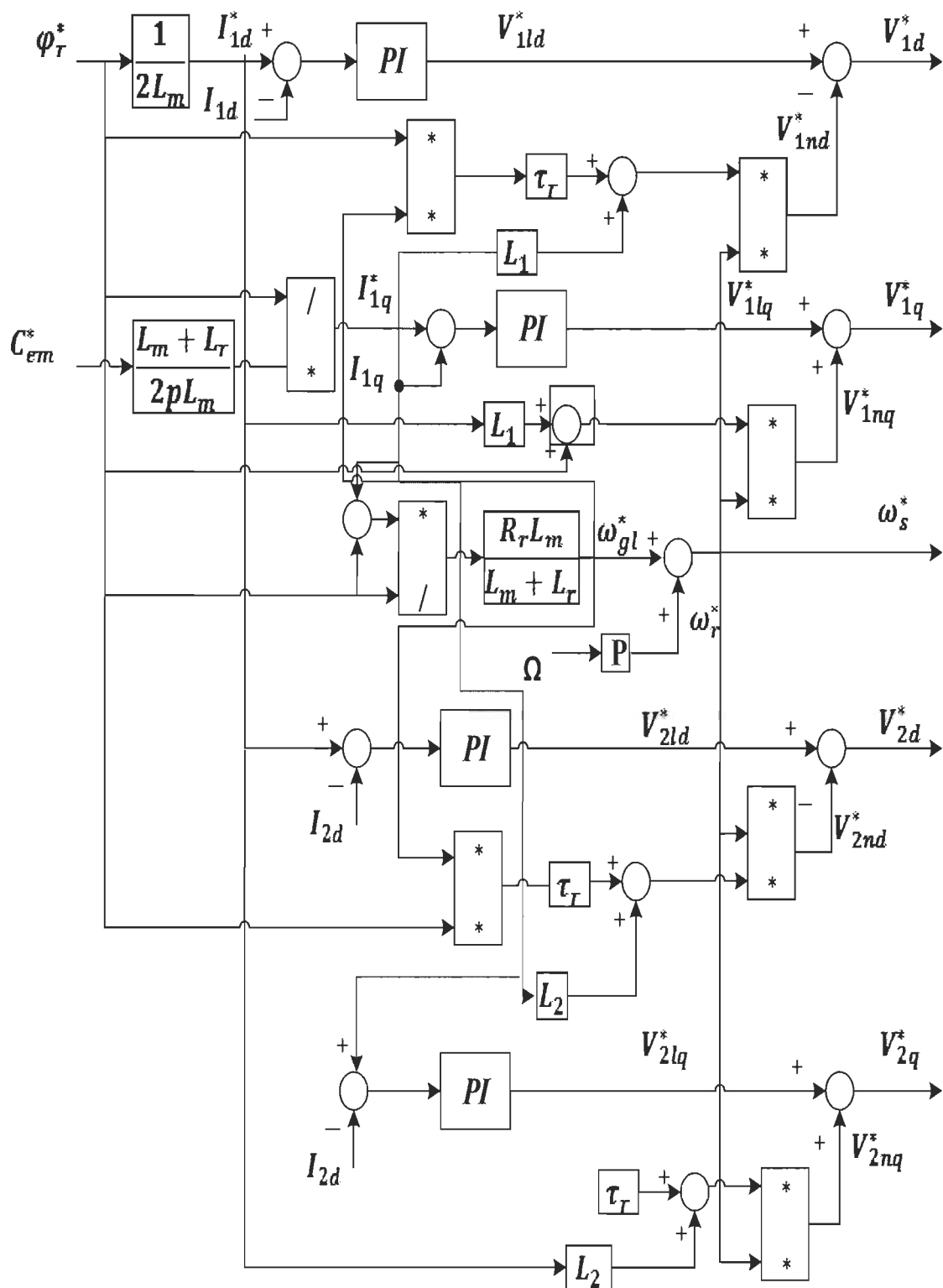


Figure 2-8 Voltage decoupling block diagram

2.5 Numerical simulation and results discussion

The electromagnetic and mechanic equations of the DSWIM are developed in MATLAB/SIMULINK environment. The machine parameters are presented in Appendix A.

2.5.1 Case study #1

As explained above, both DSWIM stators are supplied directly from the grid following equations (2-25), (2.26). In this case, we will study the performance of DSWIM at no load and at full-load tests. Figure 2-9 to Figure 2-12 represent the characteristics of DSWIM at no-load operation mode. The electromagnetic torque develops a peak equal to 42 N.m at the transient regime with presence of oscillations, then it decreases asymptotically till reaching its minimum value equal to 0.315 N.m at the steady state (Figure 2-9).

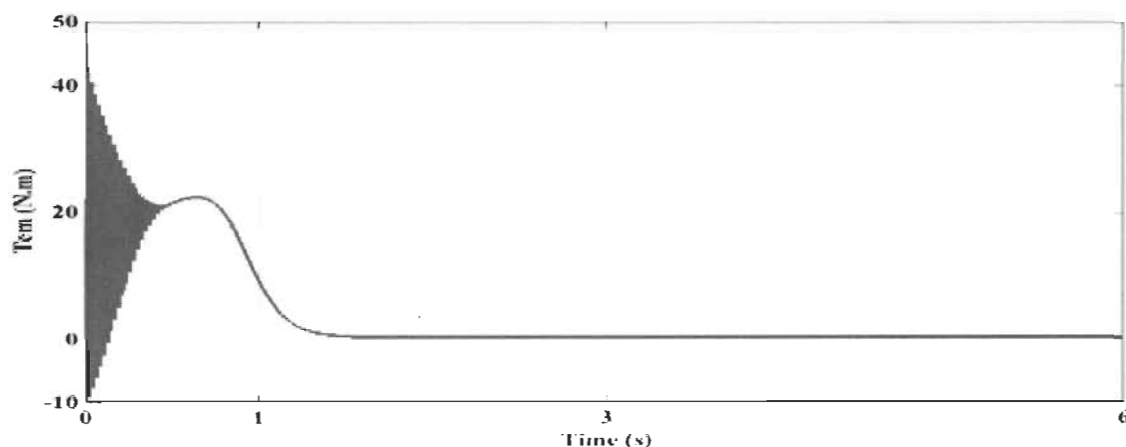


Figure 2-9 Electromagnetic torque at no-load

The speed evolves exponentially with time, and then it stabilizes at the permanent value $\omega = 2994 \text{ t/min}$ (Figure 2-10). The rotor flux progresses in the same manner as the electromagnetic torque, then it takes the permanent value almost equal to 1 Wb (Figure 2-11).

The stator I and II draw a current tends to 20 A at the transient response, then it decreases to take the permanent value 13.74A (Figure 2-12).

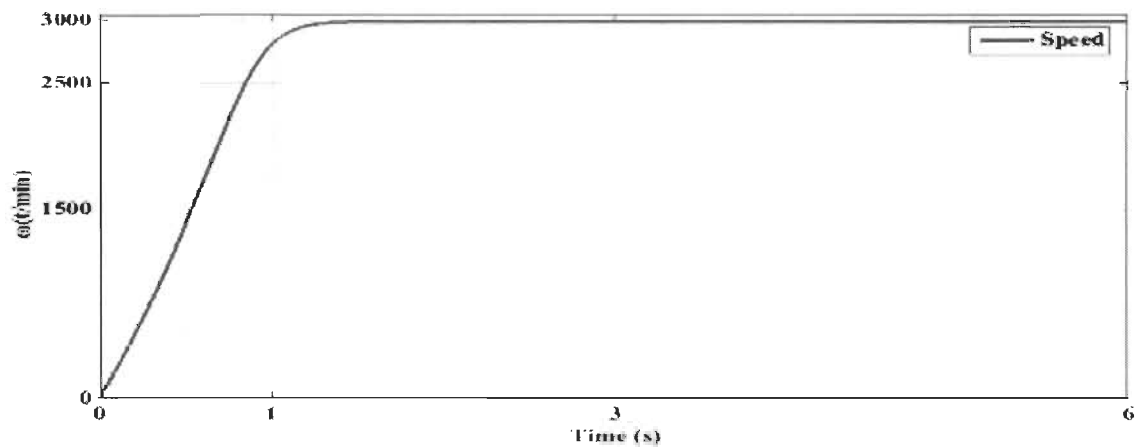


Figure 2-10 Rotor speed at no-load

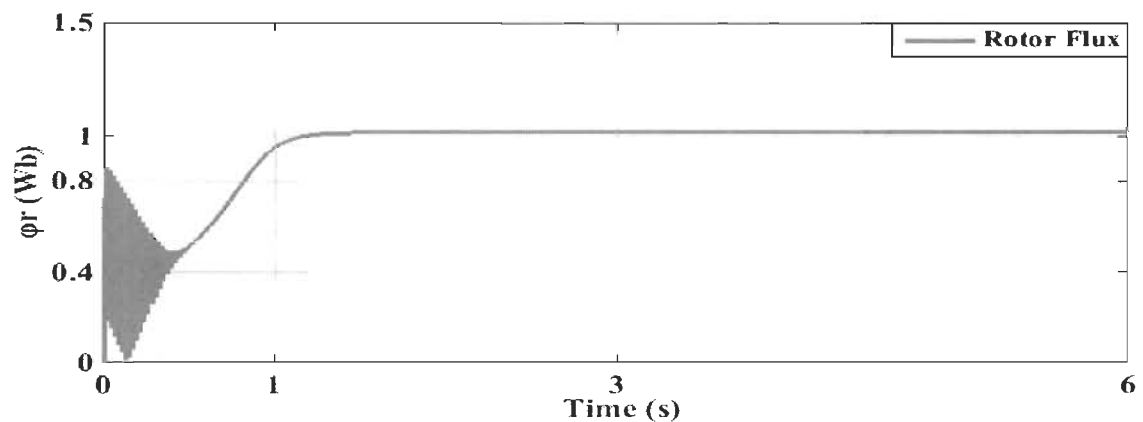


Figure 2-11 Rotor flux at no-load

In the second test, we applied a load torque $T_L = 14N.m$ at $t=3s$. The electromagnetic torque increases as shown in Figure 2-13 to compensate the load torque till reaching $14.27N.m$, while the rotor speed decreases from $2994 t/min$ to $2639 t/min$ (Figure 2-14). Both of stators absorb an important current, where at $t=3s$ it jumps from 13.74 to 17.37A. As

shown in Figure 2-15. These two tests illustrate the need of another mechanism that permits to maintain rotor speed constant at the presence of a load torque.

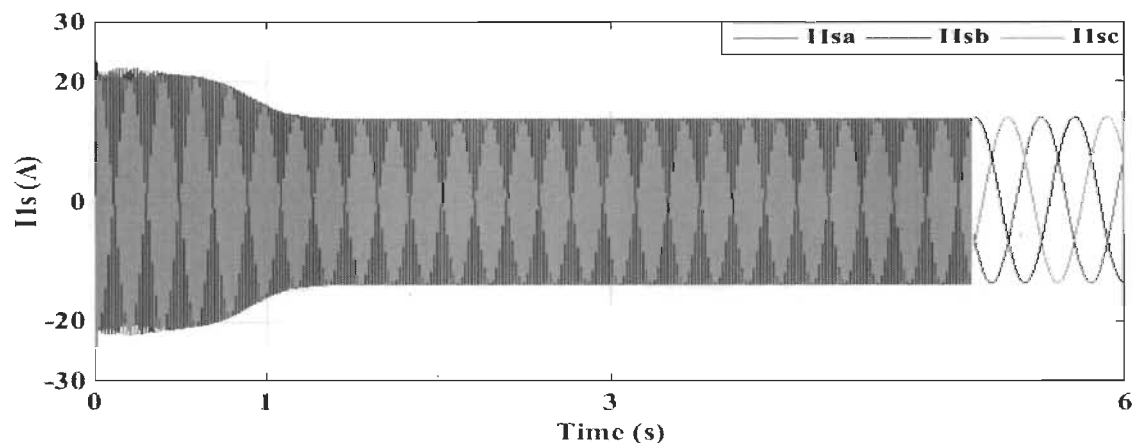


Figure 2-12 Three-phase currents of stator I at no-load

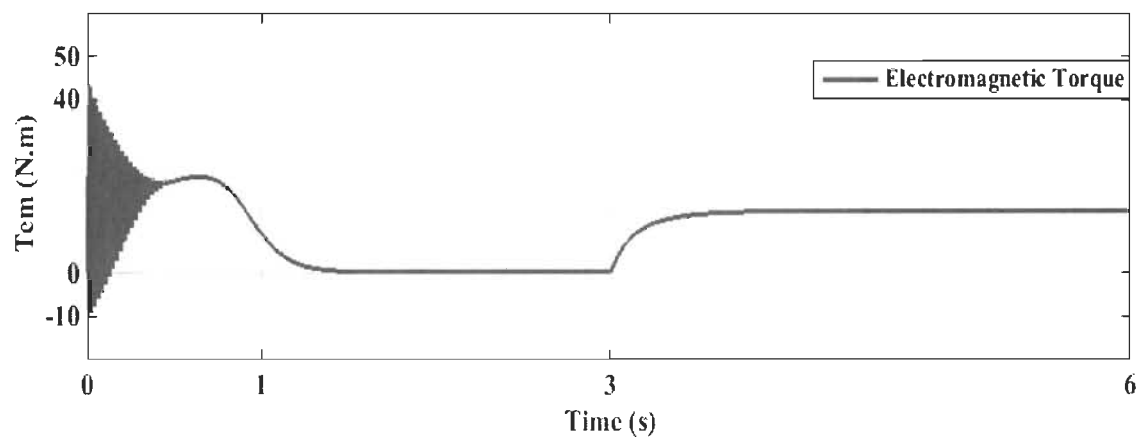


Figure 2-13 Electromagnetic torque at full-load

2.5.2 Case study# 2

In this case, both stators are supplied by two voltage source inverters control in open loop through a PWM technique. From Figure 2-16 to Figure 2-18, we observe that the same results

of the case study#1 in full-load have been obtained with the presence of harmonics in the stator currents which are induced by inverters (Figure 2-18).

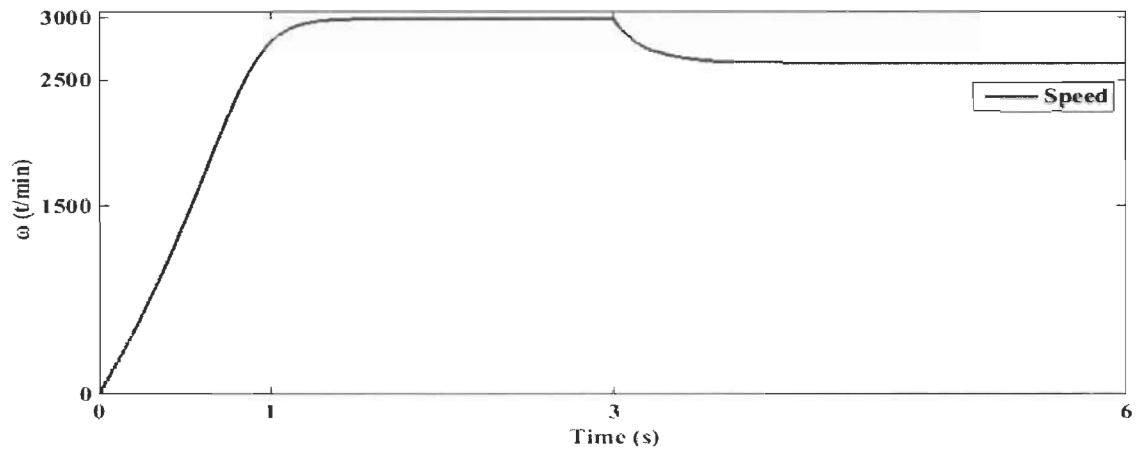


Figure 2-14 Rotor speed at full-load

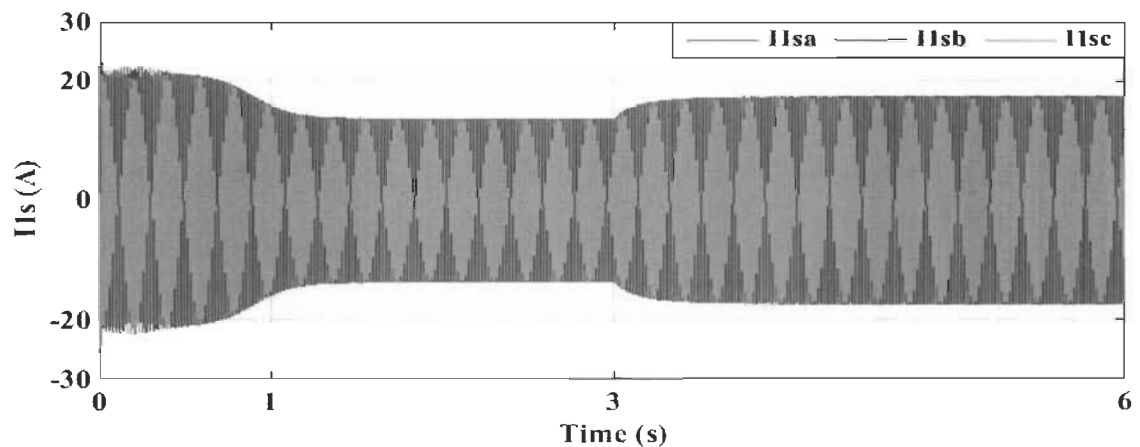


Figure 2-15 Three-phase currents of stator I at full-load

2.5.3 Case study# 3

In this case, a load torque is applied at $t=(2s-3.5s)$, $T_L = 14N.m$ and at $t=(3.5s-6s)$ $T_L = -14N.m$. The electromagnetic torque increases to $14.90 N.m$ and decreases to $-15.10 N.m$ to compensate the load torque (Figure 2-19). The presence of PI controller relieves the

influence of load torque on the speed where it tracks the reference which is equal to 3000 t/min as depicted in Figure 2-20. The rotor flux tracks the imposed reference which is equal to 1 Wb as illustrated in Figure 2-21. The rotor flux is identical to its direct component while the quadrature component is referred to zero as shown in Figure 2-22. Figure 2-23 depicts that both stators draw 15A at the start-up then it takes the permanent value which equals to 2A. At $t=2\text{s}$ and at $t=3.5$, stators absorb 6A following the presence of the load torque.

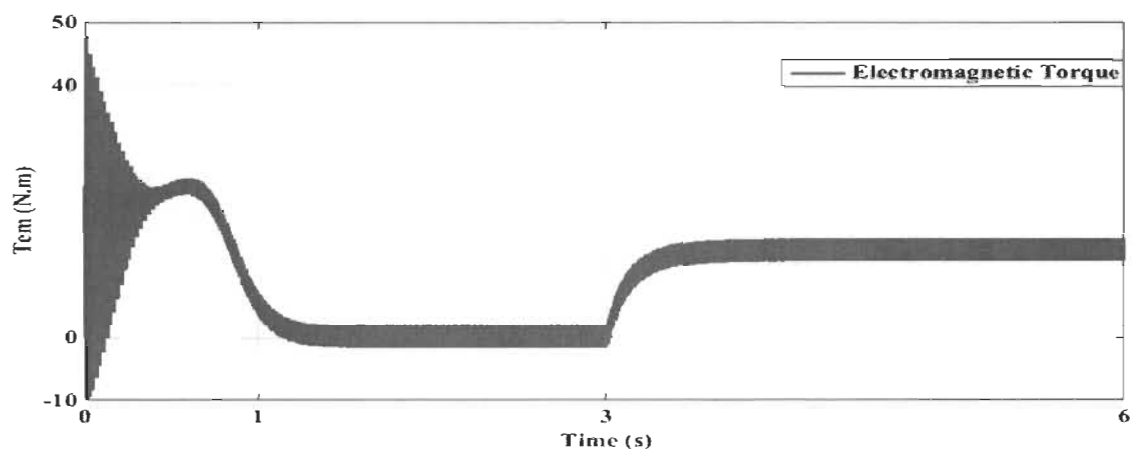


Figure 2-16 Electromagnetic torque in open loop control

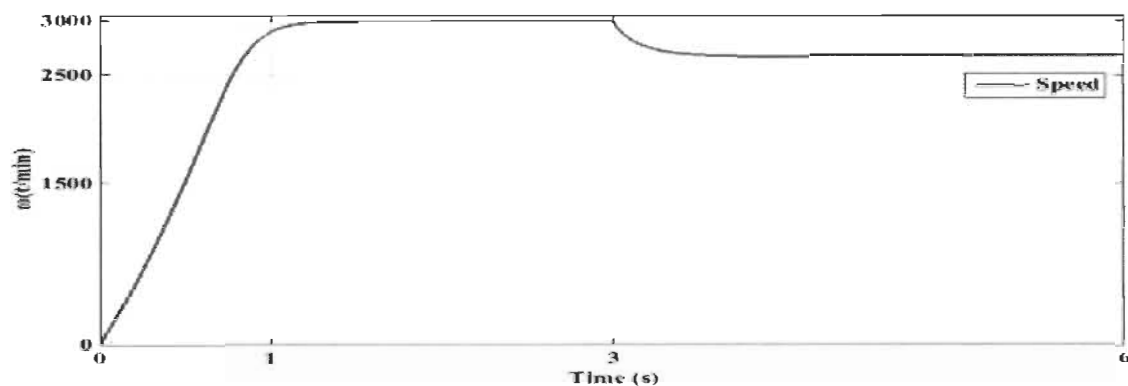


Figure 2-17 Rotor speed evolution in open loop control

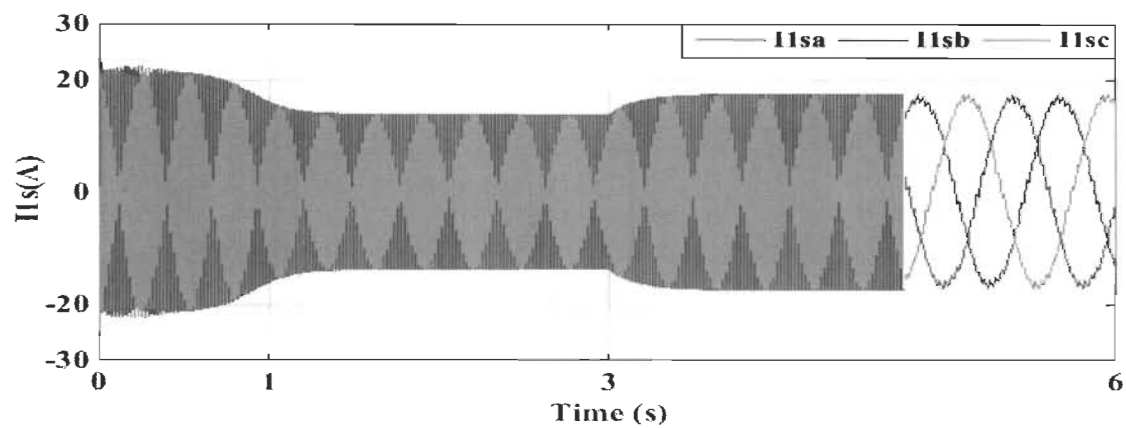


Figure 2-18 Three-phase currents of stator I

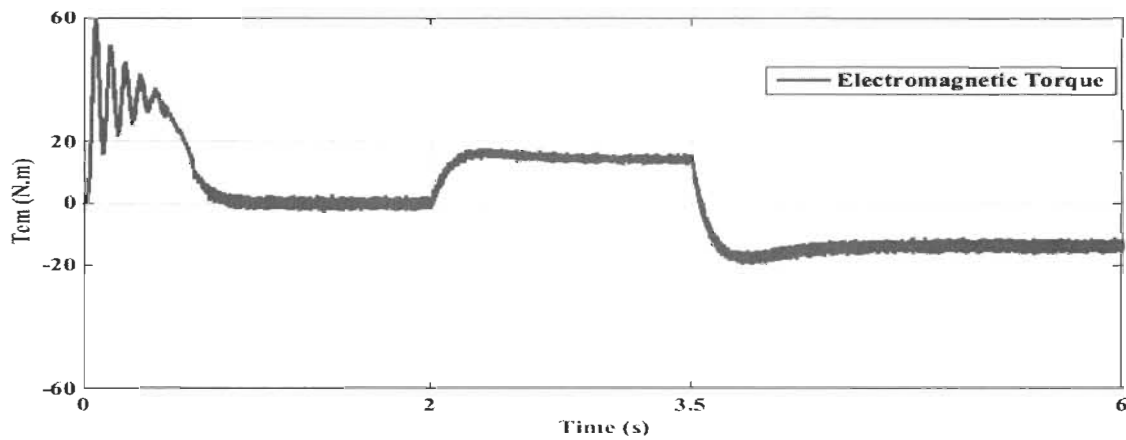


Figure 2-19 Electromagnetic torque

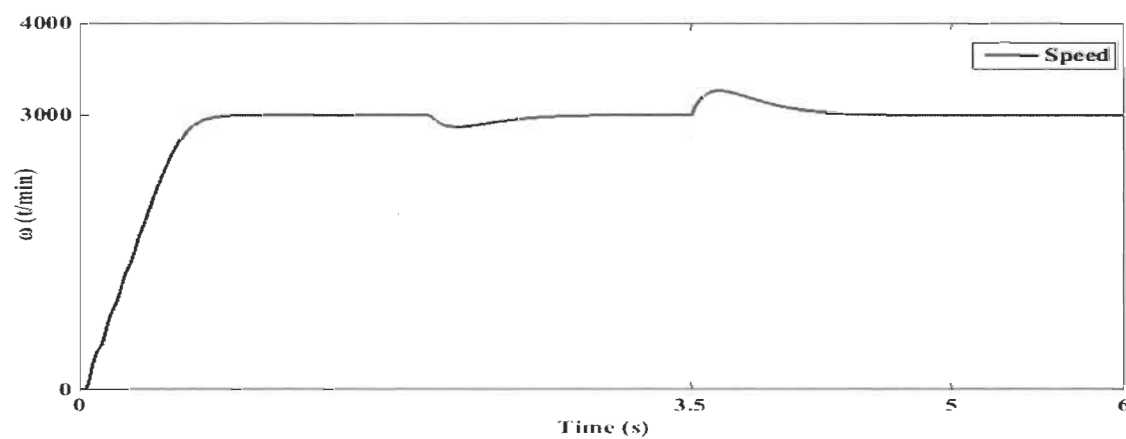


Figure 2-20 Rotor speed evolution

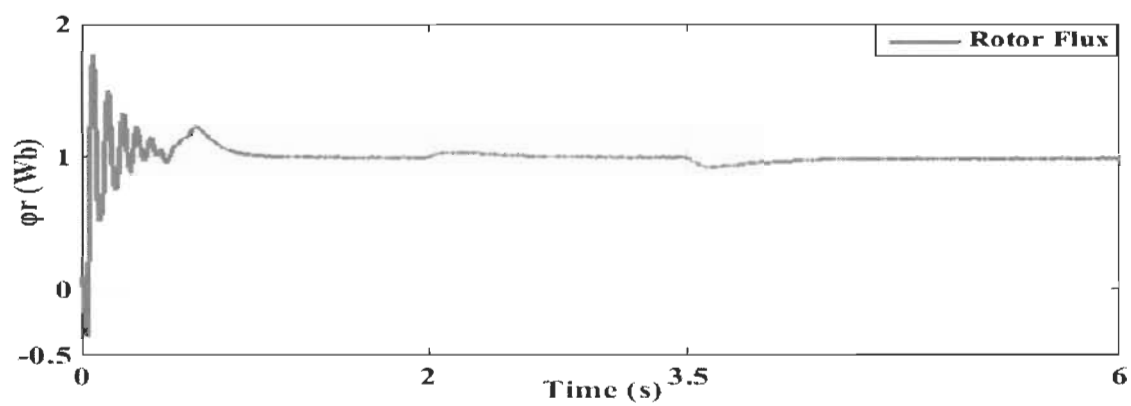


Figure 2-21 Rotor flux

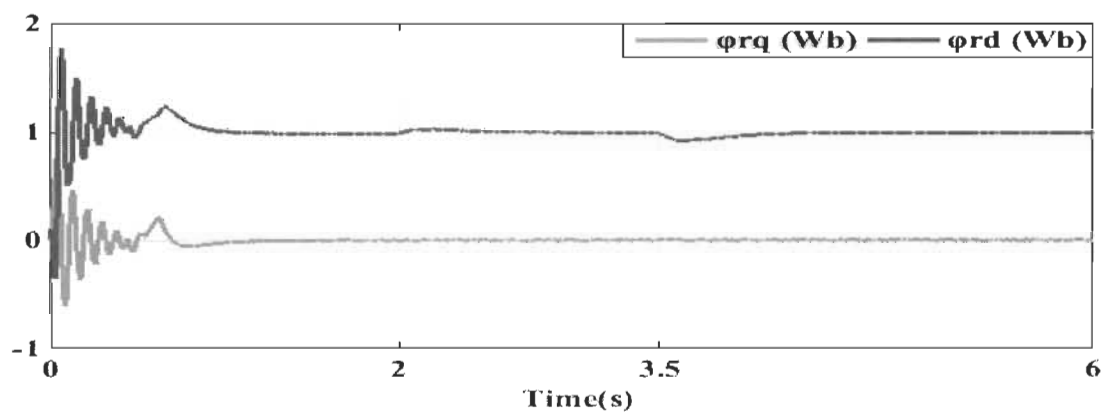


Figure 2-22 Direct and quadrature rotor flux components

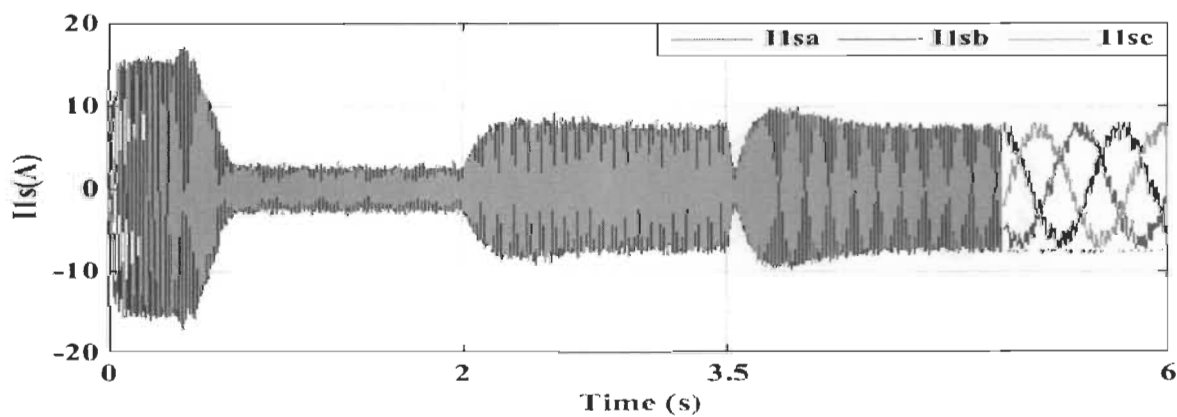


Figure 2-23 Three-phase currents of stator I

2.6 Conclusion

This chapter presents a study on a dual stator winding induction machine operating as a motor for drive applications. Based on the literature, a description and a mathematical modeling of DSWIM are proposed. Then, simulation models are developed to investigate the performance of this motor in direct grid fed condition in the first study case. In the second and third study cases, the DSWIM is supplied by two voltage source inverters in open loop control and closed loop respectively. In the case study#3, a rotor field-oriented control technique with the indirect speed regulation method is applied. This technique shows a good performance in which, the electromagnetic torque and rotor flux are totally decoupled and the speed keeps tracking the reference even in the presence of load torque variation. However, as a linear controller, PI-controller is not adequate in variable parameters conditions, which require an advanced controller such as sliding mode and fuzzy logic control techniques. We also suggest investigating the performance of DSWIM with regenerative braking for four-quadrant operation mode.

Chapitre 3 - Self-Excited-DSWIG for stand-alone application with passive compensator

3.1 Introduction

Wind power based distributed generation system becomes a mature technology, which enables producing a clean energy without using non-renewable resources. A new generation of multi-phase generators (more than six-phase) has penetrated the wind power field bringing various advantages compared to their counterpart (three-phase generator) as mentioned previously. Among multi-phase generator, self-excited dual stator winding induction generator (SE-DSWIG) has been proposed in many applications. In this chapter, we inspect the performance of SE-DSWIG in stand-alone applications feeding a variable load using both of stators. A passive compensator is proposed to mitigate power issues related to voltage in term of sag and swell.

3.2 Description of SE-DSWIG

A two pole, six-phase, self-excitation induction generator scheme is presented in Figure 3-1. It involves dual three-phase winding set and a squirrel cage rotor (r_1, r_2, r_3). The first three phase winding set is labeled ($\alpha_1, \alpha_2, \alpha_3$) and noted stator I while the second three phase windings set is denoted ($\beta_1, \beta_2, \beta_3$) and called stator II. Both of stators are shifted mutually by an angle $\theta = 30^\circ$. The rotor is displaced by θ_1 against the first stator and by θ_2 against the second one. All stators and rotor windings are scattered uniformly and every three identical windings set are shifted mutually by 120° .

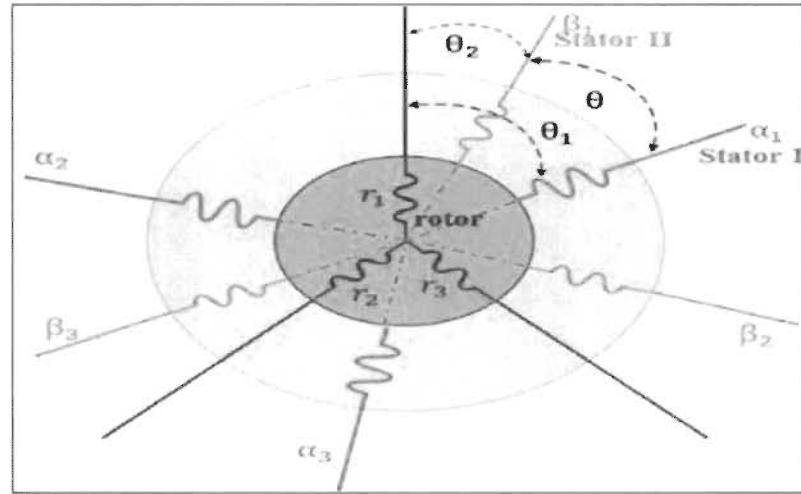


Figure 3-1 SE-DSWIG scheme

3.3 Mathematical modeling of SE-DSWIG

The SE-DSWIG mathematical model possesses ten differential equations with variable and periodic coefficients in time. The electric and magnetic equations are given in DQ-frame as follows [69].

3.3.1 Electric equations

$$V_{1sd} = -R_{s1}I_{1sd} + \frac{d}{dt}\varphi_{1sd} - \omega_s \varphi_{1sq} \quad (3-1)$$

$$V_{1sq} = -R_{s1}I_{1sq} + \frac{d}{dt}\varphi_{1sq} + \omega_s \varphi_{1sd} \quad (3-2)$$

$$V_{2sd} = -R_{s2}I_{2sd} + \frac{d}{dt}\varphi_{2sd} - \omega_s \varphi_{2sq} \quad (3-3)$$

$$V_{2sq} = -R_{s2}I_{2sq} + \frac{d}{dt}\varphi_{2sq} + \omega_s \varphi_{2sd} \quad (3-4)$$

$$V_{rd} = R_r I_{rd} + \frac{d}{dt}\varphi_{rd} - (\omega_s - \omega_r)\varphi_{rq} \quad (3-5)$$

$$V_{rq} = R_r I_{rq} + \frac{d}{dt}\varphi_{rq} + (\omega_s - \omega_r)\varphi_{rd} \quad (3-6)$$

I_m is the magnetic current given by

$$I_m = \sqrt{(-i_{1sd} - i_{2sd} + i_{rd})^2 + (-i_{1sq} - i_{2sq} + i_{rq})^2} \quad (3-14)$$

The electromagnetic torque is estimated by the afterward expression

$$T_{em} = \frac{3p}{4} \left(\frac{L_m}{L_m + L_{lr}} \right) \{ (i_{1sq} + i_{2sq}) \phi_{rd} - (i_{1sd} + i_{2sd}) \phi_{rq} \} \quad (3-15)$$

3.3.3 Excitation capacity bank model

SE-DSWIG belongs to the self-excited machine categories. It needs a capacity bank connected at the stator terminals to get the necessary reactive power to start working.

At the presence of the residual magnetism and a sufficient rotating speed, the SE-DSWIG engenders enough current which stimulates the capacity bank to inject reactive power into the windings. This operation will be repeated until getting equality between the SE-DSWIG output voltage and capacity bank terminal voltage. This will be the DSWIG operating point. The following equations express the mathematical representation of the excitation capacity bank connected to stator I and stator II terminals.

$$\begin{cases} \frac{d}{dt} V_{1sd} = \frac{1}{C_{s1}} I_{1sd} + \omega_s V_{1sq} \\ \frac{d}{dt} V_{1sq} = \frac{1}{C_{s1}} I_{1sq} - \omega_s V_{1sd} \end{cases} \quad (3-16)$$

$$\begin{cases} \frac{d}{dt} V_{2sd} = \frac{1}{C_{s2}} I_{2sd} + \omega_s V_{2sq} \\ \frac{d}{dt} V_{2sq} = \frac{1}{C_{s2}} I_{2sq} - \omega_s V_{2sd} \end{cases} \quad (3-17)$$

3.4 Passive compensator

The passive compensator (PC) becomes a mature technology, which is used to improve the power quality [70-72]. It involves lossless reactive components based inductance and/ or

capacitance. Mostly, the passive compensator is introduced in series or in shunt to the grid through switching devices. Basically, the PC mitigates issues related to voltage and current such, voltage sag, swell, disturbance, collapse, power factor, neutral current, harmonics flickers, etc [70]. As well, PC enhances the energy exploitation and improves the power flow in transient and steady-state conditions. Generally, the intervention of shunt PC is done over exchanging the reactive power with AC mains through a reactive current to control the characteristics of the grid (current and voltage) at the point of common coupling (PCC) [71]. The series PC generates a reactive current or induces a compensating voltage if the PC has a capacitive impedance [30]. In wind power, the PC has been widely used especially in fixed speed-based turbines. For instance, in the Danish concept where the generator is directly connected to the grid, the PC absorbs the stress and compensates voltage disturbances induced by a sudden change in wind speed.

3.4.1 Passive compensator design for voltage sag

In this chapter, the SE-DSWIG operates in a stand-alone application, where a variable load is connected to stator I and stator II as illustrated in Figure 3-3. The fluctuation of wind speed and the variation of end-user's impedance provokes intermittence in power generation and voltage disturbance. Hence, PC is used to maintain the voltage across the end-user at a suitable level. We describe the design procedure of the PC in series and in shunt compensation topologies, as illustrated in Figure 3-4.

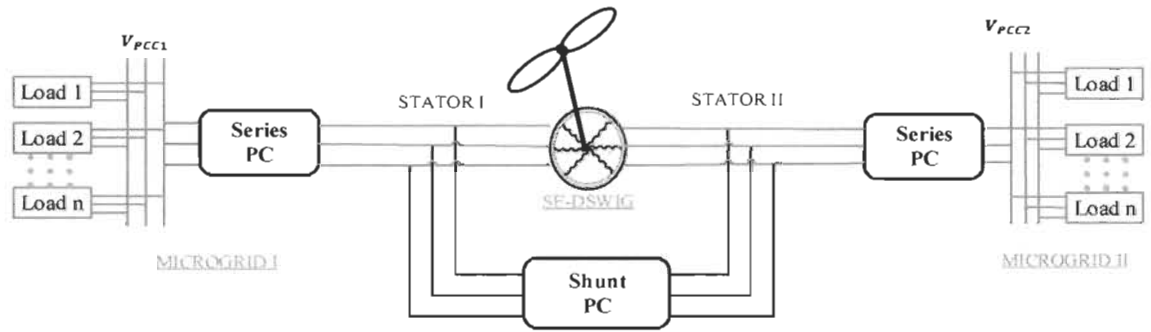


Figure 3-3 SE-DSWIG in stand-alone application

3.4.1.1 Shunt compensator design

Since the main task of the PC is to mitigate voltage droop across the end-user, hence its impedance is supposed purely capacitive. We note that the interaction between the passive compensator and the stator-winding should be taken into to reduce the resonance phenomenon. In this topology, the shunt passive compensator is inserted at the load terminals as shown in Figure 3-4 –(A). with V_{1s} , I_{1s} , R_{1s} and L_{s1} are the stator I voltage, current and impedance.

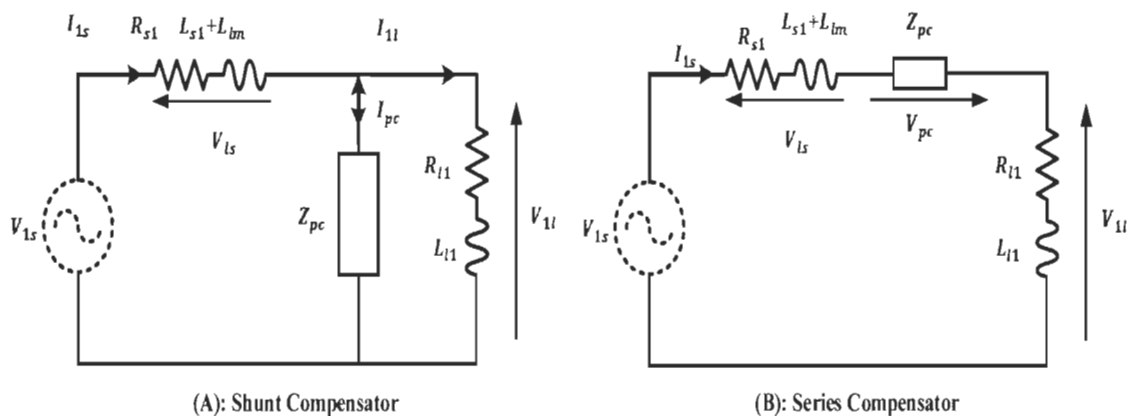


Figure 3-4 shunt and series passive compensator topologies

In the ideal conditions

$$|V_{1s}| = |V_{1l}| \quad (3-18)$$

$$|V_{1l}| = |I_{1s}| * |Z_{pc} // Z_{l1}| \quad (3-19)$$

Z_{pc} , Z_l and Z_s are defined as follows:

$$Z_{pc} = -\frac{j}{\omega_s C_{pc}} \quad (3-20)$$

$$Z_l = R_l + j\omega_s L_{l1} \quad (3-21)$$

$$Z_s = R_{s1} + j\omega_s(L_{lm} + L_{s1}) \quad (3-22)$$

Substituting $|I_{1s}|$ by its equivalent, (3-19) becomes:

$$|V_{1l}| = \frac{|V_{1s}|}{Z_s + |Z_{pc} // Z_{l1}|} * |Z_{pc} // Z_{l1}| = |V_{1s}| \quad (3-23)$$

Simplifying (3-23) we get:

$$1 = \frac{Z_{pc} * Z_{l1}}{Z_{pc} * Z_{l1} + Z_{pc} * Z_s + Z_s * Z_{l1}} \quad (3-24)$$

With

$$|Z_{pc} // Z_{l1}| = \left| \frac{Z_{pc} * Z_{l1}}{Z_{pc} + Z_{l1}} \right| \quad (3-25)$$

Resolving (3-24) it implies:

$$Z_{pc} = \left| \frac{Z_l * Z_s}{Z_s} \right| \quad (3-26)$$

The objective is to estimate the required PC capacitance to maintain (3-18) always true which is given by:

$$C_{pc} = \frac{1}{2\pi f} \frac{\sqrt{R_{s1}^2 + (\omega_s L_{s1})^2}}{\sqrt{R_{s1}^2 + (\omega_s L_{s1})^2} * \sqrt{R_{l1}^2 + (\omega_s L_{s1})^2}} \quad (3-27)$$

Figure 3-5 represents the phasor diagram of the voltage regulation at the load.

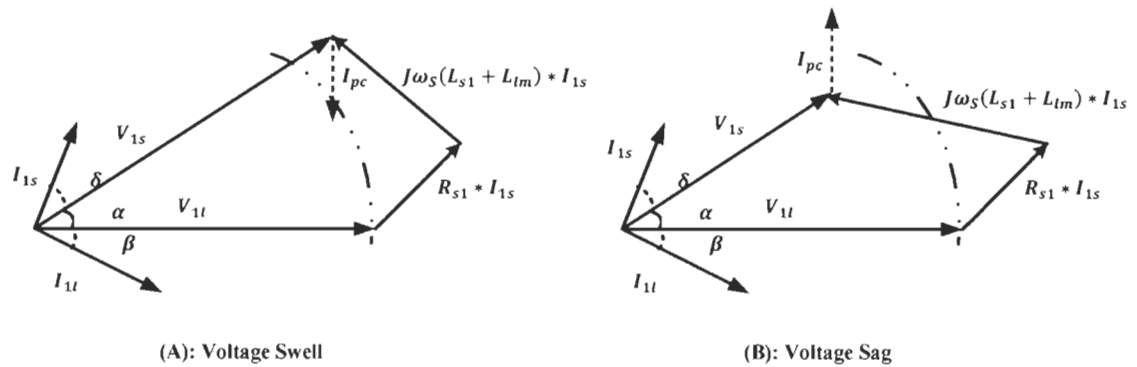


Figure 3-5 Phasor diagram of shunt passive compensator

3.4.1.2 Series compensator design

Figure 3-4 –(B) shows the series compensation topology. For the voltage across the end-user to be equal to the generated voltage, the following equality should true

$$|V_{1s}| = -|V_{pc}| \quad (3-28)$$

Since the same current goes through Z_s and Z_{pc} then

$$|Z_s| = -|Z_{pc}| \quad (3-29)$$

The (-) sign means that the series passive compensator should behave as follows

- A voltage swell occurs in the grid implies that there is an excess of reactive power. Hence, the series PC acts in the inductive mode to absorb the excess.
- In voltage sag situation, the series passive compensator behaves in the capacitive mode to inject the lack of reactive power. Figure 3-6 shows the phasor diagram of the voltage regulation at the load terminals using series passive compensator

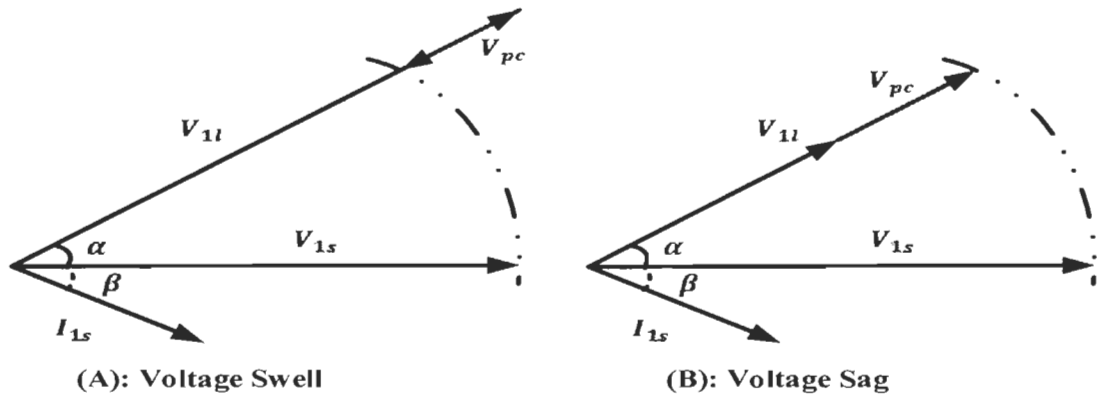


Figure 3-6 Phasor diagram of series passive compensator

3.5 Modeling of the end-user

The end user is represented by an inductive load to evaluate its influence on the performance of the SE-DSWIG. In the presence of PC, its impedance should be added to the mathematical representation of the end-user. Based on Kirchhoff law, we deduce the mathematical modeling of the end-user without PC and in the presence of the PC as bellow

3.5.1 End-user with no-passive compensator

$$\frac{d}{dt} V_{1sd} = \frac{1}{C_{s1}} [I_{1sd} - I_{1ld}] + \omega_s V_{1sq} \quad (3-30)$$

$$\frac{d}{dt} V_{1sq} = \frac{1}{C_{s1}} [I_{1sq} - I_{1lq}] - \omega_s V_{1sd} \quad (3-31)$$

$$\frac{d}{dt} V_{2sd} = \frac{1}{C_{s2}} [I_{2sd} - I_{2ld}] + \omega_s V_{2sq} \quad (3-32)$$

$$\frac{d}{dt} V_{2sq} = \frac{1}{C_{s2}} [I_{2sq} - I_{2lq}] - \omega_s V_{2sd} \quad (3-33)$$

The direct and quadratic load currents are:

$$\frac{d}{dt} I_{1ld} = \frac{1}{L_{l1}} [V_{1sd} - R_{l1} I_{1ld}] + \omega_s I_{1lq} \quad (3-34)$$

$$\frac{d}{dt} I_{1lq} = \frac{1}{L_{l1}} [V_{1sq} - R_{l1} I_{1lq}] - \omega_s I_{1ld} \quad (3-35)$$

$$\frac{d}{dt} I_{2ld} = \frac{1}{L_{l2}} [V_{2sd} - R_{l1} I_{2ld}] + \omega_s I_{2lq} \quad (3-34)$$

$$\frac{d}{dt} I_{2lq} = \frac{1}{L_{l2}} [V_{2sq} - R_{l1} I_{2lq}] - \omega_s I_{2ld} \quad (3-35)$$

3.5.2 End-user with shunt passive compensator

$$\frac{d}{dt} V_{1sd} = \frac{1}{(C_{s1} + C_{pc})} [I_{1sd} - I_{1ld}] + \omega_s V_{1sq} \quad (3-36)$$

$$\frac{d}{dt} V_{1sq} = \frac{1}{(C_{s1} + C_{pc})} [I_{1sq} - I_{1lq}] - \omega_s V_{1sd} \quad (3-37)$$

$$\frac{d}{dt} V_{2sd} = \frac{1}{(C_{s2} + C_{pc})} [I_{2sd} - I_{2ld}] + \omega_s V_{2sq} \quad (3-38)$$

$$\frac{d}{dt} V_{2sq} = \frac{1}{(C_{s2} + C_{pc})} [I_{2sq} - I_{2lq}] - \omega_s V_{2sd} \quad (3-39)$$

$$\frac{d}{dt} I_{1ld} = \frac{1}{L_{l1}} [V_{1sd} - R_{l1} I_{1ld}] + \omega_s I_{1lq} \quad (3-40)$$

$$\frac{d}{dt} I_{1lq} = \frac{1}{L_{l1}} [V_{1sq} - R_{l1} I_{1lq}] - \omega_s I_{1ld} \quad (3-41)$$

$$\frac{d}{dt} I_{2ld} = \frac{1}{L_{l2}} [V_{2sd} - R_{l2} I_{2ld}] + \omega_s I_{2lq} \quad (3-42)$$

$$\frac{d}{dt} I_{2lq} = \frac{1}{L_{l2}} [V_{2sq} - R_{l2} I_{2lq}] - \omega_s I_{2ld} \quad (3-43)$$

3.5.3 End-user with series passive compensator

▪ STATOR I

$$\frac{d}{dt} V_{1sd} = \frac{1}{(C_{s1})} [I_{1sd} - I_{1ld}] + \omega_s V_{1sq} \quad (3-44)$$

$$\frac{d}{dt} V_{1dcp} = \frac{I_{1td}}{(C_{pc})} + \omega_s V_{1qpc} \quad (3-45)$$

$$\frac{d}{dt} I_{1td} = \frac{1}{(L_{l1})} [V_{1sd} - V_{1dcp} - R_{l1} I_{1td}] + \omega_s I_{1lq} \quad (3-46)$$

$$\frac{d}{dt} V_{1sq} = \frac{1}{(C_{s1})} [I_{1sq} - I_{1lq}] - \omega_s V_{1sd} \quad (3-47)$$

$$\frac{d}{dt} V_{1qcp} = \frac{I_{1lq}}{(C_{s1})} - \omega_s V_{1dcp} \quad (3-48)$$

$$\frac{d}{dt} I_{1lq} = \frac{1}{(L_{l1})} [V_{1sq} - V_{1qcp} - R_{l1} I_{1lq}] - \omega_s I_{1td} \quad (3-49)$$

▪ STATOR II

$$\frac{d}{dt} V_{2sd} = \frac{1}{(C_{s2})} [I_{2sd} - I_{2ld}] + \omega_s V_{2sq} \quad (3-50)$$

$$\frac{d}{dt} V_{2dcp} = \frac{I_{2td}}{(C_{se})} + \omega_s V_{2qpc} \quad (3-51)$$

$$\frac{d}{dt} I_{2td} = \frac{1}{(L_{l2})} [V_{2sd} - V_{2dcp} - R_{l2} I_{2td}] + \omega_s I_{2lq} \quad (3-52)$$

$$\frac{d}{dt} V_{2sq} = \frac{1}{(C_{s2})} [I_{2sq} - I_{2lq}] - \omega_s V_{2sd} \quad (3-53)$$

$$\frac{d}{dt} V_{2qcp} = \frac{I_{2lq}}{(C_{se})} - \omega_s V_{2dcp} \quad (3-54)$$

$$\frac{d}{dt} I_{2lq} = \frac{1}{(L_{l2})} [V_{2sq} - V_{2qcp} - R_{l2} I_{2lq}] - \omega_s I_{2td} \quad (3-55)$$

3.6 Numerical results and discussion

To evaluate the performance of the SE-DSWIG in a stand-alone application, the power system represented in Figure 3-3 is developed in Matlab®/SimPowerSystems. This work deals with voltage sags and swells issues that occur in a distributed generation system based on wind power. The main reasons for the voltage variation are either wind speed fluctuation which has a direct influence on the generated voltage, or heavy loads suddenly connected to

the supply bus. A passive compensator has been used in series shunt and hybrid series-shunt topologies to mitigate the voltage sag and swell. The variation in speed and load are emulated by a step change, while power system parameters (SE-DSWIG, passive compensator, and end-user impedance) are given in Appendix B.

3.6.1 SE-DSWIG performance at no-load condition

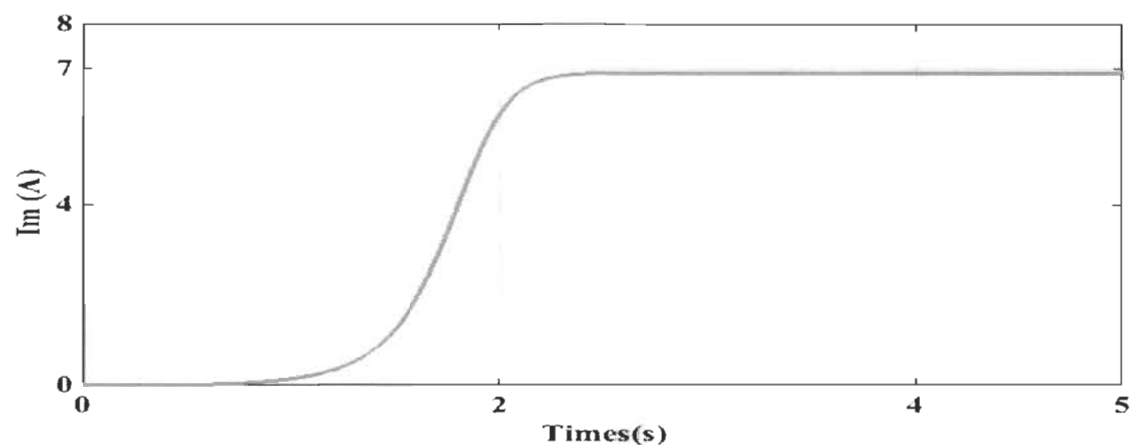


Figure 3-7 Magnetizing current

Figure 3-7 illustrates that the magnetizing current progresses exponentially with time until reaching the steady state value that equals to 6.7A at $t=2.5s$. Figure 3-8 shows that magnetizing inductance value decreases versus the increase of the magnetizing current following the polynomial equation defined in (3-13).

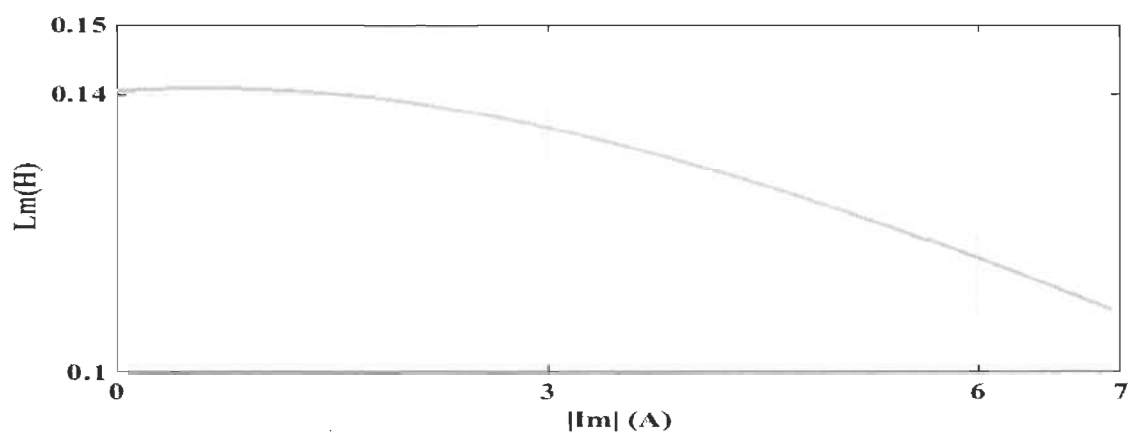


Figure 3-8 Magnetizing inductance versus magnetizing current

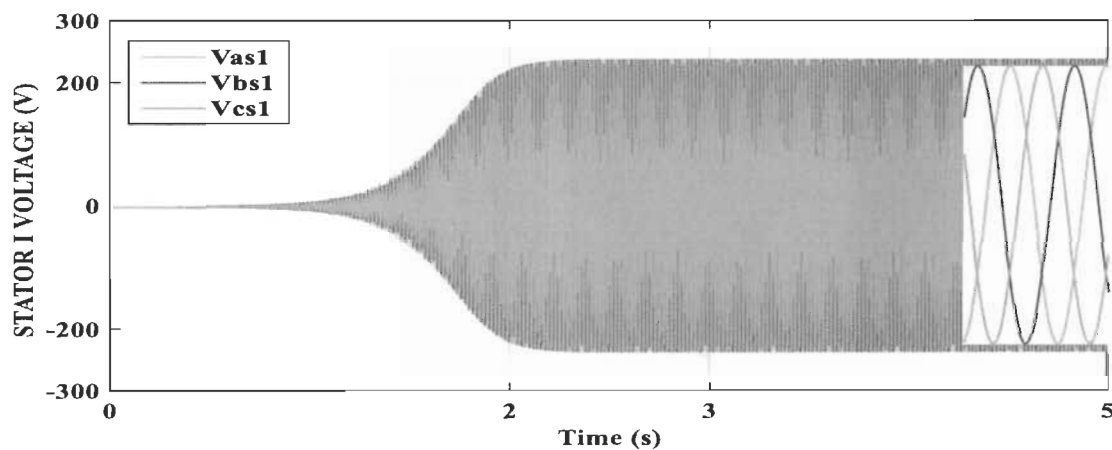


Figure 3-9 Stator I voltage evolution at no-load

Figure 3-9, Figure 3-10, Figure 3-11 and Figure 3-12 display the evolution of stator I and stator II voltages and currents respectively. They increase exponentially following the magnetizing current, then stabilize at $t=2.85$ reaching 225V and 2.8A. The magnitude of the generated voltage and current depends on the excitation capacity bank value and the prime mover speed. Figure 3-13 shows that there is a phase shift between the stator current and

voltage, in which the current is ahead emulating a capacitive power system. This is due to the presence of the excitation capacity bank.

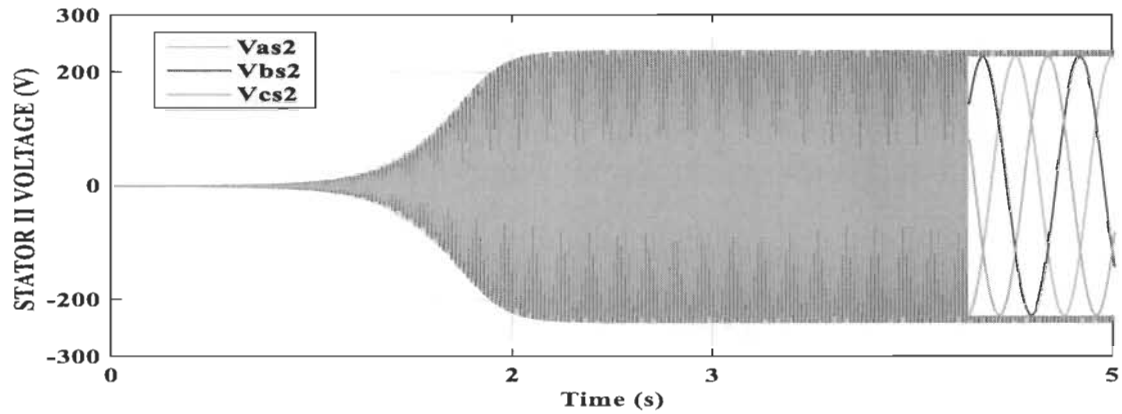


Figure 3-10 Stator II voltage evolution at no-load

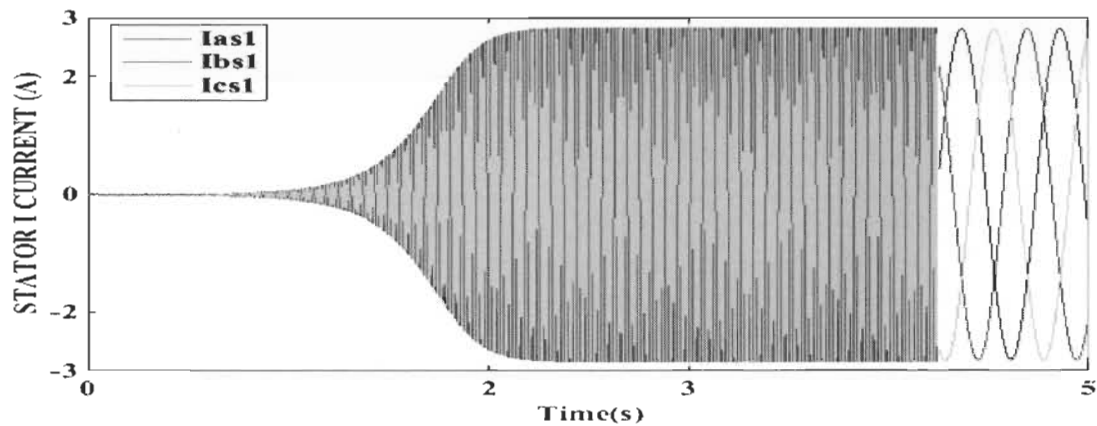


Figure 3-11 Stator I current evolution at no-load

The rotor current is significantly less compared to the stator current (Figure 3-14). It rises till reaching 0.62A during the transient regime then it stabilizes in the steady state at less than 0.2A.

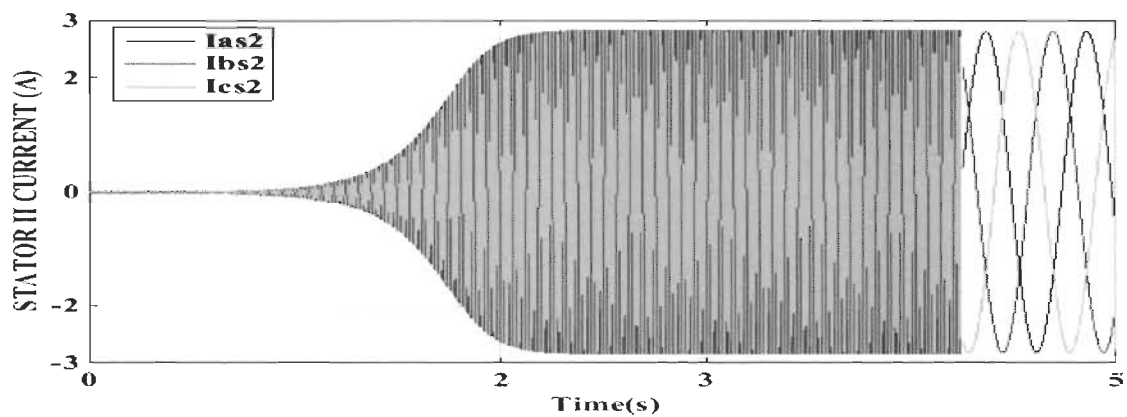


Figure 3-12 Stator II current evolution at no-load

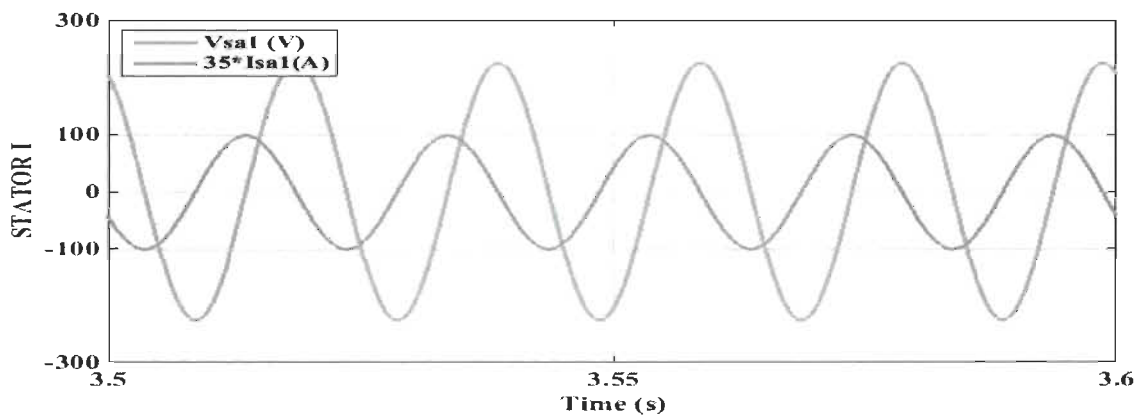


Figure 3-13 Phase shift between stator current and voltage

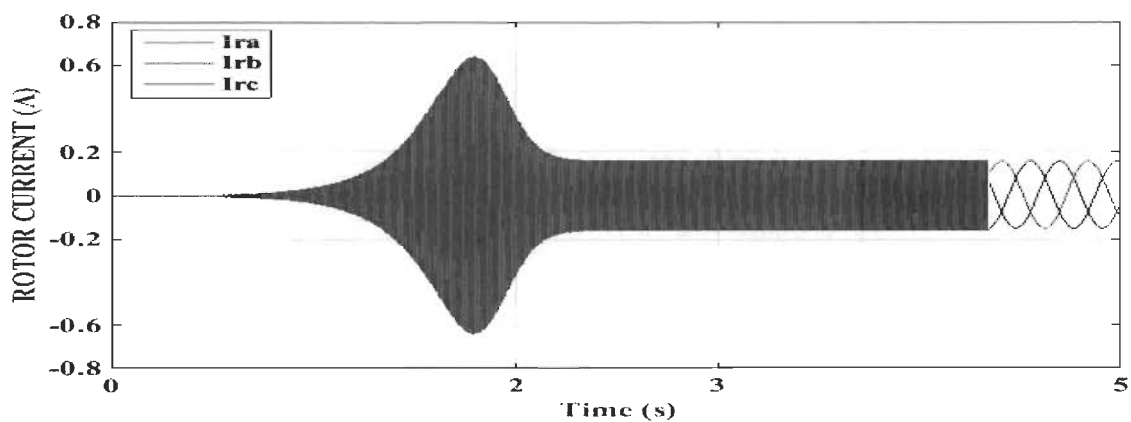


Figure 3-14 Rotor current evolution

3.6.2 SE-DSWIG performance feeding the end-user in the presence of shunt PC

In this scenario, the end user is modeled by an inductive load ($R_{l1} = R_{l2} = 300\Omega, L_{l1} = L_{l2} = 5.3mH$) the obtained results are presented in Figure 3-15 to Figure 3-18. At $t=3.5s$, the SE-DSWIG starts feeding the end-users which decreases the stator voltage and current magnitude due to a lack of reactive power which is consumed by loads. At $t=4s$, the passive compensator is connected in shunt between the generator and the end-user resulting in the remedy of the trouble translated by increasing the current and the voltage magnitude till getting the ideal state.

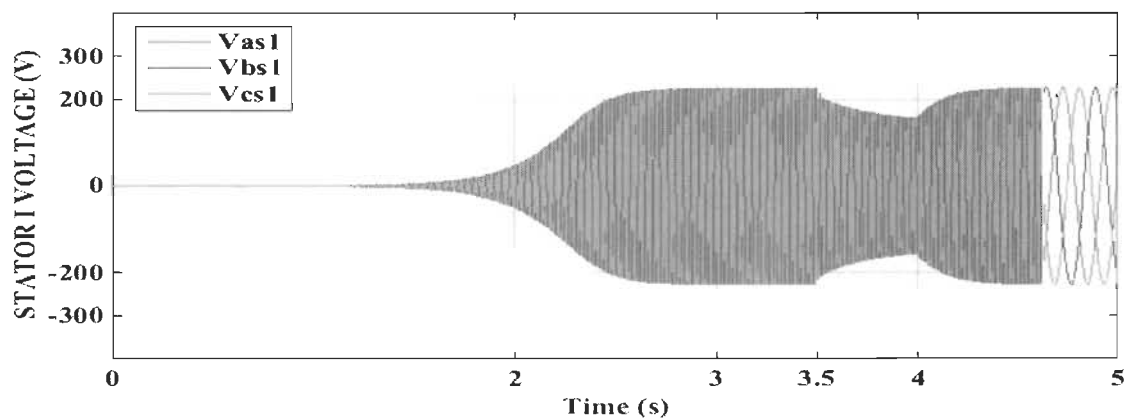


Figure 3-15 Stator I voltage evolution in the presence of shunt PC

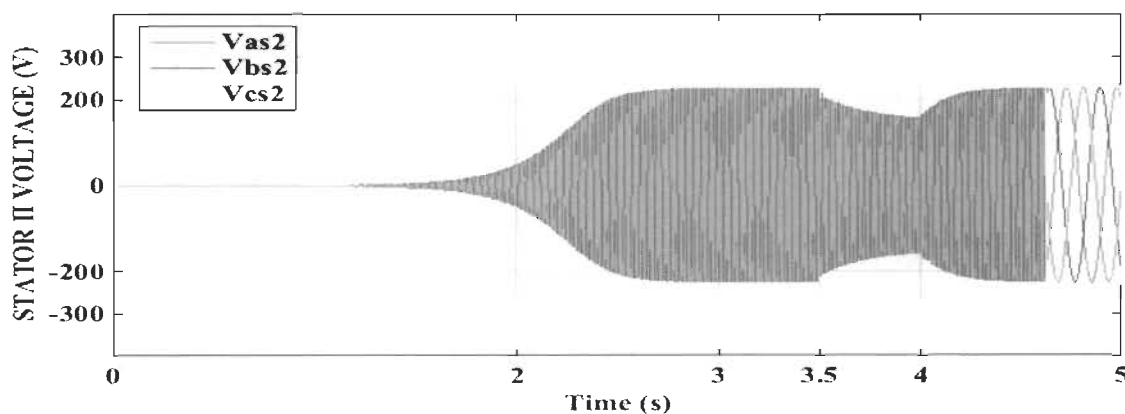


Figure 3-16 Stator II voltage evolution in the presence of shunt PC

The shunt PC introduces a quadratic current at the terminals that provokes an augmentation in current values after compensation as shown Figure 3-17 and Figure 3-18. This is due to the transfer of reactive current from PC into the power system that justifies the augmentation of current after shunt compensation.

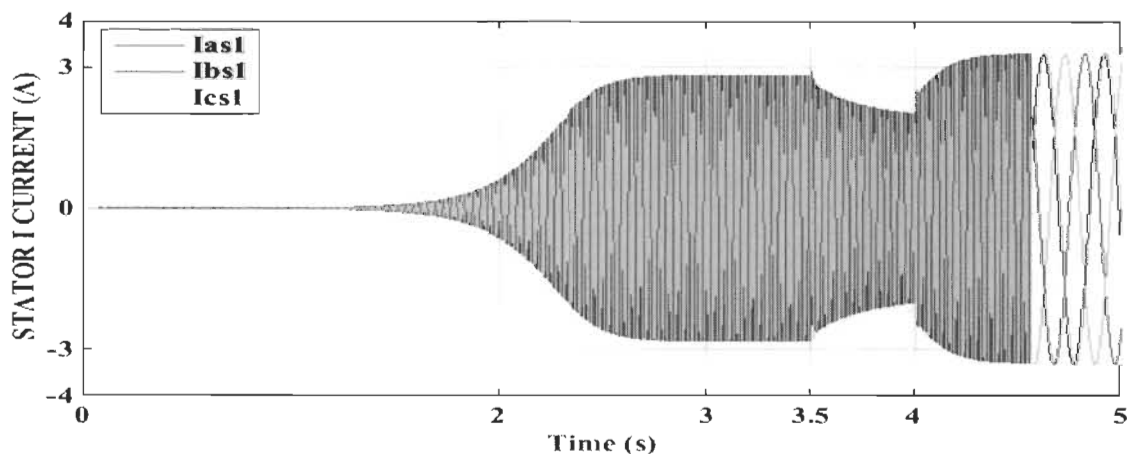


Figure 3-17 Stator I current evolution in the presence of shunt PC

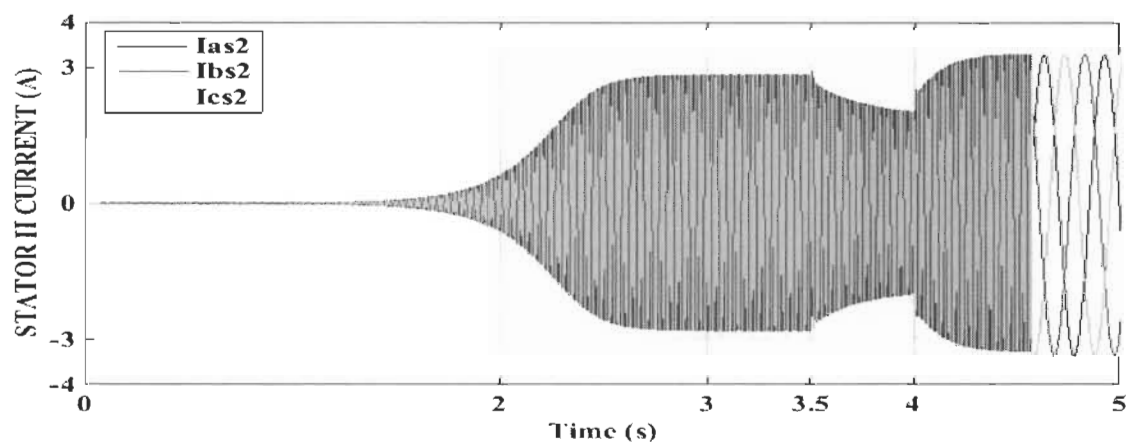


Figure 3-18 Stator II current evolution in the presence of shunt PC

3.6.3 SE-DSWIG performance feeding the end-user in the presence of series PC

In this scenario, the passive compensator is inserted in series between the generator and the end-user. The obtained results are depicted in Figure 3-19 to Figure 3-22. It's remarkable

that we get the same results as in the case where we used the shunt passive compensator, in which the current and voltage return to the ideal level after the series PC is switched on. However, the series PC intervention occurs by the generation of a compensating voltage on the same phase as the stator voltage without affecting the stator current magnitude as shown in Figure 3-21 and Figure 3-22.

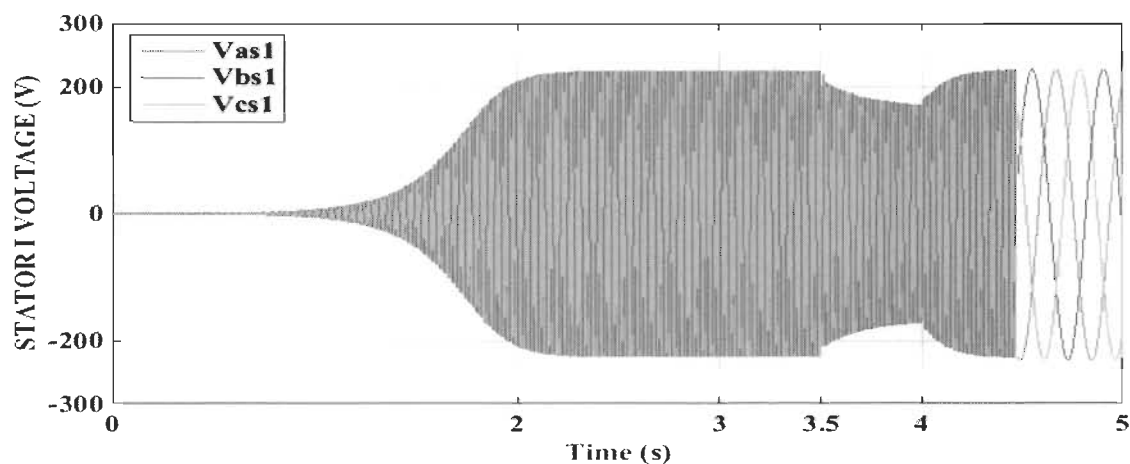


Figure 3-19 Stator I voltage evolution in the presence of series PC

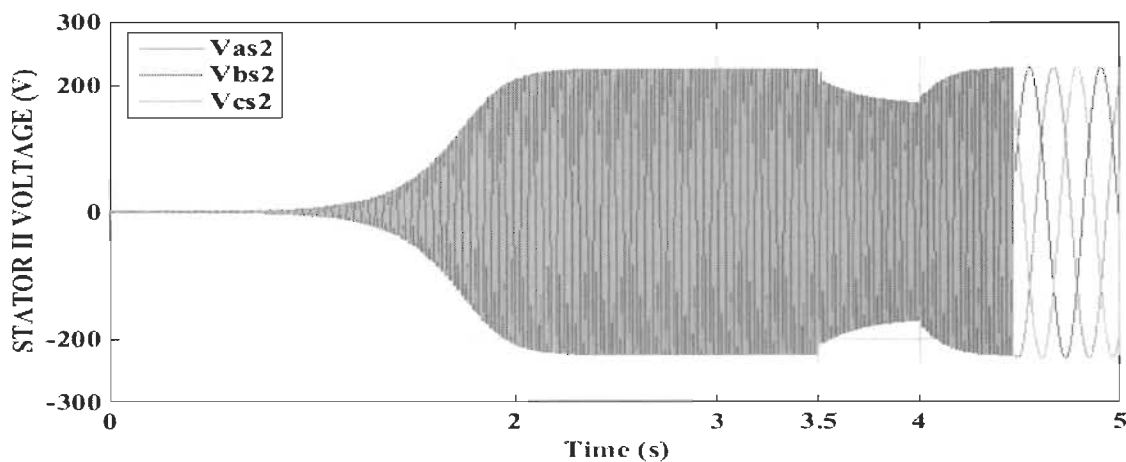


Figure 3-20 Stator II voltage evolution in the presence of series PC

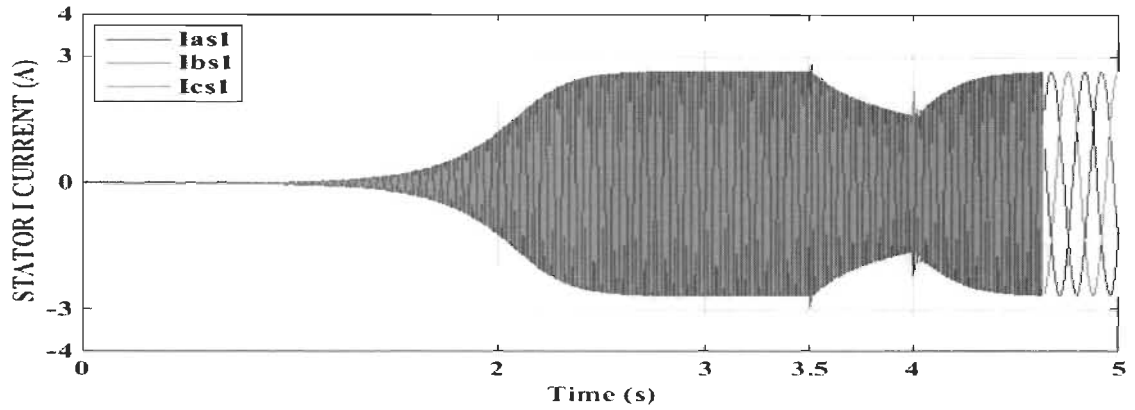


Figure 3-21 Stator I current evolution in the presence of series PC

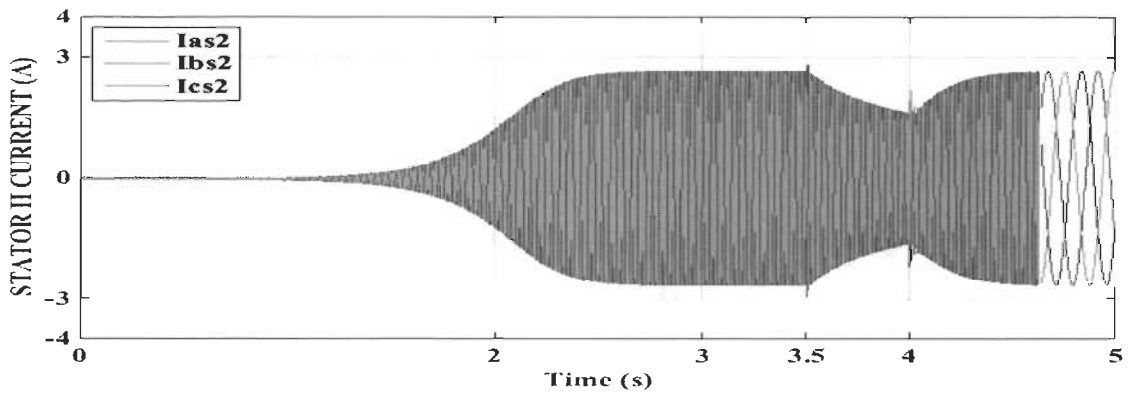


Figure 3-22 Stator II current evolution in the presence of series PC

3.6.4 SE-DSWIG performance with a step change in load impedance

In this case, the SE-DSWIG is exposed to a step change in load impedance emulating the variation of end-user load. At $t=3.5\text{s}$, the first load is connected ($R_{l1} = R_{l2} = 300\Omega$, $L_{l1} = L_{l2} = 5.3\text{mH}$), and at $t=4\text{s}$ a second one with the same impedance is connected. A hybrid series-shunt passive compensator (SSPC) has been used at the same time. From Figure 3-23 to Figure 3-26, we draw that the increase in load impedance has terrible side effect on SE-DSWIG characteristics. The increase of load impedance absorbs more active and reactive

power which implies a reduction in voltage and current magnitude where it falls from 225V, 2.8A in steady state to 86V, 1.2A respectively.

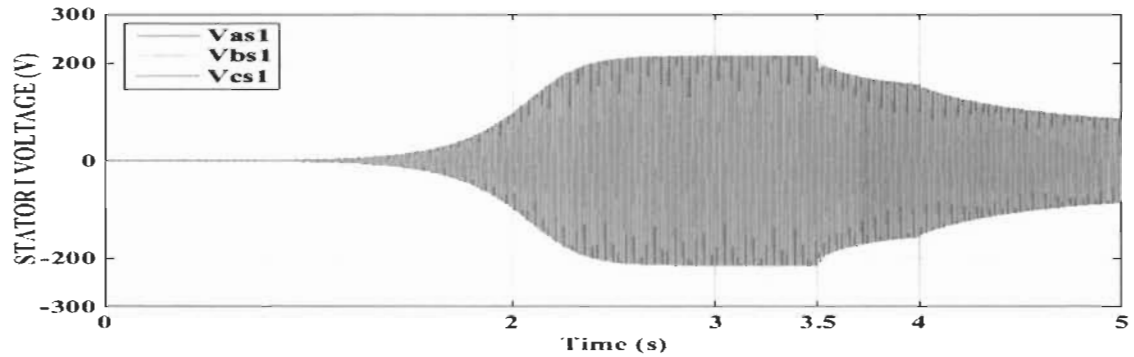


Figure 3-23 Stator I voltage evolution with step change in load without SSPC

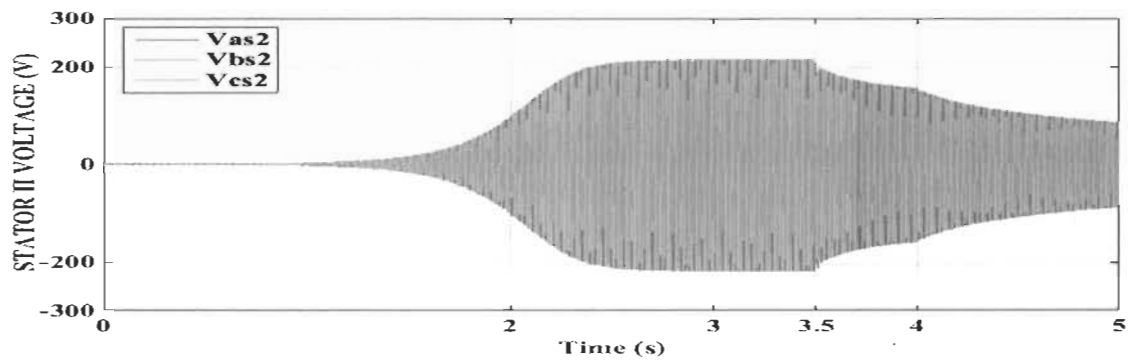


Figure 3-24 Stator II voltage evolution with step change in load without SSPC

Figure 3-27 to Figure 3-30 illustrate that the hybrid series-shunt passive compensator (SSPC) provides the required reactive power resulting in the mitigation of voltage and current collapse. The series part generates a compensating voltage while the shunt one injects a reactive current. The analytical design of the passive compensators shows that the size of reactive elements used in SSPC are much less than those used in the series or shunt PC, which brings more flexibility for the power system and maintains the load and generator voltage at a suitable level at low cost.

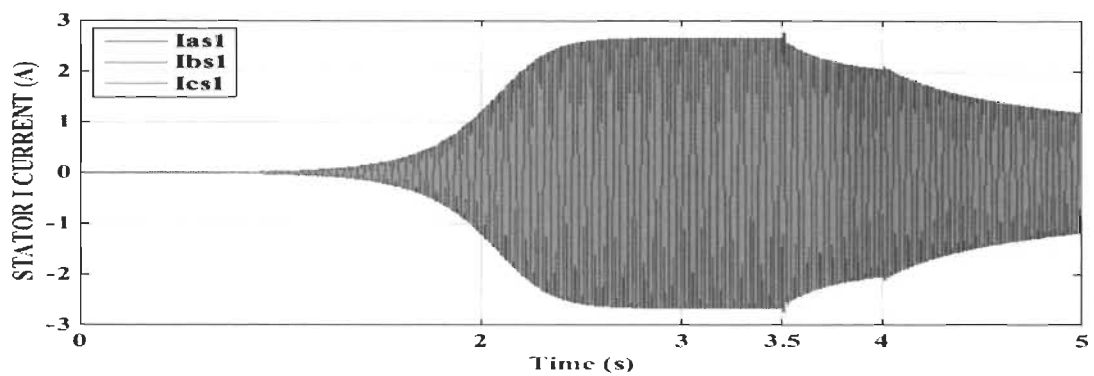


Figure 3-25 Stator I current evolution with step change in load without SSPC

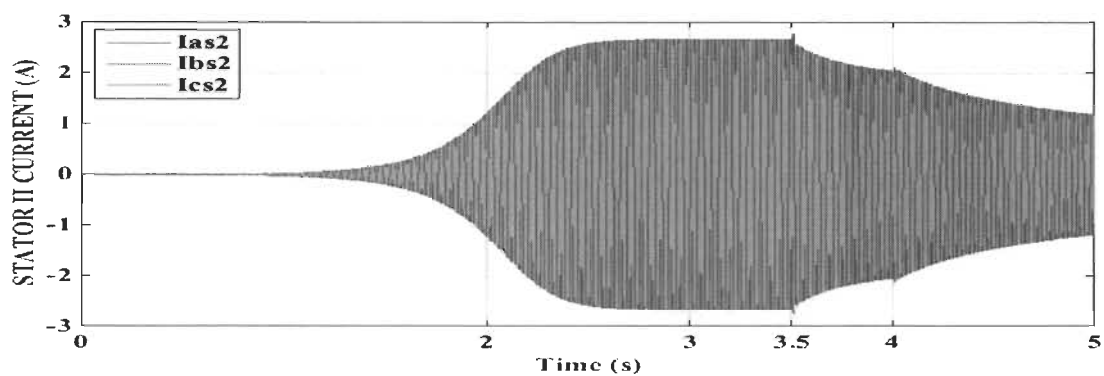


Figure 3-26 Stator II current evolution with step change in load without SSPC

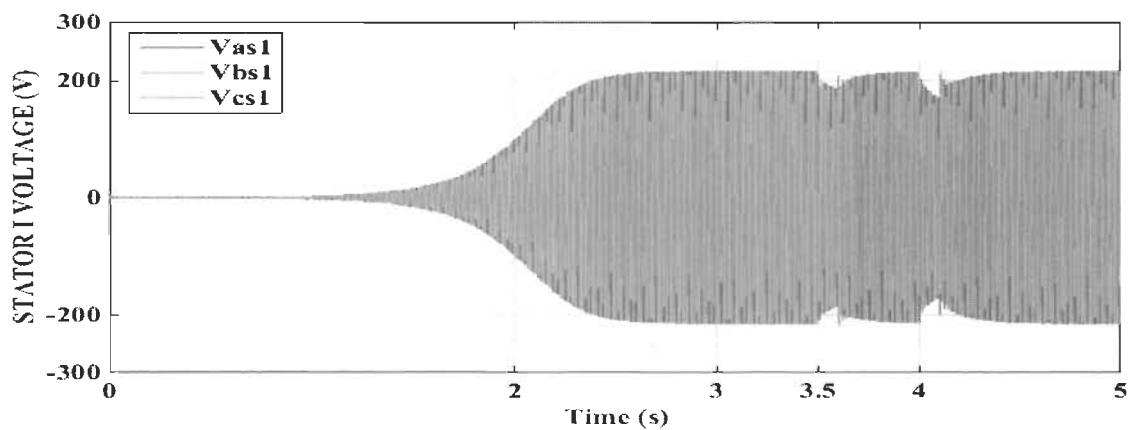


Figure 3-27 Stator I voltage evolution with step change in load with SSPC

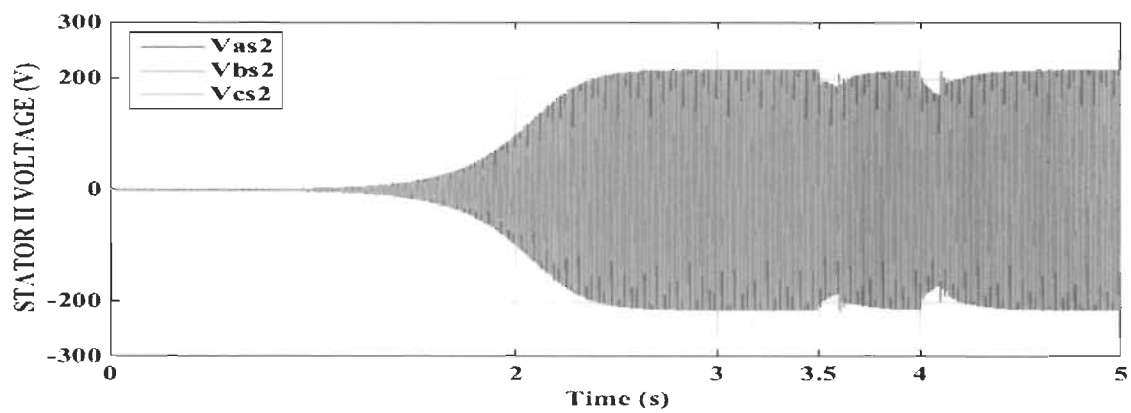


Figure 3-28 Stator II voltage evolution with step change in load with SSPC

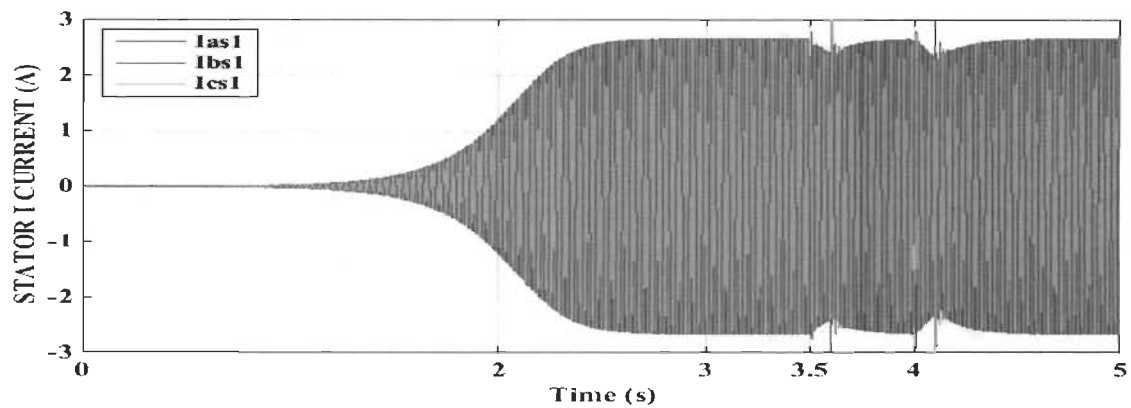


Figure 3-29 Stator I current evolution with step change in load with SSPC

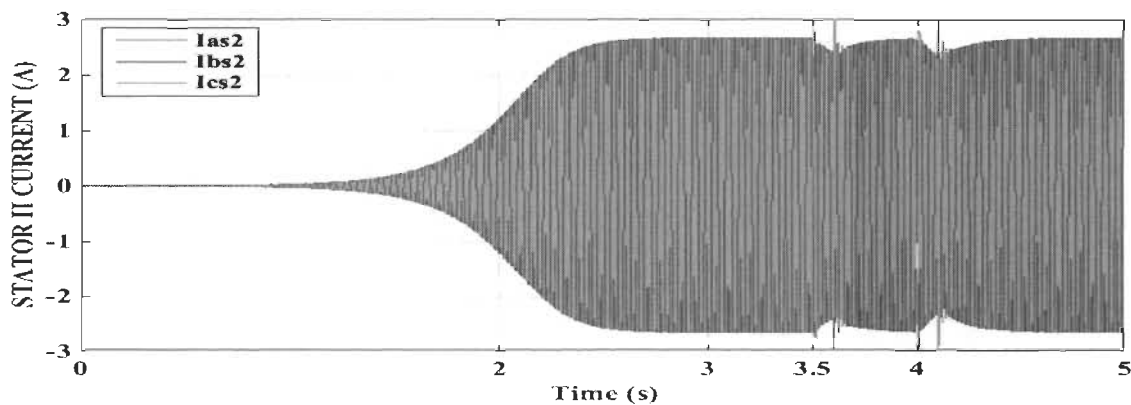


Figure 3-30 Stator II current evolution with step change in load with SSPC

3.6.5 SE-DSWIG performance with a step change in prime mover speed

In this scenario, we applied a step change in the prime mover speed, emulating the variation of wind speed in real condition as shown in Figure 3-31. An hybrid series-shunt passive compensator is inserted between the grid and the end-user. The obtained results in Figure 3-32 to Figure 3-35 illustrate that the diminution of speed at $t=3s$ provokes voltage and current collapse and the step up at $t=4s$ induces an increase in magnitude. However, the intervention of SSPC at $t=3.5s$ and at $t=5.5s$ rectifies the trouble.

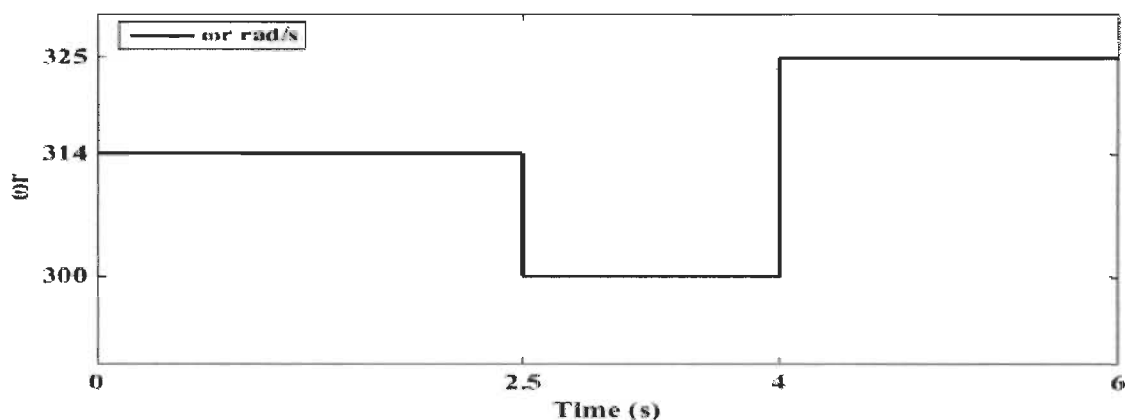


Figure 3-31 Rotor speed variation

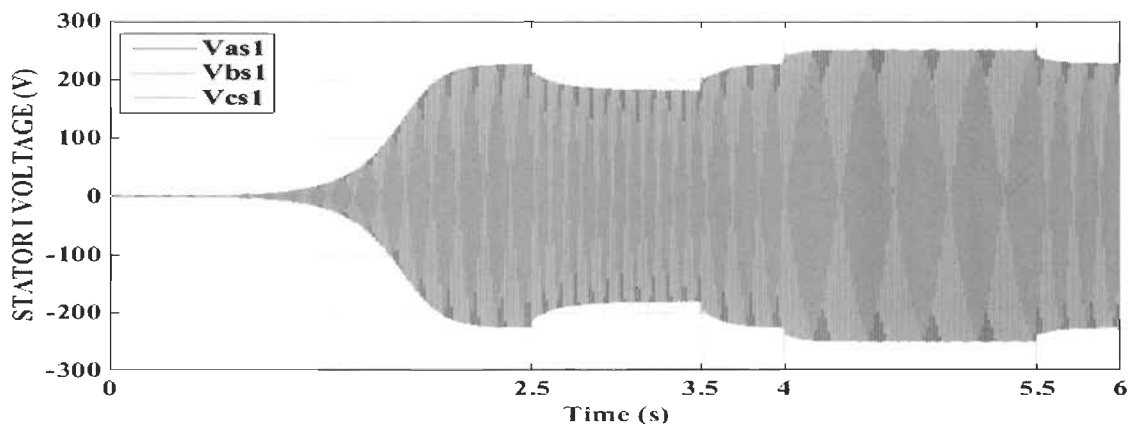


Figure 3-32 Stator I voltage evolution with step change in speed with SSPC

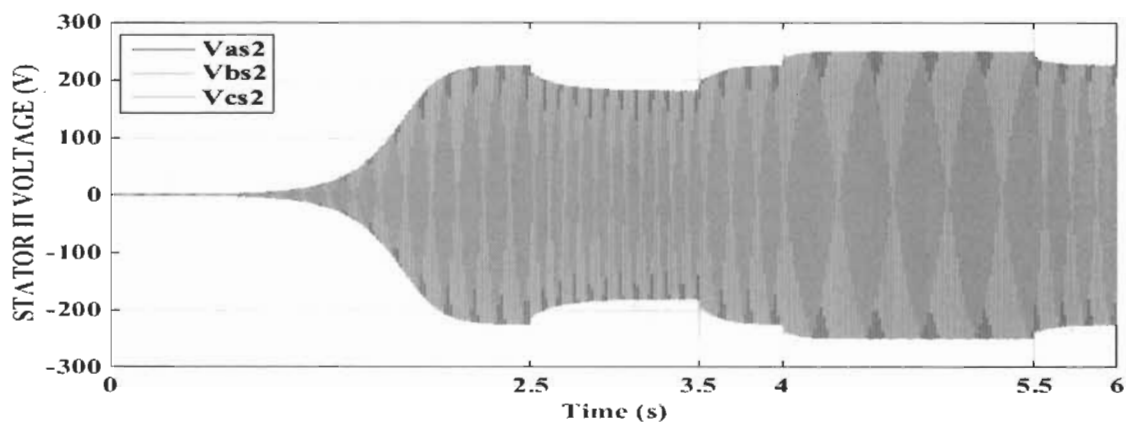


Figure 3-33 Stator II voltage evolution with step change in speed with SSPC

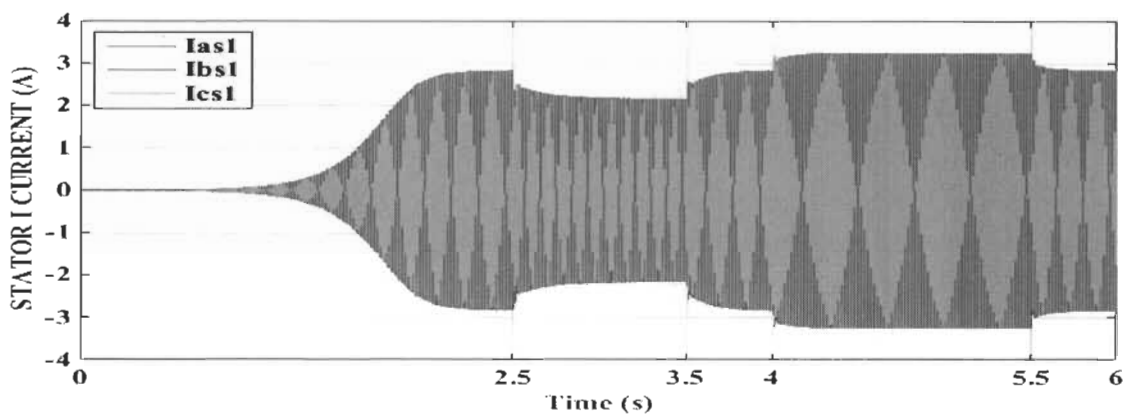


Figure 3-34 Stator I current evolution with step change in speed with SSPC

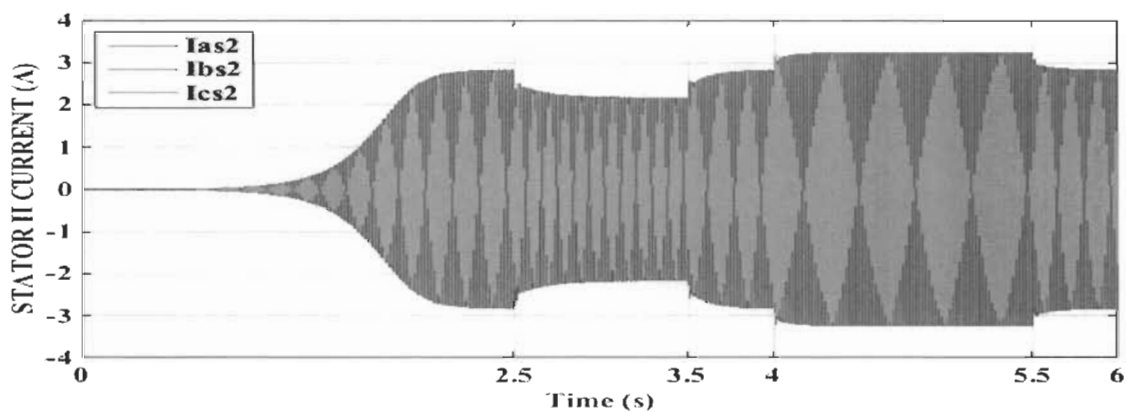


Figure 3-35 Stator II current evolution with step change in speed with SSPC

3.7 Conclusion

This chapter is dedicated to the wind power generation in stand-alone applications. A self-excitation dual stator winding induction generator is used as distributed generation system feeding the end-user through both of stators. We started this chapter by a mathematical modeling of the SE-DSWIG with considering the common mutual leakage inductance between stators and the magnetizing inductance which plays a principal role in the stabilization of the output voltage in the steady state. Then, the design of the passive compensation with the mathematical modeling of the end-user is presented. The performance of SE-DSWIG was evaluated through several scenarios in Matlab Simulink. We start by the study of SE-DSWIG at no-load conditions, then feeding the end-user which is modeled by an inductive load. A step variation is applied to the load impedance and the prime mover speed to investigate their influence on the SE-DSWIG characteristics. A passive compensator is inserted in series, shunt and in hybrid (series-shunt) between the generator and the end user to mitigate the power issues in term of sag and swell. The SE-DSWIG shows a good performance in different operating modes and gives the opportunity to build several topologies such as feeding two different end users or a stator connected to the grid utility and the other one feeding a customer. The passive compensator especially the SSPC supervised the power system stability and mitigated the voltage sag and swell perfectly. Nevertheless, the passive compensator needs to be adapted for every intervention, depending on the prime mover speed and the load size. The drawback of this technique is its slowness compared with the rapidity variation of both of loads size and weather conditions, so new technique is needed to allow to better adapting with these requirements. Customer power devices (CPD) and flexible AC transmission system (FACTS) connected in series or in parallel such as D-

STATCOM, DVR or hybrid such as UPFC; UPQC will be proposed to meet the demands in terms of rapidity and efficiency. In addition, the use of an advanced control algorithm is necessary to supervise the function of the active compensators (DVR, D-STATCOM, etc.) that participate in the improvement of the power flow and the mitigation of power quality issues.

Chaptre 4 - Study of D-STATCOM and DVR for poor power correction, voltage sag and swell mitigation

4.1 Introduction

The wind turbine is a promising technology, proposed to be an alternative solution to produce sustainable and clean power. However, its high sensibility against grid faults and the unpredictability of climatic conditions (wind speed), sets doubts about its ability to produce uninterrupted power [73]. For that, several grid codes have been issued to manage the behavior of wind turbine, which is called to act as a traditional power station in terms of power quality (PQ) [29]. Furthermore, the PQ concept preoccupies the energy suppliers, especially with the awareness of customers toward the lack of power service reliability and its consequences. For the end users, a good power quality means to get free-outage services. Whereas, a short-duration disturbance may not provoke an electricity interruption but surely it can burn expensive goods. Distributed Flexible AC Transmission Systems (D-FACTS) could be used to improve the low voltage ride through capability (LVRT) capability of a wind turbine and to mitigate power issues such as reactive power, harmonics, voltage sag, swells, surge, neutral current etc. [74-76]. D-FACTS family involves parallel active compensator (PAC), series active compensator (SAC), and hybrid series-parallel active compensator (SPAC). In this chapter, we explore the performance of a Distributed Static Synchronous Compensator (D-STATCOM) and a Dynamic Voltage Restorer (DVR) which belong respectively to parallel and series active compensator. D-STATCOM is used for

power factor correction, harmonic elimination, while the DVR deals with all issues related to voltage.

4.2 Distributed Static Synchronous Compensator (D-STATCOM)

D-STATCOM is mainly used for mitigating poor power factor, unbalanced current, neutral current, etc [76-88]. It has been also used for zero voltage regulation in isolated distributed generation systems [89-93]. D-STATCOM is able to enhance the performance of a wind turbine by controlling the reactive power evolution that permits the amelioration of LVRT capability [74, 89, 92, 94, 95]. In this chapter, we investigate the behavior of a D-STATCOM against poor power factor.

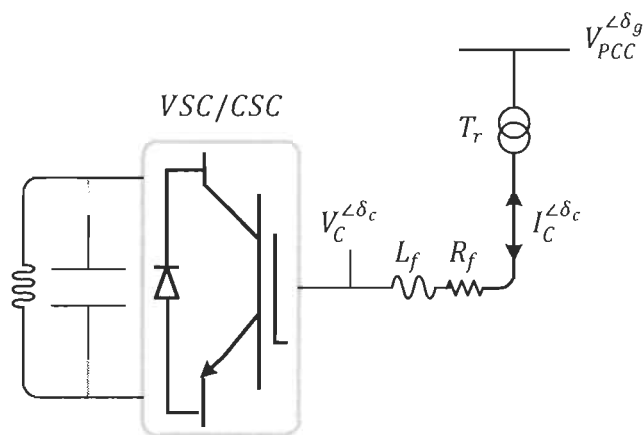


Figure 4-1 D-STATCOM connected to the grid

D-STATCOM is voltage source converter (VSC) or current source converter (CSC) depending on its DC-side that could be an inductance or a capacitance as shown in Figure 4-1 [71, 96, 97]. The VSC or CSC consists of turn-off based power switch like Insulated Gate Bipolar Transistors (IGBT), Gate Turn-Off (GTO) build up in single or multiphase topology (Figure 4-2) [71]. The intervention of D-STATCOM over the power issues occurs through

exchanging a reactive current with the grid. The direction of the exchanged current depends on D-STATCOM output voltage magnitude versus the grid voltage. Assuming that the D-STATCOM operates in zero active power loss conditions, its output voltage evolves with the same phase shift of the grid voltage [74]. In the presence of an energy storage system at the DC-side, D-STATCOM gets the possibility to exchange also the active power with the grid.

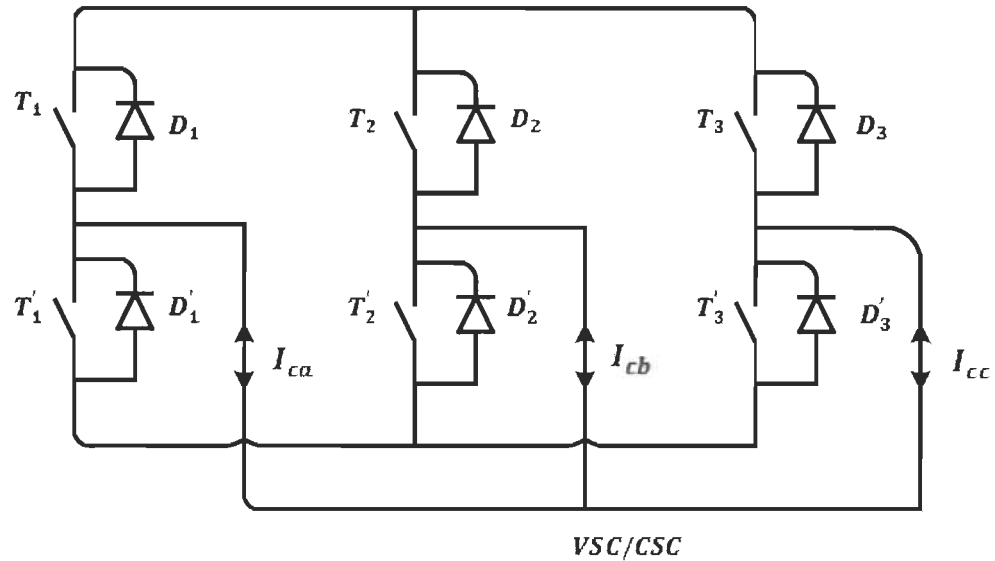


Figure 4-2 Three legs voltage /current source converter

4.2.1 D-STATCOM configuration

Figure 4-3 represents the configuration of the system under study. It consists of a balanced three-phase power source feeding the end-user which is modeled by a reactive load. In this chapter, the main task of D-STATCOM is to compensate the reactive power. In the proposed topology, the D-STATCOM consists of the three-phase three-wire voltage source converter (VSC) with a self-supporting DC-side voltage using a large capacitor. A first order interfacing filter is inserted between the compensator and the grid to minimise the harmonic propagation.

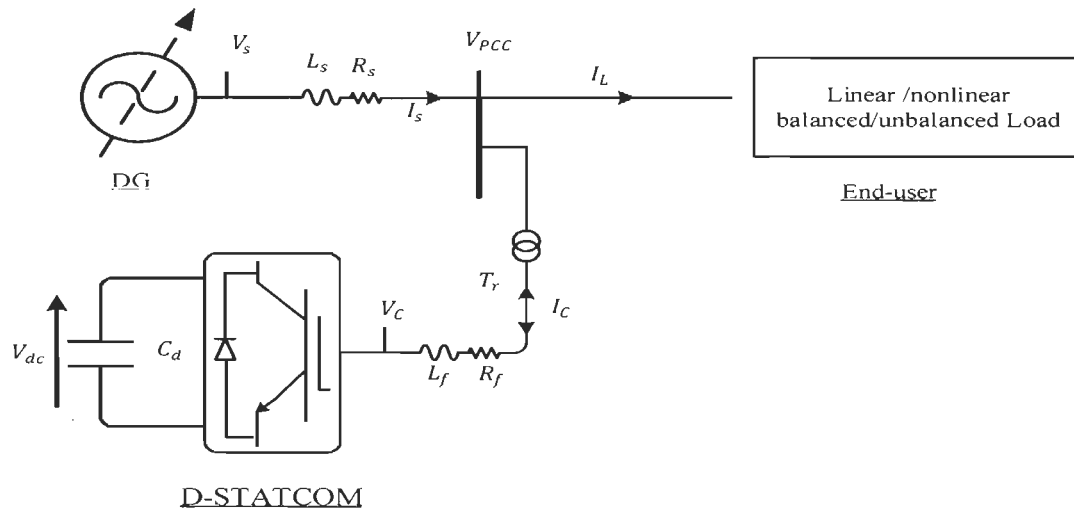


Figure 4-3 Configuration of D-STATCOM

4.2.1.1 Mathematical modeling of the power system with D-STATCOM

The mathematical representation of the proposed power system in *ABC*-frame is given as follows [71]:

$$\begin{cases} V_{sa}(t) = \sqrt{2}V_{srms} * \sin(\omega_s t) \\ V_{sb}(t) = \sqrt{2}V_{srms} \sin(\omega_s t - \frac{2\pi}{3}) \\ V_{sc}(t) = \sqrt{2}V_{srms} \sin(\omega_s t - \frac{4\pi}{3}) \end{cases} \quad (4-1)$$

$$\begin{cases} V_{sa}(t) - V_{La}(t) = (L_s \frac{d}{dt} + R_s)I_{sa}(t) \\ V_{sb}(t) - V_{Lb}(t) = (L_s \frac{d}{dt} + R_s)I_{sb}(t) \\ V_{sc}(t) - V_{Lc}(t) = (L_s \frac{d}{dt} + R_s)I_{sc}(t) \end{cases} \quad (4-2)$$

$$\begin{cases} V_{La}(t) - V_{Ca}(t) = (L_s \frac{d}{dt} + R_s)I_{Ca}(t) \\ V_{Lb}(t) - V_{Cb}(t) = (L_s \frac{d}{dt} + R_s)I_{Cb}(t) \\ V_{Lc}(t) - V_{Cc}(t) = (L_s \frac{d}{dt} + R_s)I_{Cc}(t) \end{cases} \quad (4-3)$$

The end-user absorbs a current noted I_L which is calculated using nodes law as follows:

$$\begin{cases} I_{La}(t) = I_{sa}(t) + I_{Ca}(t) \\ I_{Lb}(t) = I_{sb}(t) + I_{Cb}(t) \\ I_{Lc}(t) = I_{sc}(t) + I_{Cc}(t) \end{cases} \quad (4-4)$$

Based on (4-2), we substitute I_{sabc} by their equivalent which implies

$$\begin{cases} I_{La}(t) = \frac{V_{sa}(t) - V_{La}(t)}{(R_s + j\omega_s L_s)} + I_{Ca}(t) \\ I_{Lb}(t) = \frac{V_{sb}(t) - V_{Lb}(t)}{(R_s + j\omega_s L_s)} + I_{Cb}(t) \\ I_{Lc}(t) = \frac{V_{sc}(t) - V_{Lc}(t)}{(R_s + j\omega_s L_s)} + I_{Cc}(t) \end{cases} \quad (4-5)$$

The current and voltage quantities are difficult to be controlled in the ABC frame because they oscillate with time. For that, it's necessary to represent these quantities in another referential where they become almost constant with time to simplify the control design. The Park referential is calculated as follows [98, 99].

$$A_{dq0} = [P(\theta)] * A_{abc} \quad (4-6)$$

$$A_{abc} = [P(\theta)]^{-1} * A_{dq0} \quad (4-7)$$

With A_{abc} , A_{dq0} is a quantity in ABC frame and its representation in DQ frame. $[P(\theta)]$, $[P(\theta)]^{-1}$ are Park transformation matrix and its inverse given by

$$[P(\theta)] = \frac{2}{3} \begin{bmatrix} \cos(\theta) & \cos(\theta - \frac{2\pi}{3}) & \cos(\theta + \frac{2\pi}{3}) \\ -\sin(\theta) & -\sin(\theta - \frac{2\pi}{3}) & -\sin(\theta + \frac{2\pi}{3}) \\ \frac{1}{2} & \frac{1}{2} & \frac{1}{2} \end{bmatrix} \quad (4-8)$$

$$[P(\theta)]^{-1} = \frac{2}{3} \begin{bmatrix} \cos(\theta) & \sin(\theta) & 1 \\ \cos(\theta - \frac{2\pi}{3}) & \sin(\theta - \frac{2\pi}{3}) & 1 \\ \cos(\theta + \frac{2\pi}{3}) & \sin(\theta + \frac{2\pi}{3}) & 1 \end{bmatrix} \quad (4-9)$$

Applying the Park transformation to (4-2), (4-3) and (4-5), we get

$$\begin{cases} L_s \frac{d}{dt} I_{sd} + R_s * I_{sd} = (V_{sd} - V_{Ld}) + \omega_s L_s * I_{sq} \\ L_s \frac{d}{dt} I_{sq} + R_s * I_{sq} = (V_{sq} - V_{Lq}) - \omega_s L_s * I_{sd} \end{cases} \quad (4-10)$$

$$\begin{cases} L_f \frac{d}{dt} I_{Cd} + R_f * I_{Cd} = (V_{Ld} - V_{Cd}) + \omega_s L_f * I_{Cq} \\ L_f \frac{d}{dt} I_{Cq} + R_f * I_{Cq} = (V_{Lq} - V_{Cq}) - \omega L_f * I_{Cd} \end{cases} \quad (4-11)$$

$$\begin{cases} I_{Ld} = \frac{V_{sd} - V_{Ld}}{(R_s + j\omega_s L_s)} + I_{Cd} \\ I_{Lq} = \frac{V_{sq} - V_{Lq}}{(R_s + j\omega_s L_s)} + I_{Cq} \end{cases} \quad (4-12)$$

4.2.1.2 Phase-Locked-Loop

The electrical angle of the grid is necessary to make the Park transformation, which is estimated using a Phase Locked Loop (PLL) technique as shown in Figure 4-4. The quadratic component of the grid voltage is settled to zero and filtered using a feedback PI-compensator. The integration of the PI-compensator output corresponds to the electrical angle. The closed loop representation of a PLL is given as following [98, 100]

$$H_{PLL}(s) = \frac{K_f(s)V_{smax}}{s + K_f(s)V_{smax}} \quad (4-13)$$

With

$$K_f(s) = K_{pPLL} \frac{s + \frac{1}{K_{IPLL}}}{s} \quad (4-14)$$

Identifying (14-13) with the second order characteristic polynomial function (2-15), we obtain

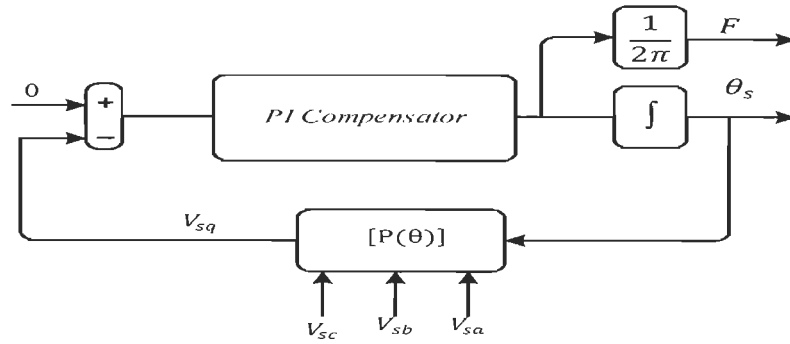


Figure 4-4 Phase Locked Loop

$$H_{PLL}(s) = \frac{2\xi\omega_n s + \omega_n^2}{s^2 + 2\xi\omega_n s + \omega_n^2} \quad (4-15)$$

$$\begin{cases} K_{pPLL} = \frac{2\xi\omega_n}{V_{smax}} \\ K_{iPLL} = \frac{1}{\omega_n} \sqrt{V_{smax} * K_{pPLL}} \end{cases} \quad (4-16)$$

With

V_{smax} , ξ , ω_n are respectively the grid voltage magnitude, damping ratio and natural frequency.

4.2.2 Design of D-STATCOM components

The high effectiveness of the compensator against power quality issues depends on a good estimation of its parameters such as DC-side voltage, supporting capacitor, interfacing filter and so on. The procedure of the parameters selection is given below [71, 101, 102]

4.2.2.1 Estimation of DC-side voltage and capacitor

The DC-side voltage should be equal at least two times the line-to-line peak voltage of the main distribution AC system. The DC-side capacitor value is extracted using the energy

conservation law. The capacitor depends on the necessary energy that should be stored in it, to achieve a successful intervention against power issues occurring in the grid. The DC-side voltage and capacitor are defined respectively as the following

$$V_{dc} = \frac{2\sqrt{6}}{3*m} * V_{S(L-L)} \quad (4-16)$$

With m is the modulation index equal to one, $V_{S(L-L)}$ is the line-to-line grid voltage [71].

$$C_d = \frac{6*k_1*\alpha*I_s*t_m}{(V_{dc}^2 - V_{dc1}^2)} V_s \quad (4-17)$$

Where t_m is recovering time of the DC-side voltage, I_s is the grid current magnitude, α is the overloading factor, k_1 is the energy variation during transient mode, V_{dc1} is the minimum value that could be for the DC-side voltage, generally it is equal to two times of grid line-to-line voltage magnitude ($V_{S(L-L)}$).

4.2.2.2 Estimation of the interfacing filter

The presence of a first-order interfacing filter at the compensator output brings more stability to the power system. In addition to that, the inductance eliminates the major part of harmonics induced by the VSC switches according to IEEE-519 standard. Hence, the design of the interfacing inductance takes into account the switching frequency and output harmonic current of the compensator. The inductance value is specified by the next expression [71]:

$$L_f = \frac{\sqrt{3}}{12} \frac{m*V_{dc}}{\alpha*f_s*I_{fh}} \quad (4-18)$$

f_s is the switching frequency and I_{fh} is the output harmonic current of the compensator.

4.2.2.3 Frequency response of the power system

With considering the impedance of the grid, the transfer function of the system under study becomes:

$$G(s) = \frac{I_s}{V_c} = \frac{1}{(L_f + L_s)s + (R_f + R_s)} \quad (4-19)$$

Figure 4-5 shows the frequency domain representation of the system under study. It illustrates that the phase margin never reaches the -180 degrees that justifies the infinity of the gain margin which implies the stability of the system.

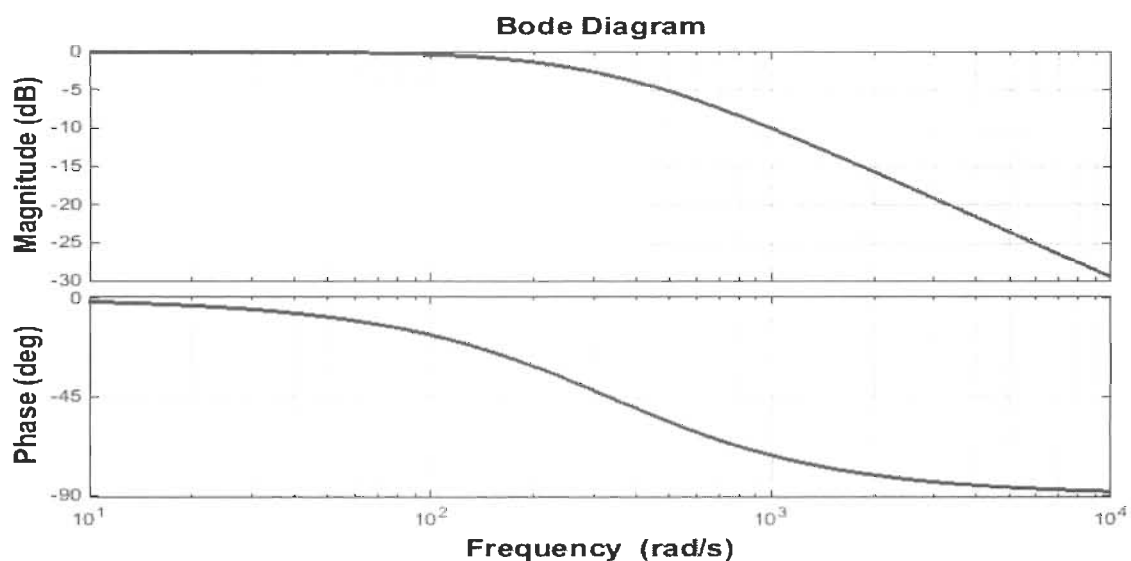


Figure 4-5 Bode diagram of the transfer function

The interfacing filter has a big impact on the power system stability. For that, we evaluated the influence of its parameters variation (L_f and R_f) on the frequency response of the system. PWM technique is used to control the compensator, for that it is necessary to take into account the time delay and the proportion D_{PWM} of the PWM. The transfer function of the power system becomes:

$$G(s) = \frac{D_{PWM}}{1+s\frac{T_s}{2}} \frac{1}{(L_f+L_s)s+(R_f+R_s)} \quad (4-20)$$

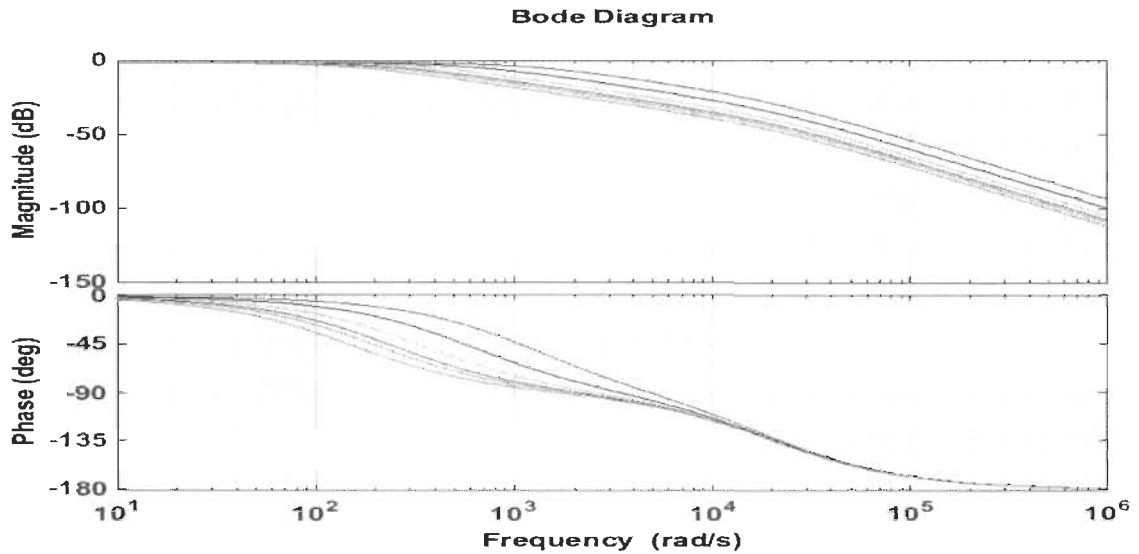


Figure 4-6 Bode diagram of power system transfer function with variation of L_f

From Figure 4-6, it is observable that the variation of the interfacing inductance L_f has a direct influence on the magnitude and the phase of the frequential response. The increase of the inductance decreases the magnitude in medium and high frequencies that means the decrease of the cut-off frequency, which enhances the performance of the interfacing filter against harmonics. In addition to that, the variation of inductance has no influence on the magnitude in low frequencies while it affects the phase margin around the medium frequencies, where the increase of inductance decreases also the phase margin response.

In the other side, Figure 4-7 shows that the variation of the interfacing resistance R_f provokes a variation on the magnitude at low frequencies in which, the augmentation of the resistance decreases the cut-off without affecting magnitude in the medium and high frequencies. The phase angle increases with the increase of the resistance in medium frequencies.

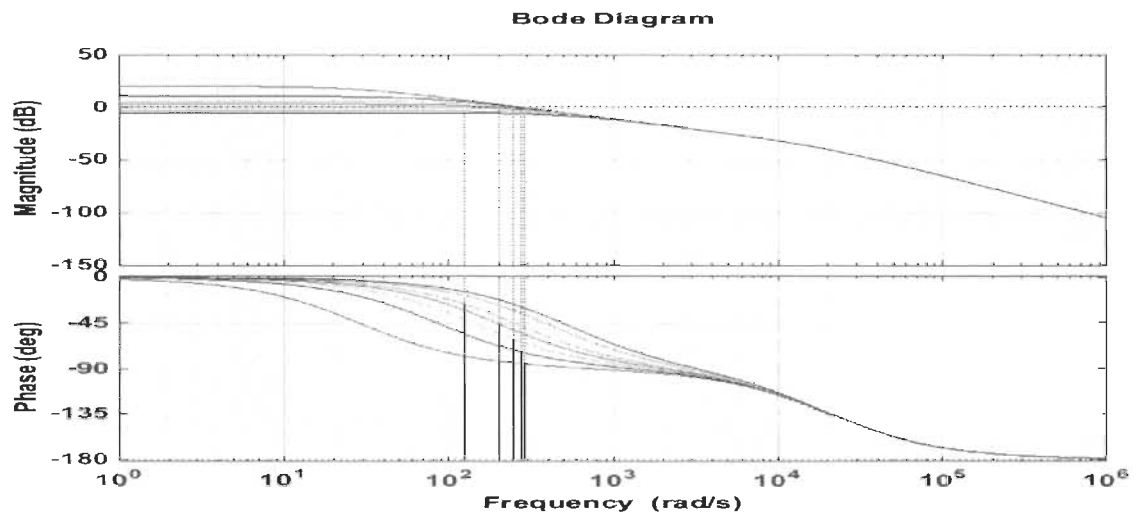


Figure 4-7 Bode diagram of power system transfer function with variation of R_f

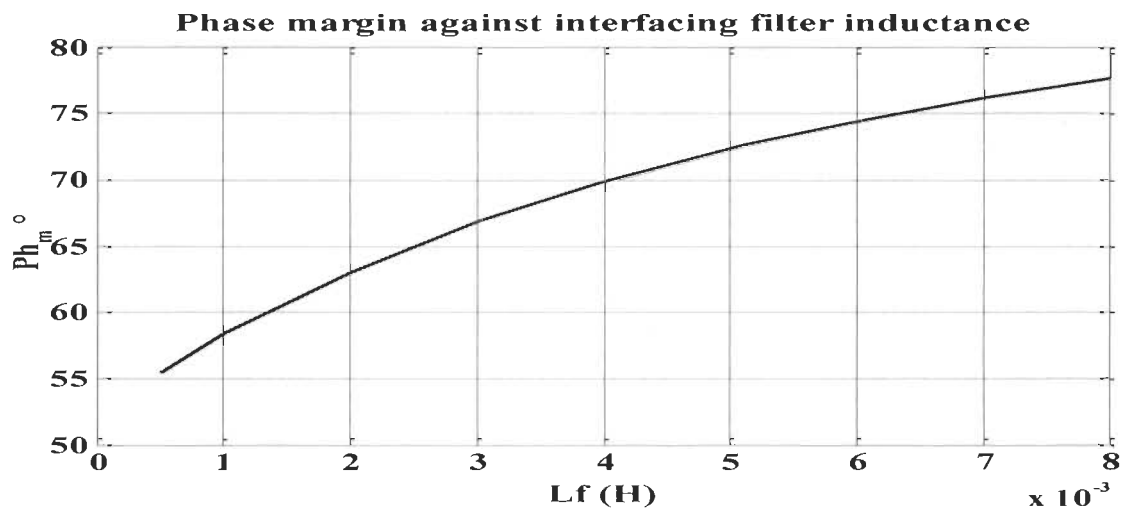


Figure 4-8 Phase margin variation with L_f

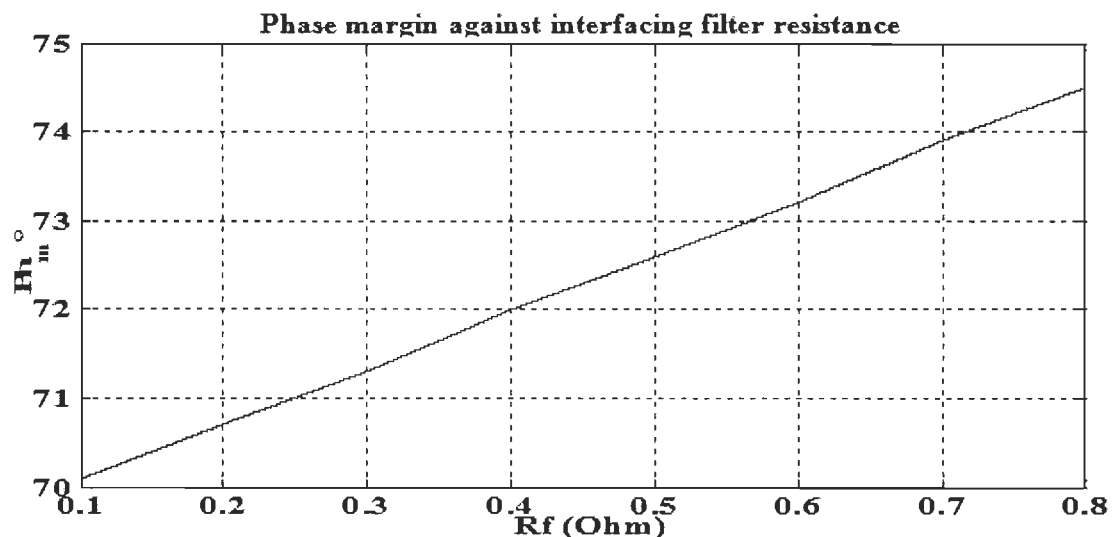


Figure 4-9 Phase margin variation with R_f

Results depicted in Figure 4-8 and Figure 4-9 support those obtained in Figure 4-6 and Figure 4-7, where the increase of the interfacing filter parameters increases the phase margin with more influence in the case of the inductance. From the obtained results in Figure 4-6 to Figure 4-9, we notice that the augmentation of the interfacing filter parameters increases the elimination of noise generated by switches but this increase has a limit or it brings backfire such as the augmentation of power losses. For that, a good performance of the compensator needs a good design procedure with taking into account all factors.

4.2.3 *D-STATCOM operation and control design*

The intense evolution of power converters obligates the use of an advanced category of control technique to ameliorate the performance of these converters in different operating modes. In this context, we propose a robust control technique based sliding mode method to maintain the control system performance at a suitable level in term of stability and reference tracking despite the parameters uncertainty. This feature allows the compensator to intervene

against faults that occur in power system with flexibility and effectiveness. Sliding mode control (SMC) typified by the discontinuous nature, it orientates the nonlinear system toward the sliding surface then tends asymptotically directly to an equilibrium state as shown in Figure 4-10 [48, 97].

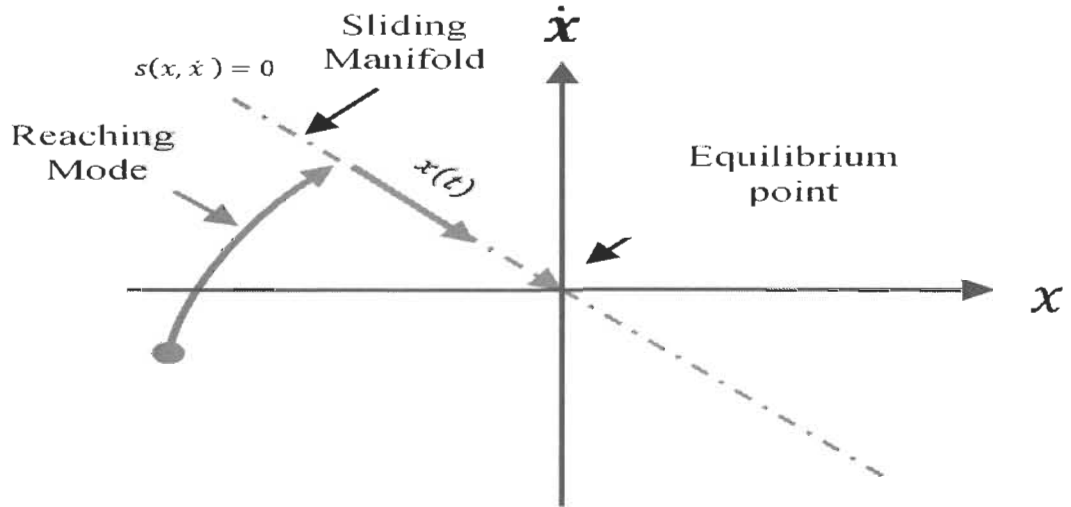


Figure 4-10 Sliding mode control process

The sliding mode controller design starts with the choice of the sliding surface [103]

$$S(x) = \left(\frac{d}{dt} + \lambda \right)^{r-1} e(x) \quad (4-21)$$

With $e(x)$ represents the error between the controller element and its desired value. While r : is the number of time that the function should be derived to insure the controllability of the state vector. λ : is a positive gain. It should be well chosen to make $e(x)$ tend toward 0. Then, a control law should be found to verify the condition of existence and convergence. A Lyapunov approach is proposed in this case [104].

$$V(x) = \frac{1}{2} S^2(x) \quad (4-22)$$

Deriving (4-21), we obtain

$$\dot{V}(x) = S(x) \dot{S}(x) \quad (4-23)$$

With:

$$S(x) \dot{S}(x) < 0 \quad (4-24)$$

To satisfy the conditions of existence and convergence, the control vector is represented by:

$$U = U_{eq} + U_n \quad (4-25)$$

U_{eq} is the equivalent control used to maintain the controlled variable on sliding surface where $S(x)$ tend to zero. The power system is defined in state equation as follows [103]

$$[\dot{X}] = [A][X] + [B][U] \quad (4-26)$$

The derivative of the sliding surface is

$$\dot{S}(x) = \frac{\partial S}{\partial x} \{ [A][X] + [B]U_{eq} \} + \frac{\partial S}{\partial x} [B]U_n = 0 \quad (4-27)$$

When the system reaches the sliding surface (sliding mode), $U_n = 0$, then

$$U_{eq} = - \left\{ \frac{\partial S}{\partial x} [B] \right\}^{-1} \left\{ \frac{\partial S}{\partial x} [A][X] \right\} \quad (4-28)$$

Taking $\frac{\partial S}{\partial x} [B] \neq 0$ and during the reaching mode $U_n \neq 0$

Substituting (2-27) in (4-26), (4-28) is obtained

$$\dot{S}(x) = \frac{\partial S}{\partial x} [B]U_n \quad (4-29)$$

Substituting (4-29) in (4-24)

$$\begin{cases} V_d = V_{Ld} - V_{Cd} + \omega_s I_{Cq} \\ V_q = V_{Lq} - V_{Cq} - \omega_s I_{Cd} \end{cases} \quad (4-32)$$

Then (4-11) could be represented by state equation as follows

$$\frac{d}{dt} \begin{bmatrix} I_{Cd} \\ I_{Cq} \end{bmatrix} = \begin{bmatrix} -\frac{R_f}{L_f} \\ -\frac{R_f}{L_f} \end{bmatrix} \begin{bmatrix} I_{Cd} \\ I_{Cq} \end{bmatrix} + \frac{1}{L_f} \begin{bmatrix} V_d \\ V_q \end{bmatrix} \quad (4-33)$$

The application of the sliding mode control starts with the choice of the sliding manifolds:

$$\begin{cases} S(I_{Cd}) = I_{Cd}^* - I_{Cd} \\ S(I_{Cq}) = I_{Cq}^* - I_{Cq} \end{cases} \quad (4-34)$$

The derivation of (4-34) leads to:

$$\begin{cases} \dot{S}(I_{Cd}) = \dot{I}_{Cd}^* - \dot{I}_{Cd} \\ \dot{S}(I_{Cq}) = \dot{I}_{Cq}^* - \dot{I}_{Cq} \end{cases} \quad (4-35)$$

Substituting (4-35) in (4-33), the control law becomes:

$$\frac{d}{dt} \begin{bmatrix} S(I_{Cd}) \\ S(I_{Cq}) \end{bmatrix} = \begin{bmatrix} \dot{I}_{Cd}^* - \dot{I}_{Cd} \\ \dot{I}_{Cq}^* - \dot{I}_{Cq} \end{bmatrix} = \begin{bmatrix} I_{Cd}^* - (-\frac{R_f}{L_f} I_{Cd} + \frac{1}{L_f} V_d) \\ I_{Cq}^* - (-\frac{R_f}{L_f} I_{Cq} + \frac{1}{L_f} V_q) \end{bmatrix} \quad (4-36)$$

Then

$$\begin{cases} V_d = V_{d_{eq}} + V_{d_{N}} \\ V_q = V_{q_{eq}} + V_{q_{N}} \end{cases} \quad (4-37)$$

Substituting (4-37) in (4-36), we get

$$\frac{d}{dt} \begin{bmatrix} S(I_{Cd}) \\ S(I_{Cq}) \end{bmatrix} = \begin{bmatrix} \dot{I}_{Cd}^* - \dot{I}_{Cd} \\ \dot{I}_{Cq}^* - \dot{I}_{Cq} \end{bmatrix} = \begin{bmatrix} I_{Cd}^* - (-\frac{R_f}{L_f} I_{Cd} + \frac{1}{L_f} (V_{d_{eq}} + V_{d_{N}})) \\ I_{Cq}^* - (-\frac{R_f}{L_f} I_{Cq} + \frac{1}{L_f} (V_{q_{eq}} + V_{q_{N}})) \end{bmatrix} \quad (4-38)$$

On the sliding manifold $S(I_{Cd}) = S(I_{Cq}) = 0, \dot{S}(I_{Cd}) = \dot{S}(I_{Cq}) = 0, V_{d_{N}} = V_{q_{N}} = 0$

$$\begin{cases} V_{d_eq} = L_f \dot{I}_{Cd}^* + R_f I_{Cd} \\ V_{q_eq} = L_f \dot{I}_{Cq}^* + R_f I_{Cq} \end{cases} \quad (4-39)$$

The following equality should be always verified to ensure the existence and convergence conditions.

$$\begin{cases} S(I_{Cd}) * \dot{S}(I_{Cd}) < 0 \\ S(I_{Cq}) * \dot{S}(I_{Cq}) < 0 \end{cases} \quad (4-40)$$

Substituting (4-40) in (4-38) we obtain

$$\begin{cases} \dot{S}(I_{Cd}) = -\frac{1}{L_f} V_{d_N} \\ \dot{S}(I_{Cq}) = -\frac{1}{L_f} V_{q_N} \end{cases} \quad (4-41)$$

Replacing (4-41) in (4-40) we obtained

$$\begin{cases} -\frac{1}{L_f} V_{d_N} * S(I_{Cd}) < 0 \\ -\frac{1}{L_f} V_{q_N} * S(I_{Cq}) < 0 \end{cases} \quad (4-42)$$

(4-42) should always be true, for that sV_{d_N} and V_{q_N} are estimated by the following equation

$$\begin{cases} V_{d_N} = \sigma_d \text{sign}(S(I_{Cd})) \\ V_{q_N} = \sigma_d \text{sign}(S(I_{Cq})) \end{cases} \quad (4-43)$$

Then substituting V_{d_N} , V_{q_N} and V_{d_eq} , V_{q_eq} by their relations in (4-37), we obtain the following

$$\begin{cases} V_d = L_f \dot{I}_{Cd}^* + R_f I_{Cd} + \sigma_d \text{sign}(S(I_{Cd})) \\ V_q = L_f \dot{I}_{Cq}^* + R_f I_{Cq} + \sigma_d \text{sign}(S(I_{Cq})) \end{cases} \quad (4-44)$$

To eliminate the undesirable noise due to the chattering phenomena, a smooth saturation function is used instead of sign function (Figure 4-12), then (4-43) becomes

$$V_{d_N} = \begin{cases} \sigma_{(d)} \text{sign}(S(I_{cd})), & |S(I_{cd})| > \varepsilon \\ \frac{\sigma_{(d)}}{\varepsilon} \text{sign}(S(I_{cd})), & |S(I_{cd})| < \varepsilon \end{cases} \quad (4-45)$$

$$V_{q_N} = \begin{cases} \sigma_{(q)} \text{sign}(S(I_{cq})), & |S(I_{cq})| > \varepsilon \\ \frac{\sigma_{(q)}}{\varepsilon} \text{sign}(S(I_{cq})), & |S(I_{cq})| < \varepsilon \end{cases} \quad (4-46)$$

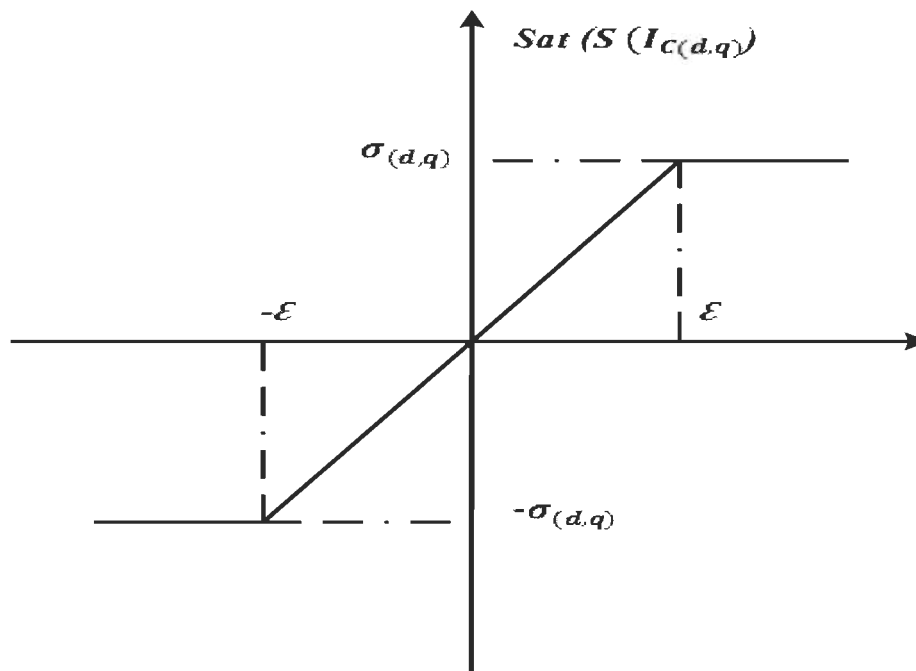


Figure 4-12 Saturation function

4.2.3.2 SMC application in the outer loop

In the outer loop, the sliding mode technique is used to control the DC-side voltage and the voltage magnitude at the point of common coupling to generate references for the inner loop. For the space limitation, we will mention just headnotes for the application of the SMC

in the outer loop. The sliding mode expression used in the outer loop based on the following equality [105, 106]

$$S(x) = ae(t) + a_1 \frac{de(t)}{dt} \quad (4-47)$$

$e(t)$ represents the error between the measured and desired value.

With $S(x) \dot{S}(x) < 0$ to ensure that the system converges to the sliding surface.

After a mathematical calculation, we get the direct and the quadratic injected current references given by the following expressions:

$$\begin{cases} I_{cd}^* = \eta_1 \text{sign}S(V_{dc}^* - V_{dc}) + \eta_2 \text{sign}S(\dot{V}_{dc}^* - \dot{V}_{dc}) \\ I_{cq}^* = \xi_1 \text{sign}S(|V|_L^* - |V|_L) + \xi_2 \text{sign}S(|\dot{V}|_L^* - |\dot{V}|_L) \end{cases} \quad (4-48)$$

4.3 Dynamic Voltage Restorer (DVR)

DVR mainly used as an interfacing between the power source and the end user to improve the reliability and mitigating faults. Recently, DVR has been also exploited in renewable energy where it has been installed between the turbine and network to sustain the power quality and to protect the turbine of grid faults [107]. In this chapter, we investigate the DVR performance against voltage sag and swell.

4.3.1 DVR configuration

DVR is a VSC (CSC) could be connected to the distribution grid (power receiving point) through a series transformer [71]. It is engaged to mitigate all events related to voltage in terms of sag, swells, disturbance etc[108-113]. DVR could also be installed in transmission grid at the sending power station level in which it operates as Static Synchronous Series Compensator (SSSC) [75]. In this case, SSSC is used to adjust the reactive power that permits

controlling transmissibility of power in the grid [114]. The, DVR is installed at the end user terminals in which it exchanges an active and reactive power with the grid translated by the generation of a compensating voltage variable in phase and magnitude to overcome the trouble. Figure 4-13 illustrates DVR connected to the power grid in distribution level.

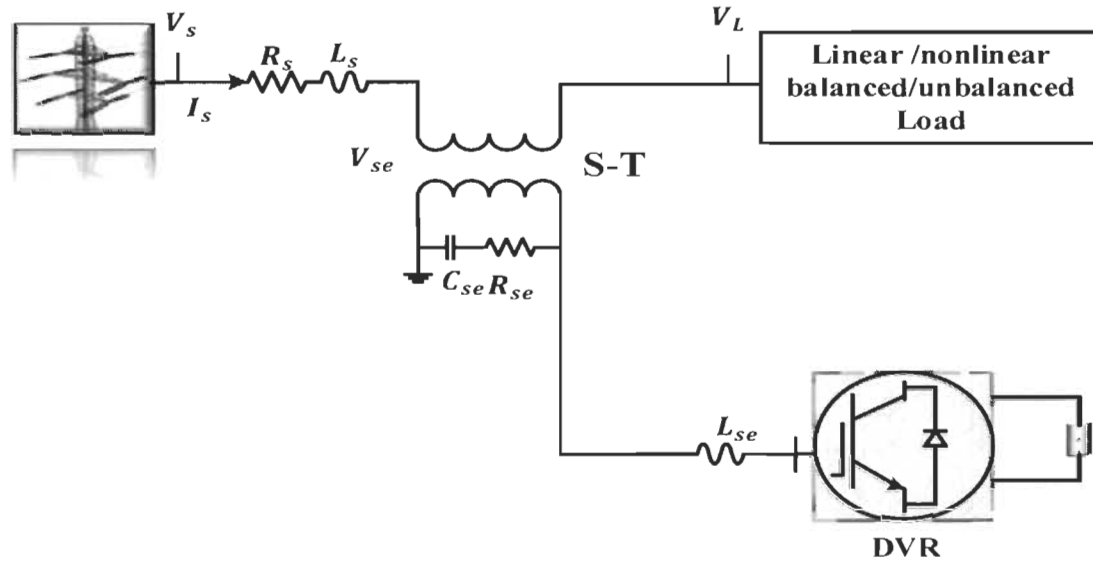


Figure 4-13 DVR configuration

4.3.2 Mathematical modeling of the power system with DVR

The mathematical representation of the power system shown in Figure 4-13 in the presence of DVR in ABC and DQ frames are the following

$$\begin{cases} V_{sa}(t) - V_{sea}(t) - V_{La}(t) = (L_s \frac{d}{dt} + R_s)I_{sa}(t) \\ V_{sb}(t) - V_{seb}(t) - V_{Lb}(t) = (L_s \frac{d}{dt} + R_s)I_{sb}(t) \\ V_{sc}(t) - V_{sec}(t) - V_{Lc}(t) = (L_s \frac{d}{dt} + R_s)I_{sc}(t) \end{cases} \quad (4-49)$$

$$\frac{d}{dt} \begin{bmatrix} I_{sd} \\ I_{sq} \end{bmatrix} = \begin{bmatrix} -\frac{R}{L} & \omega_s \\ -\omega_s & -\frac{R}{L} \end{bmatrix} \begin{bmatrix} I_{sd} \\ I_{sq} \end{bmatrix} + \frac{1}{L_s} \begin{bmatrix} V_{sd} - V_{sed} - V_{Ld} \\ V_{sq} - V_{seq} - V_{Lq} \end{bmatrix} \quad (4-50)$$

DVR induces a series voltage shifted by a specific angle against the grid voltage, enabling the compensation of issues. The phasor diagram of the DVR intervention is depicted in Figure 4-14 [71].

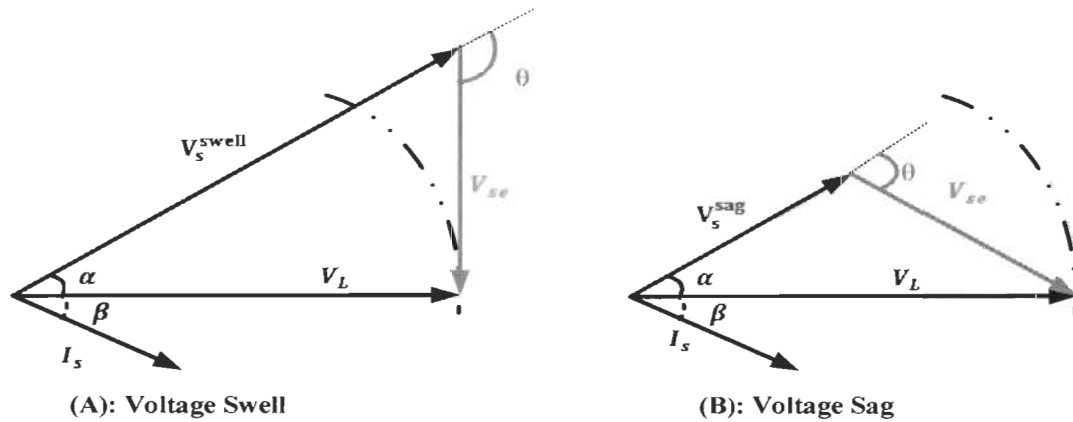


Figure 4-14 Phasor diagram of DVR intervention

4.3.3 Design of DVR components

Design of DVR involves the design of the injected voltage rating, DVR apparent power rating, injection transformer rating, interfacing filter, DC-side voltage rating [71, 111].

4.3.3.1 Injected voltage rating

The injected voltage is the required voltage that should be induced to compensate the voltage sag and swell. We supposed that the DVR has the ability to compensate voltage variation turn around $\pm 50\%$ of the grid voltage rating. Basing on the phase diagram presented in Figure 4-14, the load voltage is given as follows

$$\vec{V}_L = \vec{V}_{se} + \vec{V}_s \quad (4-51)$$

Then, the magnitude of the injected voltage is

$$V_{se} = \sqrt{|V_L|^2 - |V_s|^2} \quad (4-52)$$

4.3.3.2 Apparent power of DVR

Basically, the apparent power of a three-phase power system is calculated by the following relation

$$S = \sqrt{3} * V * I \quad (4-53)$$

With V and I are respectively the grid voltage and current magnitude. Since the injected transformer is connected in series with the grid then, the current that goes through the secondary winding is the same as the grid current. Supposing that the transformer ratio is one, then the apparent power of the DVR is

$$S_{se} = \sqrt{3} * V_{se} * I_s \quad (4-54)$$

4.3.3.3 Current rating of DVR

As we said above, the current passes through the grid is the same as the secondary that implies the same current in the primary ($\frac{V_{se2}}{V_{se1}} = 1$). The current rating of DVR is calculated by the following equation:

$$I_s = \frac{S_s}{\sqrt{3}V_s} \quad (4-55)$$

4.3.3.4 DC-side voltage

An energy storage system has been used instead of self-supporting capacity. For that, the DC-side voltage should be equal at least two time the grid line to line voltage

$$V_{rdc} = 2 * \sqrt{3}V_s \quad (4-56)$$

4.3.3.5 DVR interfacing filter

A passive damping LC filter is inserted between DVR and the grid. An inductance L_{se} and a capacitance C_{se} are used to remain switching ripples of DVR current and voltage within an acceptable range. The resistance R_{se} is inserted in series with the capacitance to bring more stability to the system. The interfacing filter parameters are given by the following [71].

$$L_{se} = \frac{\sqrt{3}}{12} * \frac{V_{rdc}}{K_{se} * \partial I_s * f_s} \quad (4-57)$$

$$C_{se} = \frac{1}{4 * \pi * R_{se} * f_s} \quad (4-58)$$

With K_{se} is the overload factor, ∂I_s is the tolerated harmonic rate equal 2%. f_s is the switching frequency.

4.3.4 DVR operation and control

Figure 4-15 represents the control scheme applied on DVR. A simple hysteresis-based control technique is built up to supervise the performance of DVR. The main task of the DVR is to maintain the load voltage at an ideal level whether voltage wave quality or magnitude. For that, three-phase voltage at the load terminals are sensed to estimate the voltage magnitude which is calculated as follows [115]:

$$V_{Lmax} = \sqrt{\frac{2}{3}} \sqrt{V_{La}^2 + V_{Lb}^2 + V_{Lc}^2} \quad (4-59)$$

Three-phase vectors with a magnitude equal to one and shifted from each other by 120° are calculated equation (4-58).

$$\begin{bmatrix} u_{la} \\ u_{lb} \\ u_{lc} \end{bmatrix} = \frac{1}{V_{Lmax}} \begin{bmatrix} V_{La} \\ V_{Lb} \\ V_{Lc} \end{bmatrix} \quad (4-60)$$

These unity vectors are multiplied by the desired magnitude of load voltage V_{Lmax}^* to get references.

$$\begin{bmatrix} V_{La}^* \\ V_{Lb}^* \\ V_{Lc}^* \end{bmatrix} = \frac{1}{V_{Lmax}^*} \begin{bmatrix} u_{la} \\ u_{lb} \\ u_{lc} \end{bmatrix} \quad (4-61)$$

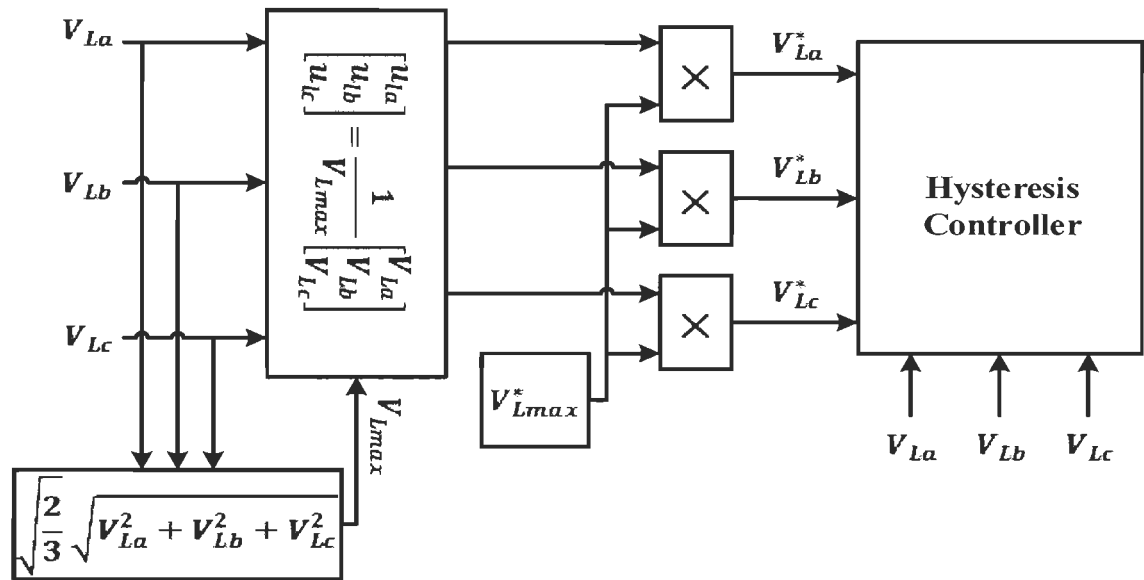


Figure 4-15 Hysteresis control of DVR

4.4 D-STATCOM and DVR performance analysis

To evaluate the performance of D-STATCOM and DVR, the power systems represented in Figure 4-3 and Figure 4-13 have been developed using Matlab®/SimPowerSystems. Parameters used in both power systems are presented in Appendix C. This chapter deals with poor power factor and voltage sag and swell issues that occur in the distribution grid.

4.4.1 Simulation results with D-STATCOM

In an attempt to investigate the performance of D-STATCOM against poor power factor, a variable load based inductive/capacitive impedance has been used. At $t=0.2s$, the inductive load is switched on and switched off at $t=0.5s$, while the capacitive load is switched on. Figure 4-16 and Figure 4-17 show the evolution of grid voltage and current in the presence of inductive and capacitive load respectively. The inductive and capacitive loads destabilize the reactive power evolution in the grid translated by the phase-shift between the grid voltage and current. At $t=0.3s$, D-STATCOM injects 6kvar to compensate the reactive power consumed by the inductive load and at 0.7s absorbs the surplus of reactive power which comes from the capacitive load as shown in Figure 4-18. Based on Figure 4-19, we observe that the quadratic current component of D-STATCOM tracks the reactive power evolution and the direct current component tends to zero because the active power losses are almost equal to zero.

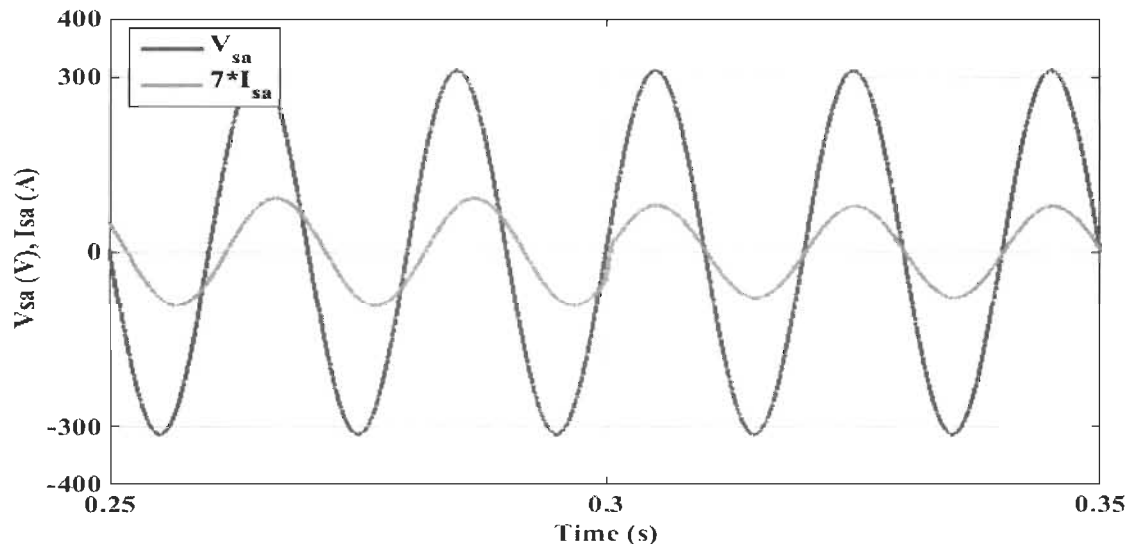


Figure 4-16 Grid voltage and current in the case of inductive load

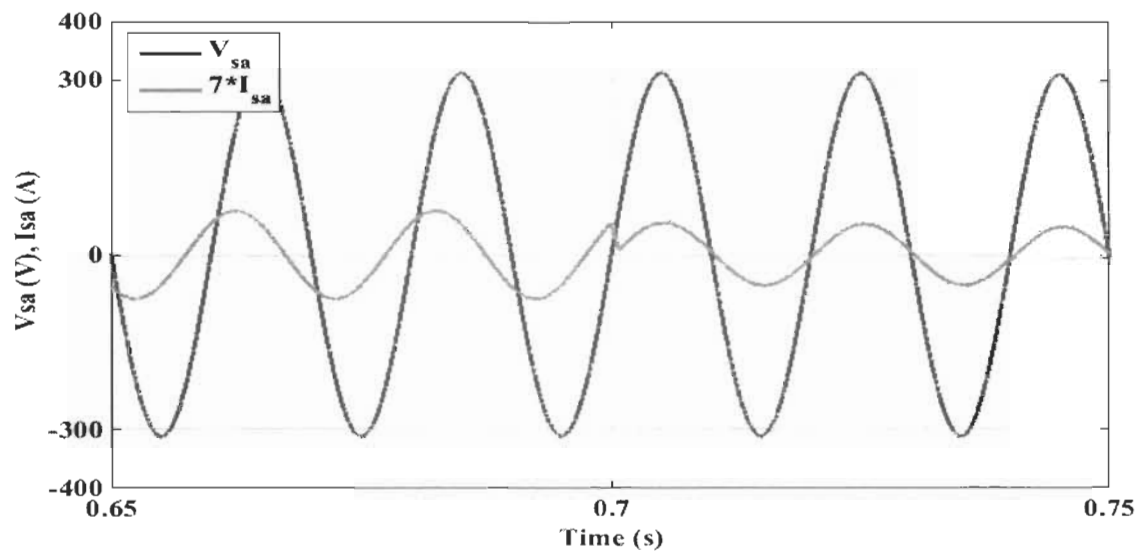


Figure 4-17 Grid voltage and current in the case of capacitive load

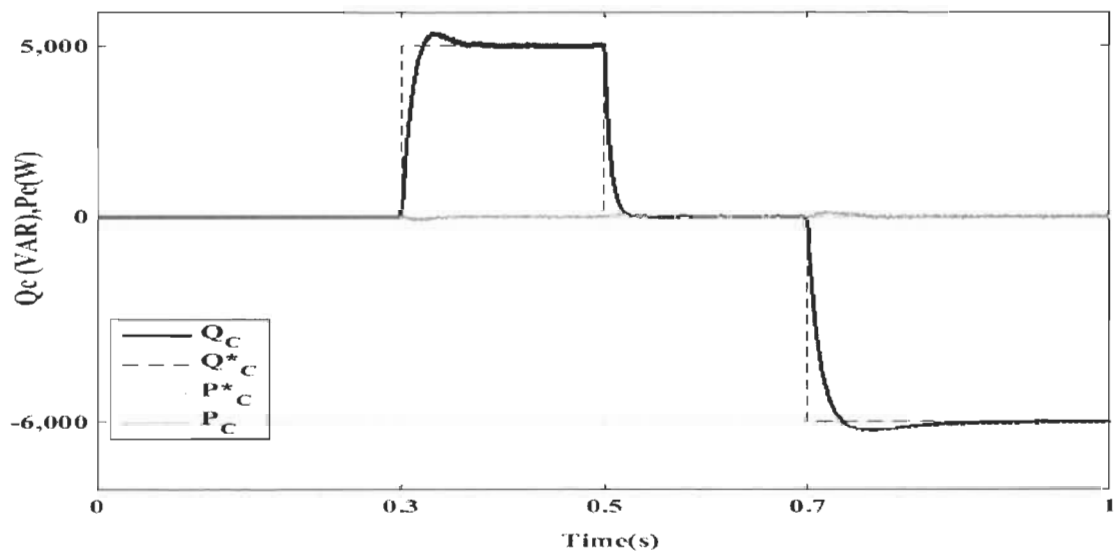


Figure 4-18 Active and reactive power transfer between the grid and D-STATCOM

Figure 4-21 and Figure 4-22 illustrate that the reactive power evolution between the grid and the compensator depends on the voltage difference between them. They have the same phase but not the same magnitude. For inductive load, D-STATCOM voltage is higher than

grid voltage, which means that the reactive power is transferred from the D-STATCOM to the grid. This is translated by the positive value of reactive current in 0.3 to 0.5s (Figure 4-19). In the case of a capacitive load, the reactive current is negative in 0.7 to 1s which implies that grid voltage is higher than D-STATCOM voltage.

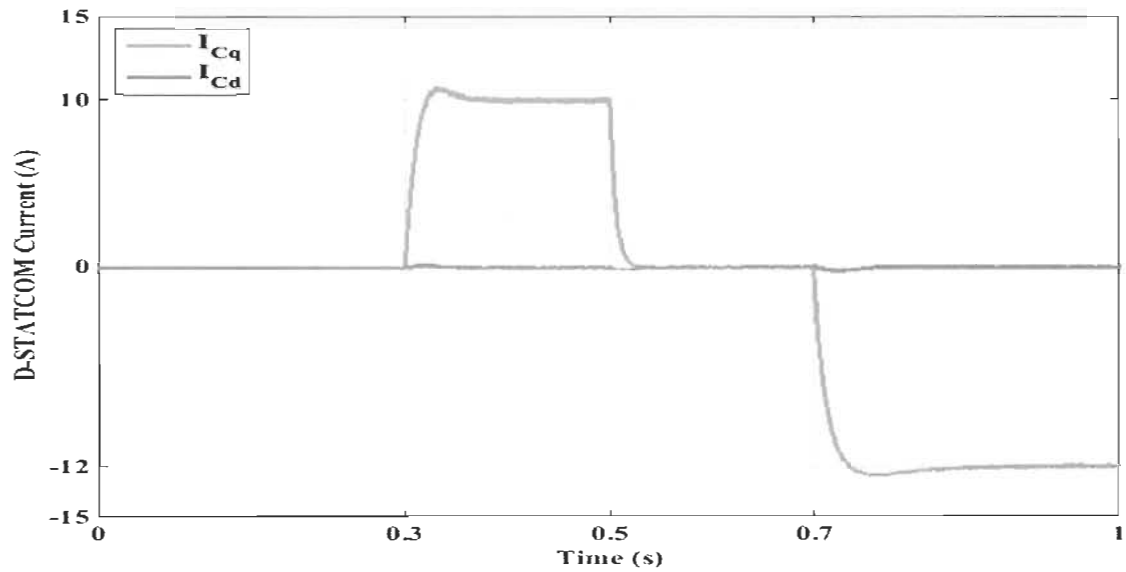


Figure 4-19 D-STATCOM output current in DQ frame

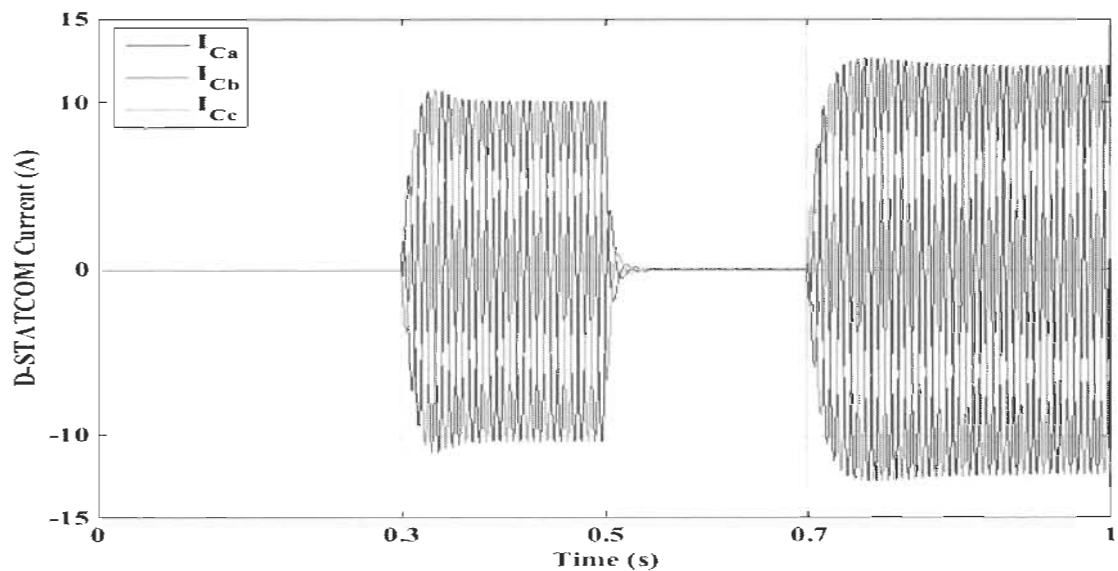


Figure 4-20 D-STATCOM output current in ABC frame

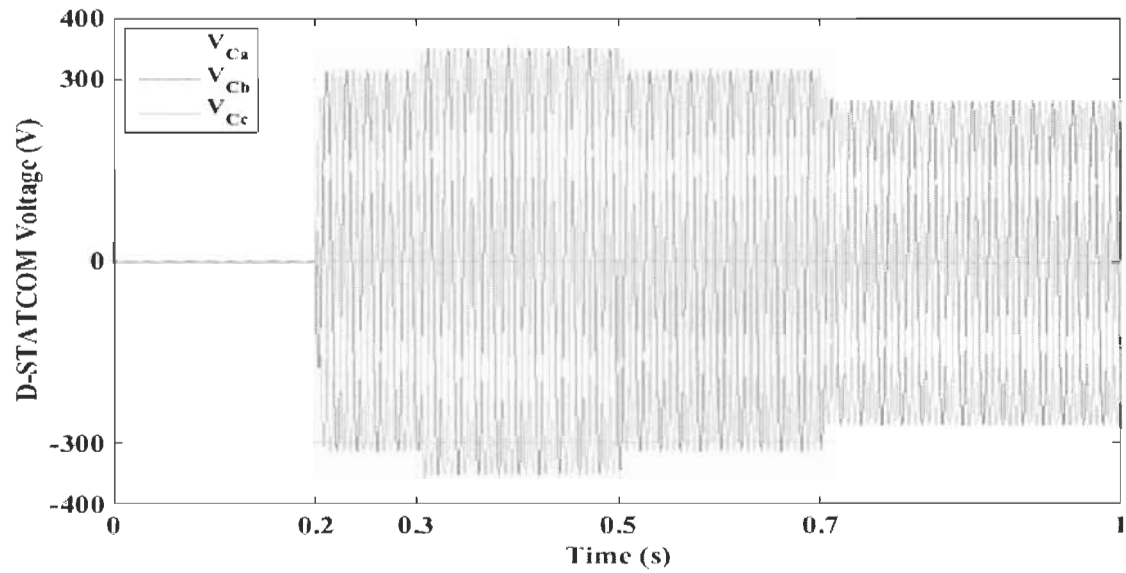


Figure 4-21 D-STATCOM output voltage evolution

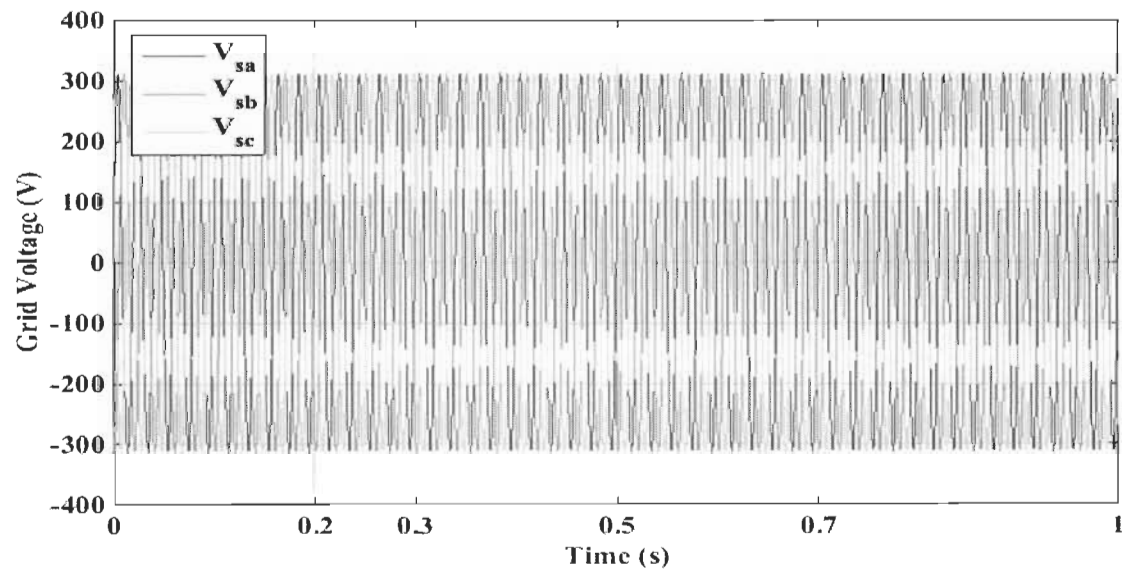


Figure 4-22 Grid voltage

Figure 4-23 shows the DC-side voltage evolution supervised using sliding mode and PI controllers. At the presence of SM, the DC-side voltage tracks the reference perfectly with the reduction of chattering phenomena compared to PI controller.

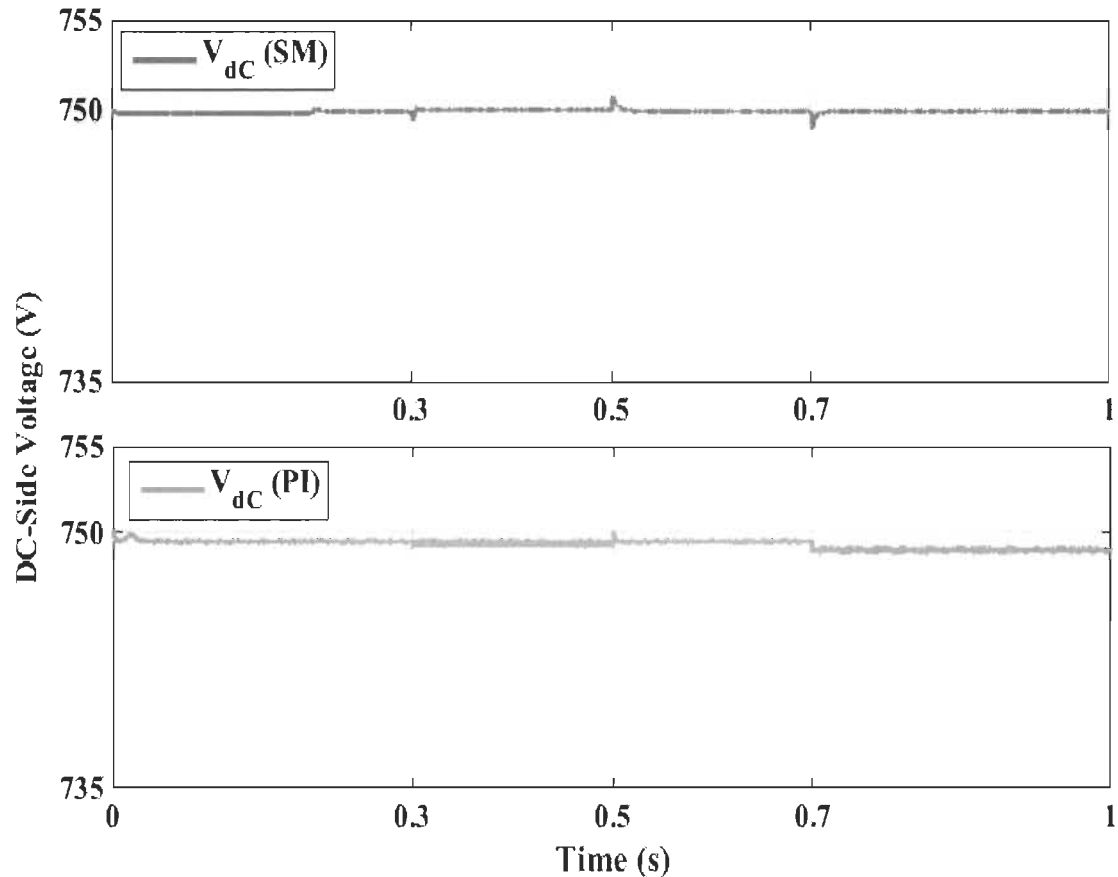


Figure 4-23 DC-side voltage of D-STATCOM

4.4.2 Simulation results with DVR

DVR behavior is performed during grid faults where the objective is to maintain the load terminal voltage at an ideal level. Voltage sag and swells are emulated using a variable power source. Figure 4-24 illustrates that the grid voltage increases to $1.6 \cdot V_s$ at $t=0.3s$, and decreases till reaching $0.6 \cdot V_s$ at $t=0.5s$ in Figure 4-27. However, the DVR generates a compensating voltage as an addition to the supply voltage as shown in Figure 4-25 and Figure

4-28. With DVR, the voltage across load terminals remains at the ideal level as shown in in Figure 4-26 and Figure 4-29.

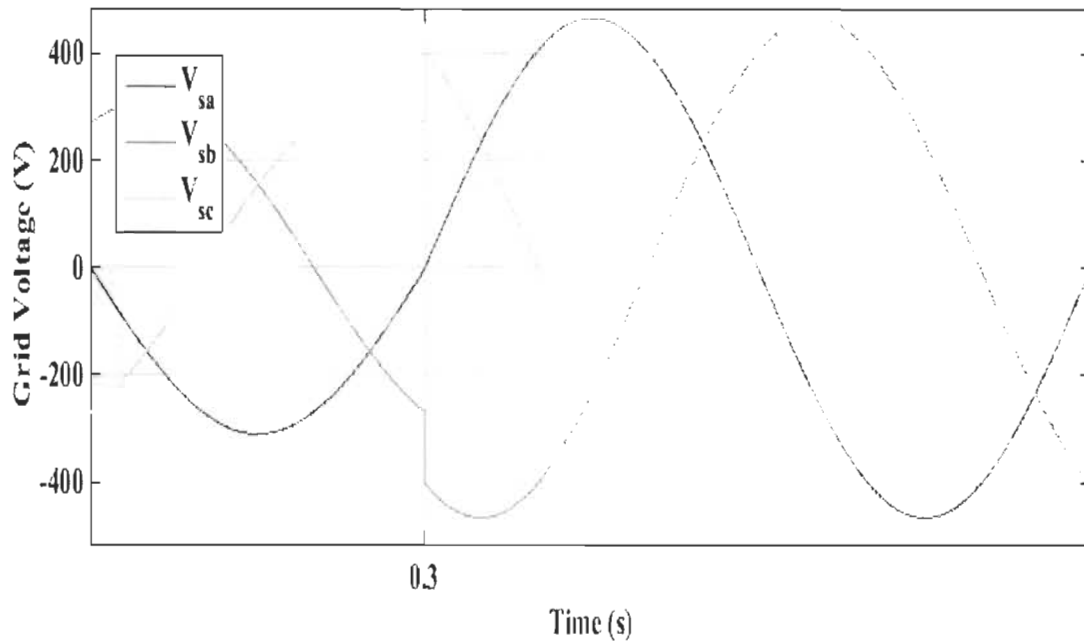


Figure 4-24 Voltage swell occurs in the grid

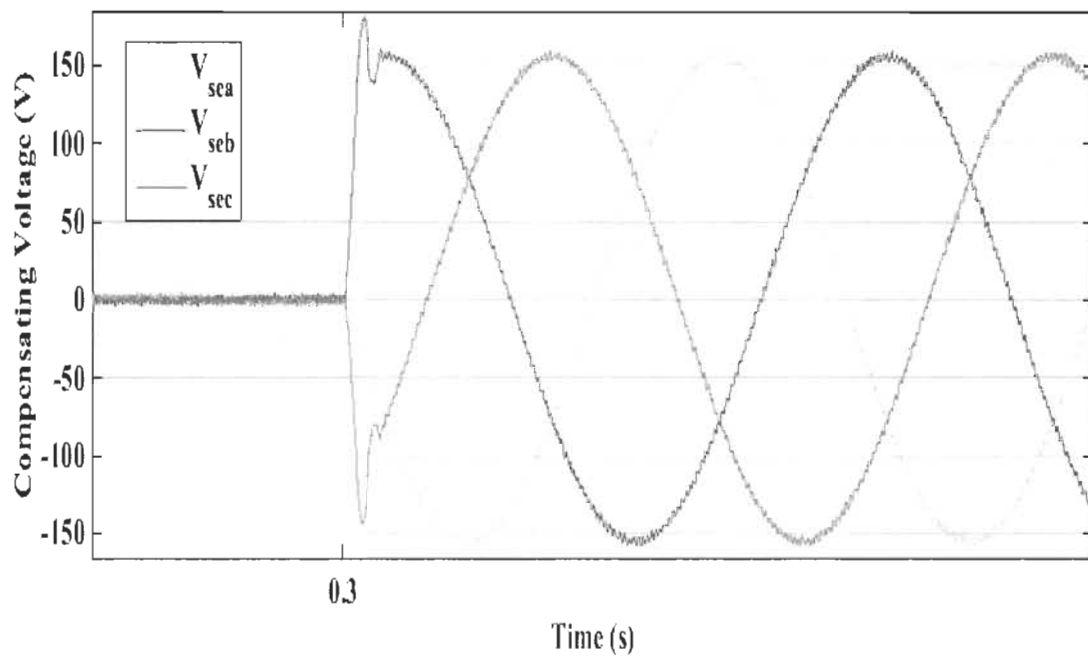


Figure 4-25 DVR intervention against voltage swell

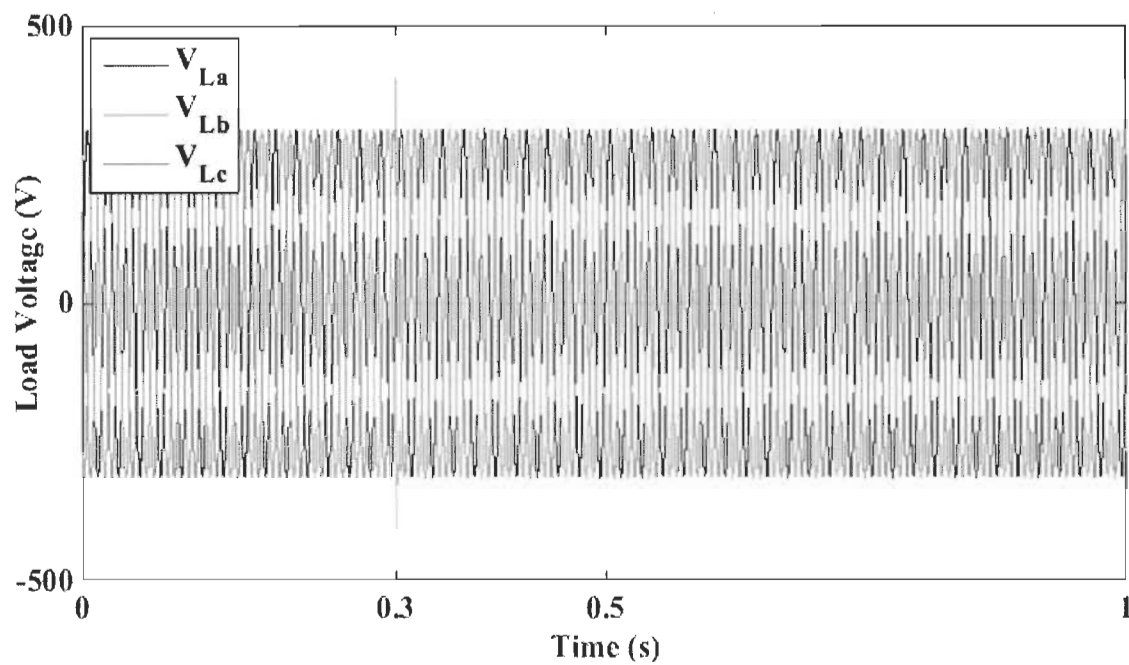


Figure 4-26 Load voltage after intervention against swells

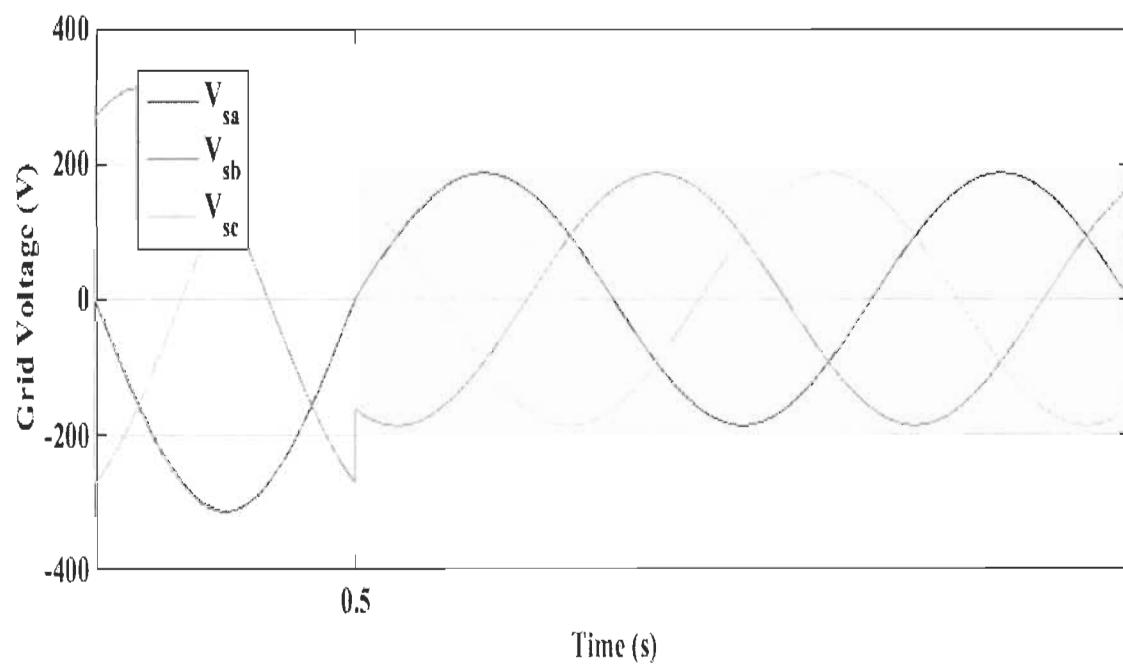


Figure 4-27 Voltage sag occurs in the grid

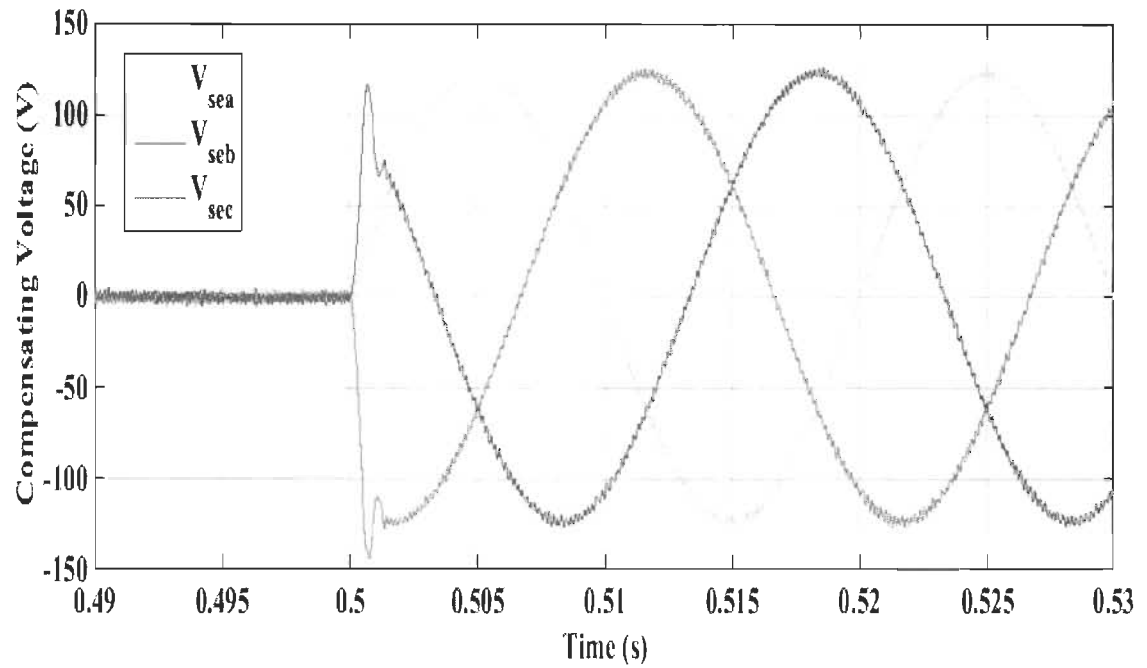


Figure 4-28 DVR intervention against sag

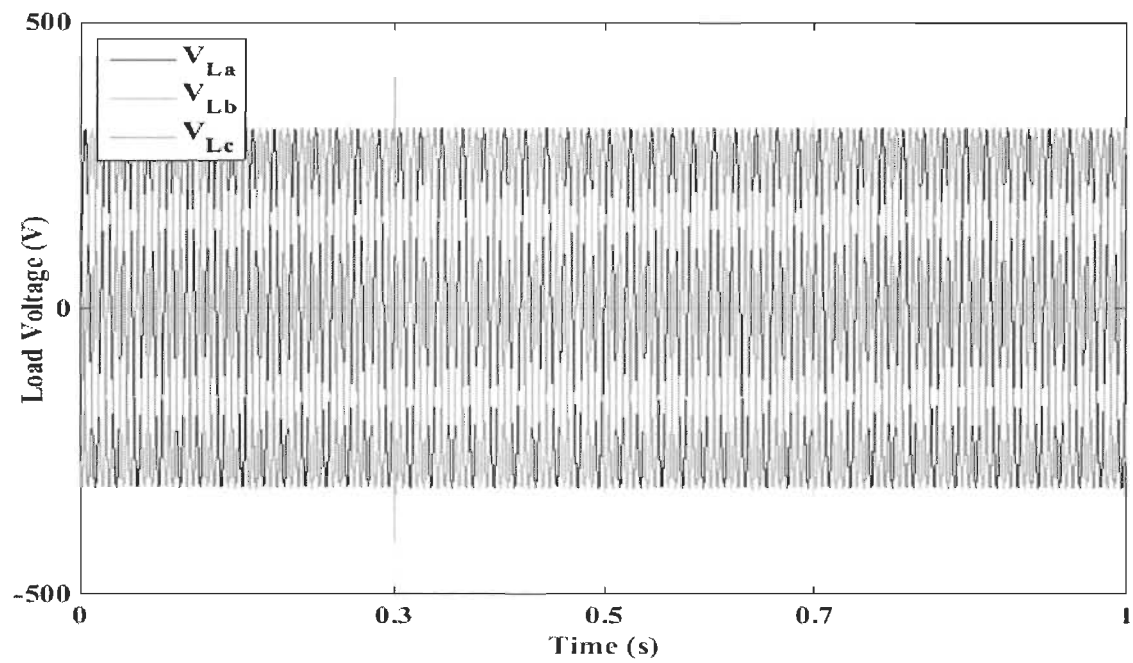


Figure 4-29 Load voltage after intervention against sag

4.5 Conclusion

This chapter presents a brief study of the series and the shunt active compensators based DVR and D-STATCOM, exploited in the distribution grid. We explored the performance of D-STATCOM and DVR against poor power factor and voltage sag and swell respectively. A systematic procedure is proposed to design both of compensators. A sliding mode technique has been used to control D-STATCOM, while a simple hysteresis control technique is employed to supervise DVR. According to the obtained results, DVR and D-STATCOM have good performances and proved their capability against power quality issues. The next step is the pairing between the D-STATCOM and the DVR to get a power device that has the capability to deal with all issues related to voltage and current in the same time

Chaptre 5 - A Study on the UPQC for power quality improvement

5.1 Introduction

The power quality (PQ) improvement more and more preoccupies the main attention of utilities. Basically, the power quality events are a collection of issues derived from voltage and current disturbances. Linear and nonlinear loads, as well as the increase of power-sharing of intermittent renewable resources sources, have an adverse effect on the PQ [116]. Voltage sag/ swell, flicker, interruption, surge, notch, excessive source voltage and load current unbalance, harmonic and neutral currents are samples of power quality issues that occur at power distribution level. Hence, utilities invest a lot of money in research and development to design a new mitigation techniques using current and voltage issues-based compensators [117]. A few decades ago, with the progress in the area of microelectronics, a new generation of active compensators called D-FACTS has been realized [118]. D-STATCOM and DVR are the most popular of D-FACTS family, which have been studied in chapter 4.

The most recent technology used in this field is the one called unified power quality conditioner (UPQC) [116]. It is a combination of a series (DVR) and shunt (D-STATCOM) voltage source converters connected back to back through a power source that could be a self-supporting capacity, battery or it even another rectifier used to interface a renewable or a conventional power source [119]. UPQC as two degrees of freedom compensator has the possibility to mitigate all power quality issues related to both voltage and current at the same

time. UPQC also has the capability to operate as unified power flow controller (UPFC) in high-voltage power transmission level where the main task is to supervise the reactive power evolution in the grid to improve its transmissibility with the fundamental frequency [120]. Obviously, UPQC was a subject of several papers with various topologies which could be classified following the number of phases, the type of control, the role assigned to both series and the shunt compensators and finally the placement of the UPQC in the grid [71, 121]. For instance, in [122] authors dealt with power issues that occur in three phases four wires power system, using a Universal Power Line Conditioner (UPLC). The UPLC aimed to emulate the behavior of UPQC and UPFC against the active and reactive power instability in addition to the mitigation of zero and negative sequence voltage and current issues. The UPLC is supervised by the instantaneous real and imaginary power control method. However, based on simulation results the decoupling between active and reactive power is not achieved due to the poor performance of PI- controller in transient response. In [123], authors used the same power system circuit represented in the [122] with the same tasks, but the contribution of this paper is carried out by using an integrated control technique which is a combination between the classical feedback control technique and an intelligent management algorithm used to collect information about the state of the power system. Authors believed that the proposed control technique is of interest; however, details regarding its design are missing. In [124], authors employed UPQC as an Active Power Filter (APF) to mitigate harmonics, voltage disturbance and to compensate reactive power in the industrial area. The control technique applied on UPQC is based on the comparison between the measured signals extracted from the distorted supplying source and a distortion-free reference signal. The difference between them used to generate the control signals applied to the shunt

compensator. In [125-127], authors studied the steady-state performance of UPQC against voltage sag/swell and harmonics caused by a polluted load. In these cases, the UPQC is controlled using unit vector template generations that allow it to inject a voltage with a phase angle that varies between 0 radian and 2π .

In distribution grid, power quality issues related to voltage are short duration events that mean the intervention of the series part of UPQC is less compared to the shunt part which should mitigate long duration issues such as reactive power, filtering harmonic coming from nonlinear loads, etc. For that, authors in [120],[128] and [129] proposed control techniques that allow sharing burden between the shunt and the series part of the UPQC. Both articles based on the same approach where the series part has to inject the compensating voltage with a specific angle to create a phase shift between the source and load voltages with preserving the same magnitude [120]. While in [129], the series part of the UPQC injects the compensation voltage ahead against the source voltage and perpendicular to the load current. There are two others control topologies applied on the UPQC, one of them is called active power control approach where the series part of the UPQC injects the compensating voltage with the same phase of the grid voltage. The other one called reactive power control approach which is characterized by the injection of a series voltage in quadrature against the grid voltage [71]. Recently, UPQC has also penetrated the renewable energy based distributed generation [130] [131]. In wind power area, the UPQC is basically employed to manage and to improve the power quality especially with the dependence on wind speed evolution that makes it relatively unstable [132-134].

In this chapter, we attempt to evaluate the performance of UPQC in critical situations. Both the series and the shunt parts of the UPQC supervise independently the evolution of the

grid current and voltage. The shunt compensator (D-STATCOM) deals with all issues coming from the end-user related to the current such as harmonics whereas the series one mitigates all issues coming from the power sources related to the voltage such as sag/ swell, unbalance, etc. The control technique applied on the UPQC is an adaptive fuzzy logic controller (AFLC). The proposed control technique emulates the human reasoning and uses this knowledge to supervise the power quality with no impact on the parameters uncertainty and with high tolerance against the inaccurate model.

5.2 Topology of the system under study with UPQC

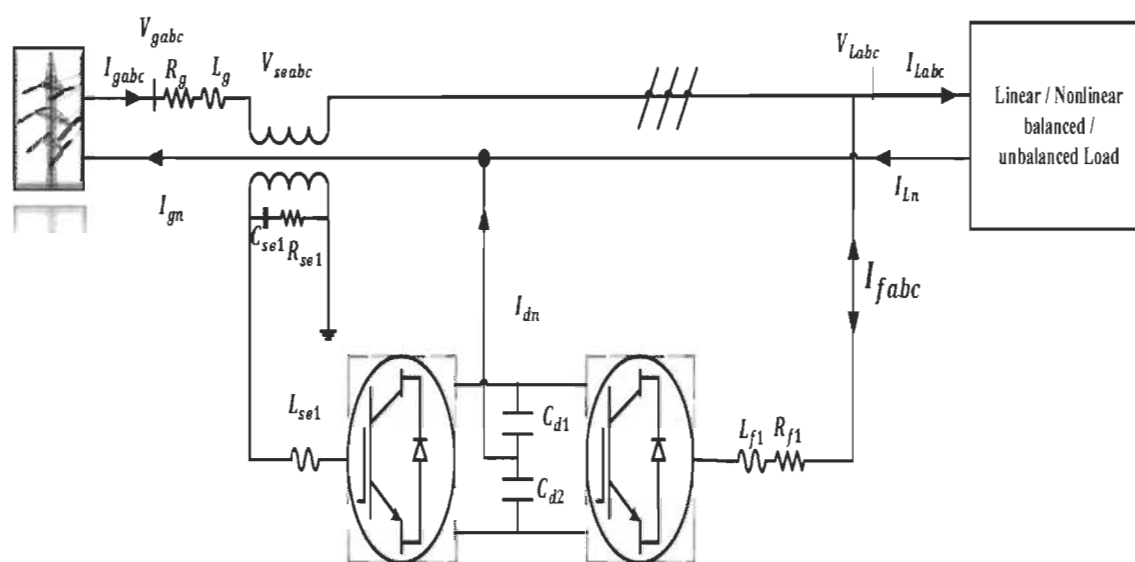


Figure 5-1 Topology of the UPQC in the proposed power system

5.2.1 Description of the system under study

The system under study consists of three-phase four wires power source, feeding the end-user (clients), which is modeled by a linear/nonlinear, balanced/unbalanced load. The UPQC compensator is connected to the grid between the source and the end user. The UPQC

consists of two Neutral Point Clamped Converters (NPCs) connected back to back by a dc-link. One of the NPCs emulates the behavior of the dynamic voltage restorer (DVR) which is connected in series to the grid through three single phase injection transformers. The series part of the UPQC (DVR) deals with all kinds of issues related to voltage such as sag/ swell, disturbance and so on. While the second one of NPCs operates as a D-STATCOM, connected in parallel to the grid. The main task of the parallel part of the UPQC (D-STATCOM) is to protect the grid and the sensitive load of harmonics and balance the unbalanced current, eliminate the neutral current. The proposed topology of UPQC with the system under study is depicted in Figure 5-1.

5.2.2 Mathematical modeling of the system under study

The mathematical modeling of the system under study is represented in dq –frame by the following equations

- Unified power quality conditioner (UPQC) [135], [136, 137]

$$\begin{cases} L_{f1} \frac{d}{dt} I_{fd} + R_{f1} I_{fd} = (V_{Ld} - V_{cd}) + \omega L_{pi} * I_{fq} \\ L_{f1} \frac{d}{dt} I_{fq} + R_{f1} I_{fq} = (V_{Ld} - V_{cd}) - \omega L_{pi} * I_{fd} \end{cases} \quad (5-1)$$

$$\begin{cases} L_{se1} \frac{d}{dt} I_{sed} = (V_{gd} - V_{sed} - V_{Ld}) + \omega L_s * I_{seq} \\ L_s \frac{d}{dt} I_{seq} = (V_{gq} - V_{seq} - V_{Lq}) - \omega L_s * I_{sed} \end{cases} \quad (5-2)$$

- Grid mathematical representation

$$\begin{cases} L_g \frac{d}{dt} I_{gd} + R_g * I_{gd} = V_d + \omega L_g * I_{gq} \\ L_g \frac{d}{dt} I_{gq} + R_g * I_{gq} = V_q - \omega L_g * I_{gd} \end{cases} \quad (5-3)$$

$$\begin{cases} V_d = V_{gd} - V_{sed} - V_{Ld} \\ V_q = V_{gq} - V_{seq} - V_{Lq} \end{cases} \quad (5-4)$$

5.2.3 Phasor diagram of UPQC

The phasor diagram of the UPQC intervention is depicted in the Figure 5-2.

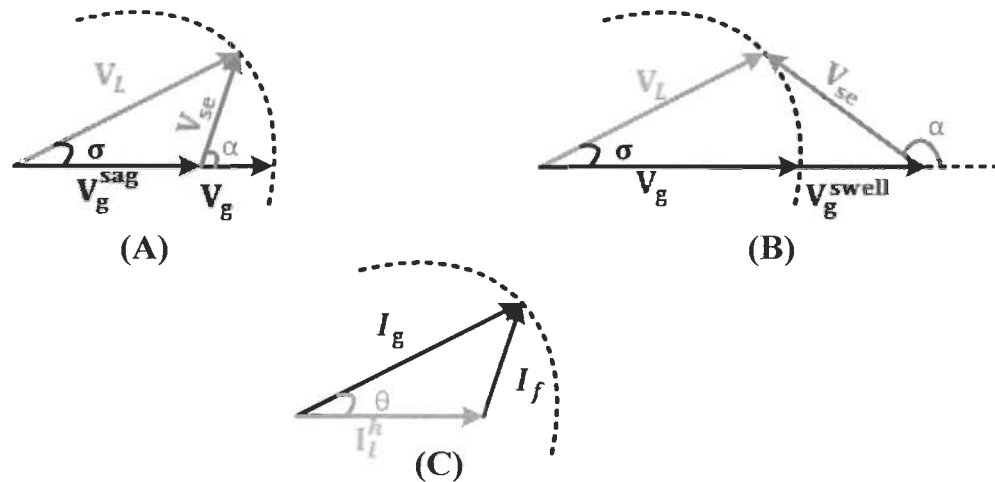


Figure 5-2 Phasor diagram of the UPQC intervention (A): against voltage sag, (B): against voltage swell, (C): against current issues.[71].

As we said previously, the intervention of the UPQC against events occurs through the parallel and the series parts. The parallel one (D-STATCOM) behaves as an active power filter, in which it is devoted to suppressing harmonics injected in the grid by the nonlinear load, poor power factor correction, balancing current and neutral current elimination. The compensating mechanism of D-STATCOM is based on the extraction of ripples at the terminal of the nonlinear load. Then the compensator has to inject a conditioning signal following the instantaneous active and reactive power ($p - q$) –control theory [138, 139]. Meanwhile, the series part (DVR) of the UPQC is engaged in the mitigation of the voltage disturbance. It generates a series voltage in the power system shifted by a specific angle

against the grid voltage [71]. In addition to the voltage sag and swell compensation, this property gives the UPQC the ability to control also the active power in the grid and to compensate the load reactive power [140]. The DVR shares with the D-STATCOM the burden of compensating the reactive power.

5.3 Control system design

The trend toward the development of grid utility using smart, flexible technologies and clean resources, gains the worldwide attention. In meantime, the intermittent service of renewable resources brings instability to the grid voltage and frequency. Following these challenges, D-FACTS know an intense evolution to meet these requirements. Nevertheless, the complexity of issues that could occur in a power system necessitates the use of an advanced category of control technique, to ameliorate the behavior of these appliances (D-FACTS) in different operating mode. In this chapter, a control technique has been used to enhance the performance of the UPQC in terms of harmonic elimination, balancing unbalanced current, canceling neutral current, compensating reactive power and mitigating voltage disturbance. The control strategy proposed in this work consists of an instantaneous $(p - q)$ –control theory applied on the parallel part of the UPQC-S (D-STATCOM), while a modified synchronous reference frame theory is used to control the series (DVR). Both the two control strategies are used to draw out the measured values of the current and the voltage based on Clarke's and Park's transformations, to estimate the compensating signals. Next subtitles give more details about the proposed control strategies.

5.3.1 Control strategy applied on DVR

The series part of the UPQC is assigned to deal with voltage disturbance occurs in the grid. For that, we propose a modified synchronous reference frame theory, which also allows supervising the active and reactive power flow in the grid. To do so, we start by the instantaneous active and reactive power of the grid, which is defined in DQ frame by

$$\begin{pmatrix} P_g \\ Q_g \end{pmatrix} = \frac{3}{2} V_{gd} \begin{pmatrix} 1 & \frac{V_{gq}}{V_{gd}} \\ 1 & -\frac{V_{gq}}{V_{gd}} \end{pmatrix} \begin{pmatrix} I_{gd} \\ I_{gq} \end{pmatrix} \quad (5-5)$$

From (5-5), we extract the direct and quadratic components of the grid current which are given as following

$$\begin{pmatrix} I_{gd}^* \\ I_{gq}^* \end{pmatrix} = \sqrt{\frac{3}{2}} \frac{1}{\sqrt{V_{gd}^2 + V_{gq}^2}} \begin{pmatrix} P_g^* & -Q_g^* \\ Q_g^* & P_g^* \end{pmatrix} \begin{pmatrix} V_{gd} \\ V_{gq} \end{pmatrix} \quad (5-6)$$

In the ideal operating condition the P_g^* is equal to the nominal grid power while Q_g^* is referred to zero. In this case, we get:

$$\begin{pmatrix} I_{gd}^* \\ I_{gq}^* \end{pmatrix} = \sqrt{\frac{3}{2}} \frac{1}{\sqrt{V_{gd}^2 + V_{gq}^2}} \begin{pmatrix} P_g^* & 0 \\ 0 & P_g^* \end{pmatrix} \begin{pmatrix} V_{gd} \\ V_{gq} \end{pmatrix} \quad (5-7)$$

Based on the feedback control theory and using (5-4) and (5-5), we elicit the direct and the quadratic components of grid voltage. By adding the compensating terms, we extract the measured value of the compensating voltage.

In this case, DVR should inject a compensating voltage which is estimated by the following equation:

$$\begin{cases} V_{sed} = V_{gd} - V_{Ld} \\ V_{seq} = V_{gq} - V_{Lq} \end{cases} \quad (5-8)$$

The whole control scheme used to supervise the DVR is represented in the Figure 5-3.

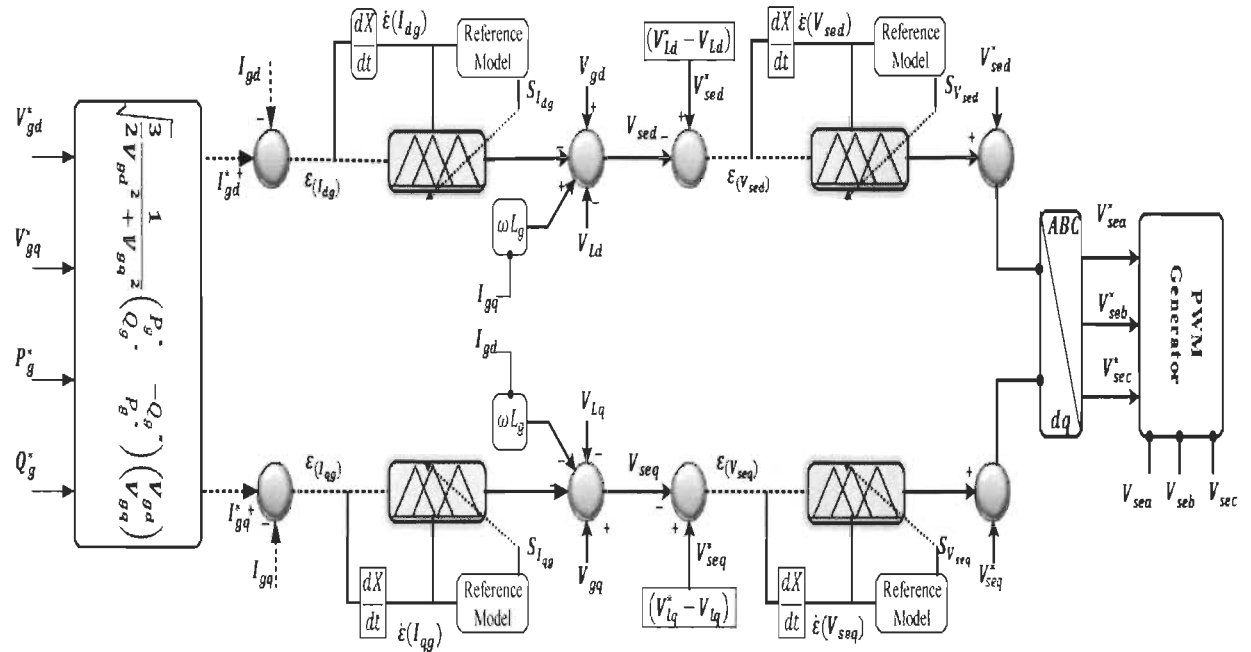


Figure 5-3 Control algorithm applied on the series part of the UPQC

5.3.2 Control strategy applied on D-STATCOM

The instantaneous ($p - q$) –control theory is an innovative idea was proposed in [138], permits to represent the current and voltage in bidimensional frame. Based on the new real and imaginary quantities of power, D-STATCOM injects a compensating current into the grid to balance the unbalanced current and to filter harmonics induced by the nonlinear load. The application ($p - q$) –control theory on the system under study, passes through the extraction and the transformation of the grid current and voltage from the abc -frame into $\alpha\beta$ -frame using the following equality [139]:

$$\begin{bmatrix} I_{g\alpha} \\ I_{g\beta} \end{bmatrix} = \sqrt{\frac{2}{3}} \begin{bmatrix} 1 & -\frac{1}{2} & -\frac{1}{2} \\ 0 & \frac{\sqrt{3}}{2} & -\frac{\sqrt{3}}{2} \end{bmatrix} \begin{bmatrix} I_{ga} \\ I_{gb} \\ I_{gc} \end{bmatrix} \quad (5-9)$$

$$\begin{bmatrix} V_{g\alpha} \\ V_{g\beta} \end{bmatrix} = \sqrt{\frac{2}{3}} \begin{bmatrix} 1 & -\frac{1}{2} & -\frac{1}{2} \\ 0 & \frac{\sqrt{3}}{2} & -\frac{\sqrt{3}}{2} \end{bmatrix} \begin{bmatrix} V_{ga} \\ V_{gb} \\ V_{gc} \end{bmatrix} \quad (5-10)$$

Since our system is a three-phase four wire system, a zero-sequence quantity should be added to the real and imaginary quantities. For that, the instantaneous active and reactive power are defined as follows [141]

$$\begin{bmatrix} P_{g0} \\ P_{g\alpha} \\ P_{g\beta} \end{bmatrix} = \begin{bmatrix} V_{g0} & 0 & 0 \\ 0 & V_{g\alpha} & V_{g\beta} \\ 0 & V_{g\beta} & -V_{g\alpha} \end{bmatrix} \begin{bmatrix} I_{g0} \\ I_{g\alpha} \\ I_{g\beta} \end{bmatrix} \quad (5-11)$$

Then the instantaneous active power of a three-phase system is estimated by

$$P_{gabc} = \sum_{k=a}^c (V_{gk} * I_{gk}) = \sum_{k_1=0}^{\beta} (V_{gk_1} * I_{gk_1}) = P_{g0} + P_{g\alpha} \quad (5-12)$$

With

$$\begin{cases} k = \{a, b, c\} \\ k_1 = \{0, \alpha, \beta\} \end{cases} \quad (5-13)$$

The ideal scenario is that the end-user draws only the positive sequence of grid current, also D-STATCOM has to cancel all harmonics and neutral current coming from the unbalanced and nonlinear load. As the power source is unbalanced, then it contains positive, negative and zero sequences of voltage and current. Hence, a positive sequence detector is necessary to estimate the magnitude and phase angle of grid current and voltage positive sequences, since only the positive sequence carries out the real power to the end user. The block diagram of the positive sequence detector is presented in Figure 5-4.

The positive sequence of grid voltage in $\alpha\beta$ -frame is given by [142]

$$\begin{bmatrix} V_{g\alpha}^{+\sim} \\ V_{g\beta}^{+\sim} \end{bmatrix} = \frac{1}{I_{g\alpha}^{+\sim 2} + I_{g\beta}^{+\sim 2}} \begin{bmatrix} I_{g\alpha}^{+\sim} & -I_{g\beta}^{+\sim} \\ I_{g\beta}^{+\sim} & -I_{g\alpha}^{+\sim} \end{bmatrix} \begin{bmatrix} \widetilde{P}_{g\alpha} \\ \widetilde{P}_{g\beta} \end{bmatrix} \quad (5-14)$$

With

$$\begin{bmatrix} \widetilde{P}_{g\alpha} \\ \widetilde{P}_{g\beta} \end{bmatrix} = \begin{bmatrix} V_{g\alpha} & V_{g\beta} \\ V_{g\beta} & -V_{g\alpha} \end{bmatrix} \begin{bmatrix} I_{g\alpha}^{+\sim} \\ I_{g\beta}^{+\sim} \end{bmatrix} \quad (5-15)$$

$\widetilde{P}_{g\alpha}$ and $\widetilde{P}_{g\beta}$ are the average power in $\alpha\beta$ -frame where a cut-off frequency of 50 Hz based low pass filter is used to eliminate harmonics and negative sequence.

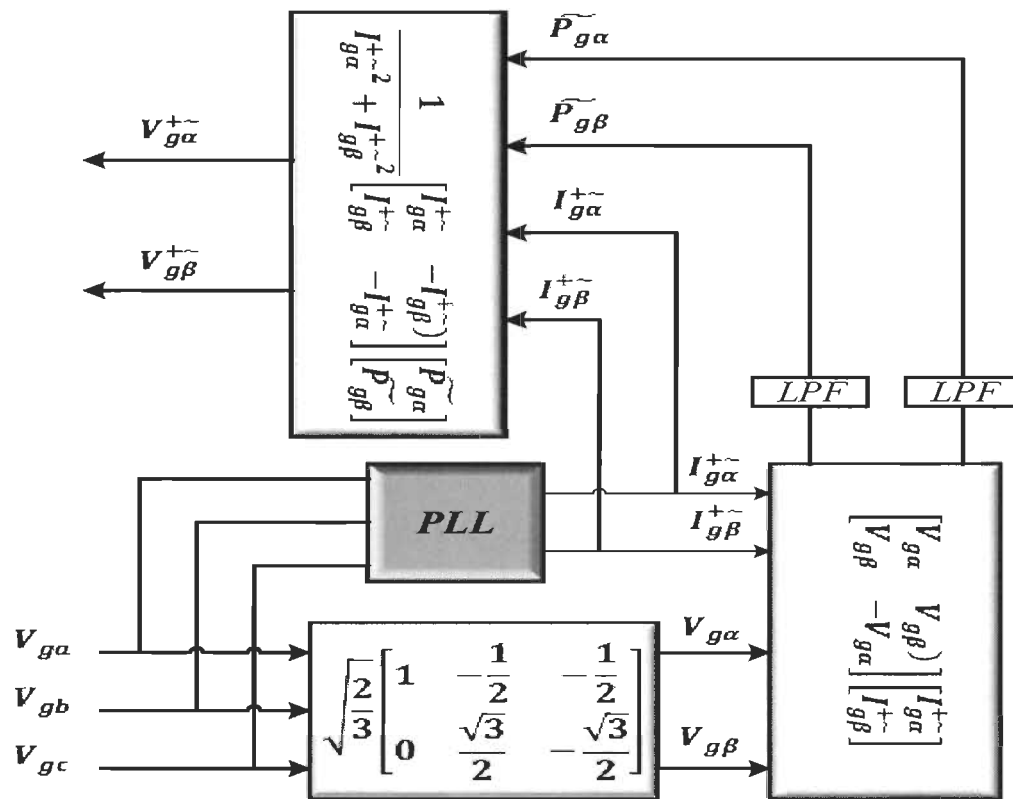


Figure 5-4 Positive sequence detector [141]

$I_{g\alpha}^{+\sim}, I_{g\beta}^{+\sim}$ are the auxiliary components of the positive sequences of the grid currents in $\alpha\beta$ -frame which are estimated using PLL presented in Figure 5-5.

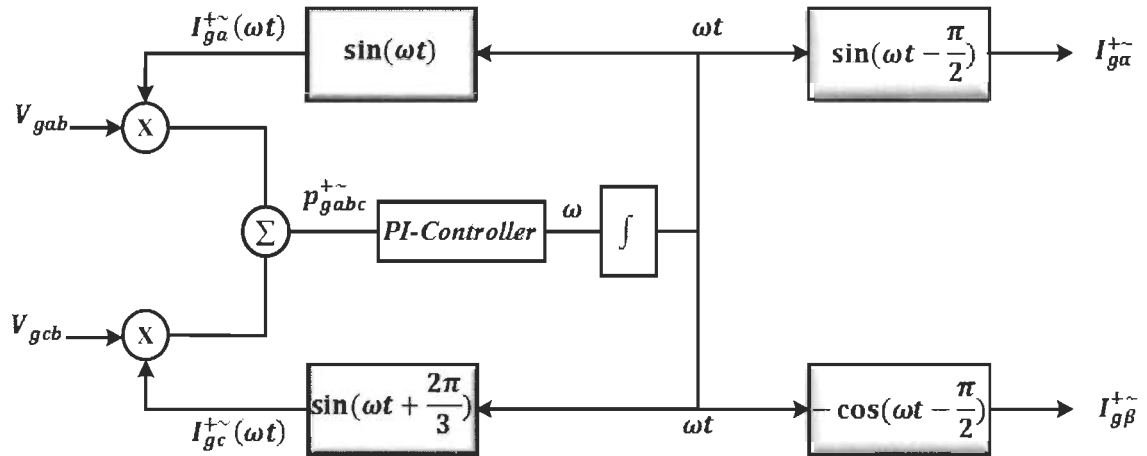


Figure 5-5 Block diagram of PLL circuit [141]

The next step is to calculate the compensating real and imaginary power (5-16) which will be used to estimate the compensating reference currents (5-17)

$$\begin{bmatrix} P_f \\ Q_f \end{bmatrix} = \begin{bmatrix} V_{g\alpha}^{+\sim} & V_{g\beta}^{+\sim} \\ V_{g\beta}^{+\sim} & -V_{g\alpha}^{+\sim} \end{bmatrix} \begin{bmatrix} I_{L\alpha} \\ I_{L\beta} \end{bmatrix} \quad (5-16)$$

$$\begin{bmatrix} I_{f\alpha}^* \\ I_{f\beta}^* \end{bmatrix} = \frac{1}{v_{g\alpha}^{+\sim 2} + v_{g\beta}^{+\sim 2}} \begin{bmatrix} V_{g\alpha}^{+\sim} & V_{g\beta}^{+\sim} \\ V_{g\beta}^{+\sim} & -V_{g\alpha}^{+\sim} \end{bmatrix} \begin{bmatrix} P_f + P_{loss} \\ Q_f \end{bmatrix} \quad (5-17)$$

$$\begin{bmatrix} I_{fa}^* \\ I_{fb}^* \\ I_{fc}^* \end{bmatrix} = \sqrt{\frac{2}{3}} \begin{bmatrix} 1 & 0 \\ -\frac{1}{2} & \sqrt{\frac{3}{2}} \\ -\frac{1}{2} & -\sqrt{\frac{3}{2}} \end{bmatrix} \begin{bmatrix} I_{f\alpha}^* \\ I_{f\beta}^* \end{bmatrix} \quad (5-18)$$

D-STATCOM output reference currents presented in (5-18) are transferred into DQ-frame and compared with the measured values which are also presented in the same referential. By adding the decoupling and feed-forward terms we extract references of D-STATCOM output voltage. The full control scheme applied on D-STATCOM is presented in Figure 5-6.

5.3.3 Adaptive fuzzy logic controller design

Traditionally, the classical PI control technique is widely used to supervise the performance of the system under study. However, several papers have been proven that the linear controller is inaccurate with the nonlinear and inexact system and not robust against parameters uncertainty [143]. To overcome these problems, we propose an adaptive fuzzy logic control (AFLC) technique. Basically, the AFLC emulates the human brain behavior and tries to apply this knowledge to the proposed system [144]. The AFLC technique brings a high tolerance with uncertainty, improves the response of the controlled element in terms of reference tracking and reduces undesirable characteristics (overshoot, rise time, etc.) without asking for an exact model of the power system [145, 146]. The AFLC technique attempts to represent the control technique by a virtual mechanism with a fuzzy decision variable between zero and one while maintaining a clear emulation of the system under control [146]. The application of the AFLC on the proposed power system passes through the next steps.

The first step is the fuzzification; it is the conversion of the input variable (ε : error between desired and the measured values) from a crisp set toward a fuzzy set, using the membership function $\mu_{\alpha}(\varepsilon)$ which varies between zero and one [147]. α is the fuzzy logic set belongs to the universe of discourse χ . In our case, the membership function of the under-control variable is represented by the triangular form, whereas the universe of discourse is performed by a standard set of the linguistic variables distributed as: Negative Large (LG), Negative Medium (NM), Negative small (NS), Zero (Z), Positive Small (PS), Positive Medium (PM), Positive Large (PL) as shown in Figure 5-7.

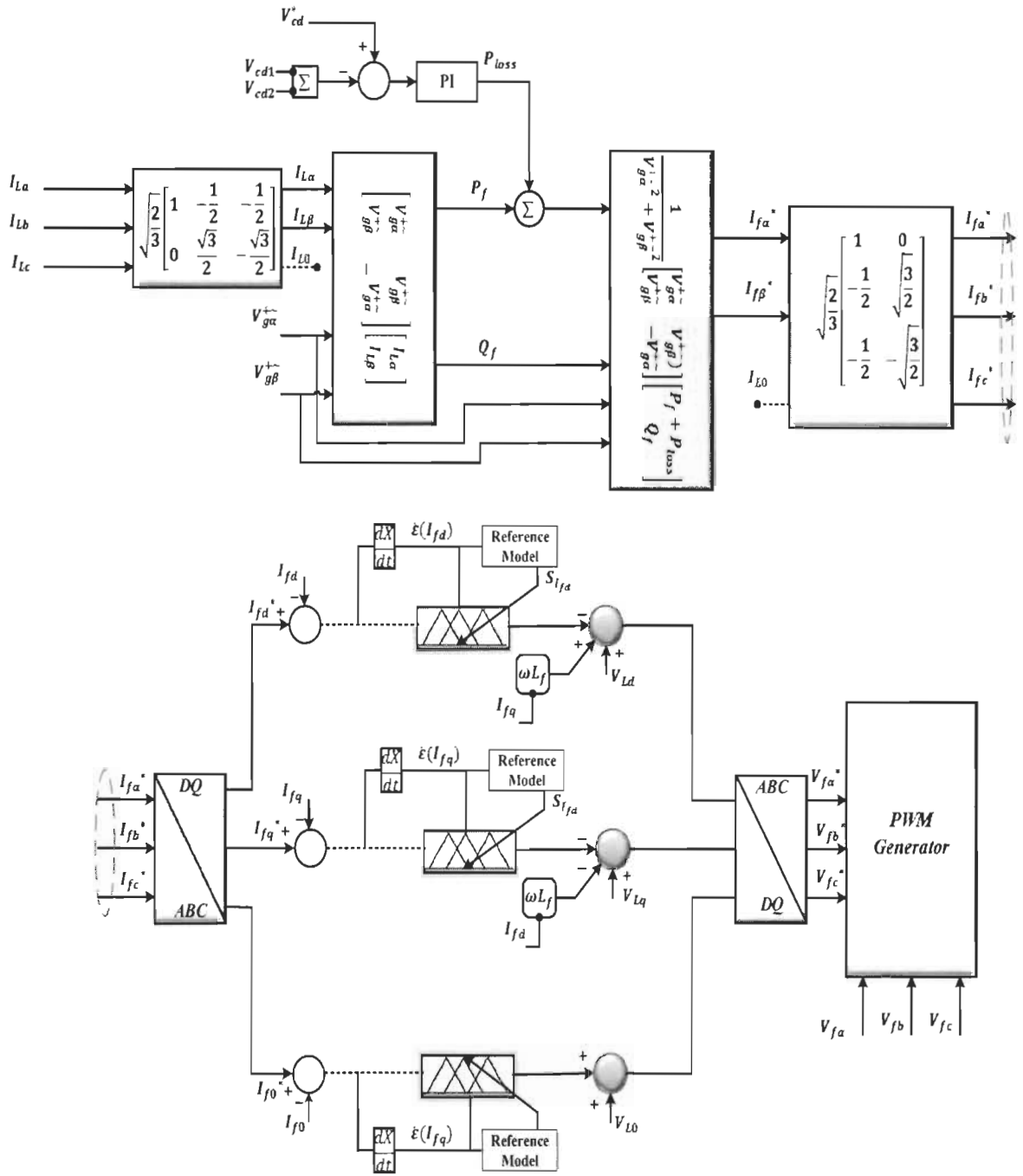


Figure 5-6 Control algorithm applied on the shunt part of the UPQC

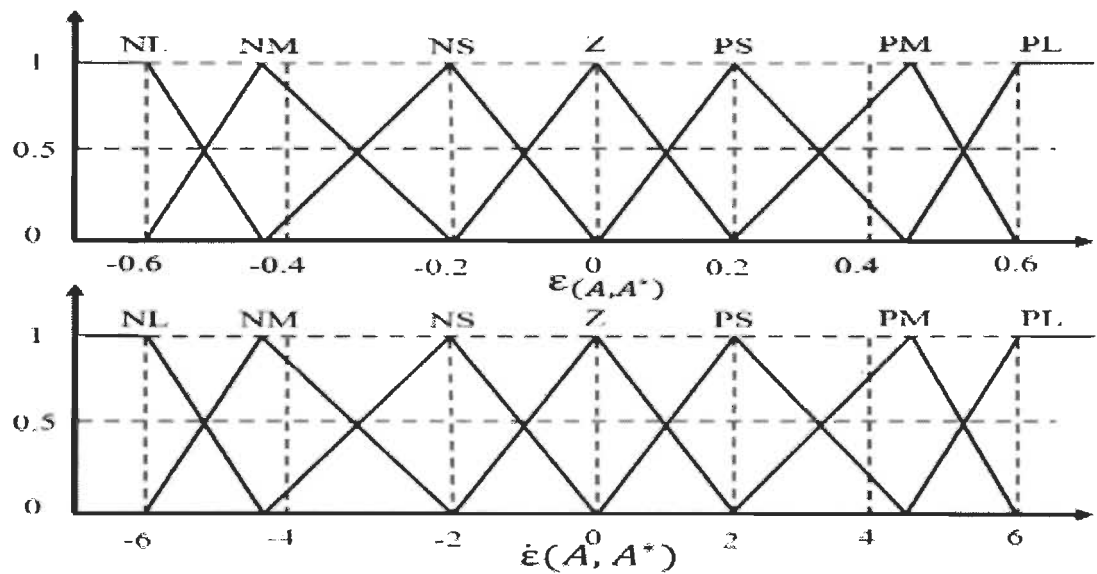


Figure 5-7 Membership function [147]

The next step is to link the input variable with its output using a collection of IF-THEN instructions, assuring the convergence between the desired and measured values following the set of rules presented in Table A. In divergence situations, the error derivative $\dot{\varepsilon}(A, A^*)$ takes a large value to force the measured element to track the reference. Otherwise, it takes a small value (Table A).

$$\varepsilon_{(A, A^*)} = A^* - A \quad (5-19)$$

$$\dot{\varepsilon}(A, A^*) = \frac{d\varepsilon_{(A, A^*)}}{dt} \quad (5-20)$$

With A^* and A are the desired and measured values

The third step is the aggregation of the knowledge stored in the database in form of IF-THEN instructions. In other words, it is the step to make a decision about the manner to deal with the fuzzified input ($\varepsilon_{(A, A^*)}$). Previously, three methods of fuzzy inference are used to achieve this goal. One of them which is proposed by Mamdani, is used in our work. It is

based on a comparison between rules to select the highest values using the min-max mathematical operations using the following equation [148].

$$\mu_{B^l}(y) = \prod_{x \in X} [\mu_{A_x}(x) \prod \mu_{R^l}(x, y)] \quad (5-21)$$

The last step of the fuzzy logic application is the conversion of fuzzified output to a crisp value (Defuzzification). The center of the area (gravity) is used in this paper to get the real value following the next formula [148]:

$$y_j(y) = \frac{\sum_{l=1}^r y_l \mu_{B^l}(y)}{\sum_{l=1}^r \mu_{B^l}(y)} \quad (5-22)$$

The crisp output is the sum of multiplication between the deduced fuzzified outputs by their numbers of membership, divide by the overall output numbers of membership.

Table A Fuzzy rules [148, 149]

		$\varepsilon(d,q)$						
		NL	NM	NS	Z	PS	PM	PL
$\varepsilon(d,q)$	NL	Z	PL	PL	PL	PL	PL	PL
	NM	NL	Z	PS	PS	PL	PL	PL
	NS	NL	NS	Z	PS	PS	PL	PL
	Z	NL	NL	NS	Z	PS	PL	PL
	PS	NL	NL	NS	NS	Z	PS	PL
	PM	NL	NL	NL	NS	NS	Z	PS
	PL	NL	NL	NL	NL	NL	PL	Z

As pointed out above, the application of the fuzzy logic control based on trial and error method, which raises doubts about the benefit of this technique compared to its complexity. For that, the proposed technique is supported by the neural network to allow it to be adapted to diverse situations and to optimize the system performance. Figure 5-8 depicts the structure of fuzzy logic control. The antecedent part (regressor) $\hat{\phi}$ is defined by the first and the second

layers, while the consequent part is represented by the third and the fourth layers through a weight matrix \widehat{W} . The output of the fuzzy controller is given by the following equation [150]:

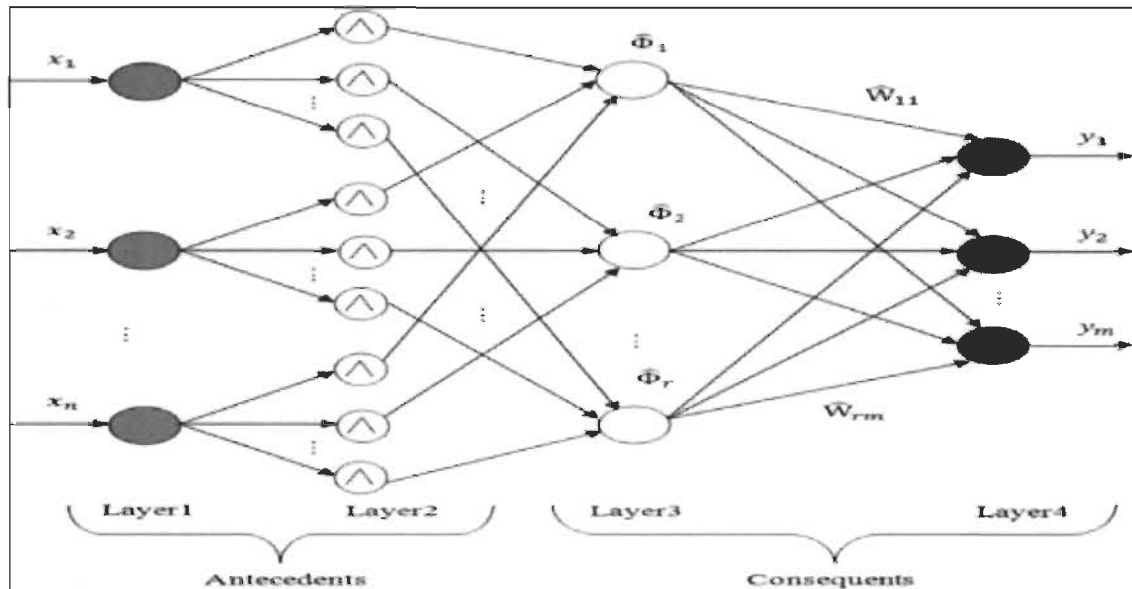


Figure 5-8 Structure of the adaptive logic control[148]

$$Y = \phi^T W + \varepsilon_{(A,A^*)} = \widehat{\phi}^T \widehat{W} \quad (5-23)$$

With $\widehat{W} \in R^{r \times m}$

Since our system is a single input single output, then $m = 1$ and the number of rules is seven. $\widehat{\phi}^T$ is the 7th-dimensional regressor functions given by [149]

$$\widehat{\phi} = \frac{\mu_{B^l(y)}}{\sum_{l=1}^7 \mu_{B^l(y)}} \quad (5-24)$$

(5-19) implies

$$\varepsilon_{(A,A^*)} = \widehat{\phi}^T \widehat{W} - \phi^T W \quad (5-25)$$

The error $\varepsilon_{(A,A^*)}$ should tend to zero. For that, the reference model represented by (5-26) generates the adaptation signal to eliminate the error.

$$S_{(A,A^*)} = \varepsilon_{(d,q)} + \psi \dot{\varepsilon}(A, A^*) \quad (5-26)$$

5.4 UPQC performance analysis

In the aim to evaluate the responsiveness and the performance of UPQC in critical situations, the power system under study presented in Figure 5-1 is modeled in Matlab®/SimPowerSystems. The UPQC is exposed to several issues, such as voltage sag/swell, unbalanced voltage, distortion in voltage supply and harmonic current generated by the nonlinear and balanced/ unbalanced load. These conditions carried out using a variable voltage source to generate voltage sag and swell. In addition to that, a disturbed power supply is emulated by a 7th, and (7th, 11th) harmonic voltage source (Figure 5-8). It induces a deformation in the voltage waveform by 22% and 31% of the fundamental. The end user is modeled by a combination nonlinear balanced and unbalanced load connected on the same bus. Parameters used in this work are presented in Appendix D.

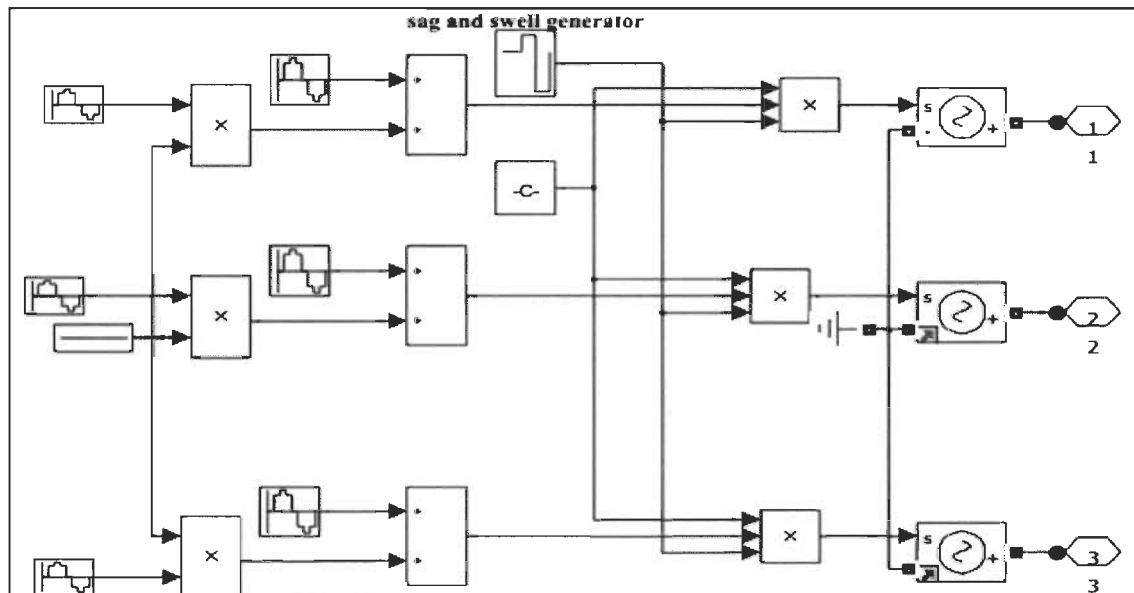


Figure 5-9 Disturbed voltage source generator

5.4.1 Performance analysis of DVR against voltage sag and swell

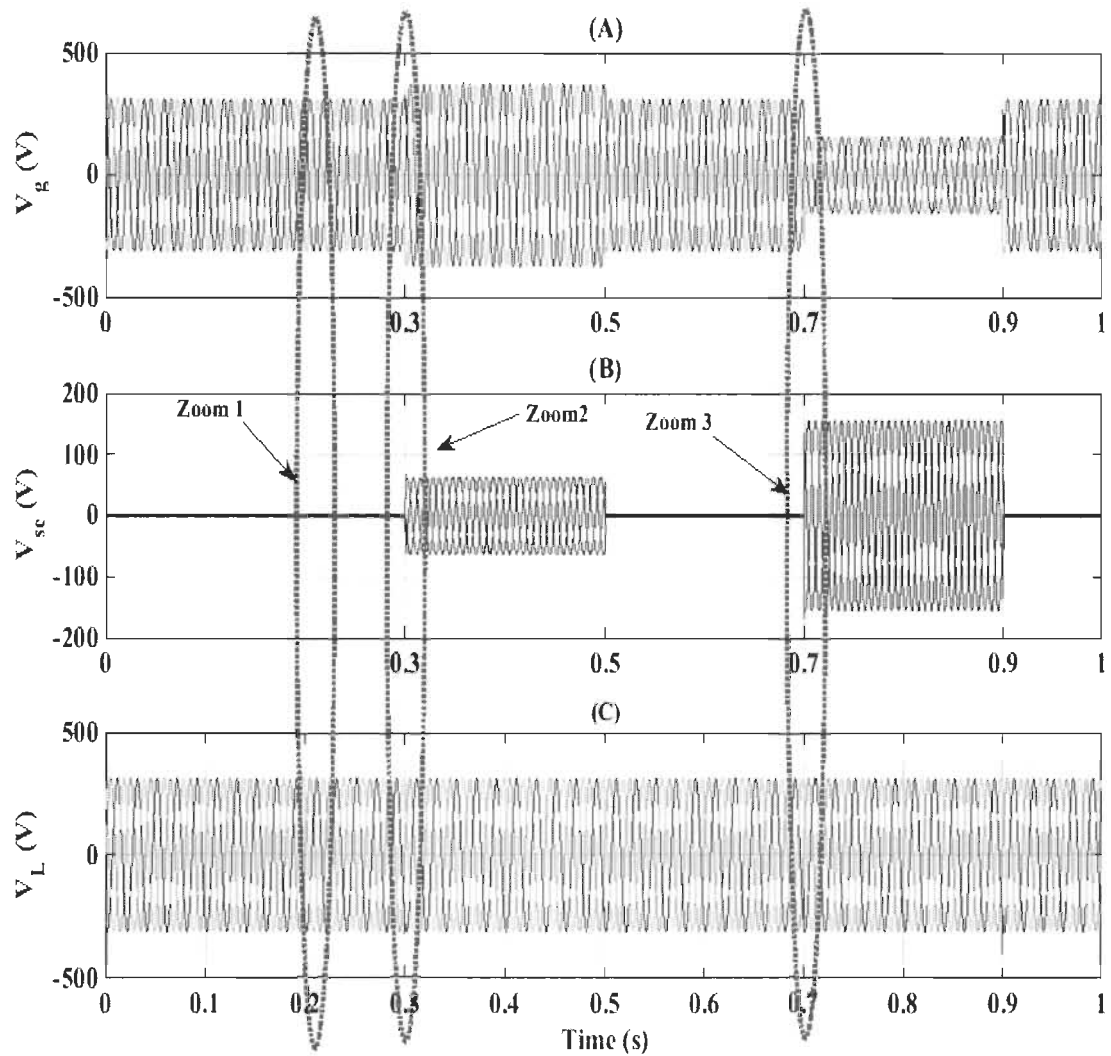


Figure 5-10 (A): Grid Voltage, (B): Compensating voltage, (C): Load terminals voltage (PCC)

Figure 5-10 shows the performance of the UPQC in the presence of voltage sag and swell that could occur in the grid. Generally, these kinds of issues are due to the fluctuation of power sources such as renewable energies and faults like a short circuit or even the start-up of high-power motors. To emulate this scenario, we used a variable voltage source. It's remarkable that the grid voltage in Figure 5-10 (A) increases (swells) by 20% at $t=0.3$ s and

decreases (sag) by 50% at $t=0.7s$. We also observe from Figure 5-10 (B) that the series part of the UPQC intervenes against these events. From Figure 5-10 (C), we see that the voltage at the load terminals (PCC) is not affected. It returns to the ideal value within a quarter cycle after the events happen as shown in zoom (Figure 5-11).

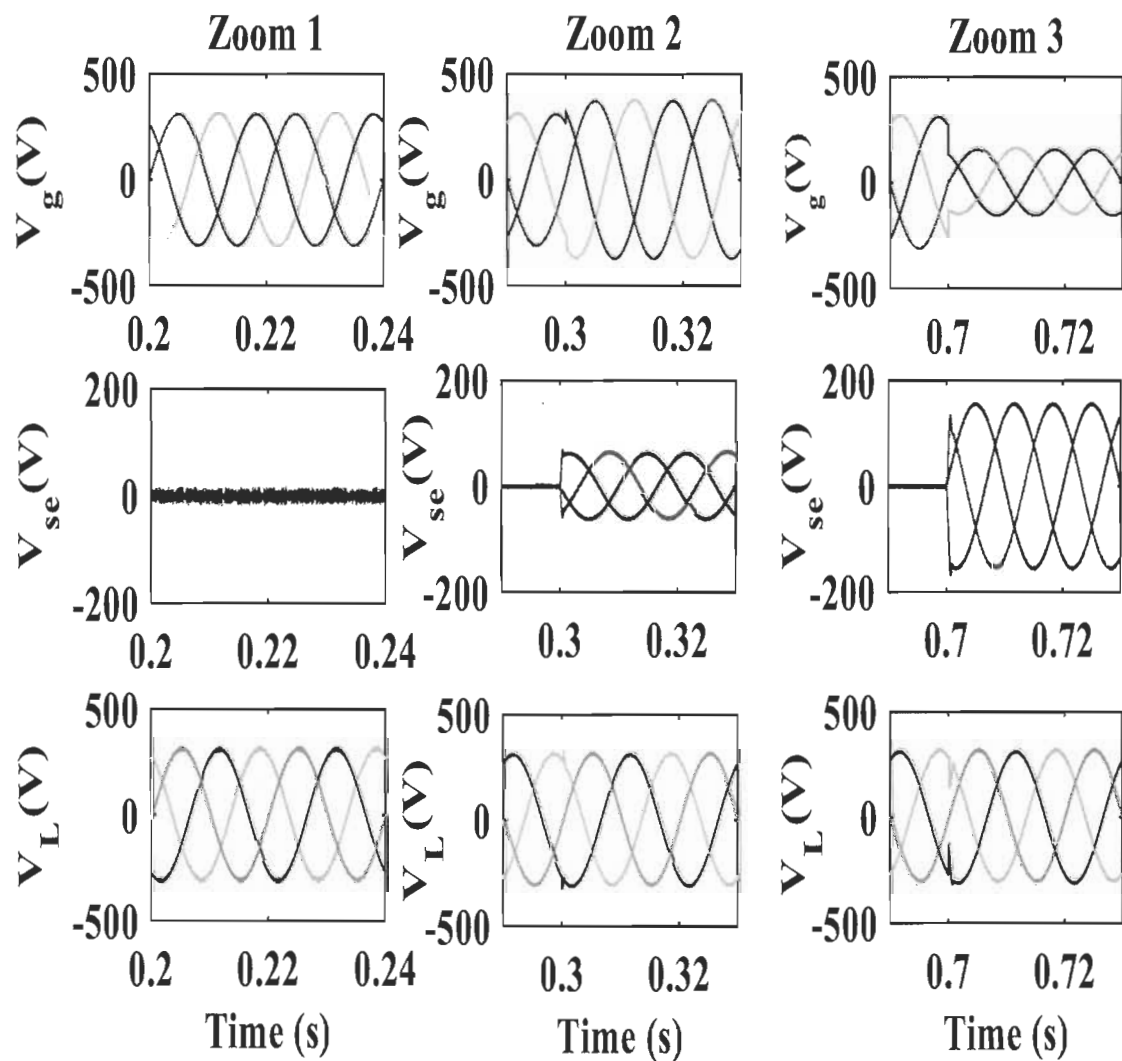


Figure 5-11 Zoom of Figure 5-10

The series part of UPQC inherently able to deal with the active and the reactive power as well as maintains them at the suitable values as depicted in Figure 5-12 where the active and reactive power track the imposed references.

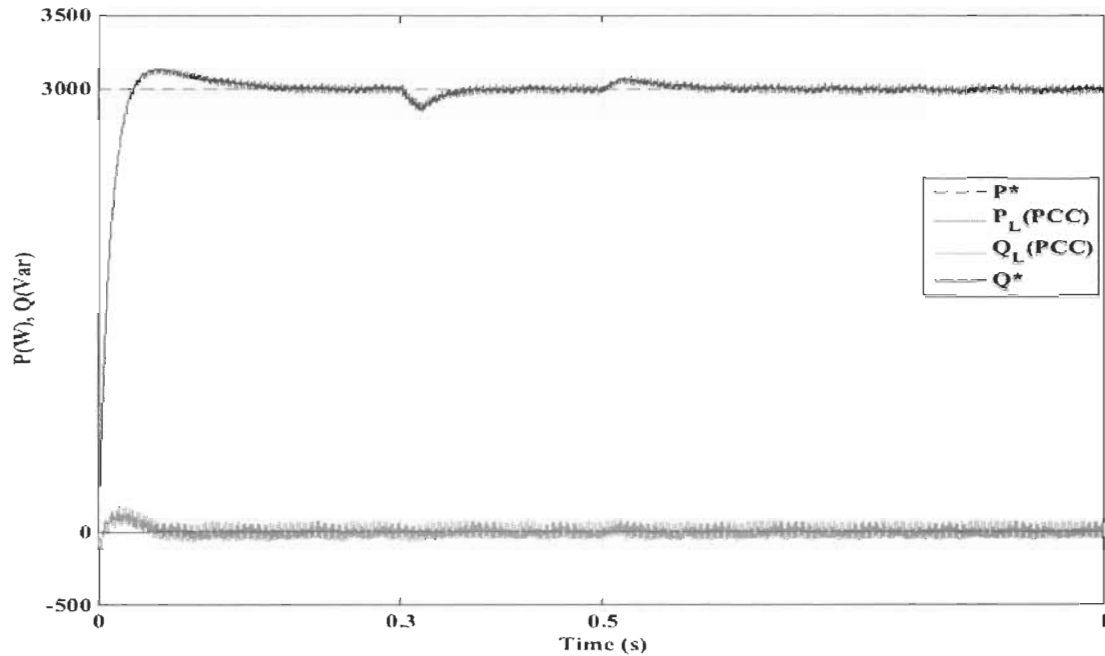


Figure 5-12 Active and reactive power at load terminals

5.4.2 Performance of DVR against distorted voltage

In this case, the power supply generates a distorted voltage with 7th voltage harmonic. The grid voltage is also affected by swells (20%) at $t=0.3s$ and sags (50%) at $0.5s$ as represented in Figure 5-13 (A). The UPQC through its series part (DVR) generates a compensating voltage (Figure 5-13 (B)) to protect the end user of the voltage disturbance as shown in Figure 5-13 (C). The THD of the grid voltage is 22% and equal to 0.82% at the loads terminal (PCC) as displayed in Figure 5-14.

To reinforce the obtained result, we used a power source that generates a 7th and an 11th voltage harmonic order at the same time. From Figure 5-15, we observe that the grid voltage THD is 31.12% while at the load terminal is equal to 1.09%. The series part of the UPQC confirms its effectiveness in the elimination of all issues related to voltage in term of sag, swell, distortion and unbalance.

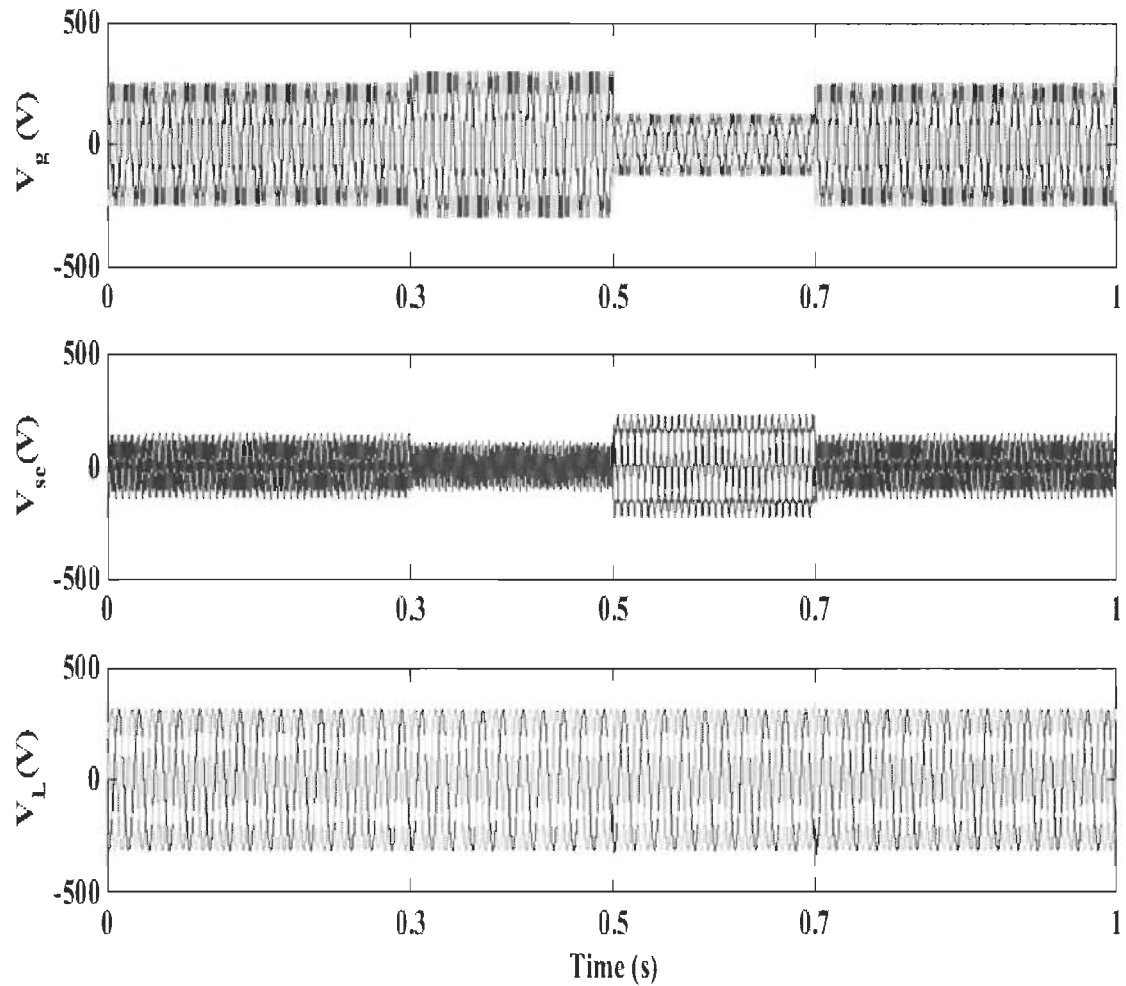


Figure 5-13 (A): Grid voltage (with harmonic generator), (B): Compensating voltage, (C): Load terminals voltage

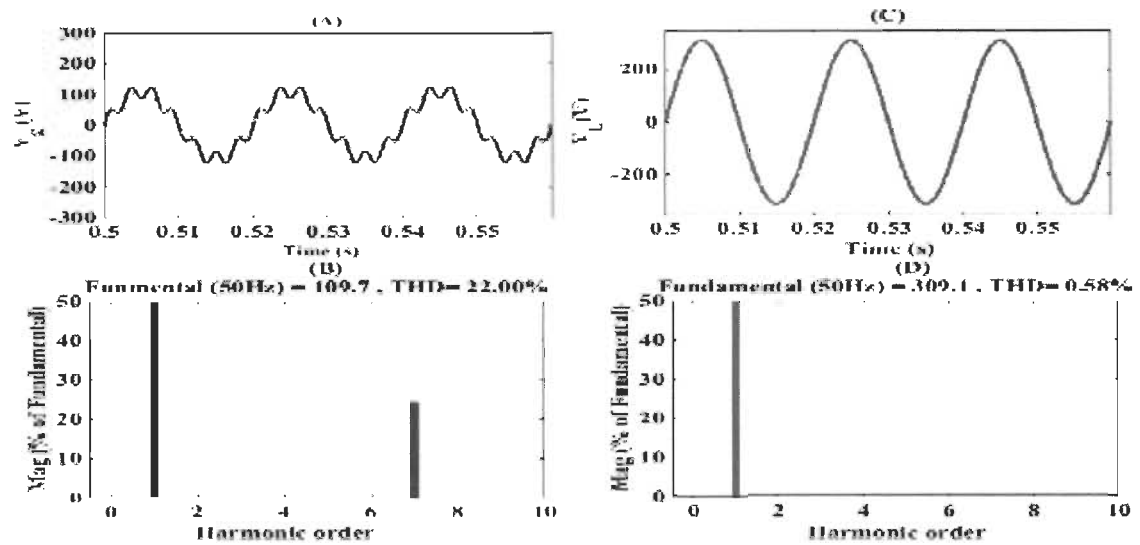


Figure 5-14 (A, B): Grid voltage and its harmonic spectrum (7th harmonic generator)
(C, D): Load terminals voltage and its harmonic spectrum

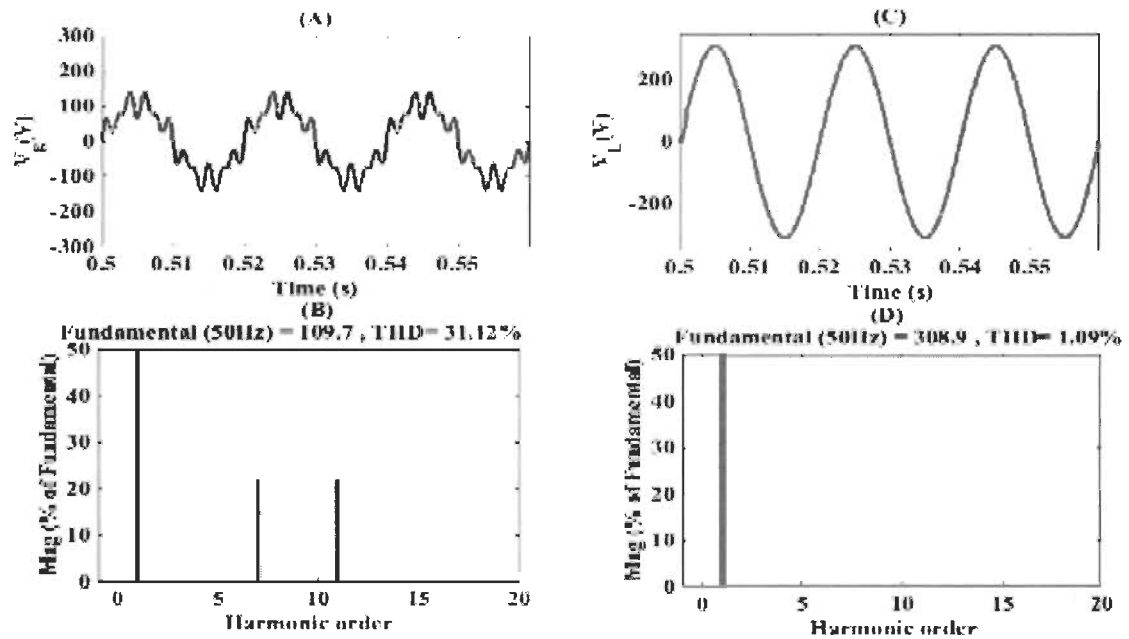


Figure 5-15 (A, B): Grid voltage and its harmonic spectrum (7th, 11th harmonic generator)
(C, D): Load terminals voltage and its harmonic spectrum

5.4.3 Performance analysis of D-STATCOM against harmonic current

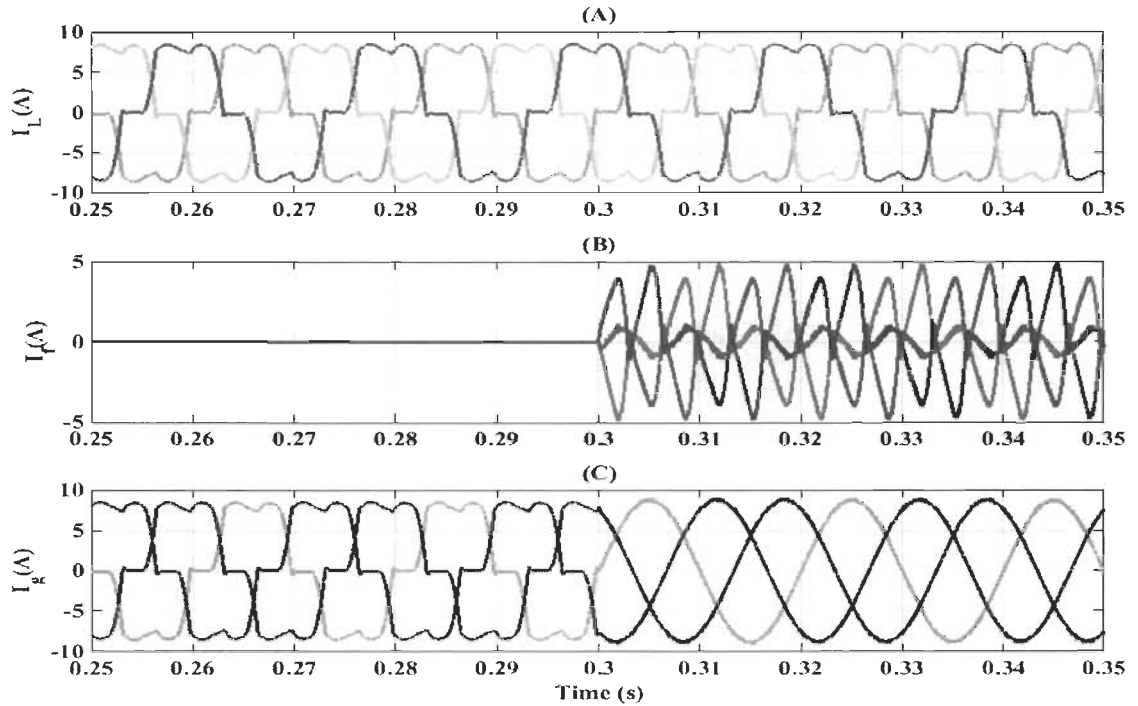


Figure 5-16 (A): Load current, (B): Compensating current (C): Grid current

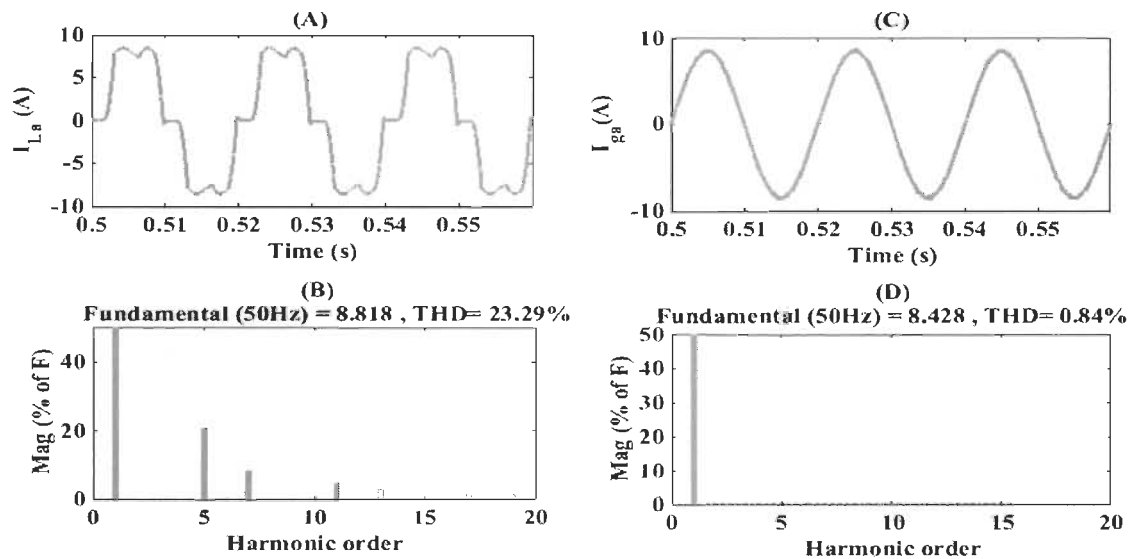


Figure 5-17 (A, B): Load current and its harmonic spectrum (C, D): Grid current, and its harmonic spectrum

The end user is modeled by a nonlinear load, for that, it draws a distorted current (Figure 5-16 (A)) where the THD is equal to 23% (Figure 5-17 (A, B)). At $t=0.3$ s the parallel part of the UPQC injects a compensating current (Figure 5-16 (B)). The intervention of the UPQC smooths the grid current (Figure 5-17 (C, D)) where the THD of grid current equal to 0.84%.

5.4.4 Performance analysis of D-STATCOM against unbalanced and neutral currents

This scenario is proposed to evaluate the behavior of D-STATCOM against the unbalanced nonlinear load. For that, only the shunt part of UPQC is operational. Figure 5-18 illustrates that the grid current is unbalanced and distorted as a side effect of the nonlinear and unbalanced loads. At $t=0.3$ s the D-STATCOM injects a compensating current as shown in Figure 5-19, resulting in the correction of trouble where the grid current is balanced and smoothly propagated (Figure 5-17).

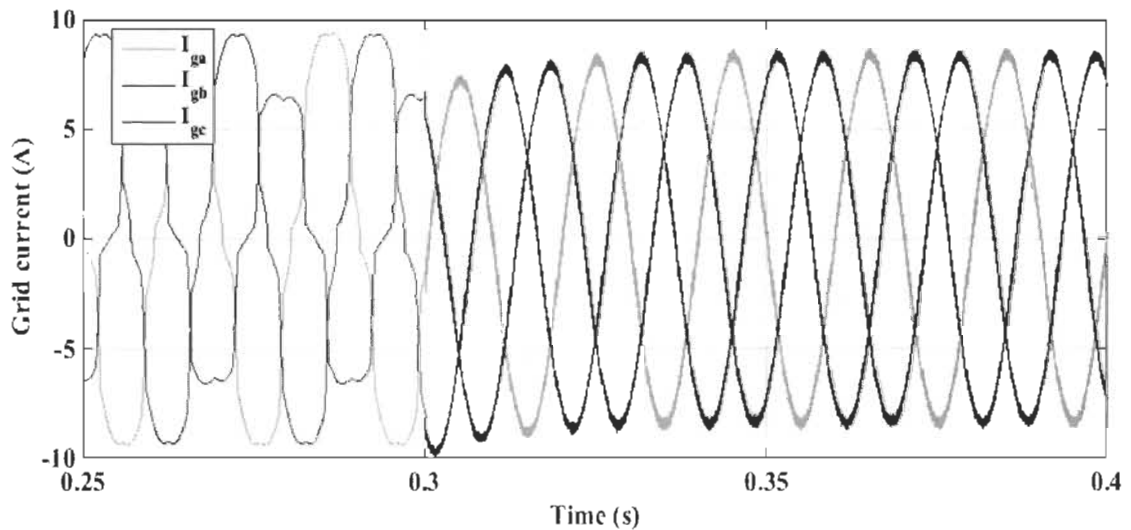


Figure 5-18 Grid current evolution with unbalanced load

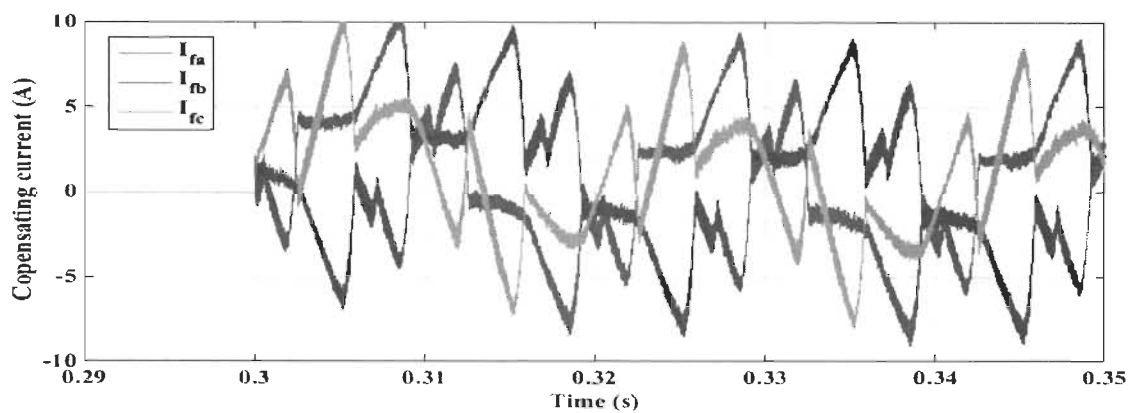


Figure 5-19 D-STATCOM output current

The proposed topology of D-STATCOM presented in Figure 5-1, also permits the elimination of the neutral current (Figure 5-20). The compensator injects a compensating current to the neutral line which is equal and against the load neutral current that prevents the propagation of this current to the grid. D-STATCOM proves its ability to compensate the reactive power consumed by the load and filtering the active power, as shown in Figure 5-21.

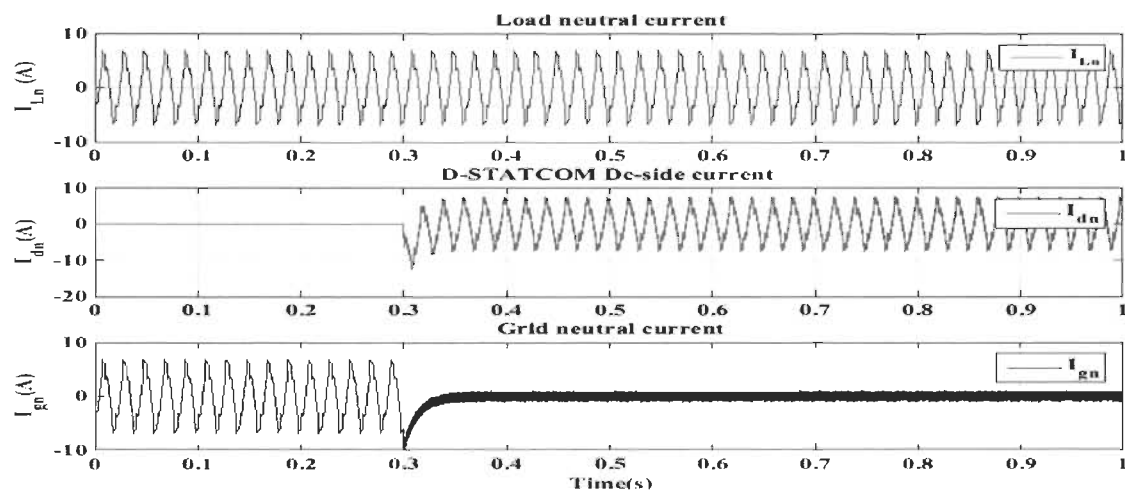


Figure 5-20 Load and grid neutral current evolution with D-STATCOM DC-side current

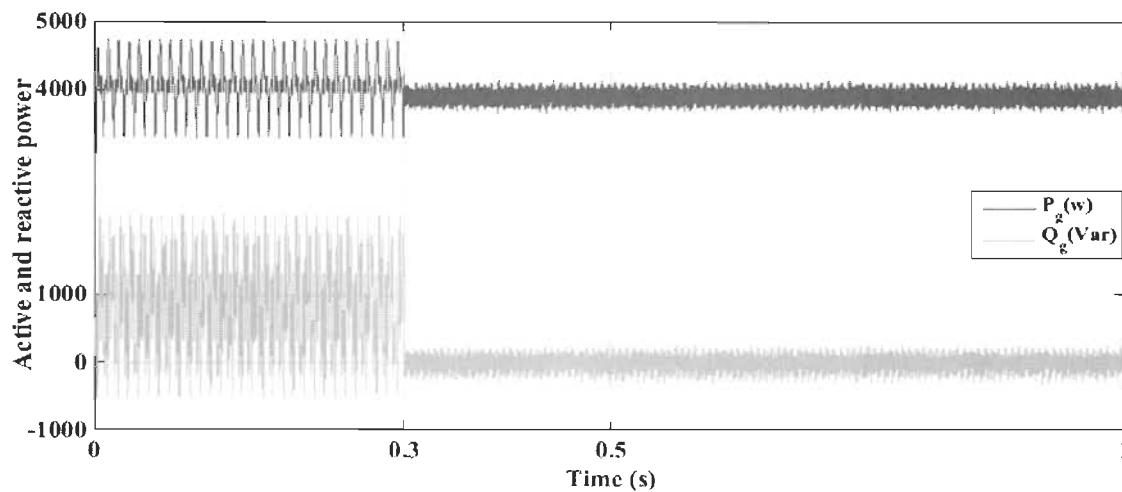
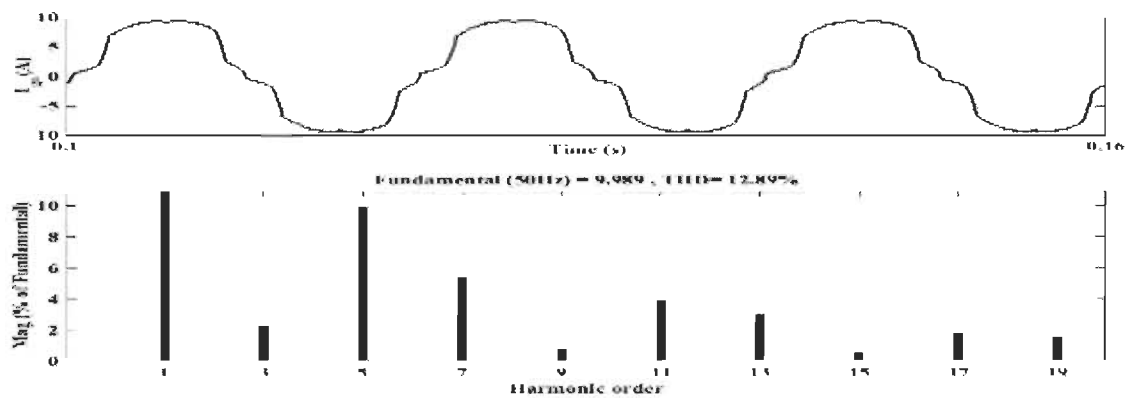
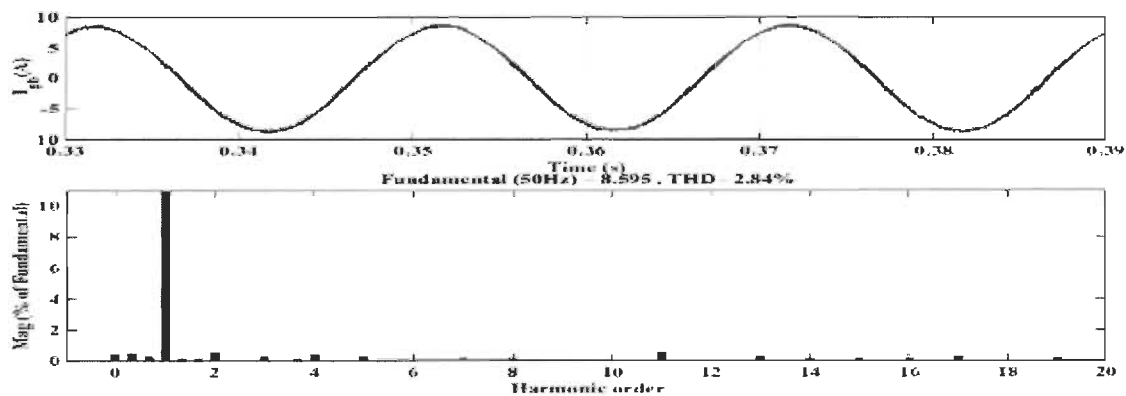


Figure 5-21 Grid active and reactive power

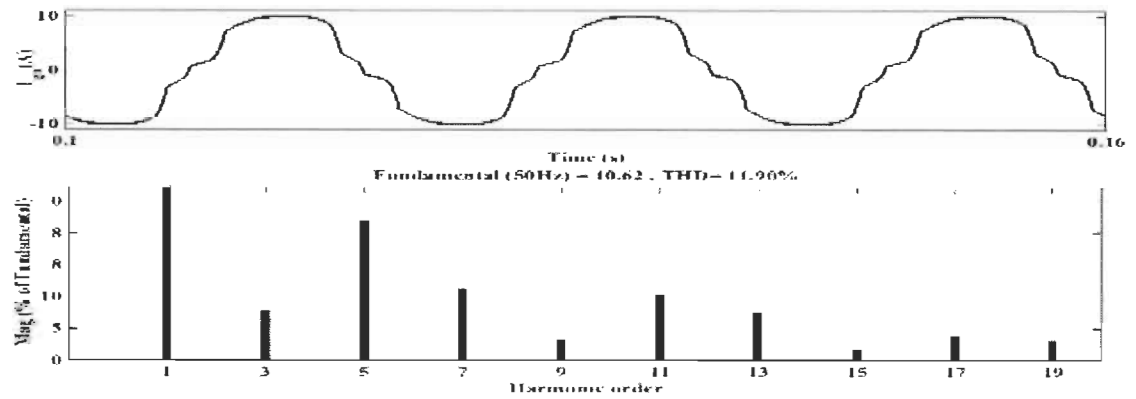


(A): Without D-STATCOM

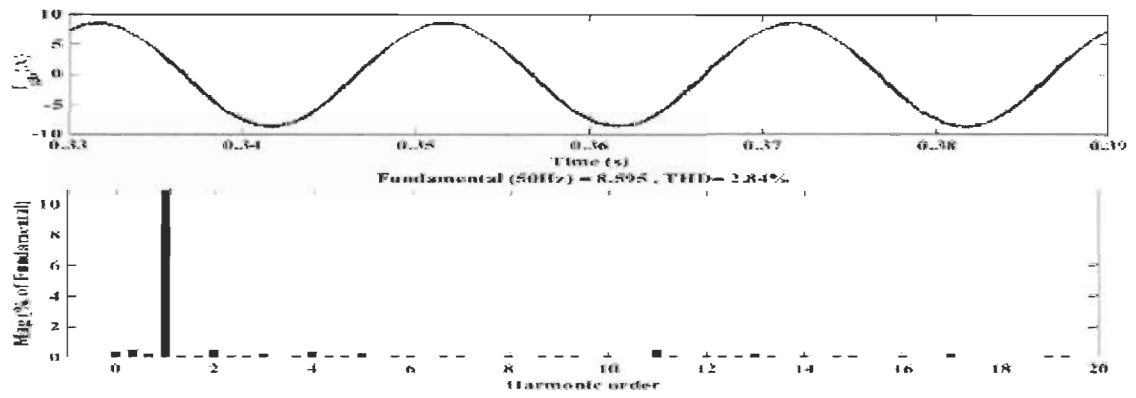


(B): With D-STATCOM

Figure 5-22 Grid current of phase A with and without D-STATCOM

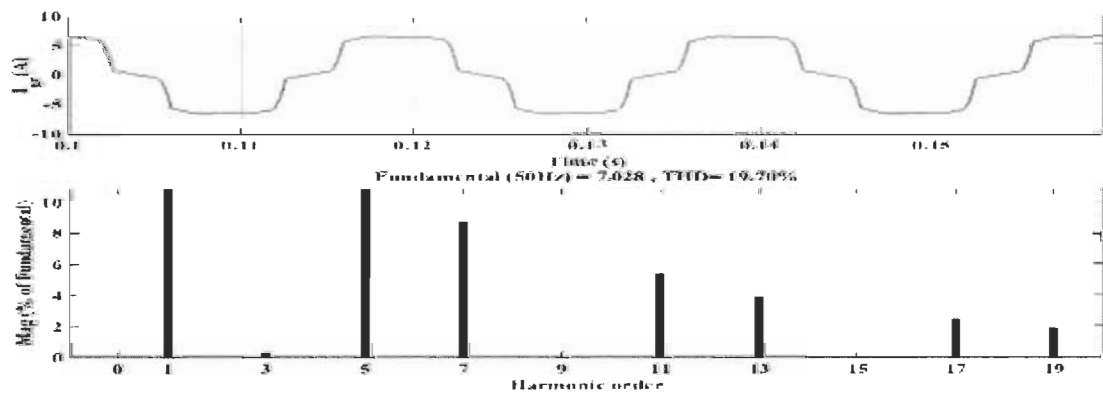


(C): Without D-STATCOM

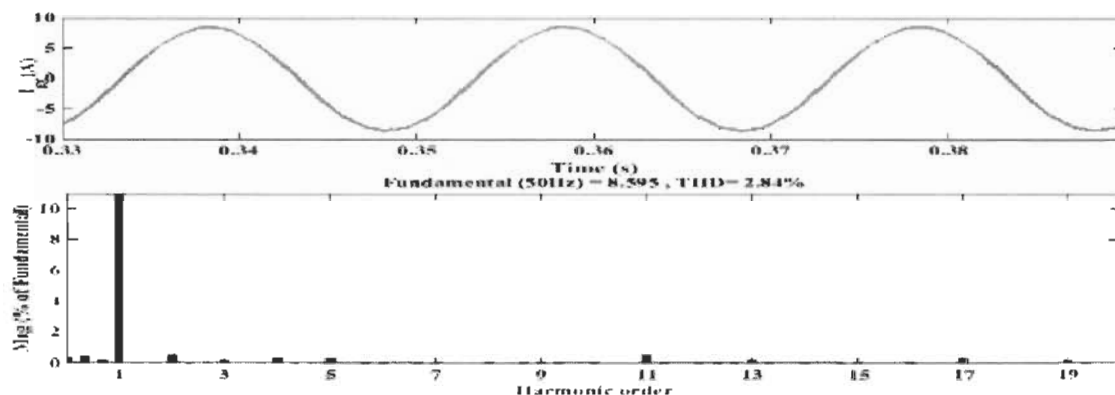


(D): With D-STATCOM

Figure 5-23 Grid current of phase B with and without D-STATCOM



(E): Without D-STATCOM



(F): With D-STATCOM

Figure 5-24 Grid current of phase C with and without D-STATCOM

Figure 5-22 to Figure 5-24 show the harmonic spectrum analysis of grid current for each phase with and without D-STATCOM. Figures illustrate that the presence of D-STATCOM limits harmonics under norms defined in IEEE-519.

5.5 Conclusion

This chapter extends our knowledge about the improvement of the power quality in the grid using Distributed Flexible AC Transmission Systems (D-FACTS). UPQC is the last generation of this category and it consists of two VSC connected back to back through a dc component. One of these VSCs is connected in series with grid and plays the role of DVR, while the other one plays the role of D-STATCOM and connected in shunt. The proposed control strategies allow the UPQC to mitigate all issues related to voltage using the DVR and issues related to current through D-STATCOM. It also allows the UPQC to supervise the active and reactive power flow in the grid. Moreover, we aim to evaluate the responsiveness and the performance of the UPQC in critical situations. A high performance has been noted in voltage sag/swell mitigation, balancing load voltage, filtering voltage distortion, balancing

of grid current and elimination of harmonics with preserving voltage and current values under IEEE-519 in all operating mode. The evaluation of the obtained results leads us to conclude that the proposed controller based on AFLC technique, ameliorates the behavior of the UPQC against power quality issues, compared to the linear controller proposed in the previous studies. The natural progression of this work is to investigate the performance of the UPQC in distributed renewable energy systems whether in the grid-tied operating mode.

Chapitre 6 - Performance improvement of SE-DSWIG using a MC-UPQC

6.1 Introduction

In wind power generation, D-FACTS proved their capability to be a good alternative for the enhancement of power quality and the mitigation of several power quality issues [151-153]. In [151], a static synchronous compensator (STATCOM) has been used to improve the ride-through of a grid connected DFIG during different faults conditions. A STATCOM connected in shunt between the grid and the grid side converter helps to suppress large surge currents induced by a sudden voltage collapse. In another case [27], Ahmad Osman Ibrahim et al. proposed a technique to enhance the low voltage ride through (LVRT) capability of DFIG connected to the grid using a dynamic voltage restorer (DVR). In [154], STATCOM has been used to control voltage and frequency of a self-excitation induction generator supplying an islanded microgrid. STATCOM shows high performance in controlling induction generators.

This thesis established a new topology of wind energy conversion systems based on self-excitation dual stator winding induction generator for simultaneous grid-tied and standalone application (Chapter 6). The idea of this strategy is built on the exploitation of D-FACTS for the enhancement of power quality and the improvement of low voltage ride through capability of the SE-DSWIG without mechanical turbine supervision. Hence, a multi-converter based unified power quality conditioner (MC-UPQC) is used to sustain the power flow and to mitigate faults. MC-UPQC involves three converters attached back-to-back through an energy storage system. Two of them are connected in series to the SE-DSWIG

terminals playing the role of DVR and dealt with all issues related to voltage, while the other converter acts as a D-STATCOM and connected in shunt to the stator terminal who is linked with the grid. A synchronous reference frame theory is used to supervise the series part of MC-UPQC, while an advanced cascade sliding mode control technique is applied to the shunt part.

6.2 Compact representation of SE-DSWIG mathematical equations

The mathematical modelling of SE-DSWIG is well presented in chapter 2, while the compact form is given by replacing the stator and rotor magnetic field by their equivalent in voltage equation. Then we obtain [64]:

$$[B][U] = [L][i] + (\omega_s - \omega_r)[C][I] + [D][I] \quad (6-1)$$

With

$$[U] = [V_{1sd} \ V_{1sq} \ V_{2sd} \ V_{2sq} \ 0 \ 0]^T \quad (6-2)$$

$$[I] = [I_{1sd} \ I_{1sq} \ I_{2sd} \ I_{2sq} \ I_{rd} \ I_{rq}]^T \quad (6-3)$$

And

$$[i] = \frac{d}{dt}[I] \quad (6-4)$$

$$[B] = \text{diag}[1 \ 1 \ 1 \ 1 \ 0 \ 0] \quad (6-5)$$

$[L]$, $[C]$ and $[D]$ are respectively given by the following matrices.

$$[L] = \begin{bmatrix} -(L_{s1} + L_{sdq}) & 0 & -L_{sdq} & 0 & L_m & 0 \\ 0 & -(L_{s1} + L_{sdq}) & 0 & -L_{sdq} & 0 & L_m \\ -L_{sdq} & 0 & -(L_{s2} + L_{sdq}) & 0 & L_m & 0 \\ 0 & -L_{sdq} & 0 & -(L_{s2} + L_{sdq}) & 0 & L_m \\ -L_m & 0 & -L_m & 0 & L_{lr} + L_m & 0 \\ 0 & -L_m & 0 & -L_m & 0 & L_{lr} + L_m \end{bmatrix}$$

$$[C] = \begin{bmatrix} 0 & 0 & 0 & 0 & 0 & 0 \\ 0 & 0 & 0 & 0 & 0 & 0 \\ 0 & 0 & 0 & 0 & 0 & 0 \\ 0 & 0 & 0 & 0 & 0 & 0 \\ 0 & L_m & 0 & L_m & 0 & L_{lr} + L_m \\ -L_m & 0 & -L_m & 0 & L_{lr} + L_m & 0 \end{bmatrix}$$

$$[D] = \begin{bmatrix} -R_{s1} & \omega_s(L_{s1} + L_{sq}) & 0 & \omega_s L_{sdq} & 0 & -\omega_s L_m \\ -\omega_s(L_{s1} + L_{sdq}) & -R_{s1} & -\omega_s L_{ld} & 0 & \omega_s L_m & 0 \\ 0 & \omega_s L_{sdq} & -R_{s2} & \omega_s(L_{s2} + L_{sdq}) & 0 & -\omega_s L_m \\ -\omega_s L_{sdq} & 0 & -\omega_s(L_{s2} + L_{sdq}) & -R_{s2} & \omega_s L_m & 0 \\ 0 & 0 & 0 & 0 & R_r & 0 \\ 0 & 0 & 0 & 0 & 0 & R_r \end{bmatrix}$$

With

$$L_{sdq} = L_{lm} + L_m \quad (6-6)$$

6.3 System under study with MC-UPQC

The scheme shown in Figure 6-1 is a wind power generation system, operates simultaneously in grid connected and standalone applications. It consists of SE-DSWIG connected to the grid through stator I and connected through stator II with a microgrid modeled by a variable load for standalone operation. An active compensator based MC-UPQC is inserted between the generator and the end-user to improve the power flow and mitigate power quality issues.

described in chapter 4, whereas the passive damping LCL filter design will be presented in the next subtitles.

6.3.1 Mathematical modeling of the proposed power system

The mathematical representation of the proposed power system in DQ – frame is given as follows:

- *Shunt branch of MC-UPQC (D-STATCOM)*

$$\begin{cases} L_{p1} \frac{d}{dt} I_{1gd} = (V_{cpd} - V_{1gd}) + \omega L_{p1} * I_{1gq} \\ L_{p1} \frac{d}{dt} I_{1gq} = (V_{cpq} - V_{1gq}) - \omega L_{p1} * I_{1gd} \end{cases} \quad (6-7)$$

$$\begin{cases} L_{p2} \frac{d}{dt} I_{2gd} = (V_{gd} - V_{2gd}) + \omega L_{p2} * I_{2gq} \\ L_{p2} \frac{d}{dt} I_{2gq} = (V_{gq} - V_{2gq}) - \omega L_{p2} * I_{2gd} \end{cases} \quad (6-8)$$

$$\begin{cases} C_p \frac{d}{dt} V_{cpd} = (I_{2gd} - I_{1gd}) + \omega C_p * V_{cpq} \\ C_p \frac{d}{dt} V_{cpq} = (I_{2gq} - I_{1gq}) - \omega C_p * V_{cpd} \end{cases} \quad (6-9)$$

- *Series branches of MC-UPQC (DVR-I and DVR-II) [135]*

$$\begin{cases} L_{d1} \frac{d}{dt} I_{se1d} = (V_{1sd} - V_{se1d} - V_{gd}) + \omega L_{d1} * I_{se1q} \\ L_{d1} \frac{d}{dt} I_{se1q} = (V_{1sq} - V_{se1q} - V_{gq}) - \omega L_{d1} * I_{se1d} \end{cases} \quad (6-10)$$

$$\begin{cases} L_{d2} \frac{d}{dt} I_{se2d} = (V_{2sd} - V_{se2d} - V_{ld}) + \omega L_{d2} * I_{se2q} \\ L_{d2} \frac{d}{dt} I_{se2q} = (V_{2sq} - V_{se2q} - V_{lq}) - \omega L_{d2} * I_{se2d} \end{cases} \quad (6-11)$$

6.3.2 Passive damping LCL filter design

The design of interfacing filters takes several aspects following norms imposed by IEEE-519 standards. For that we take into account the filter size, switching frequency, harmonic

current engendered by the compensator which should be less than 2 kHz [155]. The step by step LCL filter design procedure starts by the calculation of the based impedance and capacitance which are given by:

$$Z_b = \frac{V_s^2}{S_n} \quad (6-12)$$

$$C_B = \frac{1}{\omega_f * Z_b} \quad (6-13)$$

With V_s and S_n are respectively the line to line voltage RMS and apparent power rating of the SE-DSWIG.

The power factor is supposed to vary by 5% around the ideal value, for that the LCL-filter capacitance should be calculated as follows [156].

$$C_p = 0.05 * C_B \quad (6-14)$$

With the same way, the ripples induced by the D-STATCOM switches are supposed to be limited by the next equality.

$$I_{1g}^r = \frac{V_{dc}}{6 * f_s * L_{p1}} \quad (6-15)$$

Supposing that the current ripples at the output of D-STATCOM is equal to 10% of the nominal output current

$$I_{1g}^r = 10\% (I_{1g}) \quad (6-16)$$

In the other side, the nominal output current and the D-STATCOM side inductance are calculated respectively by equations (6-17) and (6-18) [156].

$$I_{1g} = \frac{S_n \sqrt{2}}{3 * V_{1g}} \quad (6-17)$$

$$L_{p1} = \frac{V_{dc}}{6f_s * I_{1g}^r} \quad (6-18)$$

With

$$L_{p2} = \rho * L_{p1} \quad (6-19)$$

ρ : the ratio between the LCL filter inductances, calculated in the following equation which is used to estimated the desired harmonic attenuation (δ_g) as next [155, 156].

$$\frac{I_{2g}^r}{I_{1g}^r} = \delta_g = \frac{1}{|1 + \rho * [1 - L_{p1} C_p (2\pi * f_s)^2]|} \quad (6-20)$$

The desired harmonic attenuation is assumed 20%.

The grid side inductance could be also calculated approximately by (6-21).

$$L_{p2} = \frac{\sqrt{\frac{1}{\delta_g^2} + 1}}{C_p * (2\pi * f_s)^2} \quad (6-21)$$

A resistance is inserted in series with the capacitance of the LCL filter to reduce the interaction between passive elements and to damp the resonance phenomenon.

$$R_p = \frac{1}{3 * \omega_r * C_p} \quad (6-22)$$

With

$$\omega_r = \sqrt{\frac{l_{in} + l_g}{l_{in} l_g C_f}} \quad (6-23)$$

The resonance frequency is calculated as:

$$f_r = \frac{1}{2\pi} \sqrt{\frac{L_{p2} + L_{p1}}{L_{p1} * L_{p2} * C_p}} \quad (6-24)$$

The damping LCL filter parameters are presented in Appendix E. The LCL bloc diagram is illustrated in Figure 6-2 [157].

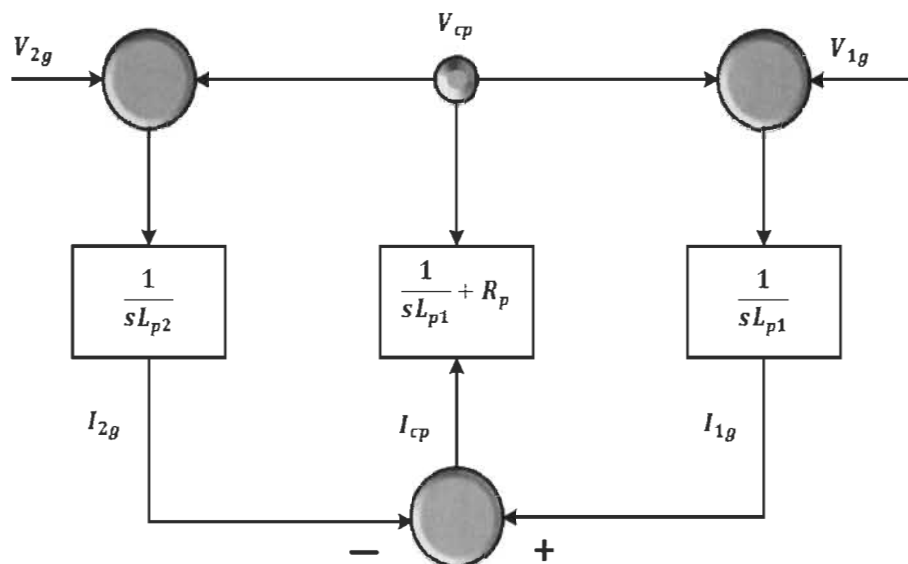


Figure 6-2 LCL-filter bloc diagram

The grid voltage is taken as an ideal source and replaced by short-circuit. Then, using Kirchhoff laws, the transfer function of the passive damping LCL-filter is given as follows [158].

$$\frac{I_{2g}}{V_{1g}} = \frac{SC_p R_p + 1}{(L_{p1}L_{p2}C_p)S^3 + C_p R_p (L_{p1} + L_{p2})S^2 + (L_{p1} + L_{p2})S} \quad (6-25)$$

$C_p R_p$ is too small and tends to zero so the transfer function becomes:

$$\frac{I_{2g}}{V_{1g}} = \frac{1}{(L_{p1}L_{p2}C_p)S^3 + (L_{p1} + L_{p2})S} \quad (6-26)$$

The frequency response of LCL filter with and without damping resistor is presented in Figure 6-3. The implementation of a resistor in series with the parallel component of the filter (C_f), damped the pick that appears around the resonance frequency f_r and smooths the global

response which tends to -180 degrees instead of -270 degrees. The system is stable in the presence of damping resistor and phase shift is around -90 degrees for closed loop bandwidth less than 1000 Hz.

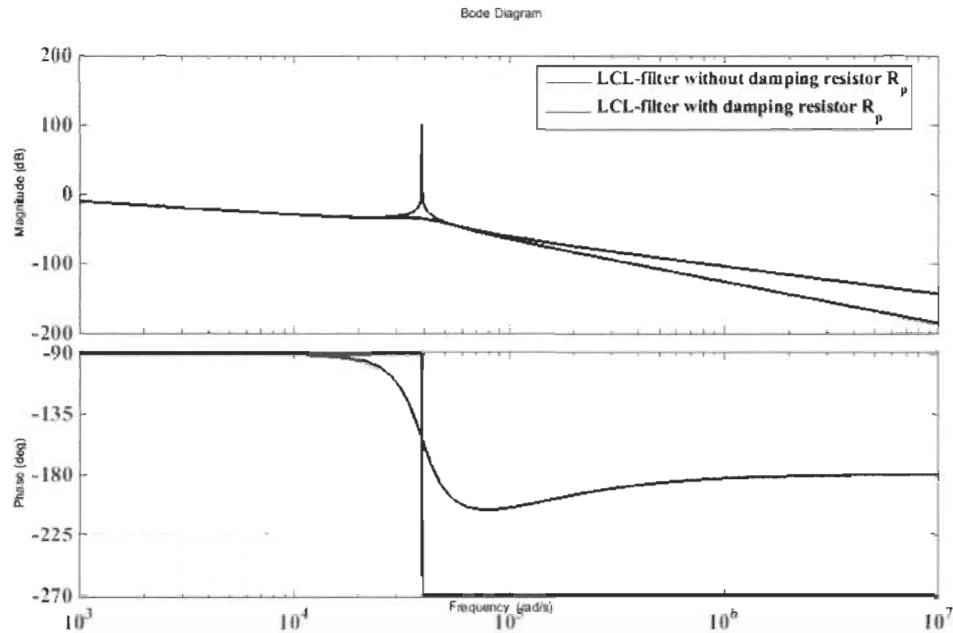


Figure 6-3 Frequency response of *LCL*-filter with and without damping resistor

6.4 Control system design

The trend toward developing a trustworthy energy road map based on wind turbines needs overcoming some burdens. The first one is the sensibility of the renewable resource in the presence of climatic change (wind speed variation), makes it unpredictable and doubtful to provide a sustainable energy. The second one is the poor voltage and frequency control during the peak demand and load variation. For that, we used power electronic devices based on MC-UPQC to overcome all issues cited above and to improve the low voltage ride through capability of the proposed power system. However, the complexity of the MC-UPQC requires the use of advanced control technique to bring more flexibility, efficiency, and fast

response. In this work, we proposed a control strategy based on a cascade sliding mode control technique applied D-STATCOM (parallel part of the MC-UPQC), while synchronous reference frame control technique is applied to the DVR-I and DVR-II (series side of the MC-UPQC). The D-STATCOM operates at the grid's frequency. A phase-locked loop (PLL) is used to extract the synchronizing angle to build the control algorithm. Meanwhile, both series parts of the MC-UPQC (DVR-I, DVR-II) operate in quadrature with the rotor flux where the frequency is estimated using direct vector control technique. The next subtitles consist of more details about the proposed control strategies.

6.4.1 D-STATCOM control

6.4.1.1 Challenges of D-STATCOM

D-STATCOM as a variable voltage source converter injects a lead/lag reactive current between the grid and SE-DSWIG to compensate the reactive power and decrease power quality issues related to current. In our case, D-STATCOM is connected through its dc-side with an energy storage system (ESS) which permits exchanging also the active power with the ac mains and generating a three-phase balanced voltage. The proposed topology gives the D-STATCOM the possibility to control the active and reactive power of the grid and shares with the DVR the burden of compensating voltage collapse and stabilizing frequency during fault conditions.

6.4.1.2 Cascade sliding mode controller design

Following the challenges entrusted, a robust control method is applied to the D-STATCOM based on sliding mode technique. It has a discrete and nonlinear behavior, acts as a good choice against parameters uncertainty, improves the control system performance

on an ideal level in terms of reference tracking and stability. The effectiveness of the proposed control technique is proved in previous works which encourages us to use it in our work [159, 160]. The sliding mode technique divide into a reaching and sliding mode as shown in Figure 6-4. It guides the controlled element from the initial conditions to the sliding manifold then tends asymptotically toward the steadiness point.

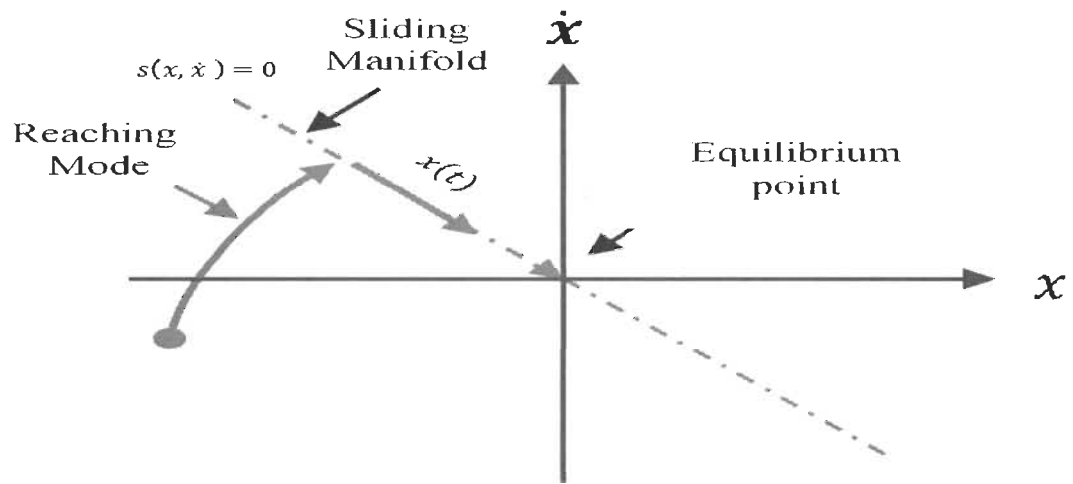


Figure 6-4 Sliding mode control process

To simplify the control algorithm applied on D-STATCOM, it has been divided into two loops. The inner loop named $L_{p1}C_p - loop$ while the outer loop is named $L_{p2} - loop$. The outer loop generates the input reference to the inner loop.

- *The inner loop*

From (6-9), we developed the following equations.

$$\begin{cases} I_{1gd} = I_{2gd} + \omega C_p * V_{cpq} - C_p \frac{d}{dt} V_{cpd} \\ I_{1gq} = I_{2gq} - \omega C_p * V_{cpq} - C_p \frac{d}{dt} V_{cpq} \end{cases} \quad (6-27)$$

Substituting I_{1gd} and I_{1gq} in (6-7), we obtain

$$\begin{cases} L_{p1} \frac{d(I_{2gd} + \omega C_p * V_{cpq} - C_p \frac{d}{dt} V_{cpd})}{dt} = (V_{cpd} - V_{1gd}) + \omega L_{p1} * I_{1gq} \\ L_{p1} \frac{d(I_{2gq} - \omega C_p * V_{cpq} - C_p \frac{d}{dt} V_{cpq})}{dt} = (V_{cpq} - V_{1gq}) - \omega L_{p1} * I_{1gd} \end{cases} \quad (6-28)$$

Doing mathematical calculations, we get the following:

$$\begin{cases} -L_{p1} C_p (V_{cpd}^{\ddot{}}) + L_{p1} (I_{2gd}^{\dot{}}) + \omega C_p L_{p1} V_{cpq}^{\dot{}} = (V_{cpd} - v_{1gd}) + \omega L_{p1} * I_{1gq} \\ -L_{s1} C_p (V_{cpq}^{\ddot{}}) + L_{p1} (I_{2gq}^{\dot{}}) + \omega C_p L_{p1} V_{cpd}^{\dot{}} = (V_{cpq} - v_{1gq}) - \omega L_{p1} * I_{1gd} \end{cases} \quad (6-29)$$

With \dot{X} is the first derivative

\ddot{X} : The second derivative

Replacing $C_f v_{cd}^{\dot{}}$ and $C_f v_{cq}^{\dot{}}$ with their corresponding values in (6-9) we get:

$$\begin{cases} -L_{p1} C_p (V_{cpd}^{\ddot{}}) + L_{p1} (I_{2gd}^{\dot{}}) + \omega L_{p1} (I_{2gq} - I_{1gq} - \omega C_p * V_{cpd}) = (V_{cpd} - V_{1gd}) + \omega L_{p1} * I_{1gq} \\ -L_{s1} C_p (V_{cfq}^{\ddot{}}) + L_{s1} (I_{2gq}^{\dot{}}) + \omega L_{s1} (I_{2gd} - I_{1gd} + \omega C_p * V_{cfq}) = (V_{cfq} - V_{1gq}) - \omega L_{s1} * I_{1gd} \end{cases} \quad (6-30)$$

Simplifying the (6-30) equation we obtain:

$$\begin{cases} -L_{s1} C_p (V_{cpd}^{\ddot{}}) = (\omega^2 L_{p1} C_p + 1) V_{cpd} - L_{p1} (I_{2gd}^{\dot{}}) - \omega L_{p1} I_{2gq} + 2 \omega L_{p1} I_{1gq} - V_{1gd} \\ -L_{s1} C_p (V_{cpq}^{\ddot{}}) = (\omega^2 L_{p1} C_p + 1) V_{cpq} - L_{p1} (I_{2gq}^{\dot{}}) + \omega L_{p1} I_{2gd} - 2 \omega L_{p1} I_{1gq} - V_{1gd} \end{cases} \quad (6-31)$$

assuming the following equality:

$$\begin{cases} E_d = V_{1gd} + L_{p1} (I_{2gd}^{\dot{}}) + \omega L_{p1} I_{2gq} - 2 \omega L_{p1} I_{1gq} \\ E_q = V_{1gq} + L_{p1} (I_{2gq}^{\dot{}}) + \omega L_{p1} I_{2gd} + 2 \omega L_{p1} I_{1gd} \end{cases} \quad (6-32)$$

And,

$$\begin{cases} \frac{d}{dt} V_{cpd} = U_{cd} \\ \frac{d}{dt} V_{cpq} = U_{cq} \end{cases} \quad (6-33)$$

We obtain the state equation of the inner loop:

$$\frac{d}{dt} \begin{bmatrix} U_{cd} \\ U_{cq} \end{bmatrix} = \begin{bmatrix} -\frac{(\omega^2 L_{p1} C_{p+1})}{L_{p1} C_p} & 0 \\ 0 & -\frac{(\omega^2 L_{p1} C_{p+1})}{L_{p1} C_p} \end{bmatrix} \begin{bmatrix} V_{cpd} \\ V_{cpq} \end{bmatrix} + \frac{1}{L_{p1} C_p} \begin{bmatrix} E_d \\ E_q \end{bmatrix} \quad (6-34)$$

The application of the sliding mode control starts by selecting of the sliding surfaces defined by (6-35).

$$\begin{cases} S(U_{cd}) = U_{cdref} - U_{cd} \\ S(U_{cq}) = U_{cqref} - U_{cq} \end{cases} \quad (6-35)$$

After the derivation we get:

$$\begin{cases} \dot{S}(U_{cd}) = \dot{U}_{cdref} - \dot{U}_{cd} \\ \dot{S}(U_{cq}) = \dot{U}_{cqref} - \dot{U}_{cq} \end{cases} \quad (6-36)$$

Substituting \dot{U}_{cd} , \dot{U}_{cq} by there equivalents we obtain:

$$\begin{cases} \dot{S}(U_{cd}) = \dot{U}_{cdref} - \left(-\frac{(\omega^2 L_{p1} C_{p+1})}{L_{p1} C_p} V_{cpd} + \frac{1}{L_{p1} C_p} E_d\right) \\ \dot{S}(U_{cq}) = \dot{U}_{cqref} - \left(-\frac{(\omega^2 L_{p1} C_{p+1})}{L_{p1} C_p} V_{cpq} + \frac{1}{L_{p1} C_p} E_q\right) \end{cases} \quad (6-37)$$

Then

$$\begin{cases} E_d = E_{deq} + E_{dn} \\ E_q = E_{qeq} + E_{qn} \end{cases} \quad (6-38)$$

Equation (6-35) would be represented as follows:

$$\begin{cases} \dot{S}(U_{cd}) = \dot{U}_{cdref} - \left(-\frac{(\omega^2 L_{p1} C_{p+1})}{L_{p1} C_p} V_{cpd} + \frac{1}{L_{p1} C_p} (E_{deq} + E_{dn})\right) \\ \dot{S}(U_{cq}) = \dot{U}_{cqref} - \left(-\frac{(\omega^2 L_{p1} C_{p+1})}{L_{p1} C_p} V_{cpq} + \frac{1}{L_{p1} C_p} (E_{qeq} + E_{qn})\right) \end{cases} \quad (6-39)$$

On the sliding surface $S(U_{cd}) = 0$, $\dot{S}(U_{cd}) = 0$, $U_{dn} = 0$, $E_{dn} = 0$ which implies the next:

$$\begin{cases} U_{cdref} \dot{-} - \left(-\frac{(\omega^2 L_{p1} C_p + 1)}{L_{p1} C_p} V_{cpd} + \frac{1}{L_{p1} C_p} (E_{deq}) \right) = 0 \\ U_{cqref} \dot{-} - \left(-\frac{(\omega^2 L_{p1} C_p + 1)}{L_{p1} C_p} V_{cpq} + \frac{1}{L_{p1} C_p} (E_{deq}) \right) = 0 \end{cases} \quad (6-40)$$

After mathematical simplifications, we get:

$$\begin{cases} E_{deq} = L_{p1} * U_{cdref} + (\omega^2 L_{s1} C_p + 1) V_{cpd} \\ E_{qeq} = L_{p1} * U_{cqref} + (\omega^2 L_{s1} C_p + 1) V_{cpq} \end{cases} \quad (6-41)$$

On the sliding manifold and during the convergence mode, the following equality should be verified to get the equilibrium.

$$\begin{cases} S(U_{cd}) \dot{S}(U_{cd}) < 0 \\ S(U_{cq}) \dot{S}(U_{cq}) < 0 \end{cases} \quad (6-42)$$

Substituting (6-40) in (6-39), we get:

$$\begin{cases} \dot{S}(U_{cd}) = \frac{1}{L_{p1} C_p} E_{dn} \\ \dot{S}(U_{cq}) = \frac{1}{L_{p1} C_p} E_{qn} \end{cases} \quad (6-43)$$

From (6-36), E_{dn} and E_{qn} are estimated by the next:

$$\begin{cases} E_{dn} = \sigma_d \text{sign}(S(U_{cd})) \\ E_{qn} = \sigma_q \text{sign}(S(U_{cq})) \end{cases} \quad (6-44)$$

Replacing (6-42) in (6-36):

$$\begin{cases} E_d = L_{p1} * U_{cdref} + (\omega^2 L_{p1} C_p + 1) V_{cpd} + \sigma_d \text{sign}(S(U_{cd})) \\ E_q = L_{p1} * U_{cqref} + (\omega^2 L_{p1} C_p + 1) V_{cpq} + \sigma_q \text{sign}(S(U_{cq})) \end{cases} \quad (6-45)$$

A saturation function is used instead of sign function to reduce the chattering phenomena represented by the following function and depicted in Figure 6-5.

$$A_{(d,q)} = \text{sat}(S(U_{c(d,q)})) = \begin{cases} \sigma_{(d,q)} \text{sign} S(U_{c(d,q)}), & |S(U_{c(d,q)})| > \xi \\ \frac{\sigma_{(d,q)}}{\xi} \text{sign} S(U_{c(d,q)}), & |S(U_{c(d,q)})| < \xi \end{cases} \quad (6-46)$$

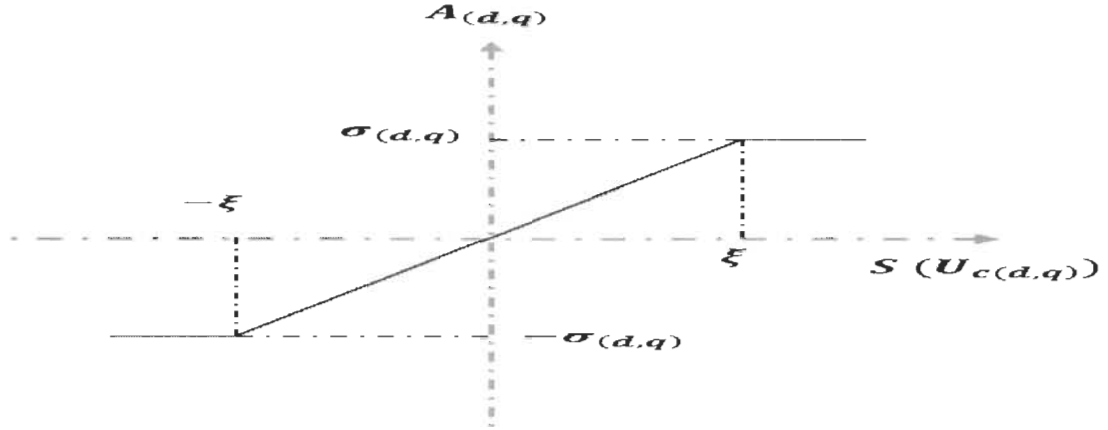


Figure 6-5 Saturation function

- *The outer loop*

The sliding mode is also applied on the outer loop which will be used to generate a specific voltage reference for the internal loop. For the space limitation, we will mention just headnotes for the application of the SMC in the outer loop. Supposing the grid side inductance has an internal resistance named R , the (6-8) equation system becomes:

$$\frac{d}{dt} \begin{bmatrix} I_{2gd} \\ I_{2gq} \end{bmatrix} = \begin{bmatrix} -\frac{R}{L_{p2}} & 0 \\ 0 & -\frac{R}{L_{p2}} \end{bmatrix} \begin{bmatrix} I_{2gd} \\ I_{2gq} \end{bmatrix} + \frac{1}{L_{p2}} \begin{bmatrix} I_d \\ I_q \end{bmatrix} \quad (6-47)$$

With:

$$\begin{cases} I_d = (V_{2gd} - V_{cpd}) + \omega L_{p2} * I_{2gq} \\ I_q = (V_{2gq} - V_{cpq}) - \omega L_{p2} * I_{2gd} \end{cases} \quad (6-48)$$

In this case, the sliding surfaces are given as the next:

$$\begin{cases} S(I_d) = I_{dref} - I_d \\ S(I_q) = I_{qref} - I_q \end{cases} \quad (6-49)$$

after mathematical calculation, we get:

$$\begin{cases} I_d = L_{p2} \dot{I}_{2gdref} + RI_{2gd} + K_q \text{Sign}(S(I_{2gd})) \\ I_q = L_{p2} \dot{I}_{2gqref} + RI_{2gq} + K_q \text{Sign}(S(I_{2gq})) \end{cases} \quad (6-50)$$

I_{2gdref} and I_{2gqref} are estimated based on the instantaneous active and reactive power theory given by:

$$\begin{pmatrix} I_{2gdref} \\ I_{2gqref} \end{pmatrix} = \frac{3}{2} \frac{1}{V_{gd}^2 + V_{gq}^2} \begin{pmatrix} P_g^* & Q_g^* \\ -Q_g^* & P_g^* \end{pmatrix} \begin{pmatrix} V_{gd} \\ V_{gq} \end{pmatrix} \quad (6-51)$$

The full control scheme applied on the parallel part of the MC-UPQC is depicted in Figure 6-6.

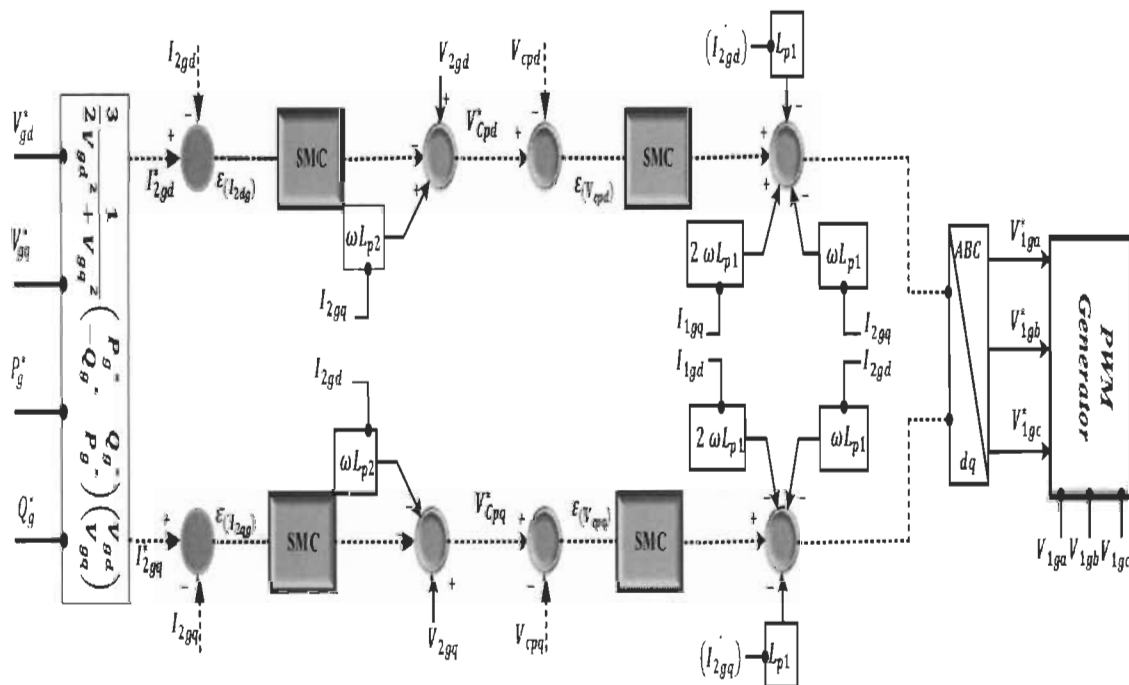


Figure 6-6 Control scheme applied on D-STATCOM

6.4.2 Control of Dynamic Voltage Restorer (DVR-I, DVR-II)

6.4.2.1 Estimation of the synchronizing unit vector

In this thesis, the series part of MC-UPQC operates on the same frequency of the rotor. For that, a direct vector control technique had been used to extract phase angle of the rotor flux as proposed in [34]. From the stator flux equations (3-7), (3-8), we extract the direct and quadratic components of the rotor current:

$$\begin{cases} I_{rd} = \frac{1}{L_m}(\varphi_{1sd} + (L_m + L_{lm} + L_{s1})I_{1sd} + (L_m + L_{lm})I_{2sd}) \\ I_{rq} = \frac{1}{L_m}(\varphi_{1sq} + (L_m + L_{lm} + L_{s1})I_{1sq} + (L_m + L_{lm})I_{2sq}) \end{cases} \quad (6-52)$$

Replacing I_{rd} and I_{rq} with their corresponding equalities respectively in (3-11) and (3-12), after mathematical simplification we get:

$$\begin{cases} \varphi_{rd} = A_d * \varphi_{1sd} + B_d * i_{1sd} + C_d * i_{2sd} \\ \varphi_{rq} = A_q * \varphi_{1sq} + B_q * i_{1sq} + C_q * i_{2sq} \end{cases} \quad (6-53)$$

With

$$\begin{cases} A_d = \frac{L_{lr} + L_{md}}{L_{md}} \\ B_d = \left[\left(\frac{L_{lr} + L_{md}}{L_{md}} \right) (L_{md} + L_{lm} + L_{l1}) - L_{md} \right] \\ C_d = \left[\left(\frac{L_{lr} + L_{md}}{L_{md}} \right) (L_{md} + L_{lm}) - L_{md} \right] \end{cases} \quad (6-54)$$

$$\begin{cases} A_q = \frac{L_{lr} + L_{mq}}{L_{mq}} \\ B_q = \left[\left(\frac{L_{lr} + L_{mq}}{L_{mq}} \right) (L_{mq} + L_{lm} + L_{l1}) - L_{mq} \right] \\ C_q = \left[\left(\frac{L_{lr} + L_{mq}}{L_{mq}} \right) (L_{mq} + L_{lm}) - L_{mq} \right] \end{cases} \quad (6-55)$$

And with

$$\begin{cases} \varphi_{1sd} = \int (v_{1sd} + R_{s1}i_{1sd} + \omega_s \varphi_{1sq}) dt \\ \varphi_{1sq} = \int (v_{1sq} + R_{s1}i_{1sq} - \omega_s \varphi_{1sd}) dt \end{cases} \quad (6-56)$$

The synchronizing sine and cosine units are given by the following [34]:

$$\begin{cases} \cos \delta_r = \frac{\varphi_{rd}}{\sqrt{\varphi_{rd}^2 + \varphi_{rq}^2}} \\ \sin \delta_r = \frac{\varphi_{rq}}{\sqrt{\varphi_{rd}^2 + \varphi_{rq}^2}} \end{cases} \quad (6-57)$$

The full synchronizing sine and cosine estimation block diagram is depicted in Figure 6-7.

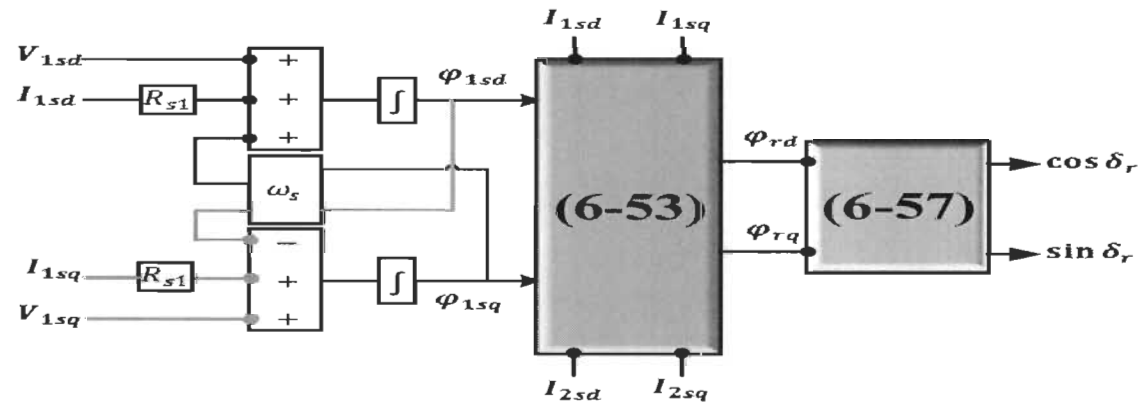


Figure 6-7 Sine and cosine estimating block diagram

6.4.2.2 Description of the SRF Control Theory applied to DVR

In wind power generation, the voltage sag/swell, collapse, and disturbance are due to the variation of the prime mover of the turbine, severe change in load impedance, grid fault and peak time demand. In our case, both DVR-I and DVR-II have the same task which is compensating all issues related to voltage. To achieve this purpose, we supervise the behavior of DVR-I and DVR-II using a synchronous reference frame (SRF) theory based PI control technique. For the space limitations we will notice the application only on DVR-II and the

same thing will be done with DVR-I. Using equation (6-11), we observe that the compensating voltage is estimated as follows:

$$\begin{cases} V_{se2d} = V_{2sd} - V_{ld} \\ V_{se2q} = V_{2sq} - V_{lq} \end{cases} \quad (6-58)$$

The load voltage amplitude is calculated through the following equation:

$$V_l^* = V_{ld}^* = \sqrt{2 * (V_{la}^2 + V_{lb}^2 + V_{lc}^2)} \quad (6-59)$$

Basically, the idea of this control technique is built up on the comparison between the load voltage in real time and its reference, afterward; we make a comparison between the load voltage and the output voltage of the generator. Figure 6-8 summarizes the proposed control technique applied to the series part of the MC-UPQC.

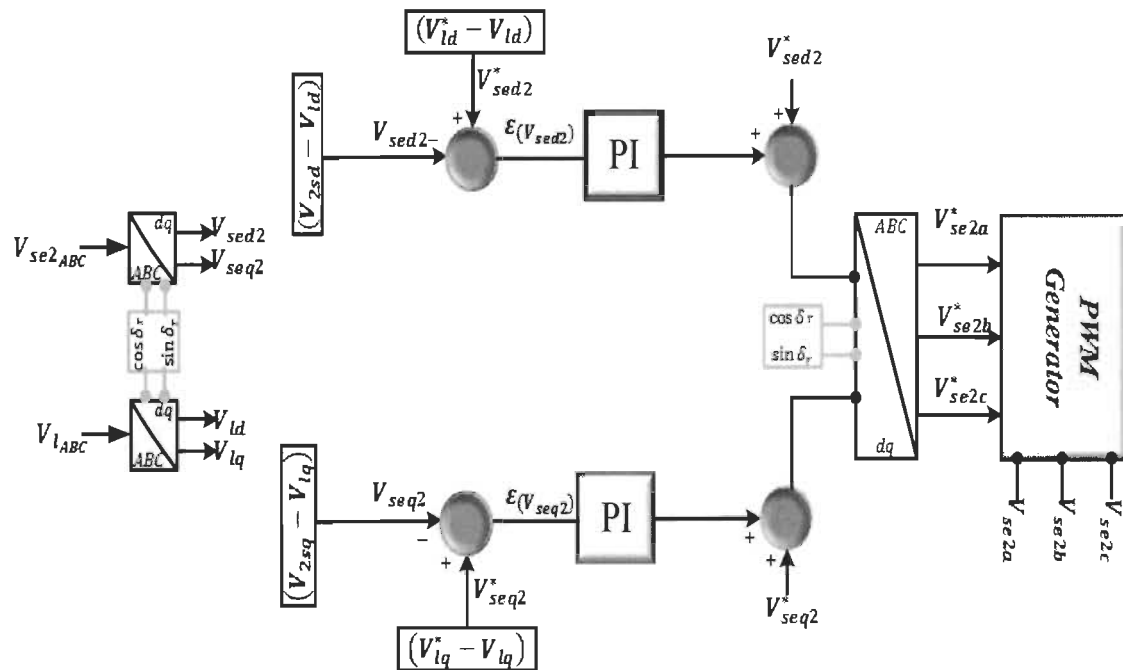


Figure 6-8 Control scheme applied DVR-I and DVR-II

6.5 Numeric results and analysis

In the aim to inspect the performance and the accuracy of the system under study, an extensive model of a 1.5MW SE-DSWIG and a MC-UPQC had been performed in Matlab®/SimPowerSystems. The proposed power system was exposed to several events in terms of voltage disturbance, wind and load variation besides grid faults to evaluate the effectiveness of the MC-UPQC and responsiveness of the control strategy. Parameters used in this work are presented in the Appendix E.

6.5.1 Characteristics of SE-DSWIG in off-grid and at no-load conditions

Figure 6-9, Figure 6-10 and Figure 6-11, show the SE-DSWIG characteristics evolution. Starting from zero speed, voltage and current stepped up exponentially till reaching the steady state at $t=2.5s$ with 220V and 19A, in which the SE-DSWIG gets the saturation.

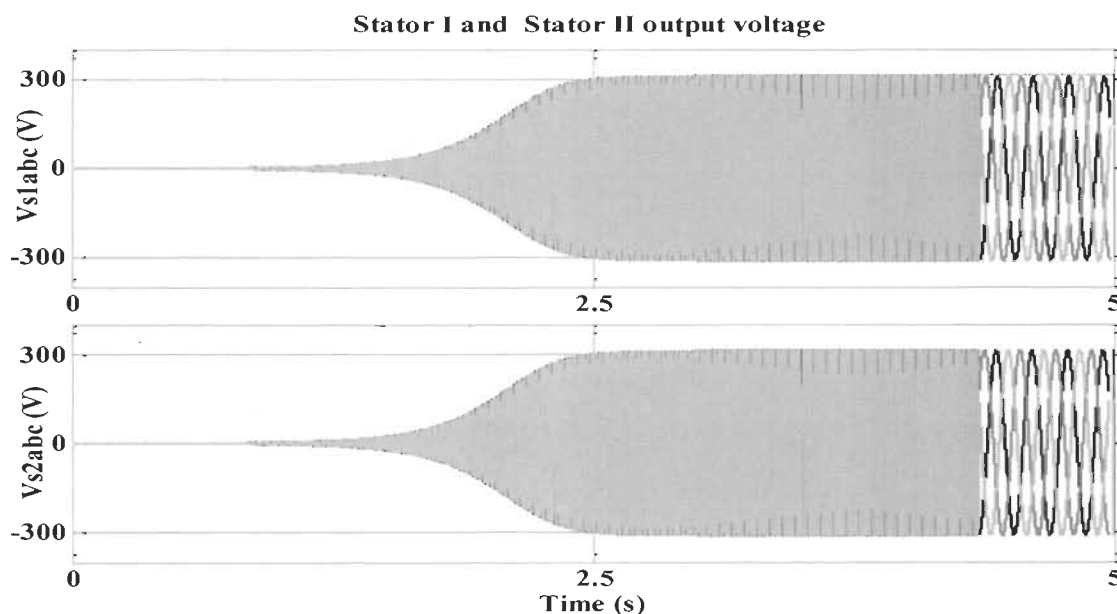


Figure 6-9 SE-DSWIG output voltage

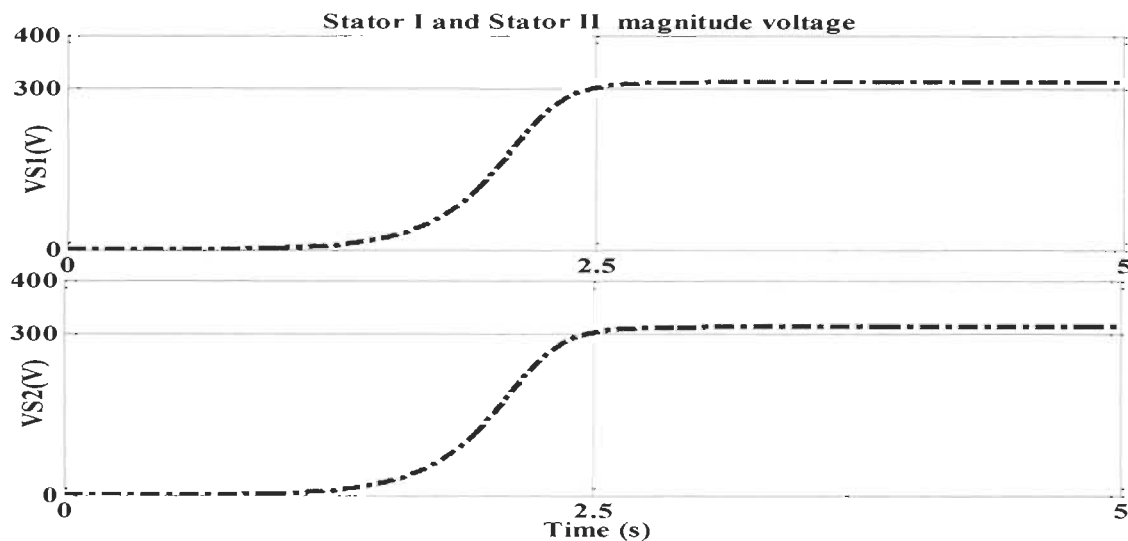


Figure 6-10 Voltage magnitude evolution

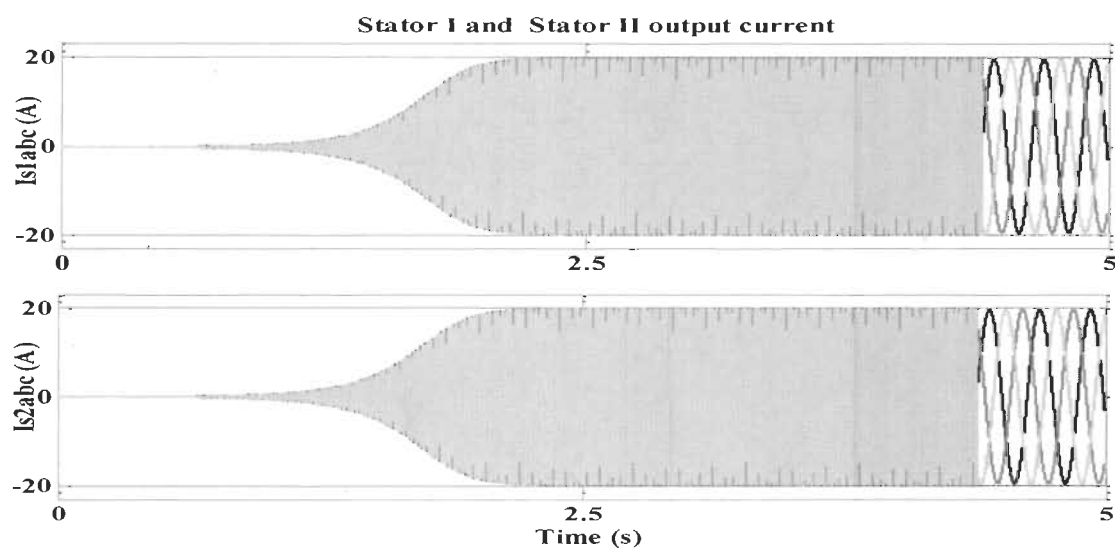


Figure 6-11 SE-DSWIG output current

6.5.2 SE-DSWIG performance in variable speed with non-compensator

In these cases, we explored the impact of speed variation on the evolution of the output voltage and end user frequency in both stand alone and grid-connected operation modes. In the beginning, the SE-DSWIG was driven by the nominal speed, then it was exposed to speed

variation going between 280 rad/s and 314 rad/s (Figure 6-12). Both the frequency and voltage are affected by this variation (Figure 6-13), which confirm the good operation of the compensator.

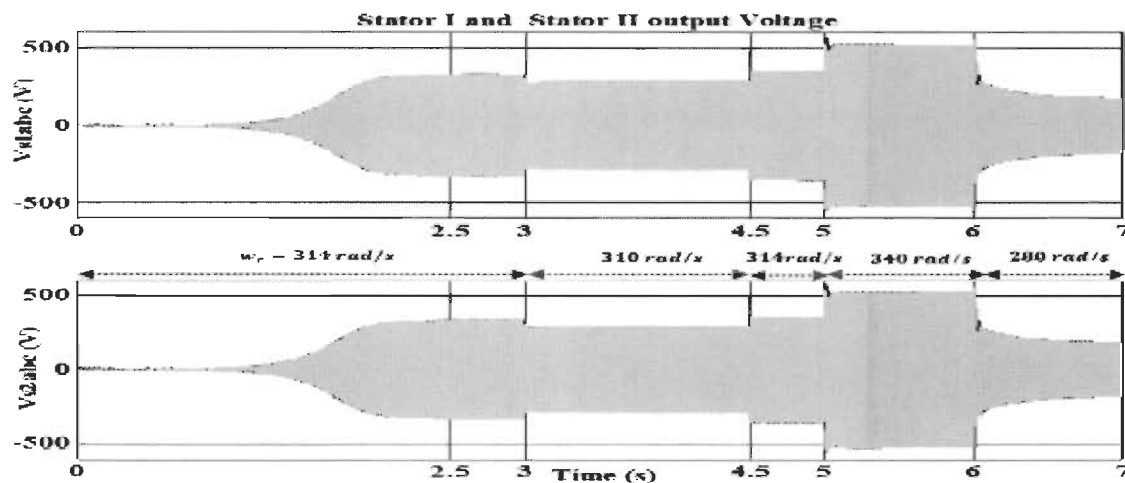


Figure 6-12 SE-DSWIG output voltage in speed variation

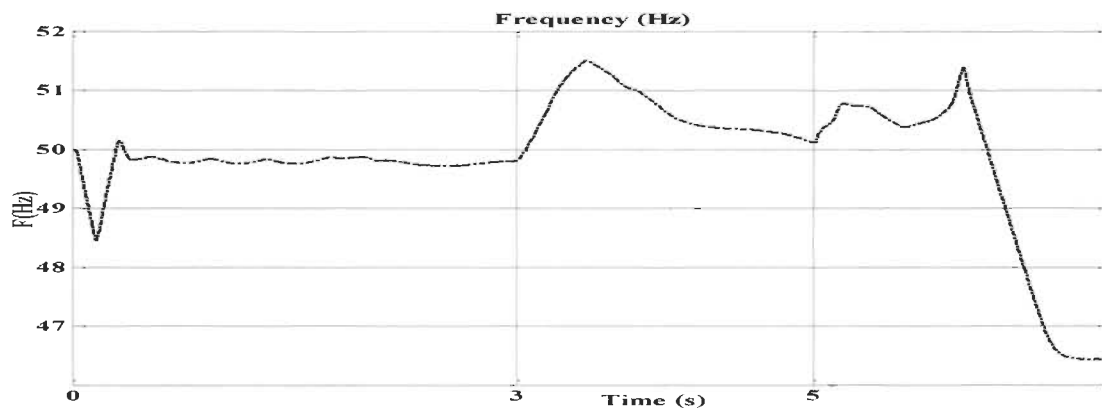


Figure 6-13 Frequency profile in variable speed

6.5.3 SE-DSWIG performance in variable speed with MC-UPQC

In this case, we investigate the behavior DVR-I and DVR-II in the presence of voltage disturbance. For that, at $t=3\text{s}$ the rotor speed was decreased from 314 rad/s to 300 rad/s

inducing a voltage sag (30% of nominal value). In $t=4.5$ s the series part of the MC-UPQC generates a series voltage shifted by a specific angle against the grid voltage (Figure 6-15) resulting in the elimination of the sag event as shown in (Figure 6-14).

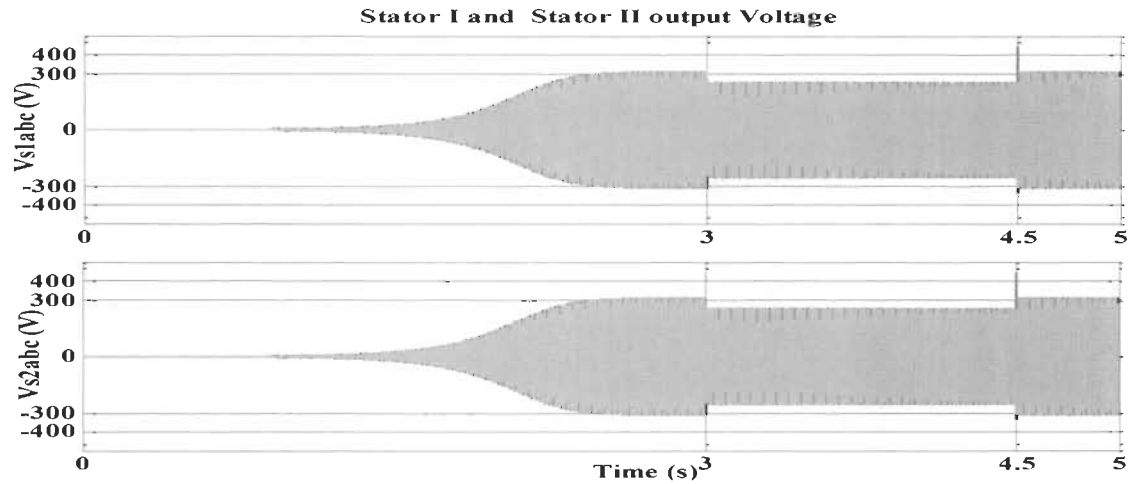


Figure 6-14 Output voltage in variable speed

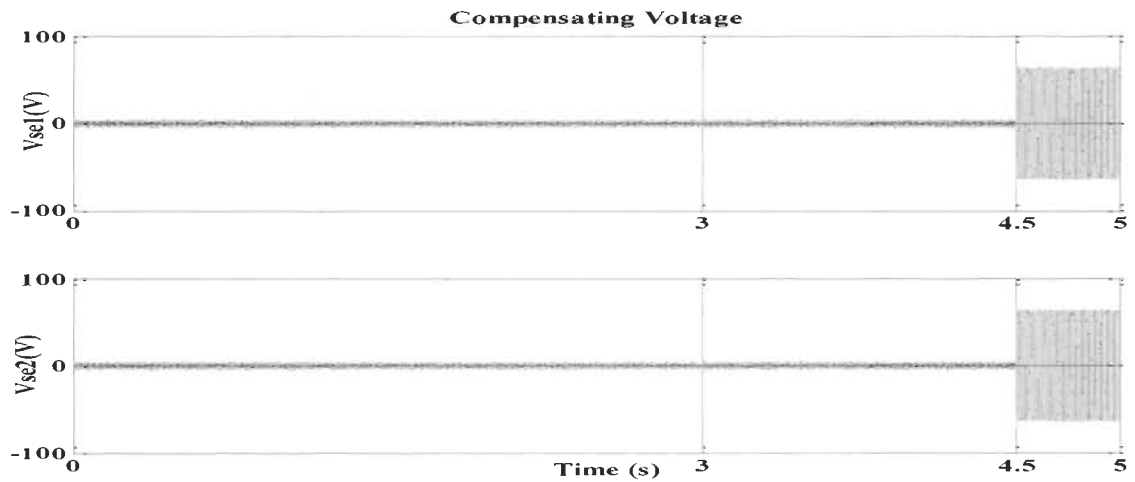


Figure 6-15 Compensating voltage generated by DVR-I and DVR-II

6.5.4 SE-DSWIG performance in standalone application with variable load

Here, the SE-DSWIG operates in standalone application with fixed speed and variable load. At $t=3$ s A resistive load equal to 600Ω is connected which creates a voltage sag by

34% of the nominal voltage and at $t=5s$ another load of $700\ \Omega$ is connected inducing a sag of 50% (Figure 6-16). In the presence of MC-UPQC, DVR-II injects a compensating voltage equal to 75V at $t=3s$ and equal to 110V at $t=5s$ (Figure 6-17), then the voltage at the PCC remains at the nominal value equal to $V_l = 220V$ (Figure 6-18).

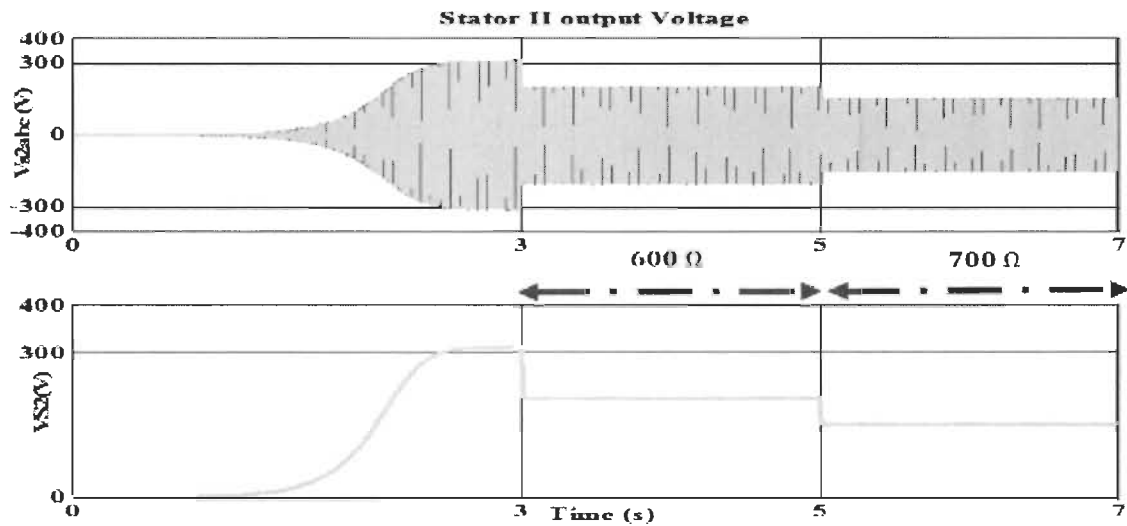


Figure 6-16 Stator II output voltage

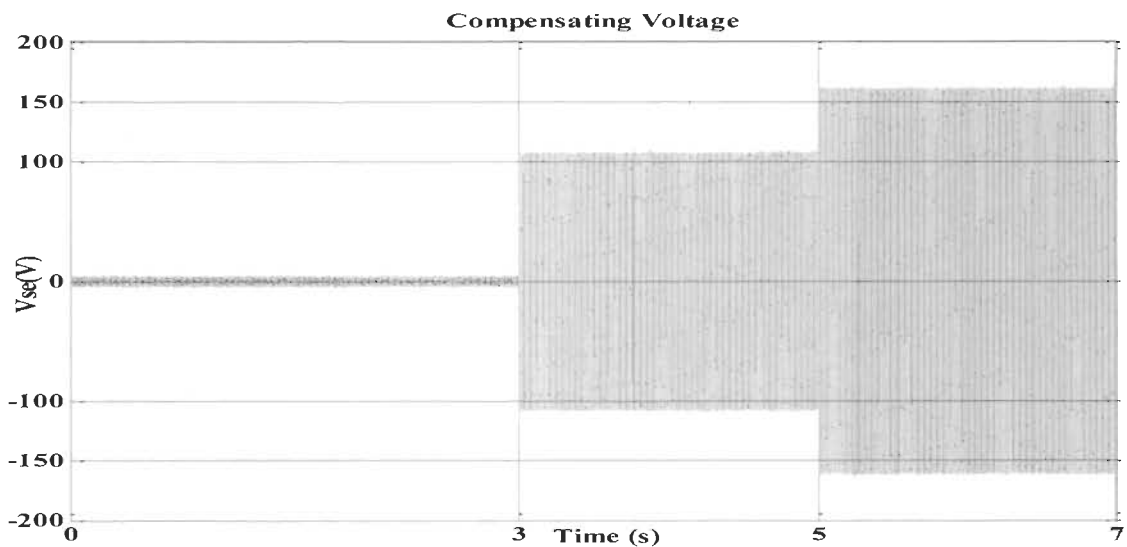


Figure 6-17 Compensating voltage

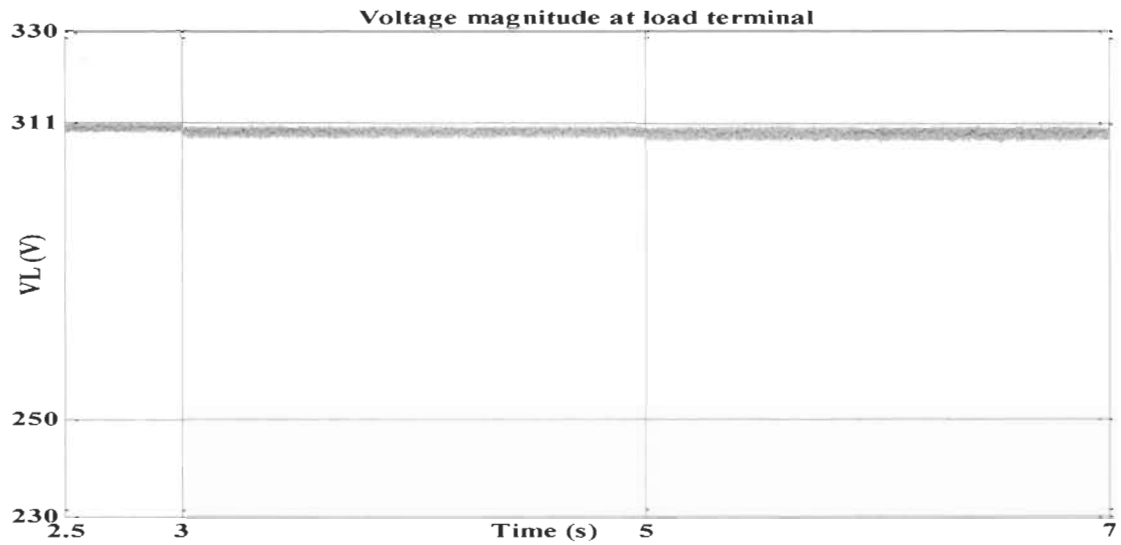


Figure 6-18 Load terminal voltage

6.5.5 SE-DSWIG performance in grid connected conditions

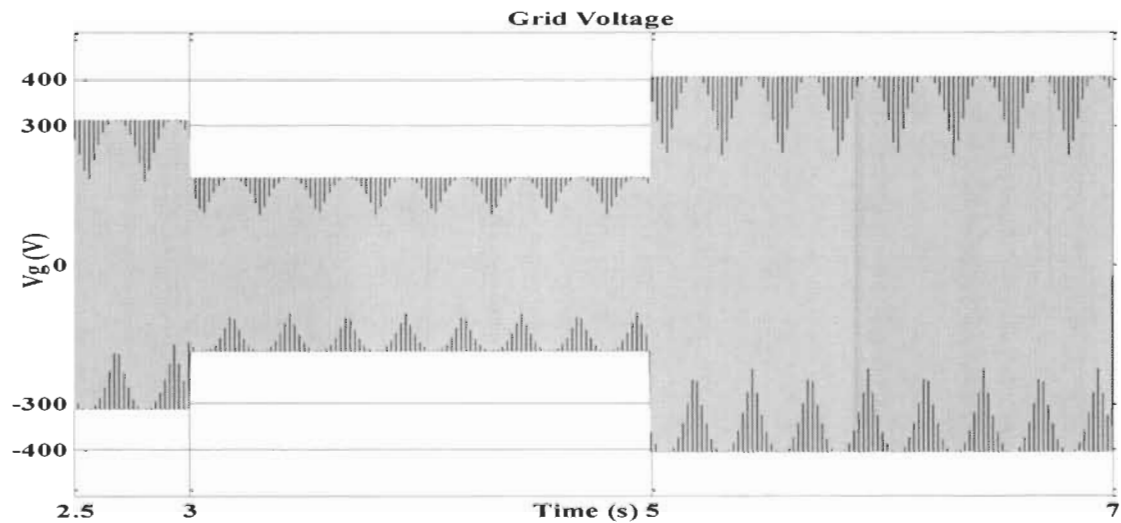


Figure 6-19 Grid voltage sag and swell

In this case, the SE-DSWIG is connected directly to the grid while a fault scenario is occurred causing voltage sag and swell as depicted in Figure 6-19, and disturbance in the grid frequency (Figure 6-20). In the presence of MC-UPQC, the DVR-1 generates a

compensating voltage to mitigate the sag and swell as shown in Figure 6-21, where the voltage magnitude tracks the nominal value (Figure 6-22). The fault scenario has also a terrible effect on the reactive power of the grid translated by the frequency disturbance (Figure 6-20).

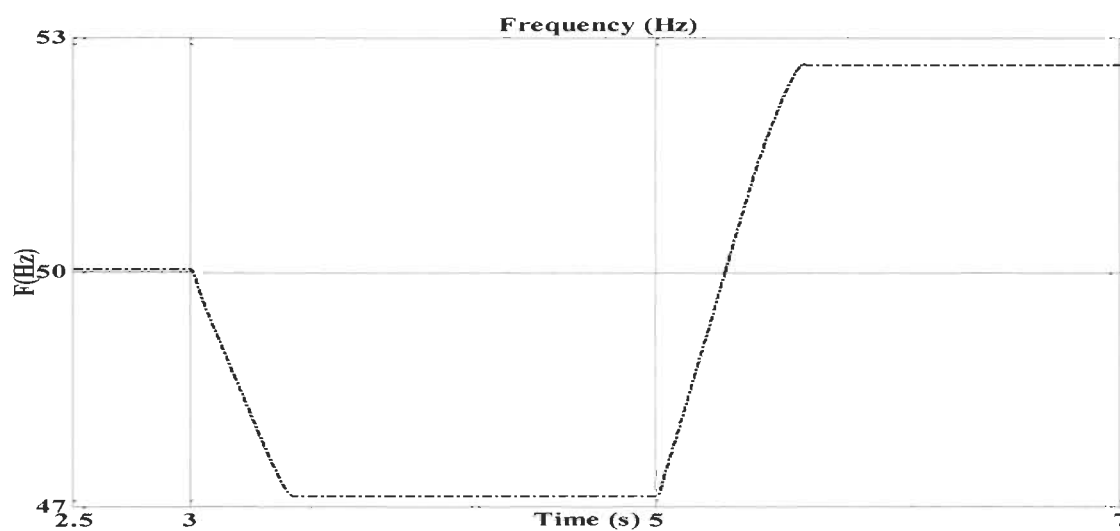


Figure 6-20 Grid frequency evolution following the voltage sag and swell

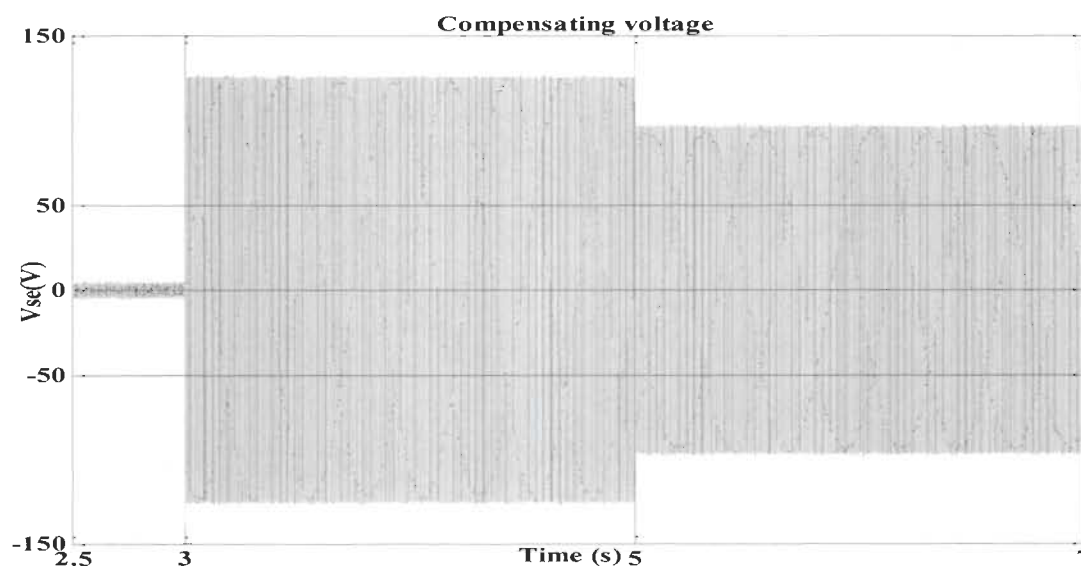


Figure 6-21 Compensating voltage generated by MC-UPQC

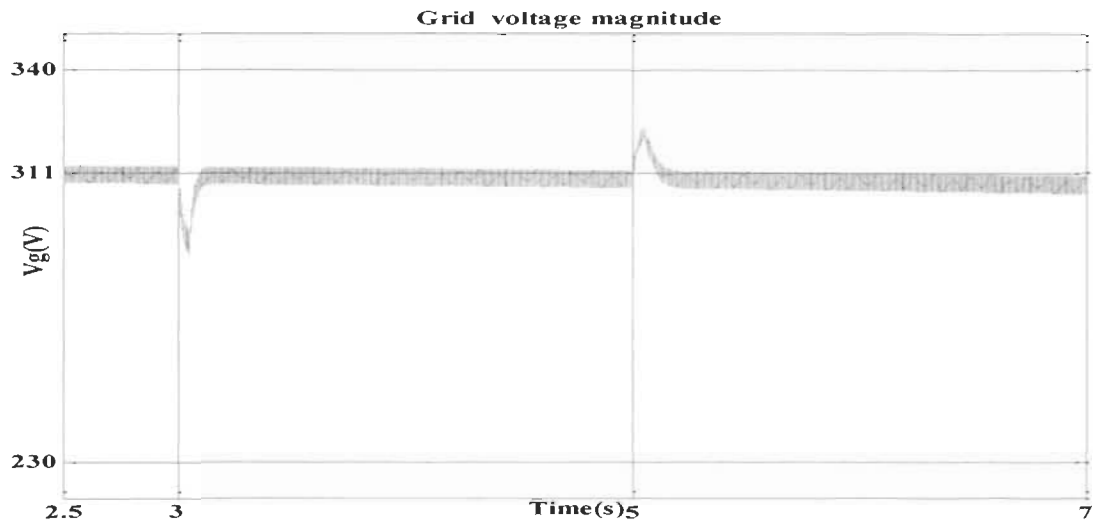


Figure 6-22 Grid voltage magnitude

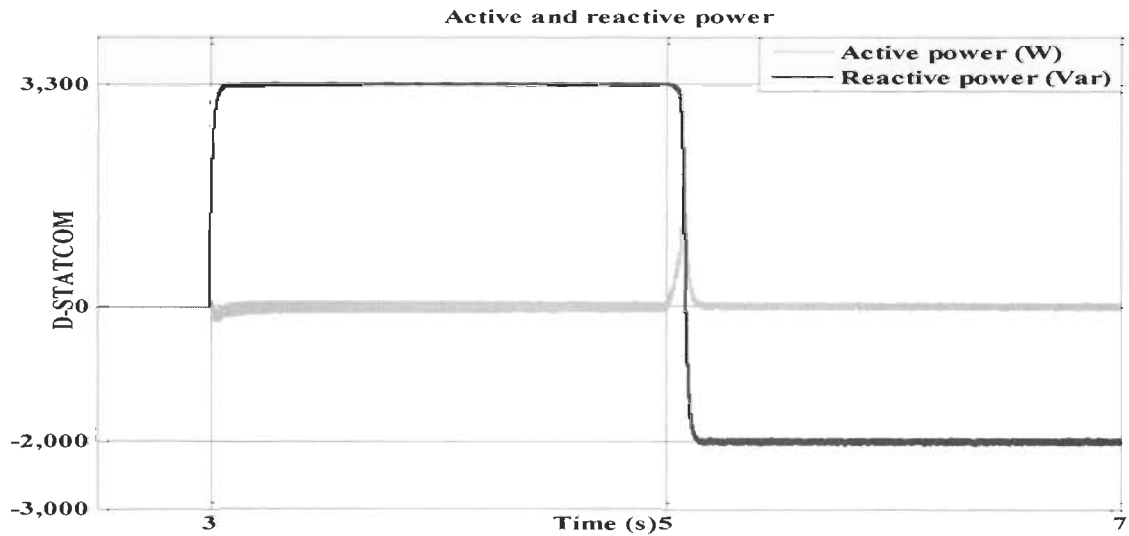


Figure 6-23 D-STATCOM active and reactive power transferred with the grid

However, in the presence of the MC-UPQC, D-STATCOM injects the lack of reactive power into the grid and absorbs the surplus (Figure 6-23) to stabilize the frequency as shown in Figure 6-24. We also observe, that MC-UPQC maintains the characteristics of SE-DSWIG

at the ideal level in terms of current (Figure 6-25) and voltage (Figure 6-22), that implies the improvement of power quality and LVRT capability of SE-DSWIG.

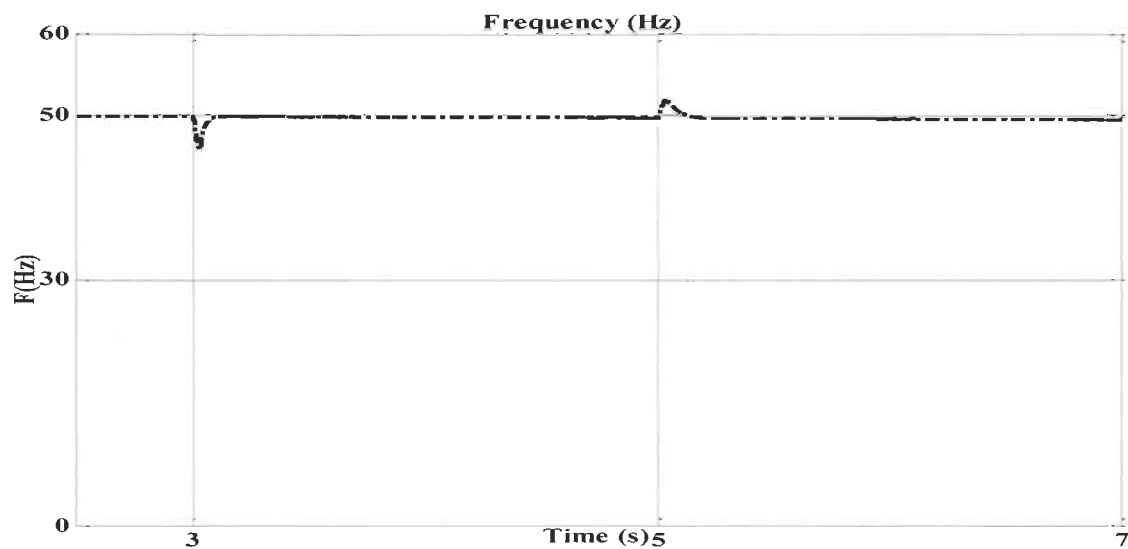


Figure 6-24 Grid frequency at the presence of MC-UPQC

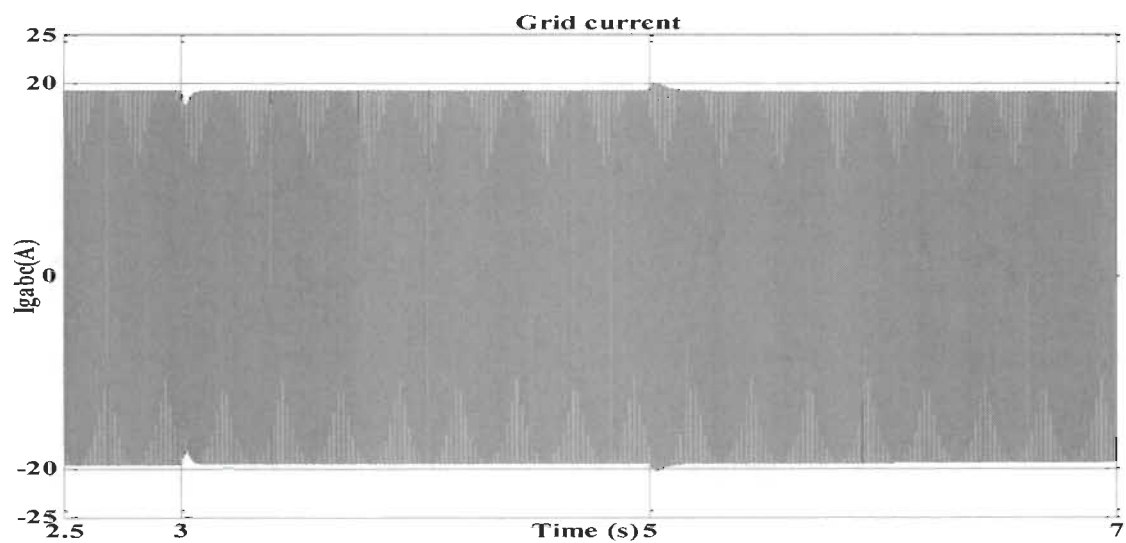


Figure 6-25 Grid current at the presence of MC-UPQC

6.5.6 Grid active and reactive power control

This scenario evaluates the capability of MC-UPQC to control the grid active and reactive power evolution, a step change in active and reactive power was applied. Initially, the SEDSWIG is driven by a sufficient speed till reaching the steady state, then the D-STATCOM was able to control the injected active and reactive power into the grid in which the active power is equal to 8KW and the reactive power is 0 KVAR as shown in Figure 6-26. After that, a step up is applied on the reactive power where it tends to 6KVAR and then is decreased to -5KVAR without affecting the evolution of active power as illustrated in Figure 6-27 and Figure 6-28.

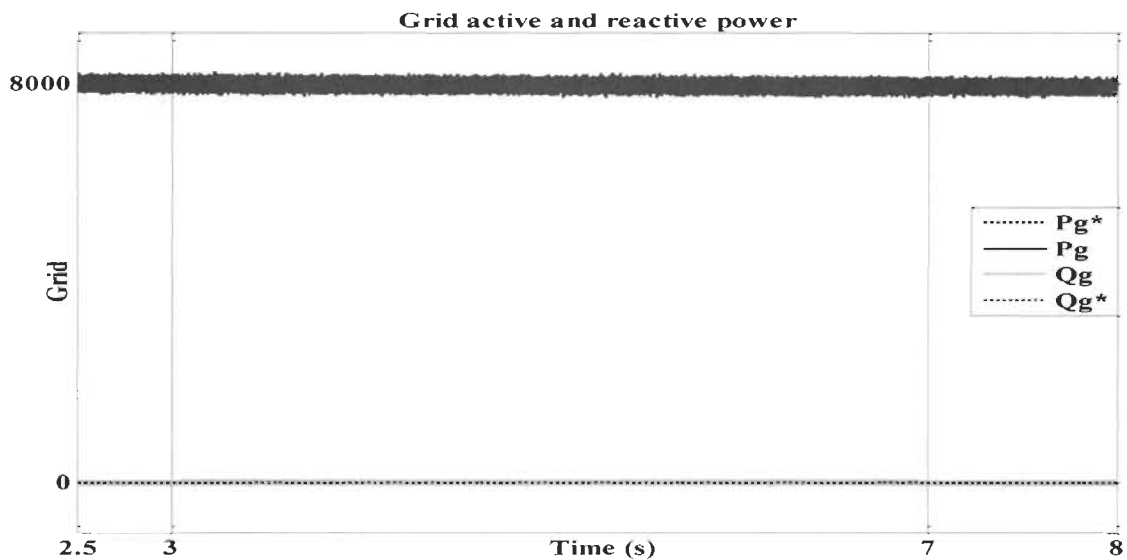


Figure 6-26 Active and reactive power evolution during reactive power injection

In Figure 6-29, we aim to examine the behavior of the control technique based cascade sliding mode control used to supervise the D-STATCOM performance. For that, a step change is applied on the active and reactive power of the grid. It's observed that both the active and reactive power track the reference perfectly with an adequate rise time without overshoot and with no error in steady state response. The presence of an energy storage

system on the dc-side of the MC-UPQC permits exchanging both the active and the reactive power with the grid through the D-STATCOM which explains the possibility of controlling the grid power.

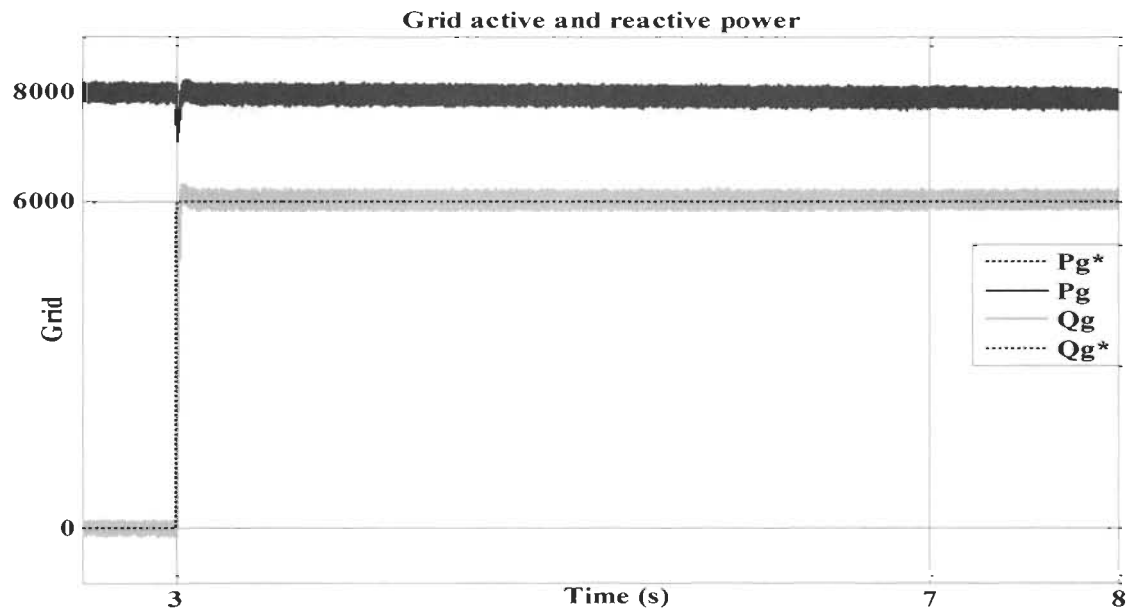


Figure 6-27 Active and reactive power evolution during reactive power injection

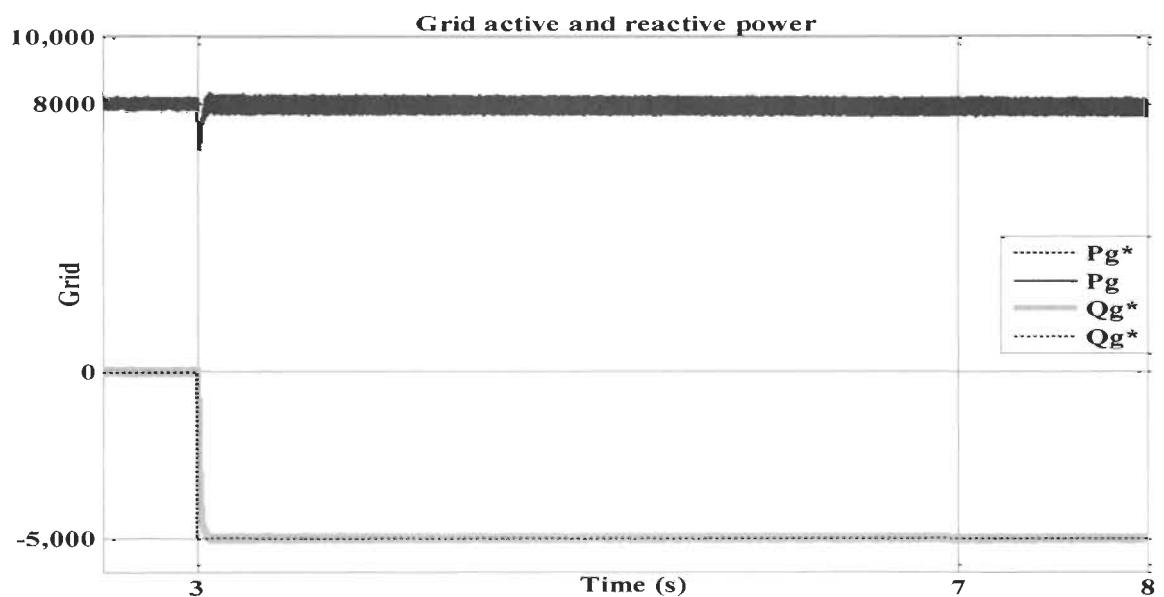


Figure 6-28 Active and reactive power evolution during reactive power absorption

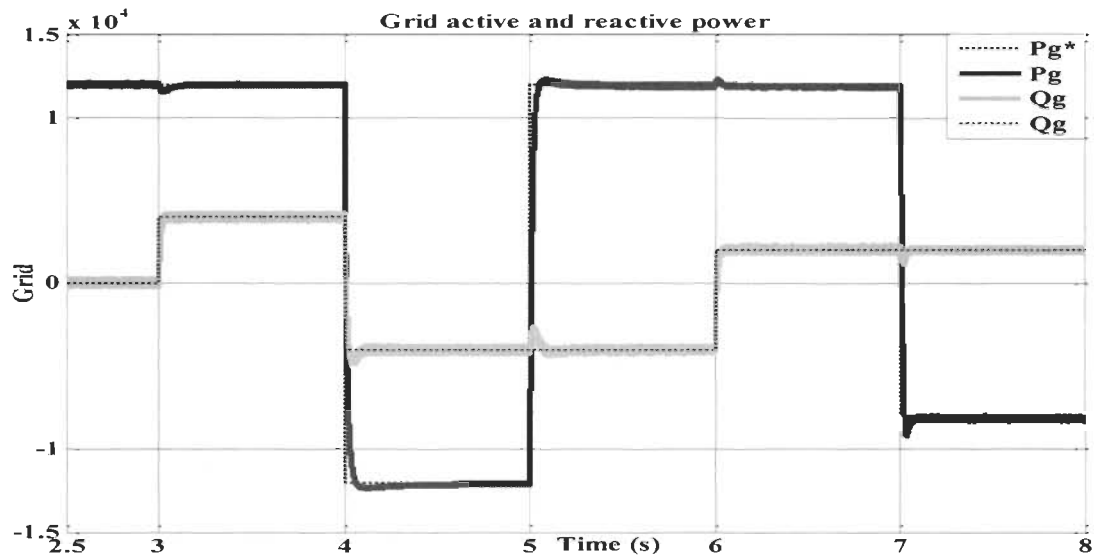


Figure 6-29 Active and reactive power in reference tracking test

6.6 Conclusion

This chapter proposes a new control strategy to sustain the active and reactive power flow from a self-excitation dual stator winding induction generator which is used simultaneously in grid tied and standalone applications. Besides, the SE-DSWIG operates in variable speed and exposed to a load variation and grid faults, causing a disturbance in voltage and frequency. For that, this attempt also assesses the possibility to improve the low voltage ride-through capability. Hence, the proposed strategy is established on the exploitation of customer power devices to mitigate power quality issues. A multi-converter based unified power quality conditioner (MC-UPQC) was used. It consists of three converters connected between them on the DC-side through an energy storage system for continuous and long duration intervention. Two converters of MC-UPQC are connected in series with the output of the SE-DSWIG playing the role of a dynamic voltage restorer. Meanwhile, the third

converter supposed as D-STATCOM, connected in shunt between the grid and a stator. A synchronous reference frame theory is used to supervise the series part of MC-UPQC, while an advanced cascade sliding mode control technique is applied on the shunt part. The analysis of the obtained results leads to conclude that the MC-UPQC ameliorates the performance of the SE-DSWIG in both grid tied and standalone applications. MC-UPQC could compensate the supplied voltage imperfection, enhance voltage and current at the PCC even in the presence of sudden faults, ameliorate the LVRT capability, and synchronize the generator on the same frequency of the grid.

Chapitre 7 - Conclusion

This dissertation proposes a new concept of the power quality improvement using Distributed Flexible AC Transmission Systems (D-FACTS), in a wind turbine based on SE-DSWIG. The objective of this thesis is twofold: the first one is the use of a dual stator winding induction generator and exploiting the multiphase feature to double the generated power compared with a simple three-phase induction generator. The other side is the proposition of new technique for the power management using multi-converter based Unified Power Quality Conditioner (MC-UPQC). The conclusion of this work can be summarized as follows:

- A survey on renewable energies with the recent statistics about their contribution to the installed power capacity has been presented.
- A classification of wind turbine topologies was proposed following the operating conditions and the type of generators used for the energy conversion.
- A state of the art on multiphase generators, specifically self-excitation dual stator winding induction generator, has been reviewed. The literature survey illustrates that multiphase generators, with number of phases more or equal to six, are more advantageous compared to their counterpart three-phase generator. Since the number of phases will be at least doubled, the generated power will be doubled. On the other hand, it also reduces harmonics, rotor losses, and torque ripples.
- In chapter two, a study has been carried out to analyse the performance of dual stator winding induction machine operates in motor mode. Its behavior in direct-fed and in

open loop control was investigated. After that, a field-oriented control technique with the indirect speed regulation method has been applied. This technique shows a good performance in terms of decoupling the torque and the rotor flux, while the speed is totally tracking the even inbn the presence of load torque variation.

- In chapter three, the performance of a wind power generation based SE-DSWIG in stand-alone application was investigated. A passive compensator based reactive elements have been designed and inserted between the generator and the end-user to improve the power quality. The proposed topology was exposed to several scenarios such as wind and load impedance variation. The SE-DSWIG with the passive compensator shows a good performance in different operating modes. However, the slowness of passive compensators and the need to redesign it for every intervention make the call to another category of compensators which have the ability to adapt quickly to the requirements.
- Chapter four and five have been dedicated to study the active compensator based D-STATCOM, DVR and UPQC for the mitigation of power issues in distribution grid. They have been evaluated against voltage sag, swell, poor power factor, distorted voltage, unbalanced current and harmonics neutral current. A control strategy based sliding mode has been applied on D-STATCOM and a simple hysteresis technique was used to control DVR, while the UPQC was supervised using an adaptive fuzzy logic control technique. The obtained results show high performance of these active compensators against the critical situations.
- Chapter six contains the contribution of this work. The SE-DSWIG operates in stand-alone and grid-connected at the same time. A multi-converter based unified power quality conditioner (MC-UPQC) has been used to improve the low voltage ride through

(LVRT) capability of the generator. MC-UPQC consists of three converters connected between them on the DC-side through an energy storage system for continuous and long duration intervention. Two converters of MC-UPQC are connected in series with the output of the SE-DSWIG playing the role of a dynamic voltage restorer (DVR). Meanwhile, the third converter supposed as D-STATCOM, connected in shunt between the grid and a stator. A synchronous reference frame theory is used to supervise the series part of MC-UPQC, while an advanced cascade sliding mode control technique is applied to the shunt part. The analysis of the obtained results leads to conclude that the MC-UPQC ameliorates the performance of the SE-DSWIG in both grid-tied and stand-alone applications. MC-UPQC could compensate the supply voltage disturbance, enhance voltage quality and current at the PCC even in the presence of sudden faults, ameliorate the LVRT capability, synchronize the generator on the same frequency of the grid.

- As future work, we are studying the possibility to use another renewable source such photovoltaic (PV) to charge the energy storage system used in the DC-side of the MC-UPQC for long duration intervention. The PV will be used to supply DC bus and to produce also an active power which will be injected through the shunt part of the MC-UPQC into the grid.

Bibliography

- [1] S. Heier, *Grid integration of wind energy: onshore and offshore conversion systems*: John Wiley & Sons, 2014.
- [2] S. S. Nandwani, "Solar Cookers solar cooker/cooking and Dryers solar dryer to Conserve Human and Planet Health," in *Solar Energy*, ed: Springer, 2013, pp. 417-440.
- [3] H. Termuehlen and W. Emsperger, "Evolutionary Development of Coal-Fired Power Plants," in *Clean and Efficient Coal-Fired Power Plants*, ed: ASME Press, 2003.
- [4] M. E. El-Hawary, *Introduction to electrical power systems* vol. 50: John Wiley & Sons, 2008.
- [5] J. E. Fleckenstein, *Three-phase Electrical Power*: CRC Press, 2015.
- [6] H. Rudnick, "Access to Electricity: Making the Expansion Worldwide [Guest Editorial]," *IEEE Power and Energy Magazine*, vol. 12, pp. 20-25, 2014.
- [7] D. Lineweber and S. McNulty, "The cost of power disturbances to industrial & digital economy companies," *Madison, WI: Primen*, 2001.
- [8] M. Arriaga, C. A. Cañizares, and M. Kazerani, "Northern lights: access to electricity in Canada's northern and remote communities," *IEEE Power and Energy Magazine*, vol. 12, pp. 50-59, 2014.
- [9] J. T. Houghton, B. A. Callander, and S. K. Varney, *Climate change 1992*: Cambridge University Press, 1992.
- [10] S. Oberthür and H. E. Ott, *The Kyoto Protocol: international climate policy for the 21st century*: Springer Science & Business Media, 1999.
- [11] REN21, "Renewables 2017 Global Status Report (www.ren21.net)," 2017.
- [12] J. Koppejan and S. Van Loo, *The handbook of biomass combustion and co-firing*: Routledge, 2012.
- [13] REN21, "Renewables 2015 Global Status Report (www.ren21.net)," 2015.
- [14] IRENA, "Geothermal Power : Technology Brief, International Renewable Energy Agency, Abu Dhabi (www.irena.org)," 2017.
- [15] A. B. e. M. a. J. L. Villate, " OES ANNUAL REPORT (www.report2016.ocean-energy-systems.org), ," 2016.
- [16] N. Khan, A. Kalair, N. Abas, and A. Haider, "Review of ocean tidal, wave and thermal energy technologies," *Renewable and Sustainable Energy Reviews*, vol. 72, pp. 590-604, 2017.

- [17] R. Guerrero-Lemus and L. E. Shephard, "Hydropower and Marine Energy," in *Low-Carbon Energy in Africa and Latin America*, ed: Springer, 2017, pp. 207-241.
- [18] e. a. w. h. o. INTERNATIONAL HYDROPOWER ASSOCIATION, "Hydropower Status Report," 2017.
- [19] F. Blaabjerg and K. Ma, "Wind Energy Systems," *Proceedings of the IEEE*, vol. 105, pp. 1311-1331, 2017.
- [20] M. G. Simões and F. A. Farret, "Modeling and Analysis with Induction Generators," third ed: CRC Press, 2015.
- [21] T. Ackermann, *Wind power in power systems*, 2nd ed.: John Wiley & Sons, 2005.
- [22] S. Muller, M. Deicke, and R. W. De Doncker, "Doubly fed induction generator systems for wind turbines," *IEEE Industry applications magazine*, vol. 8, pp. 26-33, 2002.
- [23] V. Yaramasu, B. Wu, P. C. Sen, S. Kouro, and M. Narimani, "High-power wind energy conversion systems: State-of-the-art and emerging technologies," *Proceedings of the IEEE*, vol. 103, pp. 740-788, 2015.
- [24] I. Boldea, *Variable speed generators*, 2nd ed.: CRC press, 2016.
- [25] J. A. Baroudi, V. Dinavahi, and A. M. Knight, "A review of power converter topologies for wind generators," *Renewable Energy*, vol. 32, pp. 2369-2385, 2007.
- [26] V. Yaramasu, "Predictive control of multilevel converters for Megawatt wind energy conversion systems," Ph. D. dissertation, Ryerson University, Toronto, ON, Canada, 2014, available at: <http://digital.library.ryerson.ca/islandora/object/RULA%3A3459>, 2014.
- [27] A. O. Ibrahim, T. H. Nguyen, D.-C. Lee, and S.-C. Kim, "A fault ride-through technique of DFIG wind turbine systems using dynamic voltage restorers," *IEEE transactions on energy conversion*, vol. 26, pp. 871-882, 2011.
- [28] G. Singh, "Self-excited induction generator research—a survey," *Electric Power Systems Research*, vol. 69, pp. 107-114, 2004.
- [29] M. Tsili and S. Papathanassiou, "A review of grid code technical requirements for wind farms," *IET Renewable Power Generation*, vol. 3, pp. 308-332, 2009.
- [30] F. Hamoud, M. L. Doumbia, and A. Cheriti, "Performance Study of a Self-Excitation Dual Stator Winding Induction Generator for Renewable Distributed Generation Systems," *Smart Grid and Renewable Energy*, vol. 7, p. 197, 2016.
- [31] E. Levi, "Multiphase electric machines for variable-speed applications," *IEEE Transactions on industrial electronics*, vol. 55, pp. 1893-1909, 2008.
- [32] M. J. Duran and F. Barrero, "Recent advances in the design, modeling, and control of multiphase machines—Part II," *IEEE Transactions on Industrial Electronics*, vol. 63, pp. 459-468, 2016.

- [33] S. Basak and C. Chakraborty, "Dual stator winding induction machine: Problems, progress, and future scope," *IEEE Transactions on Industrial Electronics*, vol. 62, pp. 4641-4652, 2015.
- [34] S. Basak, C. Chakraborty, and A. K. Sinha, "Dual stator induction generator with controllable reactive power capability," in *Industrial Electronics (ISIE), 2014 IEEE 23rd International Symposium on*, 2014, pp. 2584-2589.
- [35] F. Bu, W. Huang, Y. Hu, and K. Shi, "An excitation-capacitor-optimized dual stator-winding induction generator with the static excitation controller for wind power application," *IEEE Transactions on Energy Conversion*, vol. 26, pp. 122-131, 2011.
- [36] F. Bu, W. Huang, Y. Hu, and K. Shi, "An integrated AC and DC hybrid generation system using dual-stator-winding induction generator with static excitation controller," *IEEE Transactions on Energy Conversion*, vol. 27, pp. 810-812, 2012.
- [37] M. Moradian and J. Soltani, "An isolated three-phase induction generator system with dual stator winding sets under unbalanced load condition," *IEEE Transactions on Energy Conversion*, vol. 31, pp. 531-539, 2016.
- [38] H. Xu, F. Bu, W. Huang, Y. Hu, H. Liu, and Y. Zhao, "Analysis, Comparison, and Discussion of Control Strategies for Dual Stator-Winding Induction Generator DC Generating System," *IEEE Journal of Emerging and Selected Topics in Power Electronics*, vol. 4, pp. 1007-1014, 2016.
- [39] F. Bu, S. Zhuang, W. Huang, N. Su, and Y. Hu, "Asymmetrical Operation Analysis for Dual Stator-Winding Induction Generator Variable Frequency AC Generating System With Unbalanced Loads," *IEEE Transactions on Industrial Electronics*, vol. 64, pp. 52-59, 2017.
- [40] K. Nounou and K. Marouani, "Control of a dual star induction generator driven wind turbine," in *Electrical Apparatus and Technologies (SIELA), 2016 19th International Symposium on*, 2016, pp. 1-4.
- [41] F. Bu, Y. Hu, W. Huang, S. Zhuang, and K. Shi, "Control strategy and dynamic performance of dual stator-winding induction generator variable frequency AC generating system with inductive and capacitive loads," *IEEE Transactions on Power Electronics*, vol. 29, pp. 1681-1692, 2014.
- [42] Z. Wu, O. Ojo, and J. Sastry, "High-performance control of a dual stator winding DC power induction generator," *IEEE Transactions on Industry Applications*, vol. 43, pp. 582-592, 2007.
- [43] F. Bu, Y. Hu, W. Huang, S. Zhuang, and K. Shi, "Wide-speed-range-operation dual stator-winding induction generator dc generating system for wind power applications," *IEEE Transactions on Power Electronics*, vol. 30, pp. 561-573, 2015.
- [44] M. Naidu and J. Walters, "A 4-kW 42-V induction-machine-based automotive power generation system with a diode bridge rectifier and a PWM inverter," *IEEE Transactions on Industry applications*, vol. 39, pp. 1287-1293, 2003.

- [45] S. Basak and C. Chakraborty, "A brushless generation system for microgrid operation utilizing dual stator induction generator," in *Industrial Electronics (ISIE), 2014 IEEE 23rd International Symposium on*, 2014, pp. 302-307.
- [46] S. Basak and C. Chakraborty, "Improved voltage regulation of dual stator induction generator using series and shunt capacitors," in *Industrial Technology (ICIT), 2017 IEEE International Conference on*, 2017, pp. 294-299.
- [47] G. Singh, A. S. Kumar, and R. Saini, "Performance analysis of a simple shunt and series compensated six-phase self-excited induction generator for stand-alone renewable energy generation," *Energy conversion and management*, vol. 52, pp. 1688-1699, 2011.
- [48] H. Amimeur, D. Aouzellag, R. Abdessemed, and K. Ghedamsi, "Sliding mode control of a dual-stator induction generator for wind energy conversion systems," *International Journal of Electrical Power & Energy Systems*, vol. 42, pp. 60-70, 2012.
- [49] S. Chekkal, N. A. Lahaçani, D. Aouzellag, and K. Ghedamsi, "Fuzzy logic control strategy of wind generator based on the dual-stator induction generator," *International Journal of Electrical Power & Energy Systems*, vol. 59, pp. 166-175, 2014.
- [50] F. Ameer, K. Kouzi, and N. K. Merzouk, "Design and Analysis of Direct Power and Flux Control of Dual Stator Induction Generator Integrated in Wind Conversion System connected to the Grid," *Electrotehnica, Electronica, Automatica*, vol. 64, p. 47, 2016.
- [51] J. A. Barrado-Rodrigo, J. I. Talpone, and L. Martinez-Salamero, "Variable-speed wind energy conversion system based on a dual stator-winding induction generator," *IET Renewable Power Generation*, vol. 11, pp. 73-80, 2016.
- [52] F. Bu, L. Zhu, W. Huang, H. Xu, H. Liu, and Y. Gao, "Control strategy of AC& DC hybrid generating system based on dual stator-winding induction generator for micro-grid application," in *Transportation Electrification Asia-Pacific (ITEC Asia-Pacific), 2016 IEEE Conference and Expo*, 2016, pp. 723-727.
- [53] G. Singh, "Multi-phase induction machine drive research—A survey," *Electric Power Systems Research*, vol. 61, pp. 139-147, 2002.
- [54] K. Marouani, M. Khaldi, F. Khoucha, and A. Kheloui, "Switching losses and harmonic currents evaluation of PWM techniques for VSI-fed dual stator induction motor drive," in *Control and Automation, 2009. MED'09. 17th Mediterranean Conference on*, 2009, pp. 1492-1497.
- [55] E. Levi, "Advances in converter control and innovative exploitation of additional degrees of freedom for multiphase machines," *IEEE Transactions on Industrial Electronics*, vol. 63, pp. 433-448, 2016.
- [56] I. González-Prieto, M. J. Duran, and F. J. Barrero, "Fault-Tolerant Control of Six-Phase Induction Motor Drives With Variable Current Injection," *IEEE Transactions on Power Electronics*, vol. 32, pp. 7894-7903, 2017.

- [57] A. R. Muñoz and T. A. Lipo, "Dual stator winding induction machine drive," *IEEE Transactions on Industry Applications*, vol. 36, pp. 1369-1379, 2000.
- [58] X. Chen, J. Wang, V. I. Patel, and P. Lazari, "A nine-phase 18-slot 14-pole interior permanent magnet machine with low space harmonics for electric vehicle applications," *IEEE Transactions on Energy Conversion*, vol. 31, pp. 860-871, 2016.
- [59] L. Schreier, J. Bendl, and M. Chomat, "Influence of space harmonics on properties of six-phase induction machine-Part I. analysis," in *Electrical Machines (ICEM), 2010 XIX International Conference on*, 2010, pp. 1-6.
- [60] F. Barrero and M. J. Duran, "Recent advances in the design, modeling, and control of multiphase machines—Part I," *IEEE Transactions on Industrial Electronics*, vol. 63, pp. 449-458, 2016.
- [61] J. Liu, L. Huang, H. Yu, C. Wen, and W. Zhong, "Study on the characteristics of a novel six-phase fault-torrent linear permanent magnet machine for linear oil pumping," *IEEE Transactions on Applied Superconductivity*, vol. 24, pp. 1-5, 2014.
- [62] T. McCoy and M. Bentamane, "The all electric warship: an overview of the US Navy's integrated power system development programme'," in *Proc. Int. Conf. on Electric Ship ELECSHIP, Istanbul, Turkey*, 1998, pp. 1-4.
- [63] F. Terrien, S. Siala, and P. Noy, "Multiphase induction motor sensorless control for electric ship propulsion," *Alstom Power Conversion Marine & Offshore*, 2004.
- [64] H. AMIMEUR, "Contributions à la Commande d'une Machine Asynchrone Double Etoile par Mode de Glissement," Université de Batna 2, 2008.
- [65] H. Amimeur, R. Abdessemed, D. Aouzellag, E. Merabet, and F. Hamoudi, "A sliding mode control associated to the field-oriented control of dual-stator induction motor drives," *J Electr Eng*, vol. 10, 2010.
- [66] E. Merabet, "Commande Floue Adaptative d'une Machine Asynchrone Double Etoile," Université de Batna 2, 2008.
- [67] G. K. Singh, K. Nam, and S. Lim, "A simple indirect field-oriented control scheme for multiphase induction machine," *IEEE Transactions on Industrial Electronics*, vol. 52, pp. 1177-1184, 2005.
- [68] M. Zerbo, "Identification des paramètres et commande vectorielle adaptative à orientation du flux rotorique de la machine asynchrone à cage," Université du Québec à Trois-Rivières, 2008.
- [69] G. Singh, K. Yadav, and R. Saini, "Modeling and analysis of multi-phase (six-phase) self-excited induction generator," in *Electrical Machines and Systems, 2005. ICEMS 2005. Proceedings of the Eighth International Conference on*, 2005, pp. 1922-1927.
- [70] P. A. Cartwright, "A passive compensator for voltage flicker," *Electrical Engineering*, vol. 71, pp. 1032-1035, 1952.
- [71] B. Singh, A. Chandra, and K. Al-Haddad, *Power quality: problems and mitigation techniques*: John Wiley & Sons, 2014.

- [72] M. Routimo, A. MäkinenMakinen, M. Salo, R. Seesvuori, J. Kiviranta, and H. Tuusa, "Flicker mitigation with a hybrid compensator," *IEEE Transactions on Industry Applications*, vol. 44, pp. 1227-1238, 2008.
- [73] A. Elgammal and A. M. Sharaf, "Dynamic Self Adjusting FACTS-Switched Filter Compensation Schemes for Wind-Smart Grid interface Systems," *International Journal of Renewable Energy Research (IJRER)*, vol. 2, pp. 103-111, 2012.
- [74] B. Singh, "Introduction to FACTS controllers in wind power farms: A technological review," *International Journal of Renewable Energy Research (IJRER)*, vol. 2, pp. 166-212, 2012.
- [75] K. K. Sen and M. L. Sen, *Introduction to FACTS controllers: theory, modeling, and applications* vol. 54: John Wiley & Sons, 2009.
- [76] S. R. Arya, B. Singh, R. Niwas, A. Chandra, and K. Al-Haddad, "Power quality enhancement using DSTATCOM in distributed power generation system," *IEEE Transactions on Industry Applications*, vol. 52, pp. 5203-5212, 2016.
- [77] J. Sanam, S. Ganguly, and A. Panda, "Distribution STATCOM with optimal phase angle injection model for reactive power compensation of radial distribution networks," *International Journal of Numerical Modelling: Electronic Networks, Devices and Fields*, 2017.
- [78] M. Mangaraj, T. Penthia, and A. K. Panda, "Power quality improvement by a 3-phase 4-leg supercapacitor based DSTATCOM," in *Electrical, Computer and Electronics Engineering (UPCON), 2016 IEEE Uttar Pradesh Section International Conference on*, 2016, pp. 91-97.
- [79] A. M. Vural, "Self-capacitor voltage balancing method for optimally hybrid modulated cascaded H-bridge D-STATCOM," *IET Power Electronics*, vol. 9, pp. 2731-2740, 2016.
- [80] J. I. Y. Ota, Y. Shibano, N. Niimura, and H. Akagi, "A phase-shifted-PWM D-STATCOM using a modular multilevel cascade converter (SSBC)—part I: modeling, analysis, and design of current control," *IEEE Transactions on Industry Applications*, vol. 51, pp. 279-288, 2015.
- [81] J. I. Y. Ota, Y. Shibano, and H. Akagi, "A phase-shifted PWM D-STATCOM using a modular multilevel cascade converter (SSBC)—Part II: Zero-voltage-ride-through capability," *IEEE Transactions on Industry Applications*, vol. 51, pp. 289-296, 2015.
- [82] T.-L. Lee, S.-H. Hu, and Y.-H. Chan, "D-STATCOM with positive-sequence admittance and negative-sequence conductance to mitigate voltage fluctuations in high-level penetration of distributed-generation systems," *IEEE Transactions on Industrial Electronics*, vol. 60, pp. 1417-1428, 2013.
- [83] C. A. Sepulveda, J. A. Muñoz, J. R. Espinoza, M. E. Figueroa, and P. E. Melin, "All-on-chip dq-frame based D-STATCOM control implementation in a low-cost FPGA," *IEEE Transactions on Industrial Electronics*, vol. 60, pp. 659-669, 2013.

- [84] A. Çetin and M. Ermis, "VSC-based D-STATCOM with selective harmonic elimination," *IEEE Transactions on Industry Applications*, vol. 45, pp. 1000-1015, 2009.
- [85] B. Blazic and I. Papic, "Improved D-StatCom control for operation with unbalanced currents and voltages," *IEEE Transactions on Power Delivery*, vol. 21, pp. 225-233, 2006.
- [86] V. Dinavahi, R. Iravani, and R. Bonert, "Design of a real-time digital simulator for a D-STATCOM system," *IEEE Transactions on Industrial Electronics*, vol. 51, pp. 1001-1008, 2004.
- [87] G. Escobar, A. Valdez, R. Torres-Olguin, and M. Martinez-Montejano, "A repetitive-based controller in stationary reference frame for D-Statcom in unbalanced operation," in *Industrial Electronics, 2006 IEEE International Symposium on*, 2006, pp. 1388-1393.
- [88] G. Escobar, A. M. Stankovic, and P. Mattavelli, "An adaptive controller in stationary reference frame for D-statcom in unbalanced operation," *IEEE Transactions on Industrial Electronics*, vol. 51, pp. 401-409, 2004.
- [89] S. R. Arya, R. Niwas, K. K. Bhalla, B. Singh, A. Chandra, and K. Al-Haddad, "Power quality improvement in isolated distributed power generating system using DSTATCOM," *IEEE Transactions on Industry Applications*, vol. 51, pp. 4766-4774, 2015.
- [90] D. Ananth and G. N. Kumar, "Mitigation of voltage dip and power system oscillations damping using dual STATCOM for grid connected DFIG," *Ain Shams Engineering Journal*, 2015.
- [91] E. Moraes, S. De Mesquita, R. Leao, M. Neto, K. Da Silva, R. Correa, *et al.*, "The application of D-STATCOM in smart distribution grid with wind power plants," in *Industry Applications (INDUSCON), 2012 10th IEEE/IAS International Conference on*, 2012, pp. 1-6.
- [92] X. Zheng and G. Xu, "Study on LVRT of DFIG under the asymmetric grid voltage based on fuzzy PID D-STATCOM," in *Advanced Information Management, Communicates, Electronic and Automation Control Conference (IMCEC), 2016 IEEE*, 2016, pp. 237-242.
- [93] D. M. Reddy and T. Gowrimanohar, "Dynamic performance of power quality improvement using multilevel DSTATCOM with DG application," in *Current Trends in Engineering and Technology (ICCTET), 2014 2nd International Conference on*, 2014, pp. 288-295.
- [94] V. Hrishikesan, K. Venkatraman, and M. Selvan, "Performance of custom power devices in SCIG based wind farms during abnormal grid conditions," in *India conference (INDICON), 2014 annual IEEE*, 2014, pp. 1-5.
- [95] T. Phan, V. Nguyen, M. Hossain, A. To, H. Tran, and T. Phan, "Transient Responses of the Doubly-Fed Induction Generator Wind Turbine under Grid Fault Conditions," in *Advanced Computing and Applications (ACOMP), 2016 International Conference on*, 2016, pp. 97-104.

- [96] K. Padiyar, "FACTS controllers in power transmission and distribution," 2007.
- [97] B. N. Singh, B. Shigh, A. Chandra, and K. Al-Haddad, "DSP based implementation of sliding mode control on an active filter for voltage regulation and compensation of harmonics, power factor and unbalance of nonlinear loads," in *Industrial Electronics Society, 1999. IECON'99 Proceedings. The 25th Annual Conference of the IEEE*, 1999, pp. 855-860.
- [98] A. Egea-Alvarez, A. Junyent-Ferré, and O. Gomis-Bellmunt, "Active and reactive power control of grid connected distributed generation systems," *Modeling and control of sustainable power systems*, pp. 47-81, 2012.
- [99] I. Papič, "Mathematical analysis of FACTS devices based on a voltage source converter: Part I: mathematical models," *Electric Power Systems Research*, vol. 56, pp. 139-148, 2000.
- [100] S.-K. Chung, "A phase tracking system for three phase utility interface inverters," *IEEE Transactions on Power electronics*, vol. 15, pp. 431-438, 2000.
- [101] L. T. Moran, P. D. Ziogas, and G. Joos, "Analysis and design of a three-phase synchronous solid-state var compensator," *IEEE Transactions on Industry Applications*, vol. 25, pp. 598-608, 1989.
- [102] B. Singh, P. Jayaprakash, D. P. Kothari, A. Chandra, and K. Al Haddad, "Comprehensive study of DSTATCOM configurations," *IEEE Transactions on Industrial Informatics*, vol. 10, pp. 854-870, 2014.
- [103] M. A. F. M. Karim—Meroufel and A. B. Abdelber, "Input output linearization and sliding mode control of a permanent magnet synchronous machine fed by a three levels inverter," *Journal of Electrical Engineering*, vol. 57, pp. 205-210, 2006.
- [104] C. P. Coleman and D. Godbole, "A comparison of robustness: fuzzy logic, PID, and sliding mode control," in *Fuzzy Systems, 1994. IEEE World Congress on Computational Intelligence., Proceedings of the Third IEEE Conference on*, 1994, pp. 1654-1659.
- [105] L. Jinkun and W. Xinhua, "Advanced sliding mode control for mechanical systems: design, analysis and MATLAB simulation," ed: Tsinghua University Press, Beijing CrossRef Google Scholar, 2011.
- [106] M. Abbasian, "Robust control of STATCOM based on sliding mode technique," in *International Conference on Renewable Energies and Power Quality, ICREPQ'09*, 2009.
- [107] R. A. J. Amalorpavaraj, P. Kaliannan, S. Padmanaban, U. Subramaniam, and V. K. Ramachandaramurthy, "Improved fault ride through capability in dfig based wind turbines using dynamic voltage restorer with combined feed-forward and feed-back control," *IEEE Access*, vol. 5, pp. 20494-20503, 2017.
- [108] A. Ghosh and G. Ledwich, *Power quality enhancement using custom power devices*: Springer Science & Business Media, 2012.

- [109] C.-J. Huang, S.-J. Huang, and F.-S. Pai, "Design of dynamic voltage restorer with disturbance-filtering enhancement," *IEEE Transactions on Power Electronics*, vol. 18, pp. 1202-1210, 2003.
- [110] A. Ghosh, A. K. Jindal, and A. Joshi, "Design of a capacitor-supported dynamic voltage restorer (DVR) for unbalanced and distorted loads," *IEEE transactions on power delivery*, vol. 19, pp. 405-413, 2004.
- [111] F. Jowder, "Design and analysis of dynamic voltage restorer for deep voltage sag and harmonic compensation," *IET generation, transmission & distribution*, vol. 3, pp. 547-560, 2009.
- [112] I. Syed and V. Khadkikar, "A Dynamic Voltage Restorer (DVR) based interface scheme for microgrids," in *Industrial Electronics Society, IECON 2014-40th Annual Conference of the IEEE*, 2014, pp. 5143-5149.
- [113] D. Li, K. Yang, Z. Zhu, and Y. Qin, "A novel series power quality controller with reduced passive power filter," *IEEE Transactions on Industrial Electronics*, vol. 64, pp. 773-784, 2017.
- [114] S. Bhowmick, *Flexible AC Transmission Systems (FACTS): Newton Power-Flow Modeling of Voltage-Sourced Converter-Based Controllers*: CRC Press, 2016.
- [115] B. Singh and P. Venkateswarlu, "A simplified control algorithm for three-phase, four-wire unified power quality conditioner," *Journal of Power Electronics*, vol. 10, pp. 91-96, 2010.
- [116] O. P. Mahela and A. G. Shaik, "Topological aspects of power quality improvement techniques: A comprehensive overview," *Renewable and Sustainable Energy Reviews*, vol. 58, pp. 1129-1142, 2016.
- [117] L. An, X. Qianming, M. Fujun, and C. Yandong, "Overview of power quality analysis and control technology for the smart grid," *Journal of Modern Power Systems and Clean Energy*, vol. 4, pp. 1-9, 2016.
- [118] J. Dixon, L. Moran, J. Rodriguez, and R. Domke, "Reactive Power Compensation Technologies: State-of-the-Art Review," *Proceedings of the IEEE*, vol. 93, pp. 2144-2164, 2005.
- [119] C. B. Paduchuri, S. S. Dash, and S. Chinnamuthu, "Design of Two Feeder Three Phase Four Wire Distribution System Utilizing Multi Converter UPQC with Fuzzy Logic Controller," *Advances in Electrical and Electronic Engineering*, vol. 12, p. 75, 2014.
- [120] V. Khadkikar and A. Chandra, "A New Control Philosophy for a Unified Power Quality Conditioner (UPQC) to Coordinate Load-Reactive Power Demand Between Shunt and Series Inverters," *IEEE Transactions on Power Delivery*, vol. 23, pp. 2522-2534, 2008.
- [121] A. K. Panda and N. Patnaik, "Management of reactive power sharing & power quality improvement with SRF-PAC based UPQC under unbalanced source voltage condition," *International Journal of Electrical Power & Energy Systems*, vol. 84, pp. 182-194, 2017.

- [122] M. Aredes, K. Heumann, and E. H. Watanabe, "An universal active power line conditioner," *IEEE Transactions on Power Delivery*, vol. 13, pp. 545-551, 1998.
- [123] Z. Changjiang, V. K. Ramachandaramurthy, A. Arulampalam, C. Fitzer, M. Barnes, and N. Jenkins, "Universal custom power conditioner (UCPC) with integrated control," in *2001 IEEE Power Engineering Society Winter Meeting. Conference Proceedings (Cat. No.01CH37194)*, 2001, pp. 1039-1044 vol.3.
- [124] V. Khadkikar, P. Agarwal, A. Chandra, A. O. Barry, and T. D. Nguyen, "A simple new control technique for unified power quality conditioner (UPQC)," in *2004 11th International Conference on Harmonics and Quality of Power (IEEE Cat. No.04EX951)*, 2004, pp. 289-293.
- [125] V. Khadkikar, A. Chandra, A. O. Barry, and T. D. Nguyen, "Steady state power flow analysis of unified power quality conditioner (UPQC)," in *2005 International Conference on Industrial Electronics and Control Applications*, 2005, pp. 6 pp.-6.
- [126] V. Khadkikar, A. Chandra, A. O. Barry, and T. D. Nguyen, "Conceptual Study of Unified Power Quality Conditioner (UPQC)," in *2006 IEEE International Symposium on Industrial Electronics*, 2006, pp. 1088-1093.
- [127] V. Khadkikar, A. Chandra, A. O. Barry, and T. D. Nguyen, "Analysis of Power Flow in UPQC during Voltage Sag and Swell Conditions for Selection of Device Ratings," in *2006 Canadian Conference on Electrical and Computer Engineering*, 2006, pp. 867-872.
- [128] M. Singh, V. Khadkikar, A. Chandra, and R. K. Varma, "Grid Interconnection of Renewable Energy Sources at the Distribution Level With Power-Quality Improvement Features," *IEEE Transactions on Power Delivery*, vol. 26, pp. 307-315, 2011.
- [129] X. Yunfei, X. Xiangning, S. Yamin, and L. Yunbo, "Voltage sag compensation strategy for unified power quality conditioner with simultaneous reactive power injection," *Journal of Modern Power Systems and Clean Energy*, vol. 4, pp. 113-122, 2016.
- [130] S. K. Khadem, M. Basu, and M. F. Conlon, "A comparative analysis of placement and control of UPQC in DG integrated grid connected network," *Sustainable Energy, Grids and Networks*, vol. 6, pp. 46-57, 2016.
- [131] M. Gayatri, A. M. Parimi, and A. P. Kumar, "A review of reactive power compensation techniques in microgrids," *Renewable and Sustainable Energy Reviews*, vol. 81, pp. 1030-1036, 2018.
- [132] A. Pathak, M. Sharma, and M. Bundele, "A critical review of voltage and reactive power management of wind farms," *Renewable and Sustainable Energy Reviews*, vol. 51, pp. 460-471, 2015.
- [133] A. S. Kumar, S. Rajasekar, and P. A.-D.-V. Raj, "Power quality profile enhancement of utility connected microgrid system using ANFIS-UPQC," *Procedia Technology*, vol. 21, pp. 112-119, 2015.

- [134] A. Ajami and M. Armaghan, "Fixed speed wind farm operation improvement using current-source converter based UPQC," *Energy conversion and management*, vol. 58, pp. 10-18, 2012.
- [135] L. Liu, P. Zhu, Y. Kang, and J. Chen, "Design and dynamic performance analysis of a unified power flow controller," in *Industrial Electronics Society, 2005. IECON 2005. 31st Annual Conference of IEEE*, 2005, p. 6 pp.
- [136] F. Hamoud, M. L. Doumbia, and A. Ch, "Power factor improvement in WECS using cascade PI control of passive damping LCL-filter," in *2015 International Conference on Sustainable Mobility Applications, Renewables and Technology (SMART)*, 2015, pp. 1-7.
- [137] S. Morsli, A. Tayeb, D. Mouloud, and C. Abdelkader, "A robust adaptive fuzzy control of a unified power flow controller," *Turkish Journal of Electrical Engineering & Computer Sciences*, vol. 20, pp. 87-98, 2012.
- [138] H. Akagi, Y. Kanazawa, and A. Nabae, "Instantaneous Reactive Power Compensators Comprising Switching Devices without Energy Storage Components," *IEEE Transactions on Industry Applications*, vol. IA-20, pp. 625-630, 1984.
- [139] S. Mikkili and A. K. Panda, *Power Quality Issues: Current Harmonics*: CRC Press, 2015.
- [140] V. Khadkikar and A. Chandra, "UPQC-S: A Novel Concept of Simultaneous Voltage Sag/Swell and Load Reactive Power Compensations Utilizing Series Inverter of UPQC," *IEEE Transactions on Power Electronics*, vol. 26, pp. 2414-2425, 2011.
- [141] H. Akagi, E. H. Watanabe, and M. Aredes, *Instantaneous power theory and applications to power conditioning*: John Wiley & Sons, 2017.
- [142] B. Dimd, "Power Converters as smart instruments and actuators in a smarter grid," NTNU, 2015.
- [143] F. Hamoud, M. L. Doumbia, and A. Cheriti, "Hybrid PI-Sliding Mode Control of a voltage source converter based STATCOM," in *2014 16th International Power Electronics and Motion Control Conference and Exposition*, 2014, pp. 661-666.
- [144] H. Chaoui and H. Gualous, "Adaptive Fuzzy Logic Control for a Class of Unknown Nonlinear Dynamic Systems with Guaranteed Stability," *Journal of Control, Automation and Electrical Systems*, pp. 1-10, 2017.
- [145] H. Chaoui, M. Khayamy, and A. A. Aljarboua, "Adaptive Interval Type-2 Fuzzy Logic Control for PMSM Drives With a Modified Reference Frame," *IEEE Transactions on Industrial Electronics*, vol. 64, pp. 3786-3797, 2017.
- [146] H. Teiar, H. Chaoui, and P. Sicard, "Almost parameter-free sensorless control of PMSM," in *Industrial Electronics Society, IECON 2015-41st Annual Conference of the IEEE*, 2015, pp. 004667-004671.
- [147] H. Teiar, H. Chaoui, and P. Sicard, "Almost parameter-free sensorless control of PMSM," in *IECON 2015 - 41st Annual Conference of the IEEE Industrial Electronics Society*, 2015, pp. 004667-004671.

- [148] H. Chaoui and P. Sicard, "Adaptive fuzzy logic control of permanent magnet synchronous machines with nonlinear friction," *IEEE Transactions on Industrial Electronics*, vol. 59, pp. 1123-1133, 2012.
- [149] H. Teiar, H. Chaoui, and P. Sicard, "Simple adaptive fuzzy logic control structure of permanent magnet synchronous machines," in *Transportation Electrification Conference and Expo (ITEC), 2015 IEEE*, 2015, pp. 1-6.
- [150] S. Boukaka, H. Teiar, H. Chaoui, and P. Sicard, "FPGA implementation of an adaptive fuzzy logic controller for PMSM," in *Power Electronics, Machines and Drives (PEMD 2014), 7th IET International Conference on*, 2014, pp. 1-6.
- [151] D. Ananth and G. N. Kumar, "Fault ride-through enhancement using an enhanced field oriented control technique for converters of grid connected DFIG and STATCOM for different types of faults," *ISA transactions*, vol. 62, pp. 2-18, 2016.
- [152] F. Hamoud, M. L. Doumbia, A. Chériti, and H. Teiar, "Power factor improvement using adaptive fuzzy logic control based D-STATCOM," in *Ecological Vehicles and Renewable Energies (EVER), 2017 Twelfth International Conference on*, 2017, pp. 1-6.
- [153] F. Hamoud, M. L. Doumbia, and A. Chériti, "Voltage sag and swell mitigation using D-STATCOM in renewable energy based distributed generation systems," in *Ecological Vehicles and Renewable Energies (EVER), 2017 Twelfth International Conference on*, 2017, pp. 1-6.
- [154] A. M. Bouzid, P. Sicard, A. Cheriti, J. M. Guerrero, M. Bouhamida, and M. S. Golsorkhi, "Voltage and frequency control of wind-powered islanded microgrids based on induction generator and STATCOM," in *Control, Engineering & Information Technology (CEIT), 2015 3rd International Conference on*, 2015, pp. 1-6.
- [155] R. Peña-Alzola, M. Liserre, F. Blaabjerg, M. Ordonez, and Y. Yang, "LCL-filter design for robust active damping in grid-connected converters," *IEEE Transactions on Industrial Informatics*, vol. 10, pp. 2192-2203, 2014.
- [156] A. Reznik, M. G. Simoes, A. Al-Durra, and S. Muyeen, "\$ LCL \$ filter design and performance analysis for grid-interconnected systems," *IEEE Transactions on Industry Applications*, vol. 50, pp. 1225-1232, 2014.
- [157] M. Liserre, F. Blaabjerg, and S. Hansen, "Design and control of an LCL-filter-based three-phase active rectifier," *IEEE Transactions on industry applications*, vol. 41, pp. 1281-1291, 2005.
- [158] F. Hamoud, M. L. Doumbia, and A. Chériti, "Power factor improvement in WECS using cascade PI control of passive damping LCL-filter," in *Sustainable Mobility Applications, Renewables and Technology (SMART), 2015 International Conference on*, 2015, pp. 1-7.
- [159] F. Hamoud, M. Doumbia, and A. Cheriti, "Hybrid PI-Sliding Mode Control of a voltage source converter based STATCOM," in *Power Electronics and Motion Control Conference and Exposition (PEMC), 2014 16th International*, 2014, pp. 661-666.

- [160] H. Rui, C. Taibin, and Q. Bifu, "Design of sliding mode controller for STATCOM with LCL filter," in *Computer, Mechatronics, Control and Electronic Engineering (CMCE), 2010 International Conference on*, 2010, pp. 80-83.

Appendix A – Parameters of dual stator winding induction motor

<i>Nominal parameters</i>	<i>Quantity</i>	<i>Unity</i>
<i>Power</i>	4.5	KW
<i>Voltage</i>	220	V
<i>Frequency</i>	50	Hz
<i>Speed</i>	3000	tr/min
<i>Pole of pairs number</i>	1	
$R_1=R_2$	3.72	Ω
R_r	2.12	Ω
$L_1=L_2$	22	mH
L_r	6	mH
L_m	0.3672	H
J	0.0625	$Kg.m^2$
K_f	0.001	$N.m.s/rd$

Appendix B – Parameters of dual stator winding induction generator, passive compensator and the load impedance

<i>Symbol</i>	<i>Quantity</i>	<i>Unity</i>
R_{s1}, R_{s2}	1.9	Ω
R_r	2.1	Ω
L_{s1}, L_{s2}	0.0132	<i>H</i>
L_{lr}	0.0132	<i>H</i>
L_{lm}	0.011	<i>H</i>
N_n	1500	<i>tr/min</i>
$C_{s(1,2)}$	40	μF
C_{pc}	10	μF
C_{se}	35	μF
C_{pc}	5	μF
C_{se}	20	
$R_{lod1,2}$	200	Ω
$L_{lod1,2}$	0.05	<i>H</i>

Appendix C – Parameters of the system under study with D-STATCOM and DVR

<i>Symbol</i>	<i>Quantity</i>	<i>Unity</i>
S_s	20	KVA
V_s	220	V
V_{dc}	620	V
V_{se}	176	V
C_d	1100	μF
C_r	2600	μF
L_f	3.2	mH
R_f	0.4	Ω
L_s	0.04	mH
R_s	0.1	Ω
L_{se}	1.1	mH
C_{se}	5.6	μF
R_{se}	4	Ω

Appendix D – Parameters of the system under study with UPQC

<i>Symbol</i>	<i>Quantity</i>	<i>Unity</i>
V_g	220 * sqrt(3)	V
$V_{g,h}$	68	V/phase
F	50	Hz
L_g	0.4	mH
R_g	0.1	Ω
L_{se}	1.1	mH
C_{se1}	5.6	μF
R_{se1}	4	Ω
L_{f1}	5.2	mH
R_{f1}	2.3	Ω
V_{dc}	700	V
$C_{dc1}=C_{dc1}$	1500	μF
S_N	20	KVA

Appendix E – Parameters of the system under study with MC-UPQC

<i>Symbol</i>	<i>Quantity</i>	<i>Unity</i>
V_g	220	V
F	50	Hz
L_g	0.4	mH
R_g	0.1	Ω
L_{p1}	5.36	mH
L_{p2}	0.1	mH
R_p	8	Ω
C_p	6.631	μF
$L_{d1}=L_{d2}$	5.2	mH
$R_{sed(1,2)}$	4	Ω
$C_{sed(1,2)}$	5.6	μF
V_{dc}	700	V

Appendix F – Résumé étendu

F.1 Introduction

L'industrie des éoliennes connaît un progrès rapide avec une puissance tournant autour de 7-8 MW pour les éoliennes de grande puissance. Les prévisions annoncent des éoliennes de 10 à 20 MW et une capacité installée de 800 GW d'ici 2020. Plusieurs normes ont été élaborées pour gérer le comportement des éoliennes. Selon ces normes, même avec l'imprévisibilité des conditions météorologiques et la fluctuation de la vitesse du vent, les éoliennes devraient se comporter comme une centrale électrique traditionnelle en termes de qualité d'énergie. L'éolienne doit également être caractérisée par la possibilité de contrôler les puissances active et réactive fournies et supporter les caractéristiques du réseau, telles que le réglage de la fréquence et l'amélioration du profil de tension. En outre, les fabricants d'éoliennes sont invités à concevoir de nouvelles techniques pour augmenter la capacité de production d'énergie, réduire le coût de maintenance, maintenir l'éolienne connectée au réseau même avec des conditions critiques (Low voltage ride through). Dans ce sens, une des solutions les plus prometteuses est l'utilisation de générateurs multiphasés où le nombre de phases est supérieur ou égal à six. Les machines à induction polyphasées offrent de nombreux avantages, par rapport à leurs homologues triphasés. Que ce soit en mode moteur ou en mode génératrice, les machines multiphasées sont considérées comme une solution viable pour de nombreuses applications telles que la propulsion électrique des navires, la traction, les véhicules électriques et hybrides et les avions. Pour les applications d'énergie éolienne, la génératrice asynchrone à double stator (GASDS) représente plusieurs avantages par rapport à la génératrice triphasée. On peut citer la minimisation des pertes rotoriques et des

ondulations du couple, la grande fiabilité, la forte puissance, la réduction des courants harmoniques dans le rotor, la réduction du courant sans l'augmentation de tension dans chaque phase, la segmentation de la puissance. Dans des travaux antérieurs, les chercheurs ont proposé des topologies dans lesquelles un stator de la GASDS (connecté à un convertisseur statique d'excitation (SEC)) sert à fournir l'énergie réactive nécessaire pour réguler la tension dans les différentes conditions de fonctionnement; tandis que le deuxième stator est connecté au réseau ou avec des charges. (Figure F-1).

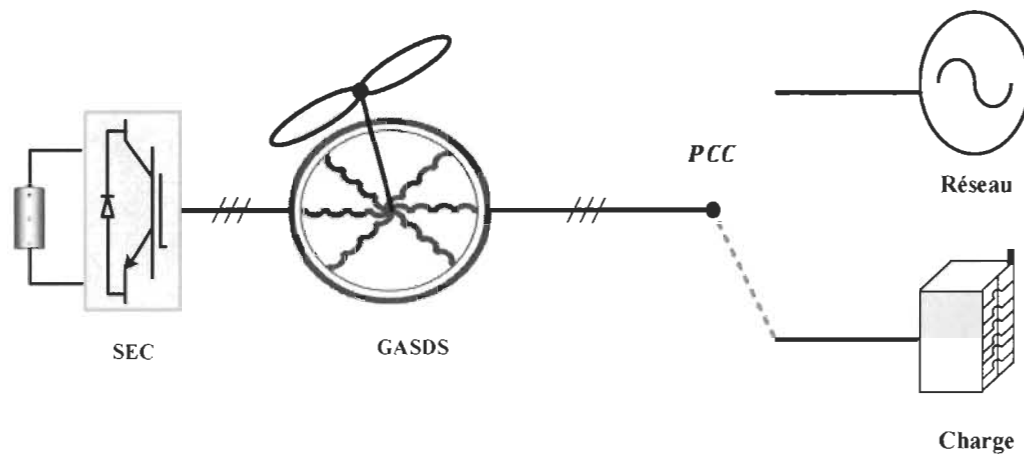


Figure F- 1 Topologie de la GASDS

F.1.1 Problématique de recherche

Au regard de la revue de littérature présentée, nous constatons que la GASDS est une technologie prometteuse pour des applications autonomes et connectées au réseau. Dans l'application à vitesse variable, SE-DSWIG a été entraîné avec une vitesse suffisante qui varie autour de la vitesse nominale. La technique MPPT est utilisée pour optimiser la puissance pour les basses et les hautes vitesses, ce qui signifie que la puissance reste dans les limites nominales acceptables. Les topologies existantes (notamment en fonctionnement à vitesse

variable) ne permettent pas d'assurer un fonctionnement adéquat durant les variations de conditions climatiques, entraînant un effondrement de la tension et l'instabilité de fréquence. Par conséquent, il est impératif de maintenir la génératrice connectée au réseau et d'améliorer l'écoulement de puissance même pendant la variation des conditions climatiques.

F.1.2 Objectifs de recherche

L'objectif de cette thèse est de proposer un nouveau concept de gestion de l'énergie dans les éoliennes à base de GASDS. D'abord la génératrice à double stator est utilisée pour augmenter deux fois la puissance générée par rapport à une génératrice triphasée conventionnelle, et ensuite une nouvelle technique est proposée pour améliorer la qualité de l'énergie dans différents scénarios.

F.1.2.1 Objectifs spécifiques

Les objectifs spécifiques se résument comme suit :

- L'étude approfondie sur la GASDS et ses avantages par rapport à la génératrice asynchrone triphasée.
- L'exploration d'une machine asynchrone à double stator pour l'entraînement à vitesse variable
- La conception et l'introduction d'un compensateur passif basé sur des inductances et capacités utilisées pour améliorer les performances de la GASDS fonctionnant en mode autonome.
- L'étude des systèmes FACTS de types parallèle (D-STATCOM), série (DVR) et hybride (UPQC) et leur capacité à améliorer la qualité de l'énergie dans une éolienne à base de GASDS

- Le dimensionnement, la modélisation et la commande classique et avancée des systèmes FACTS (D-STATCOM, DVR et UPQC)
- La conception et l'introduction des filtres de type LCL entre les FACTS et le réseau afin d'assurer une protection optimale contre les harmoniques produites par les sources et les charges.

F.1.2.2 Contribution de la thèse

Ce travail propose :

Une nouvelle topologie des systèmes éoliennes basé sur la GASDS en mode autonome et connecté au réseau.

- Un compensateur série-parallèle (MC-UPQC) connecté entre le réseau / charge et la génératrice afin de compenser l'imperfection de la tension d'alimentation, améliorer la qualité de l'onde, maintenir la génératrice connectée au réseau (LVRT).
- Un MC-UPQC constitué de trois convertisseurs connectés dos à dos à travers un système de stockage d'énergie, ce qui permet d'échanger de la puissance active entre eux. Deux convertisseurs de MC-UPQC agissent comme un compensateur série (DVR) où chacun d'entre eux est connecté via un transformateur d'injection série aux bornes des deux stators, tandis que le troisième convertisseur se comporte comme un compensateur parallèle (D-STATCOM) connecté entre le réseau le premier stator.

F.1.3 Structure de la thèse

Ce travail est organisé en sept chapitres. Le premier, consacré à l'introduction contient une revue sur les énergies renouvelables et un état de l'art sur la GASDS. Le chapitre 2 évalue les performances d'un moteur asynchrone à double stator. Le moteur asynchrone à six phases est alimenté par deux onduleurs et commandé par une technique de commande vectorielle

indirecte. Le troisième chapitre examine le comportement de la GASDS dans une application autonome, à charge et vitesse variable. Un compensateur passif est conçu pour atténuer les problèmes de la qualité de l'énergie. Le chapitre quatre présente une étude sur les compensateurs actifs de type série et parallèle. Le chapitre cinq étudie une autre catégorie plus avancée de compensateur actif de type série-parallèle appelée déphaseur régulateur universel (UPQC). Le chapitre six a évalué les performances de l'ensemble du système proposé dans cette thèse. Enfin, la conclusion générale et les perspectives de cette dissertation seront au septième chapitre.

F.2 Machine asynchrone à double stator dans le domaine des entraînements à vitesse variable

Principalement, l'idée des machines multiphasé où le nombre de phases est supérieur à six a été soutenue par la révolution des variateurs de vitesse dans les applications de haute puissance. Cette tentative a été boostée par plusieurs avantages provenant de l'augmentation du nombre de phases qui permet d'obtenir une densité de couple élevée avec une faible pulsation et moins d'harmoniques. De plus, l'alimentation électrique dans l'application d'entraînement est segmentée entre deux onduleurs, ce qui signifie plus de degrés de liberté, ce qui implique une grande tolérance aux pannes et une plus grande fiabilité. Ces avantages encouragent les entreprises industrielles à utiliser cette technologie dans plusieurs applications à savoir la nouvelle génération d'avions, la propulsion, les véhicules et la traction électrique.

Dans cette thèse, nous avons présenté une étude sur une machine asynchrone à double stator pour des applications d'entraînement. Une description et une modélisation mathématique de la machine sont proposées. Ensuite, des modèles de simulation sont

développés pour évaluer ces performances dans trois scénarios. En premier cas, le moteur est directement alimenté par le réseau. Deuxièmement, le moteur est alimenté par deux onduleurs de tension contrôlés en boucle ouverte. La vitesse et le couple sont contrôlés en ajustant la fréquence et l'amplitude de la tension du stator en utilisant les onduleurs (Figure F-2). Dans le troisième cas, une commande vectorielle par orientation du flux rotorique est appliquée sur le moteur asynchrone à double stator (Figure F-3). Cette technique montre une bonne performance dans laquelle le couple électromagnétique et le flux du rotor sont totalement découplés et la vitesse suit la référence même avec des variations du couple de charge. Cependant, en tant que contrôleur linéaire, le PI n'est pas robuste face aux variations paramétriques, ce qui nécessite l'utilisation d'un contrôleur avancé.

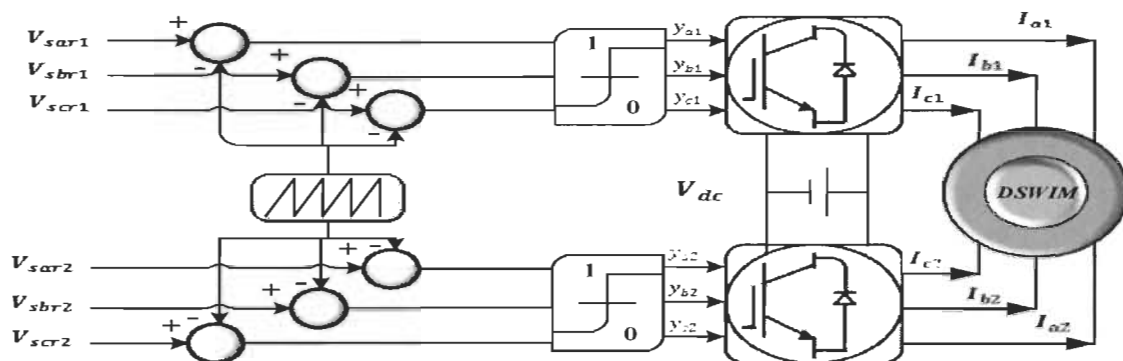


Figure F- 2 Topologie en boucle ouverte

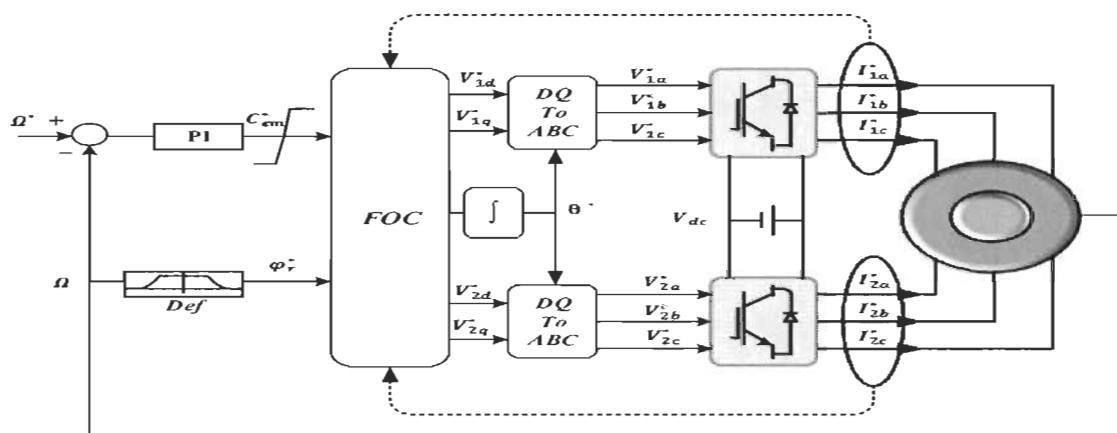


Figure F- 3 Schéma simplifié de la commande vectorielle appliquée sur le moteur

F.3 Evaluation des performances de la GASDS en mode autonome en présence d'un compensateur passif

dans le troisième chapitre, nous avons examiné les performances de GASDS en mode autonome alimentant une charge variable à travers les deux stators. Un compensateur passif est proposé pour atténuer les problèmes d'alimentation liés à la tension en termes de creux de tension et de surtensions.

F.3.1 Description de la GASDS

La génératrice asynchrone à double stator a émergé fortement dans les applications à courant alternatif. Elle présente plusieurs avantages tels que la minimisation des pertes rotoriques et des ondulations du couple, la réduction des courants harmoniques dans le rotor, la réduction du courant sans l'augmentation de tension dans chaque phase, le découplage des puissances active et réactive. La génératrice asynchrone à double stator (GASDS) est comme la génératrice asynchrone (GAS), elle ne génère pas sa propre énergie d'excitation. Pour cela, il faudra lui apporter cette énergie à l'aide d'un banc de capacités connectées aux bornes du stator en plus l'existence d'une vitesse rotorique et la présence d'un flux rémanent dans le fer rotorique, pour l'autoamorçage de la génératrice. Cependant, la génératrice asynchrone à double stator (GASDS) se compose d'un stator portant deux enroulements triphasés identiques et décalés d'un angle électrique $\theta=30^\circ$ et d'un rotor à cage d'écureuil (Figure F-4).

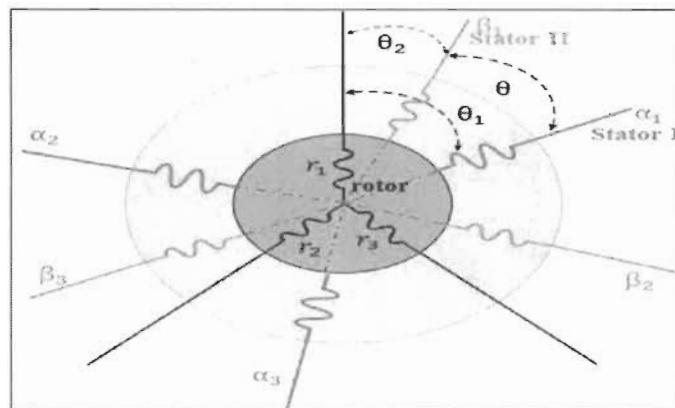


Figure F- 4 Schéma de la GASDS

F.3.2 Compensator Passif

Le compensateur passif (CP) devient une technologie mature, utilisée pour améliorer la qualité de l'énergie. Il implique des composants réactifs basés sur l'inductance et / ou la capacité. Généralement, le compensateur passif est introduit en série ou en parallèle dans le réseau à travers des dispositifs de commutation. Fondamentalement, le CP atténue les problèmes liés à la tension et au courant tels que les creux et les augmentations de tension, les harmoniques, la puissance réactive, le courant du neutre, etc. De plus, le CP améliore l'exploitation de l'énergie et améliore l'écoulement de la puissance dans le réseau. Généralement, l'intervention du CP parallèle se fait par échange de la puissance réactive avec le réseau par l'injection d'un courant réactif ce qui permet le contrôle des caractéristiques de système (courant et tension) au point de couplage commun (PCC). Tandis que le CP série génère une tension de compensation lorsqu'il a une impédance capacitive. En énergie éolienne, le CP a été largement utilisé notamment dans les turbines à vitesse fixe. Par exemple, dans le concept danois où la turbine est directement connectée au réseau, le CP est inséré en parallèle entre l'éolienne et le réseau. dans le troisième chapitre, la GASDS fonctionne en mode autonome, où une charge variable est connectée au stator I et au stator II

comme illustré dans la (Figure F-5). La fluctuation de la vitesse du vent et la variation la charge provoquent des intermittences et des perturbations de tension. Par conséquent, le CP est utilisé pour maintenir la tension à un niveau approprié.

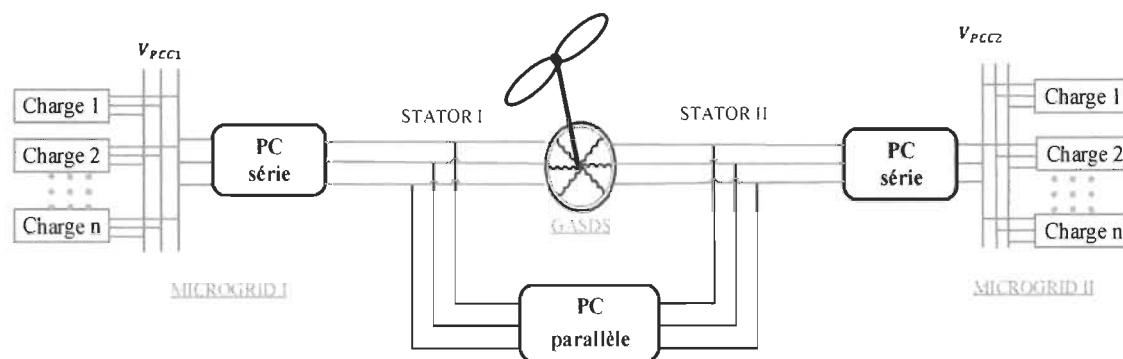


Figure F- 5 GASDS avec les compensateurs série et parallèle

À partir des résultats obtenus, la GASDS montre une bonne performance dans différents modes de fonctionnement et donne la possibilité de construire plusieurs topologies. Le compensateur passif, en particulier l'hybride (série-parallèle en même temps), a bien amélioré la stabilité du système d'alimentation et a atténué la fluctuation de la tension. Néanmoins, le compensateur passif doit être adapté à chaque intervention, en fonction de la vitesse d'entraînement et de la taille de la charge. L'inconvénient de cette technique est sa lenteur par rapport à la variation de rapidité de la charge et des conditions météorologiques. Donc, une nouvelle technique est nécessaire pour permettre une meilleure adaptation à ces exigences telles que les systèmes D-FACTS.

F.4 Étude des compensateurs actifs de types parallèle (D-STATCOM) et série (DVR) pour la compensation de la puissance réactive et les fluctuations de la tension

Le concept de la qualité d'énergie préoccupe l'attention des fournisseurs. Pour les consommateurs, une bonne qualité d'énergie signifie l'obtention de services sans avoir des coupures d'électricité. Bien qu'une perturbation de courte durée ne peut pas provoquer une interruption de l'électricité, mais sûrement elle peut endommager des biens coûteux. Les systèmes FACTS sont en bonne position pour remédier ces problèmes. Les systèmes FACTS peuvent être classés en trois catégories:

- Parallèle (D-STATCOM)
- Série (DVR)
- Hybride (UPQC)

dans le quatrième chapitre, nous avons fait une étude sur les compensateurs actifs à base de D-STATCOM et de DVR

F.4.1 Compensateur parallèle de type D-STATCOM

Le D-STATCOM a la même structure qu'un convertisseur cc-ca de tension triphasée. Il est principalement utilisé pour la compensation de l'énergie réactive afin de maintenir la tension à des valeurs désirées. Le D-STATCOM est couplé au réseau par l'intermédiaire d'un transformateur shunt comme il est présenté dans la Figure F-6.

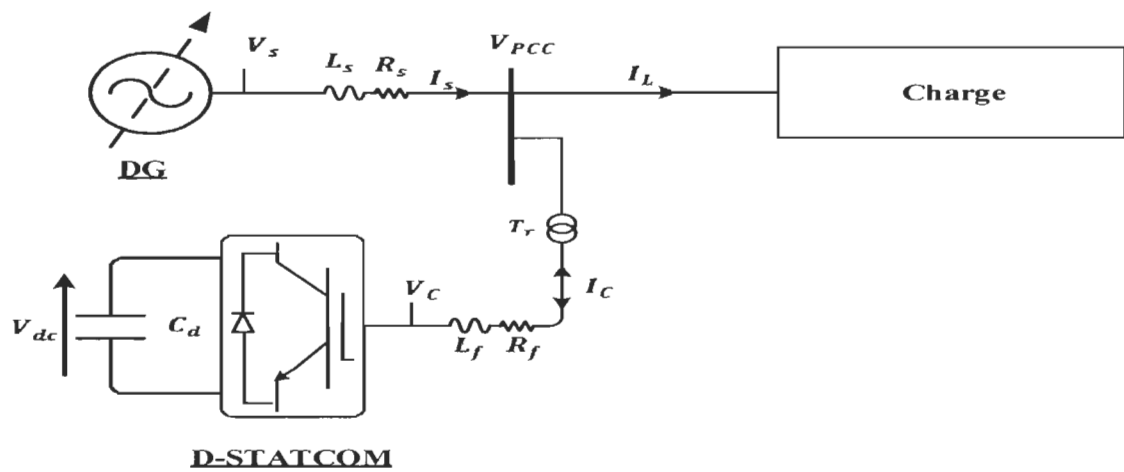


Figure F- 6 Configuration du D-STATCOM

Le transfert de la puissance réactive entre le réseau et le STATCOM se fait par le contrôle de la tension de V_c . Si la tension de sortie de STATCOM est supérieure à la tension de réseau (PCC), la puissance réactive se propage du compensateur au réseau. Il se propage dans le sens contraire dans le cas où la tension de réseau est supérieure à la tension de sortie de D-STATCOM. Dans le cas où les deux tensions sont égales, la puissance réactive échangée est nulle.

F.4.2 Compensateur série de type DVR

Le DVR est le dispositif le plus performant dans sa catégorie. Il est formé d'un convertisseur triphasé connecté au réseau à travers un transformateur série. Le principe de fonctionnement de ce dispositif est basé sur l'introduction d'une tension de même fréquence et à phase variable dans le réseau (Figure F-7).

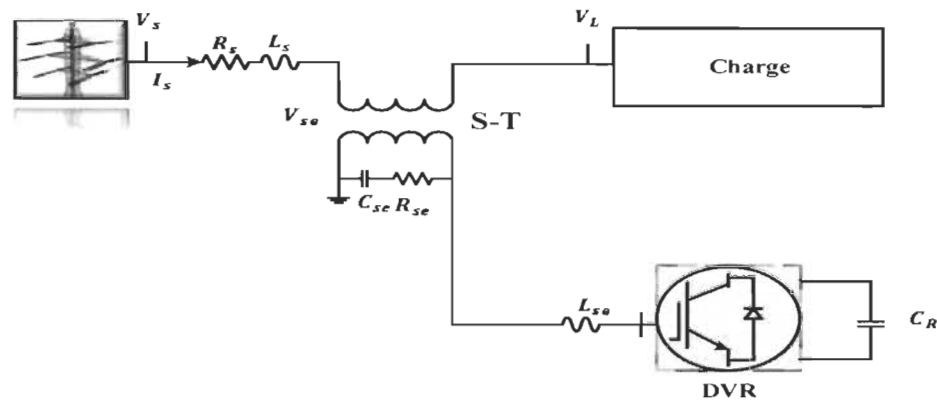


Figure F- 7 Configuration du DVR

Pour évaluer le comportement du D-STATCOM et du DVR face au problème de la qualité d'énergie, nous avons développé dans Matlab®/SimPowerSystems les modèles présentés aux Figure F-6 et Figure F-7. Nous avons remplacé la GASDS par une source de tension triphasée alimentant une charge. Des filtres passifs de type L et LC sont insérés respectivement entre les compensateurs parallèle (D-STATCOM) et série (DVR) et le réseau électrique. Le D-STATCOM est contrôlé par une technique de mode glissant, tandis que le DVR avec une simple commande par hystérésis compare les valeurs désirées et mesurées. À partir des résultats obtenus, nous observons que les stratégies utilisées apportent une amélioration à la stabilité du réseau par le contrôle de la puissance réactive.

F.5 Étude d'un compensateur hybride série-parallèle de type UPQC pour l'amélioration de la qualité de l'onde

L'UPQC (déphaseur régulateur universel) est l'élément le plus performant dans toutes les catégories de D-FACTS. L'UPQC est un système de haut degré de liberté qui peut contrôler à la fois la puissance active et réactive dans le réseau et compense tous les problèmes de qualité d'énergie. Il est constitué de deux convertisseurs de tension connectés

dos à dos à travers un bus continu comme il est montré dans la Figure F-8. Un convertisseur (D-STATCOM) connecté avec le réseau à travers un transformateur shunt et l'autre convertisseur (DVR) connecté au réseau par l'intermédiaire d'un transformateur série. L'UPQC donne la possibilité de contrôler les caractéristiques du réseau (tension, impédance de la ligne, angles de phase et courant).

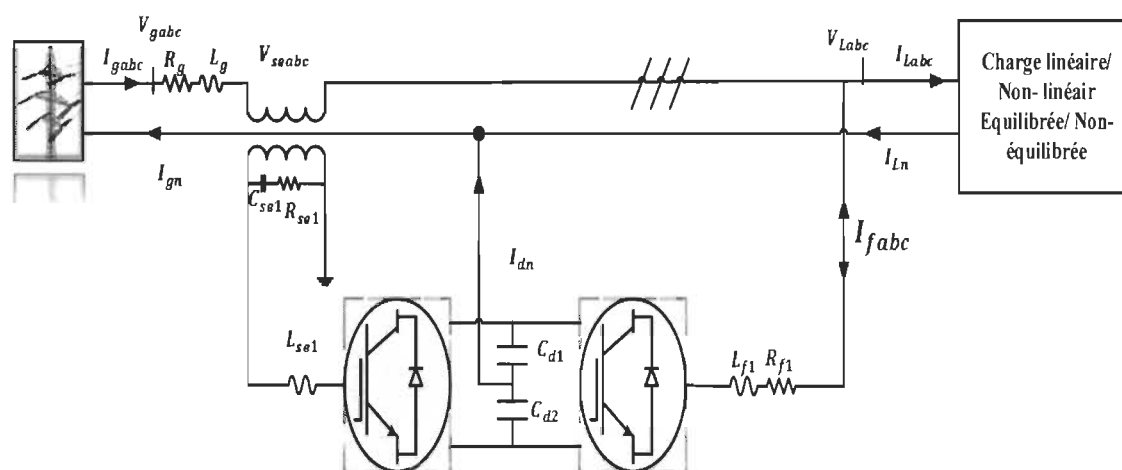


Figure F-8 Topologie de l'UPQC

dans le cinquième chapitre, l'UPQC est constitué de deux convertisseurs de type NPC (Neutral Point Clamped Converters). La partie parallèle (D-STATCOM) va se comporter comme un filtre actif pour traiter les harmoniques, éliminer le courant du neutre, équilibrer le courant de réseau, et compenser la puissance réactive. Par contre, l'autre partie va jouer le rôle d'un DVR qui va compenser les problèmes liés à la tension en termes des creux, surtension, perturbation, etc. Le DVR est supervisé par une technique en cascade dans le référentiel de Park (Synchronous Reference Frame Theory). Cette technique est basée sur la comparaison entre la tension de la source et la tension aux bornes de la charge d'un côté et entre la tension de la charge et la référence d'autre part comme présentée dans la Figure F-9. L'autre partie de l'UPQC (D-STATCOM) est contrôlée par la théorie des puissances active

et réactive. L'idée de cette technique est de décomposer les signaux de courant et de tension en séquences positive, négative et zéro. Le rôle principal du D-STATCOM est de corriger les composantes négative et zéro, puisque c'est la composante positive qui apporte l'énergie à la charge. La technique de contrôle appliquée sur le D-STATCOM est illustrée dans la Figure F-10.

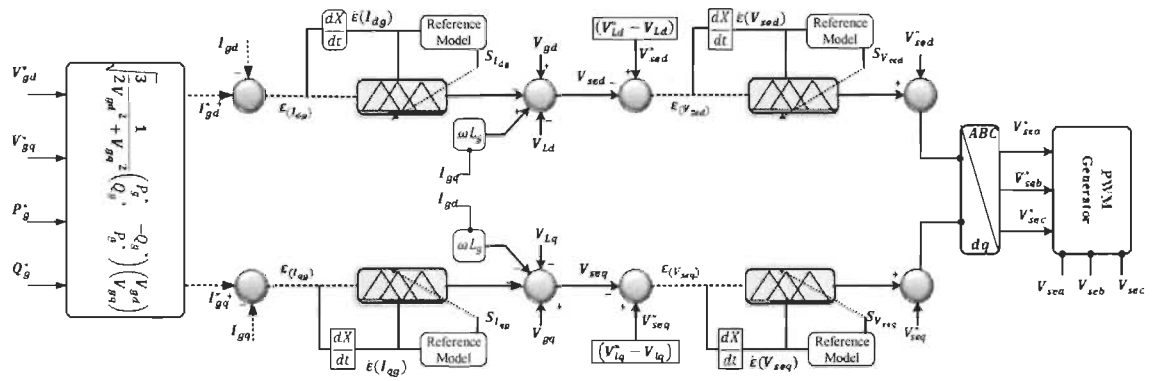


Figure F- 9 Stratégie de commande appliquée au DVR

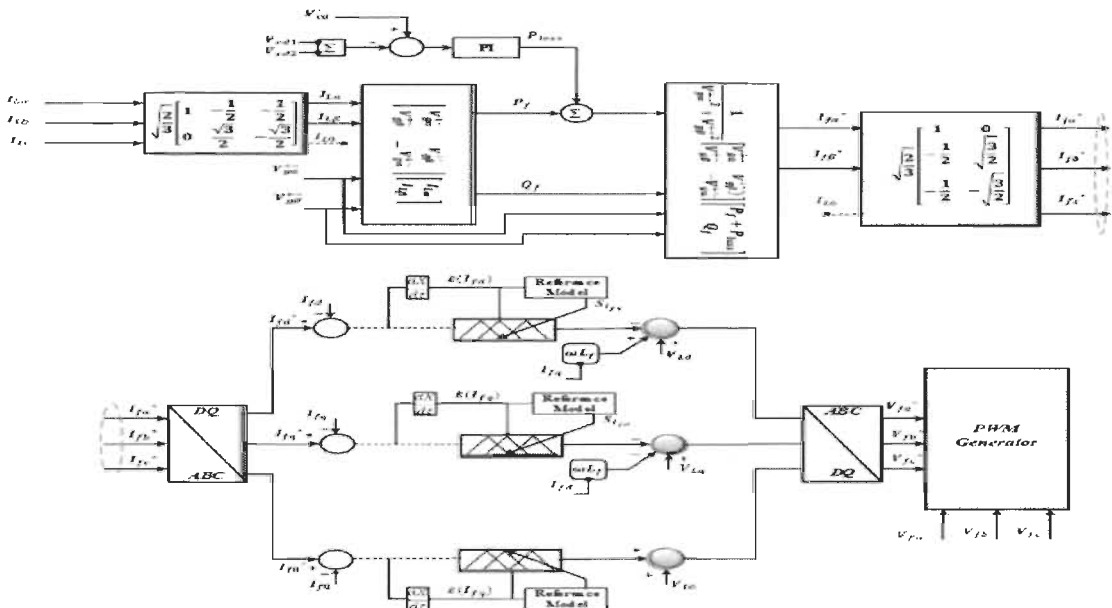


Figure F- 10 Stratégie de commande appliquée au DSTACOM

Généralement, la technique de contrôle classique à base du PI est largement utilisée pour superviser la performance du système étudié. Cependant, plusieurs articles ont prouvé que le contrôleur linéaire est inexact dans des cas où le système est non linéaire. En plus, le contrôleur PI est inexact et moins robuste face aux variations des paramètres internes. Pour remédier à ces problèmes, nous avons proposé une technique de contrôle basée sur la logique floue adaptative (LFA). Principalement, la technique de la LFA apporte une tolérance élevée à l'incertitude, améliore la réponse de l'élément commandé en termes de suivi de référence et réduit les caractéristiques indésirables (dépassement, temps de montée, etc.) sans exiger un modèle exact du système à contrôler. En se basant sur les résultats obtenus, nous constatons que l'UPQC a un bon comportement face aux scénarios étudiés. La progression naturelle de ce travail est d'étudier la performance de l'UPQC dans les systèmes d'énergie renouvelable.

F.6 Étude de l'UPQC pour l'amélioration des performances d'une GASDS

Cette thèse a établi une nouvelle topologie de système de conversion d'énergie éolienne basée sur la GASDS connectée au réseau électrique et en mode autonome en même temps. L'idée de cette stratégie repose sur l'exploitation du D-FACTS pour l'amélioration de la qualité de l'énergie et l'amélioration des possibilités de maintenir la génératrice connectée au réseau sans la supervision mécanique de l'éolienne. Par conséquent, un compensateur actif universel constitué de trois convertisseurs (Multi-Converter based Unified power Quality Conditioner) est utilisé. MC-UPQC implique trois convertisseurs reliés dos à dos à travers un système de stockage d'énergie. Deux d'entre eux sont connectés en série aux bornes de la GASDS jouant le rôle de DVR et traitent tous les problèmes liés à la tension, tandis que l'autre agit comme un D-STATCOM et est connecté en shunt (parallèle) aux bornes du stator qui est relié au réseau comme présenté à la Figure F-11. Une technique de contrôle en cascade

dans le référentiel de Park (Synchronous Reference Frame Theory) est utilisée pour superviser la partie série de MC-UPQC, ainsi que la partie shunt qui est commandée par une technique de contrôle en mode glissant. La partie shunt (D-STATCOM) est synchronisée en même phase que le réseau à travers la technique de PLL. Par contre, le DVR a la même phase que le rotor de la génératrice. Pour détecter l'angle de flux rotorique, nous avons utilisé une technique vectorielle comme illustrée dans la Figure F-12. L'analyse des résultats obtenus conduit à conclure que le MC-UPQC améliore les performances de la GASDS que ce soit en mode autonome ou bien connectée au réseau électrique.

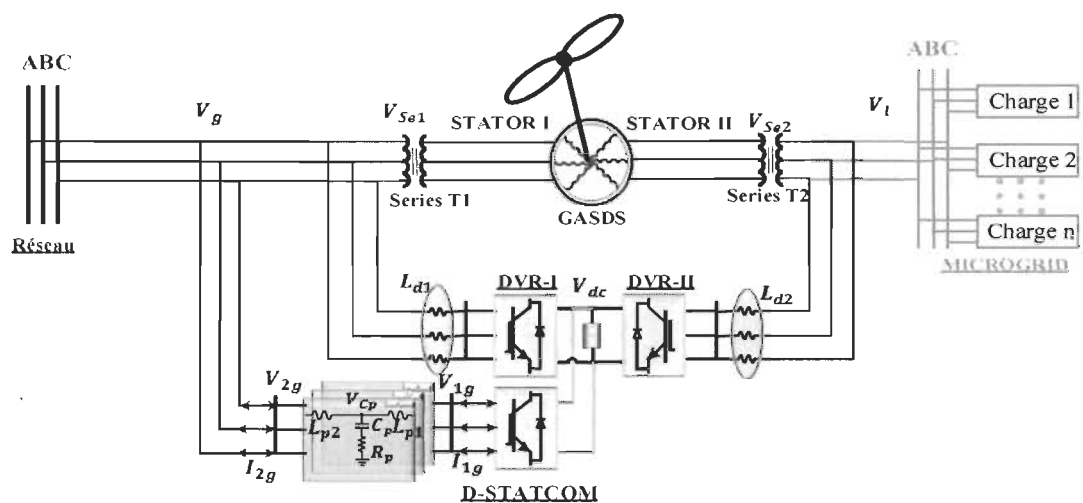


Figure F- 11 GASDS avec MC-UPQC

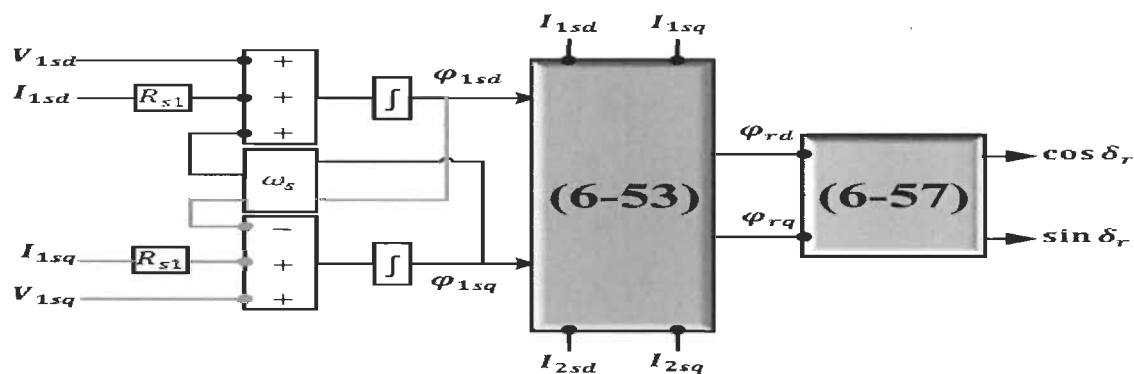


Figure F- 12 Schéma fonctionnel d'estimation du sinus et du cosinus

F.7 Conclusion

Cette thèse propose un nouveau concept pour améliorer la qualité de l'énergie d'une éolienne à base de GASDS. Il vise deux objectifs. Le premier concerne l'exploitation de la GASDS pour doubler la puissance générée par rapport à une simple génératrice triphasée. Le deuxième porte sur la proposition d'une nouvelle technique de gestion de l'énergie en utilisant un compensateur actif (MC-UPQC) qui est constitué de trois convertisseurs.

Pour les travaux futurs, nous recommandons la possibilité d'utiliser une autre source d'énergie renouvelable telle que le photovoltaïque (PV) pour charger le système de stockage d'énergie utilisé du côté DC du MC-UPQC pour étendre la durée d'intervention du compensateur. Le PV sera utilisé pour alimenter le bus continu et pour produire également une puissance active qui sera injectée au réseau à travers la partie shunt du MC-UPQC.